

Imperial College
London

Effect of Polymer and Metal Oxide Properties on Hybrid Light Emitting Diodes

Jorge Costa Dantas Faria

**Centre for Plastic Electronics
Imperial College London**

May 2016

A thesis submitted in partial fulfillment of the requirements for
the degree of
Doctor of Philosophy

Declaration of Originality

I declare that the work contained in this thesis is my own unless stated otherwise or referenced specifically in-text. Where work was done in collaboration with others, the contribution and the persons who carried it out are stated. The copyright of this thesis rests with the author and is made available under a Creative Commons Attribution Non-Commercial No Derivatives licence. Researchers are free to copy, distribute or transmit the thesis on the condition that they attribute it, that they do not use it for commercial purposes and that they do not alter, transform or build upon it. For any reuse or redistribution, researchers must make clear to others the licence terms of this work.

© Copyright by Jorge Costa Dantas Faria, 2016.

All rights reserved.

Abstract

Hybrid organic/inorganic light-emitting diodes (HyLEDs) combine thin, metal oxide layers together with light-emitting organic semiconductors to create devices that are more resilient to ambient conditions than standard devices. In this thesis, HyLED performance is measured as a function of the individual organic and oxide layer properties with the aims of addressing several perceived gaps within reported literature and to consequently optimise future device design.

Reported herein are the results of the insertion of a vertical zinc oxide nanorod array as a non-planar, bottom-cathode electron injection layer. Using facile solution-processing methods, a well-aligned and uniform array was deposited into which the light emitting polymer poly(9,9'-dioctylfluorene-co-benzothiadiazole) (F8BT) was then melt-processed to create a massive, 3D interfacial contact area for electron injection. This study recorded, for the first time, efficiency and luminance values for a vertical nanorod-based LED with maximum figures of 1.66 cd/A and 8602 cd/m² showing their potential for display and lighting applications. The successful demonstration of these nanorod HyLEDs was due to the insertion of a poly[(9,9'-dioctylfluorenyl-2,7-diyl)-co-(4,4'-(N-(4-sec-butylphenyl)diphenylamine))] (TFB) at the F8BT/anode interface to block electrons and reduce the probability of interfacial exciton dissociation. Using post-deposition annealing and solution processing, a robust method of casting TFB onto F8BT without the need for lift-off steps is presented. In planar devices, the insertion of TFB increases the maximum recorded efficiencies from 0.024 to 1.0 cd/A and its role as an optical emission tuning layer was also demonstrated; by simply varying the layer thickness the F8BT electroluminescence was tuned from green emission to orange. Finally, the molecular weight of F8BT was seen to significantly influence the performance of HyLEDs, with six separate batches ranging from 36 to 300 kg/mol providing a systematic device study. Importantly, these batches were extracted from a single commercial source using gel permeation chromatography to negate the possible influence of different synthesis routes and chain ends.

The thesis is organised into six chapters. Chapter 1 focuses on the principles behind device design and operation with an overview of the current state of HyLED literature and a discussion of the principle materials studied. Chapter 2 provides a general description of the experimental procedures and techniques used throughout. Chapters 3 to 5 each focus on a specific experimental investigation and are largely self-contained with each presenting - along with a discussion of the results - a literature review, a list of aims and an experimental section particular to the study conducted. Finally, Chapter 6 provides general concluding remarks, expanding on the ideas of further work discussed within Chapters 3-5.

Acknowledgements

I am eternally grateful to both of my supervisors, Dr Alasdair Campbell and Dr Martyn McLachlan for all of their wisdom, patience and advice over the last four years. It is because of them that I was able to work on such a variety of interesting topics, but with the freedom to pursue my own interests within them. They gave me the opportunities to present my work at international events and collaborate on international projects, whilst always pushing me out of my comfort zone. Above all, I most value their belief in me, especially during the times when I severely doubted my capabilities to undertake and continue this PhD - and such times were many! Thank you, both.

I have to also thank Dr Xuhua Wang for all the hours she spent (and continues to spend) on servicing the EXSS glovebox and evaporators. Without her constant efforts, I would have nothing to present. Her expansive knowledge on device fabrication and measurement was invaluable and her questioning of my work kept me constantly on my toes. I have to also thank Dr Paul Stavrinou for his advice on the optical effects of OLEDs, particularly for pointing me towards reflectance measurements. Also, Chapter 5 only exists because Dr Bob Schroeder agreed to purify our commercial polymer - he has my deepest thanks especially as no-one had imagined how laborious and time-consuming the purification of this polymer would be! I thank Dr Lethy Jagadamma for seeing the value in my work and for showing me a whole host of experimental techniques that I had been previously unaware of. Thanks, too, to the many people who helped me to get trained on various bits of equipment for their time, ongoing advice and expertise: Ecaterina Ware and Dr Mahmoud Ardakani for help with SEM; Richard Sweeney for his help on XRD; and Dr Ying Yang for all the initial device fabrication training. In physics mechanical workshop, I owe my thanks to both Steve Cussell and Martin Pettifer for constructing various bits of experimental equipment.

I would have lost my sanity a long time ago were it not for the lovely people of the McLachlan group: Jon Downing for his incredible patience at having to put up with a physicist who had never stepped into a wet chemical lab before; Rob Hewlett for endless discussions on music (but not the Mexican jokes); Kirsty Roy for always pushing me to try new things; Yoann Porte for all his delicious baking and being my bouldering buddy; and also Claire Burgess, Rob Maller, Becky Kilmurray, Maurizio Morbidoni, Bob Xu, Jiaqi Zhang, Xuemei Zhang, Joe Franklin and Tian Du for generally useful discussions and often surreal office banter. I am very lucky to have started my second time at Imperial College with my fellow Plastic Electronics cohortees and, though it became harder to stay in touch once all the pressures of PhD life truly kicked in, any time I would meet up with Jasvir Bhamrah, Joby Hollis, Abby Casey, Celia Pacheco Moreno, George Richardson, Alex Ramadan and Sarah Holliday I would frequently leave with my face hurting from having laughed so hard. And a massive thank you to Lisa Cheung for looking after all of us.

Finally, I owe so much to my family. My mum, Teresa, for her love, support and for teaching me to value those around me; and to my sisters, Sofia and Laura, for constantly reminding me of the world outside academia. Lastly, thank you to my wonderful boyfriend, Jaime, for his incredible understanding and patience and for sticking with me despite distance and unsociable work hours for the past 4 years. Thank you.

Foreword

The work discussed in this thesis was carried out at Imperial College London between October 2012 and September 2015. A lot of the initial device and nanorod array characterisation was completed prior to the commencement of this work and can be found in the Masters thesis titled "Optimisation of Zinc Oxide as a Charge Injection Layer for Hybrid Organic-Inorganic Light Emitting Diodes" and completed in September 2012 at Imperial College London. Where needed to support the discussion of the current work, this previous report is cited and the relevant results included in Appendix A for the convenience of the reader. All work was carried out by me with the exception of polymer purification and gel permeation chromatography procedure discussed in Appendix C which resulted in the polymer fractions listed in Table 5.1 in Chapter 5; this work was carried out by Dr Bob Schroeder.

The work of Chapters 3 and 4 of this thesis have been published in the following articles:

- **Faria, J. C. D.**; Campbell, A. J.; McLachlan, M. A.; "*ZnO nanorod arrays as electron injection layers for efficient organic light emitting diodes*" Adv. Fun. Mater. 2015.
- **Faria, J. C. D.**; Campbell, A. J.; McLachlan, M. A.; "*Fluorene Copolymer Bilayers for Emission Colour Tuning in Inverted Hybrid Light-Emitting Diodes*" J. Mat. Chem. C. 2015.

Furthermore, a book chapter was contributed to a reference text during this period of research and relevant content, including figures, are utilised in Chapter 1:

- **Faria, J. C. D.** and McLachlan, M. A. "*Materials for LEDs and OLEDs*" in P. P. Edwards, V. L. Kuznetsov & D. Payne (Eds), "*Advanced Materials for a Sustainable Energy Future*", Chichester, West Sussex, John Wiley & Sons, Ltd (In press).

The following work is not discussed in this thesis, but was completed during this period of research in collaboration with others:

- Zhang, J.; **Faria, J. C. D.**; Morbidoni, M.; Porte, Y.; Harrabi, K.; and McLachlan, M. A. "Low Temperature Solution Porcessed ZnO Interlayers ZnO as a Cathodic Interlayer for Inverted Polymer Solar Cells" Adv. En. Mater. 2016.
- Campbell, A. J.; Rawcliffe, R.; Guite, A.; **Faria, J. C. D.**; Mukherjee, A.; McLachlan, M. A.; Bradley, D. D. C.; "*Charge-carrier density independent mobility in amorphous fluorene-tertiaryamine copolymers*" Adv. Fun. Mater. 2016
- Jagadamma, L. K.; Al-Senani, M.; El Labban, A.; Gereige, I.; Ndjawa, G. O. N.; **Faria, J. C. D.**; Kim, T.; Zhao, K.; Anjum, D. H.; McLachlan, M. A.; Beaujuge, P. M.; Amassian, A.; "*Polymer Solar Cells with Efficiency >10% Enabled via a Facile Solution-Processed Al-doped ZnO Electron Transporting Layer*" Adv. Energy Mater. 2015.

- Jagadamma, L. K. Hu, H., Kim, T., Ndjawa, G. O. N. Mansour, Labban, E. L., **Faria, J. C. D.** Mahmood, K., Zhao, K., Anjum, D. H., McLachlan M. A. and Amassian, A. "*Solution-Processed Molybdenum Oxide Top Interlayers for Highly Efficient Reflective and Semitransparent Organic Solar Cells*" Nano Energy (submitted).

Also, the following conference presentations were given in support of the work discussed:

- **Faria, J. C. D.**; Campbell, A. J.; McLachlan, M. A.; "*Fluorene Copolymer Bilayers for Emission Colour Tuning in Inverted Hybrid LEDs*" Invited Oral Presentation, Symposium on Recent Advances in Organic Electronics, Hong Kong, November 2014.
- **Faria, J. C. D.**; Campbell, A. J.; McLachlan, M. A.; "*Fluorene Copolymer Bilayers for Emission Colour Tuning in Inverted Hybrid LEDs*" Oral Presentation, SID Organic Electronics, London, September 2014.
- **Faria, J. C. D.**; Campbell, A. J.; McLachlan, M. A.; "*Tuning Emission Colour of Hybrid LEDs – the Influence of Polymer and Metal Oxide Thickness*" Poster, SPIE Optics and Photonics conference, San Diego, August 2014.

Abbreviations

AFM	Atomic Force Microscopy
Alq ₃	Tris(8-hydroxyquinolino)aluminium
BHJ	Bulk-heterojunction
CB	Conduction band
CE	Current Efficiency
Cr	Chromium
DSC	Differential scanning calorimetry
DI	De-ionised
E_g	Energy band-gap
EIL	Electron injecting layer
EL	Electroluminescence
EQE	External quantum efficiency
F8BT	Poly(9,9'-dioctylfluorene-co-benzothiadiazole)
FWHM	Full width at half maximum
GIXS	Grazing-incidence X-ray scattering
GPC	Gel permeation chromatography
η_{CE}	Current Efficiency, measured in cd/A
η_{PE}	Power Efficiency, measured in lm/W
$\eta_{PE,CE}$	Power Efficiency, measured in lm/W, at maximum CE
HE	High-energy emissive state
HIL	Hole-injection layer
HMW	High-molecular weight
HOMO	Highest occupied molecular orbital
HTL	Hole-transport layer
HyLED	Hybrid organic/inorganic light-emitting diode
IL	Injection layer

iLED	Inorganic light-emitting diode
IQE	Internal quantum efficiency
ITO	Indium tin oxide
J	Current density
J_{CE}	Current density at maximum CE
J_{SC}	Short-circuit current
λ_{abs}	Absorption Peak
L_v	Luminance
$L_{v,max}$	Maximum luminance
$L_{v,CE}$	Luminance at max current efficiency
LE	Low-energy emissive state
LED	Light-emitting diode
LEP	Light-emitting polymer
LMW	Low-molecular weight
LUMO	Lowest unoccupied molecular orbital
MCE	Microcavity Effect
M_e	Molecular mass between entanglements
M_n	Number average molecular weight
MoO _x	Molybdenum Oxide
M_w	Weight average molecular weight
MW	Molecular weight
n_r	Refractive index
NRA	Nanorod array
OLED	Organic light-emitting diode
OPV	Organic photovoltaic
OSC	Organic semiconductor
P3HT	Poly(3-hexylthiophene-2,5-diyl)
PCE	Power conversion efficiency

PE_{CE}	Power efficiency at max current efficiency
PEI	Polyethylenimine
PEDOT:PSS	Poly(3,4-ethylenedioxythiophene)-poly(styrenesulfonate)
PFO	Polyfluorene
PL	Photoluminescence
PLED	Polymer light-emitting diodes
PLQE	Photoluminescence quantum efficiency
PPV	Poly(p-phenylene vinylene)
RZ	Recombination zone
SCLC	Space charge limited current
SEM	Scanning electron microscopy
SIC	Silicon carbide
SMOLED	Small molecular organic light-emitting diode
SMU	Source measure unit
SSL	Solid state lighting
TFB	Poly[(9,9-dioctylfluorenyl-2,7-diyl)-co-(4,4'-(N-(4-sec-butylphenyl)diphenylamine)]
T_g	Glass-transition temperature
T_m	Melting temperature
UV	Ultraviolet
VB	Valence band
V_{CE}	Voltage at max current efficiency
V_{L-on}	Light turn-on voltage
V_{on}	Device turn-on voltage
XRD	X-ray diffraction
ZnO	Zinc oxide
ZnS	Zinc sulfide

Contents

ABSTRACT.....	ii
ACKNOWLEDGEMENTS.....	iii
Foreword.....	iv
Abbreviations.....	vi
Chapter 1: Introduction	1
1.1. A History of Light-Emitting Diodes.....	1
1.2. Origin of Electrical Behaviour in Organic Semiconductors.....	4
1.2.1. Hybridisation of Carbon Orbitals	4
1.2.2. Polarons and Excitons.....	5
1.3. Optical Processes in OSCs	7
1.4. Charge Transport	10
1.5. Charge Injection.....	12
1.5.1. Space Charge Limited Current.....	14
1.6. Organic Light-Emitting Diodes.....	16
1.6.1. Operating Principle	16
1.6.2. OLED Efficiency	17
1.6.2.1. Charge Balance	18
1.6.2.2. Outcoupling of Light.....	19
1.7. Characterisation of Light Emission.....	20
1.8. HyLEDs.....	22
1.9. Materials	26
1.9.1. ZnO.....	26
1.9.2. Conjugated Polymers	28
1.9.2.1. F8BT.....	28
1.9.2.2. TFB.....	30
1.10. Summary	31
1.11. References	31
Chapter 2 – Experimental Methods	37
2.1. Spin Coating	37
2.2. General Device Fabrication.....	37
2.2.1. Substrate Cleaning.....	37
2.2.2. Planar ZnO Deposition	38

2.2.3.	Polymer Solutions	39
2.2.4.	HyLEDs	39
2.2.5.	Single-Carrier Devices	40
2.2.5.1.	Electron-only Devices	40
2.2.5.2.	Hole-only Devices	41
2.3.	Device Characterisation	41
2.3.1.	Efficiency and Luminance Measurements	41
2.3.2.	Electroluminescence and Chromaticity Measurements	41
2.4.	Optical Characterisation	41
2.4.1.	UV-vis Spectra	41
2.4.2.	Photoluminescence Spectra and PLQE	42
2.4.3.	Reflectance	44
2.5.	Material Characterisation	44
2.5.1.	Thickness Measurements	44
2.5.2.	Scanning Electron Microscopy	45
2.5.3.	Atomic Force Microscopy	46
2.5.4.	X-ray Diffraction	47
2.5.5.	Differential Scanning Calorimetry	48
2.5.6.	Contact Angle	50
2.6.	References	50
Chapter 3 – ZnO Nanorod Arrays as an Electron Injection Layers for Hybrid Light-Emitting Diodes		52
3.1.	ZnO Nanorods in Literature	52
3.1.1.	Growth and Characterisation	52
3.1.2.	Applications: Organic Photovoltaics	54
3.1.3.	Applications: Light-Emitting Diodes	55
3.2.	Growth and Characterisation of the ZnO Nanorod Array	58
3.3.	ZnO NRA HyLED Devices	59
3.3.1.	Device Preparation	59
3.3.2.	Preliminary Devices	60
3.3.3.	Optimisation with Electron Blocking Layer	62
3.4.	Causes of Device Variability	66
3.5.	Further Work	66
3.5.1.	Electron-Only Devices	67

3.5.2.	F8BT Chain Packing Due to the NRA.....	69
3.5.3.	Effect of Nanorod Length on Devices.....	74
3.6.	Conclusions	74
3.7.	References	75
Chapter 4 – Copolymer Fluorene Bilayers for Colour Tuning in Inverted HyLEDs		78
4.1.	Relevant Background	78
4.1.1.	Deposition of Multilayer Devices	78
4.1.1.1.	TFB/F8BT and F8BT/TFB Bilayers.....	80
4.1.2.	Optical Interference Effects in OLEDs.....	80
4.2	Bilayer Deposition.....	82
4.2.1.	Contact Angle and Film Thickness	82
4.2.2.	F8BT/TFB Bilayer for Planar Devices.....	85
4.2.3.	Impact of F8BT Morphology on Bilayer Formation.....	86
4.2.4.	Bilayer Casting Procedure	88
4.3.	Device Characterisation	89
4.3.1.	Emission Spectra	90
4.3.2.	Evidence of Weak Microcavity Effects.....	91
4.3.3.	Efficiency and Luminance Characterisation.....	95
4.4.	Device Operation	99
4.5.	Conclusions and Outlook	101
4.6.	References.....	102
Chapter 5 – Effects of Polymer Molecular Weight on Device Performance.....		106
5.1.	Literature	106
5.1.1.	Polymer Properties as a Function of Molecular Weight.....	106
5.1.2.	Influence of Molecular Weight on Device Performance	108
5.1.2.1.	Polymers for Organic Photovoltaics	108
5.1.2.2.	Polymers for Light-Emitting Diodes	110
5.2.	Experimental Methods.....	113
5.2.1.	F8BT Purification and Fractionation	113
5.2.2.	Solution Concentration vs. Film Thickness	114
5.2.3.	Device Fabrication.....	115
5.2.4.	Material Characterisation	116
5.3.	Results of Material and Optical Characterisation	116
5.3.1.	Thermal Analyses	116

5.3.1.1.	Determination of Crystalline Fraction	118
5.3.2.	X-ray Diffraction	120
5.3.3.	Absorbance and Photoluminescence Spectra	122
5.4.	Device Characterisation	125
5.4.1.	HyLEDs	125
5.4.1.1.	F8BT-only HyLEDs	125
5.4.1.2.	Bilayer HyLED.....	127
5.4.2.	PLEDs	128
5.4.3.	Summary of Device Results	129
5.5.	Charge Transport	129
5.5.1.	Unipolar Current Measurements	130
5.5.2.	Dependence of Charge Transport Parameters on Molecular Weight	132
5.5.2.1.	Determination of Charge Transport Regime	132
5.5.2.2.	Estimation of Built-In Potential.....	136
5.5.2.3.	Extraction of hole β and μ_0	137
5.5.3.	Summary of Single Carrier Devices	140
5.6.	Outlook and Conclusion	143
5.7.	References.....	144
Chapter 6 – General Conclusions and Future Work		147
6.1.	References	149
Appendix A.....		151
Appendix B.....		154
Appendix C		155
Appendix D.....		157
D.1.	F8BT-Only HyLED Devices.....	157
D.1.1.	As-cast devices.....	157
D.1.2.	T_g devices	161
D.1.3.	T_m devices	163
D.2.	Bilayer HyLED Devices	167
D.3.	Standard PLED Devices	171
D.3.1.	As-cast devices.....	171
D.3.2.	T_g devices	174
Appendix E		177

Chapter 1: Introduction

The purpose of this chapter is to review the fundamentals of organic semiconductors (OSCs) and their relevance to the operation of organic light emitting diodes (OLEDs). A brief history of electroluminescence from semiconductor materials is provided comparing the development of the more established inorganic light emitting diodes (iLEDs) against the rapid rise in the performance of their organic counterparts over the past three decades. The combination of thin metal oxide films as transporting layers with light-emitting OSCs has resulted in a relatively new class of LEDs which promises to enhance the stability and lifetime of otherwise all-organic OLEDs whilst providing an alternative low-cost, rapid solution-processing route to device fabrication unachievable with iLEDs. Since the first demonstration of these so-called hybrid organic-inorganic LEDs (HyLEDs) a decade ago, the technology has positioned itself as a totally viable route to simplified, more ambient stable diodes; a general overview of the development of HyLEDs is also given in this chapter. During this PhD, the contribution of a chapter was made to the reference text "Advanced Materials for a Sustainable Energy Future" titled "Materials for LEDs and OLEDs"; some sections and figures here have been adapted from that chapter^[1].

1.1. A History of Light-Emitting Diodes

Electroluminescence (EL) from semiconducting materials was first documented in 1907 when Henry Round reported the emission of light as a result of passing a current through SiC crystals^[2]. He noted the emission of light from biases as low as 10 V, attributing the effect to the applied current. Despite his concluding plea ("The author would be glad of references to any published account of an investigation of this or any allied phenomena") there appears to be no evidence of documented work into this effect until it was once again independently rediscovered by Oleg Losev twenty years later. In this case, Losev published a series of papers exploring the effect of, for instance, temperature and current on the emitted spectrum and going as far as suggesting applications for light relays^[3-5]; he is widely considered to have invented the first LED. With improvements in the growth of semiconductor crystals, the first *practical* LEDs did not emerge until the 1960s with Holonyak and Bevacqua being widely credited for developing the first visible light LED based on doped Ga in 1962 for use in simple indicator applications^[6] along with low-cost red, green and yellow LEDs which followed soon after^[7]. Nowadays, however, inorganic LEDs are used for a wide range of high quality, all-colour lighting and display purposes particularly following the breakthrough discovery of efficient blue LEDs in 1995^[8] - a discovery which awarded its inventors Isamu Akasaki, Hiroshi Amano and Shuji Nakamura the 2014 Nobel Prize for Physics.

As the first inorganic LEDs were being developed, observations of electroluminescence from conjugated organic small molecule crystals were also beginning to emerge. Bernanose, Comte

and Vonaux reported light emission when quinacrine and acridine orange crystals were subjected to alternating electric fields of 2000 V in 1953^[9]. Pope, Kallmann and Magnante (1963) recorded light emission from tetracene-doped anthracene single crystals at 400 V D.C. operation, but this was still considerably larger than the 1.3 V needed for inorganic visible-spectrum LEDs^[6]. Hampered by such high operating voltages, it was not until Tang and Van Slyke's seminal work in the 1980s that showed for the first time that such organic LEDs could indeed be used for lighting and display applications. This device consisted of vacuum deposited sub-100 nm diamine and Alq₃ layers, respectively, as hole-transporting and light-emitting layers, and demonstrated efficiencies comparable to commercially available ZnS LEDs at operating voltages of < 10 V. This breakthrough was closely followed by the work of Burroughes and Bradley who demonstrated emission from solution cast conjugated polymers^[10], opening the possibility that, unlike iLEDs, organic materials could provide low-cost and rapid solution processing routes to possible large-area flexible displays. Furthermore, OLEDs demonstrated efficient white emission before inorganic LEDs and between 1994 and 2014 efficiencies for white OLEDs increased from 1 lm/W^[11] with fluorescent emitters to a record 139 lm/W with phosphorescent emitters^[12]. In this short space of time, the commercial applications of OLEDs now encompass displays from everyday handheld technology to high-end ultrathin, flexible televisions. Figure 1.1 summarises some of the key developments demonstrated by both types of diode.

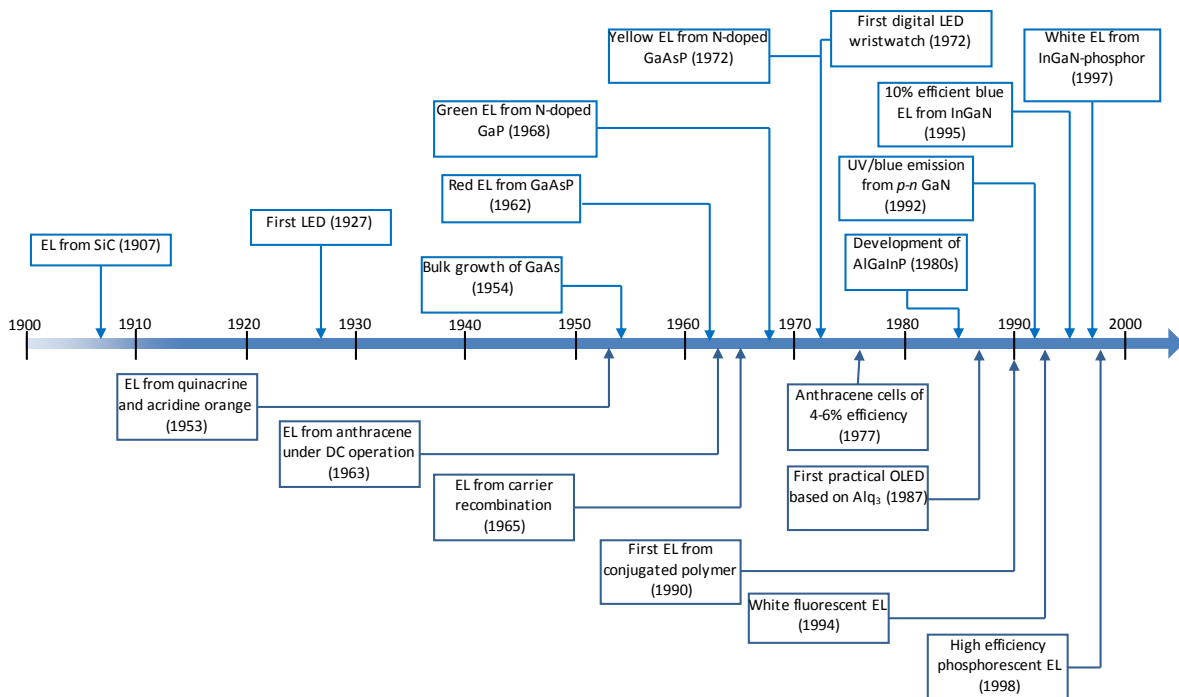


Figure 1.1: Key developments of LEDs and OLEDs over the 20th century.

iLEDs and OLEDs (both of which constitute the area of 'solid state lighting', SSL) are seen as a route to reduce the amount of energy currently spent on general lighting. International reports put the proportion of electrical energy used for lighting at 15-20%^[13,14] whilst a recent European Commission report states that public lighting in European cities accounts for 60% of all public electrical costs^[15]. The combined use of OLEDs and iLEDs is projected to reduce energy consumption in this area by a third by 2025^[16]. The 2014 US Department of Energy Solid State Lighting report makes a usage comparison between LEDs and OLEDs:

“At this time, the global market for SSL is dominated by LED-based lighting products, while OLED lighting is currently confined to decorative luminaires and custom-built fittings, designed more to enhance the ambiance than to produce light.”

This is indicative of the current higher cost of emergent OLED lighting panels versus the more established LED fixtures (\$500/klm versus \$16/klm)^[16]. However, the pace of progress of OLEDs and their considerable design advantages has led to industry projections of organic lighting systems dominating the interior lighting market by 2025^[17,18].

Throughout the course of this PhD, a relatively recent class of LEDs combining inorganic metal oxide layers with OSC layers was used as a basis to explore the properties of both material classes and their influence over device performance. Metal oxide thin films can be cast from solutions just as organic thin films can; these hybrid organic-inorganic LEDs seek to combine the high transparency, and superior electrical and thermal properties of metal oxides with the easily tunable optoelectronic characteristics of OSCs with the ultimate goal of creating wholly solution processed diodes^[19]. The structure of such HyLEDs has already been demonstrated to give more stable, longer operating lifetimes under ambient conditions compared to 'standard' OLEDs reducing the need for complex encapsulation layers to protect the active components from moisture and oxygen^[20]. Until very recently, however, these devices have been limited in their efficiencies compared to other classes of OLED. In order to understand why this is the case, sections 1.2-1.7 review the working principles of OSCs and OLEDs before a review of current HyLED literature is presented.

OSCs include small molecule and polymeric materials and OLEDs making use of either of these material classes are usually abbreviated to SMOLEDs and PLEDs, respectively. However, unless a distinction needs to be made, the term 'OLED' will be used generally throughout this thesis to refer to any diode making use of a light-emitting OSC.

1.2. Origin of Electrical Behaviour in Organic Semiconductors

When one is asked to think of materials that can conduct electricity, those that are 'organic' or 'plastic' and carbon-based do not immediately come to mind. However, due to the presence of delocalised electrons arising from *conjugated* (alternating) single (C-C) and double (C=C) bonds between adjacent carbon atoms, it is indeed possible to pass a current through such materials. The emergence of a direct energy gap E_g is analogous to that of classic inorganic semiconductors such as GaAs and GaN allowing OSCs to be used for similar applications, but with the added benefit of rapid, low-cost, solution processed deposition techniques. Here, the origins of the semiconducting behaviour in OSCs are explored.

1.2.1. Hybridisation of Carbon Orbitals

The second electron shell of carbon contains 4 electrons arranged with the configuration $2s^2 2p_x 2p_y$ and a vacant $2p_z$ orbital (figure 1.2ai). One of the electrons in the $2s$ shell may be promoted to the $2p_z$ orbital thereby allowing all four orbitals to accept an electron from another atom in the formation of a covalent bond (figure 1.2aii). This specific case arises due to the linear combination of the $2s$ and $2p$ wavefunctions in a process called hybridisation; a carbon atom which forms four covalent bonds with four separate atoms is sp^3 hybridised. Of importance to OSCs is when only the $2s$, $2p_x$ and $2p_y$ orbitals hybridise leaving the $2p_z$ orbital at a higher energy state (figure 1.2aiii). Here, the carbon atom is sp^2 hybridised. In the case of ethene when two such carbon atoms are combined (figure 1.2b), a covalent bond involving sp^2 orbital electrons is formed between the two carbons, with the remaining pair of sp^2 orbital electrons on each carbon forming covalent bonds with hydrogen atoms. These bonds are called σ -bonds and all lie in along the same plane. The left-over $2p_z$ orbital electron from each carbon atom is oriented perpendicularly to this plane and overlap with each other to form a π -bond completing the C=C bond. The overlap of these orbitals is called *conjugation* and is what allows the electrons to delocalise through an organic molecule. The linear combination of each of these orbitals gives rise to bonding π and anti-bonding π^* states; the highest of the π states is called the highest occupied molecular orbital (HOMO) whereas the lowest unoccupied molecular orbital (LUMO) is the lowest energy π^* state. These states are, respectively, analogous to the valence and conduction bands (VB and CB) of inorganic semiconductors and are, similarly, separated by an energy gap E_g . Adding further C_2H_4 units to the ethene chain serves to increase the number of both π and π^* states simultaneously higher in energy than the HOMO and lower in energy than the LUMO. Increasing the length of conjugation (i.e. the number of continuously overlapping $2p_z$ orbitals) therefore reduces E_g as shown in figure 1.2c.

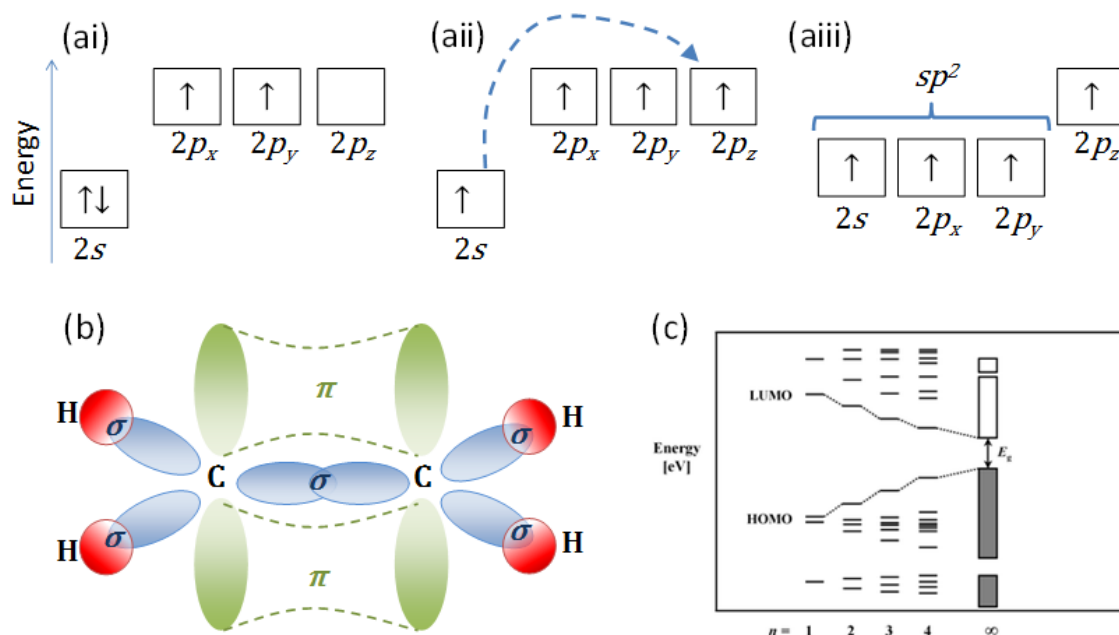


Figure 1.2: (ai) Box-arrow representation of carbon's second electron shell. (aii) The promotion of a $2s$ electron to the empty $2p_z$ state. (aiii) Hybridisation of the $2s$, $2p_x$ and $2p_y$ states. (b) Schematic of an ethene molecule formed from the combination of two sp^2 -hybridised carbon atoms. The hybridised orbitals form σ -bonds in the plane of the molecule while the $2p_z$ orbital is delocalised over the C-C bond perpendicular to the plane of the molecule. (c) Increasing the number of π -conjugated units reduces the size of E_g (adapted from reference [21]).

This would imply the eventual overlap of the HOMO with LUMO giving rise to metallic behaviour, but in reality the two do not converge to the same energy as the number of monomers increases to infinity. This is a consequence of the fact that the C=C bond is shorter than the C-C bond and an electron experiences an energetic barrier as it moves from one to another in a conjugated chain (Peierl's distortion). The electron is also affected by distortions to the molecule chain and lattice vibrations further impeding its movement through the chain. Thus a finite E_g remains with the number of monomers needed to reach the saturated E_g value known as the *effective conjugation length*^[22]. The Su-Schrieffer-Heeger theory describes this phenomenon and is further explored in, for example, Geoghegan and Hadziioannou^[23].

1.2.2. Polarons and Excitons

The size of E_g is typically greater than 1.5 eV and thus conjugated polymers are intrinsically insulating. However, OSCs may be doped through the reduction or oxidation of the molecule. Doing so leaves the OSC in an excited state with an overall net charge strongly coupled to the electronic environment. Such a state is called a polaron and its presence leads to distortions of the molecular lattice which shifts the HOMO/LUMO levels into the band-gap to stabilise the charge; a polaron is therefore coupled to the chain^[24]. The removal of an electron (oxidation) results in the appearance of an electronic state just above the HOMO occupied by a positive

polaron; the addition of an electron (reduction) results in the appearance of a state occupied by a negative polaron just below the LUMO (figure 1.3). The strong coupling of a polaron to the molecule is one of the fundamental reasons for the poor charge mobility in OSCs^[25]. For simplicity, negative polarons and positive polarons will be henceforth referred to as electrons and holes, respectively.

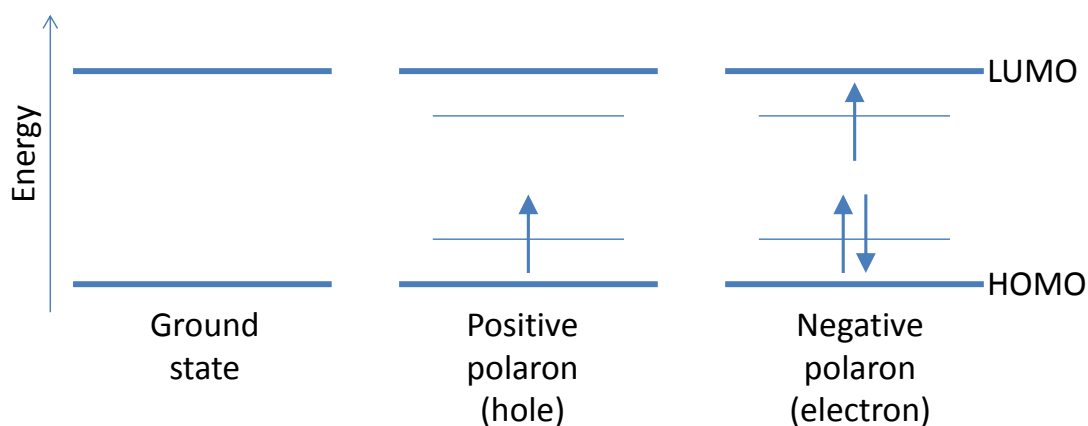


Figure 1.3: representation of the HOMO and LUMO energy levels and the appearance of energy states in the band gap as an electron is either removed to leave a hole just above the HOMO, or added to fill a state just below the LUMO.

Generated holes and electrons may interact with each other via the coulomb force to form an exciton; the energy states of this quasiparticle are further relaxed into the band gap with respect to the individual charges. Such an exciton may exist solely on one molecule (Frenkel exciton) or may be spread across two different molecules (charge transfer exciton) depending on the location of the charges^[26]. Excitons in OSCs are characterised by large binding energies which can exceed 1 eV and are consequently stable to room temperature thermal dissociation (~ 25 meV). Excitons can be further characterised as either singlet or triplet excitons. This is determined by the fact that each charge has a spin s of either $+\frac{1}{2}$ (\uparrow) or $-\frac{1}{2}$ (\downarrow) (indicated by the arrows in figure 1.3) and further due to the fact that, as charged particles, they also have a magnetic angular momentum which determines the phase of the charge relative to a magnetic field. Thus charges that have opposite spin, and are also out-of-phase, will form singlet excitons with a spin wavefunction $\psi_{s,s}$:

$$\psi_{s,s} = \frac{1}{\sqrt{2}} (\uparrow_1 \downarrow_2 - \downarrow_1 \uparrow_2). \quad 1.1$$

If both charges exhibit spins in the same direction (both up or both down), or exhibit opposite spins that are both in phase, then the exciton formed will be in the triplet state, of which there are three degenerate possibilities $\psi_{s,T}$:

$$\psi_{S,T} = \begin{cases} (\uparrow_1 \uparrow_2) \\ \frac{1}{\sqrt{2}} (\uparrow_1 \downarrow_2 + \downarrow_1 \uparrow_2) \\ (\downarrow_1 \downarrow_2) \end{cases} \quad 1.2$$

If one assumes that the spins of the charges are random, it is clear that triplet states are three times more likely to form than singlet states.

We have seen that the combination of multiple sp^2 hybridised carbon atoms leads to the formation of π and π^* states and that these states are separated by E_g . The size of E_g is instrumental in guiding the OSC towards particular applications. Charges can be added to the LUMO or extracted from the HOMO and this can be done via direct charge injection from an electrode to either level or through optical excitation of an electron in the HOMO to a state in the LUMO. Excitons arise as a result of the interaction between a hole and an electron. As discussed in section 1.3, whether an exciton forms in a singlet or triplet state has important implications on the optical characteristics of the OSC.

1.3. Optical Processes in OSCs

Because the presence of charge on the OSC causes energy states to shift into the band gap, the energies associated with optical processes are usually smaller than E_g . Thus, absorption measurements (Chapter 2) give the value of the *optical band gap* E_{op} which can be expressed as:

$$E_{op} = E_g - E_B \quad 1.3$$

where E_B is the exciton binding energy. Indeed, exposing an OSC to sufficiently high photon energies will lead to the promotion of a HOMO electron to a state below the LUMO such that it remains bound to the vacancy created in the HOMO; i.e. an exciton is formed. As E_g is dependent on the conjugation length (figure 1.2c), so too is E_{op} and longer conjugation lengths (up to the effective conjugated length) would result in lower energy transition processes. The impact of E_B , too, is large due to the generally low dielectric constant in organic materials providing a weak screening between charges thereby increasing their Coulombic interaction (this differs from inorganic semiconductors where the high dielectric constant results in weakly-bound Mott-Wannier excitons)^[23, 26]. Absorption occurs over a period of femtoseconds and excitons created in this manner are found in the singlet states; S_1 is the lowest energy singlet state. Triplet states T_x are not generally formed via optical excitation as this requires a change in total angular momentum, but may form as a result of electrically injected charges under the action of an applied voltage. Triplet states are in a lower energy state relative to the corresponding singlet

state; due to the charges being in the same spin state they have to be separated (due to the Pauli Exclusion Principle), reducing the coulombic repulsion between the charges^[23].

Singlet excitons can decay back to the ground state S_0 via the emission of a photon in a process called fluorescence which occurs over a period of nanoseconds. Due to their spin, the radiative decay of triplets to S_0 is normally forbidden and can only happen in certain materials where the selection rules are broken via spin-orbit coupling and then only over a longer period of time (micro-milliseconds) via phosphorescence. The longer triplet state lifetime however makes it more likely that they will decay via nonradiative processes, however, through collisions or vibrational means (processes which can also effect singlet excitons). Figure 1.4 shows a Jabloński diagram highlighting some of these transitions. Note that it is possible for a singlet exciton to decay to a triplet state via intersystem crossing (ISC); as this involves a change in the spin state it is also a forbidden transition, but the probability of it occurring is increased in OSCs containing heavy metal atoms. In fact, the conversion of singlet excitons to triplet excitons is an important process in the development of efficient emitters based purely on phosphorescence, particularly in the area of general lighting^[27-29].

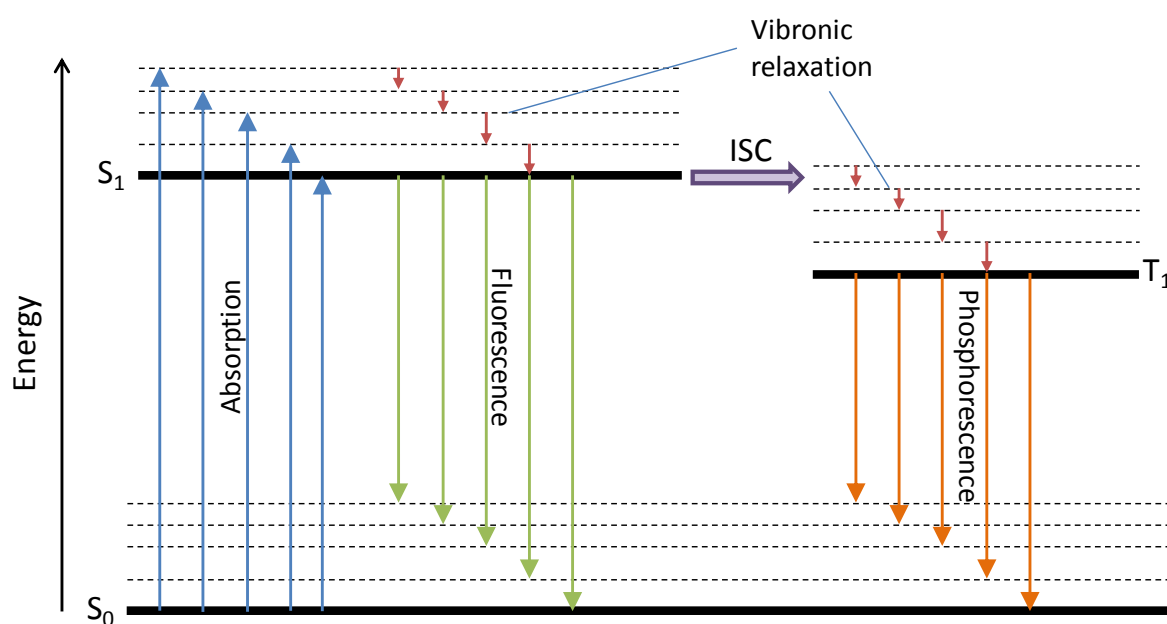


Figure 1.4: Jabloński diagram showing the optical transitions between ground and excited states of an OSC, with the vibrational energy levels shown as dashed lines. Only the first singlet and triplet excited states are shown; higher levels of each one are possible, however.

The ground, singlet and triplet states are further composed of closely spaced vibrational energy levels which give rise to finer detail in the absorption and emission spectra. In absorption, electrons are excited from the lowest energy level in S_0 to many vibrational states in S_1 . All

conjugation lengths (and hence the distribution of energy gaps) are sampled meaning that absorption spectra tend to be broad with fewer distinguishable features compared to emission spectra. This is because, following excitation, excitons will then diffuse to the smallest energy. The molecule will undergo a series of energetic relaxations as bond lengths adjust to the presence of the excited species. For fluorescence, emission then occurs from the lowest S_1 state to vibronic states in S_0 in sites of longer conjugation and as it is only these states involved in the emission process, it is possible to identify which vibronic state the S_1 state is decaying to. Because of the subsequent relaxation mechanisms, the emitted spectrum experiences a Stoke's shift relative to the absorption spectra.

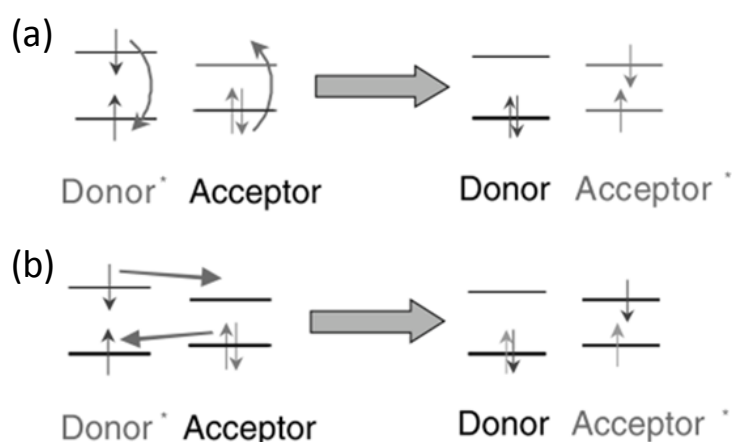


Figure 1.5: The propagation of excitons through an organic layer via (a) Förster or (b) Dexter transfer. Adapted from reference [30].

Energy losses also occur as the exciton diffuses through the OSC prior to the decay of the molecule back to the S_0 state. Figure 1.5 shows that this can occur primarily via two paths. Firstly, as an oscillating dipole, the exciton may cause a resonance via the Coulomb force on a nearby molecule promoting an electron from the HOMO to the LUMO in a process known as Förster energy transfer. The dipole-dipole interactions, and consequently the efficiency of this energy transfer, scales with distance r as $1/r^6$; the process can take place over comparatively large distances of 5-10 nm and taking a mere ~ 10 ps to do so. In the second instance, an overlap of the frontier electronic orbitals allows either the hole or the electron to tunnel to an adjacent molecule or chain. This is known as Dexter energy transfer and is only important for direct neighbours when the molecules are very close together; consequently, transfers occur over smaller distances compared to the Förster mechanism^[23]. In both cases, the second ('acceptor') molecule is now in an excited state, whereas the first (the 'donor') has relaxed back to S_0 . As these transfers primarily occur to lower energy sites, the emitted wavelength will experience a

bathochromic shift and therefore consideration of these processes is important particularly in situations where more than one type of OSC is present.

The discussion in this section has centred mainly on emission processes as a result of optical absorption. However, as indicated in the discussion regarding triplets, emission may also be the result of charge that has been electrically injected into the OSC via an electrode, i.e. electroluminescence. In this case, holes and electrons move through the bulk material under the influence of an applied electric field, eventually interacting to form an exciton. The next section considers the transport of charge through an OSC.

1.4. Charge Transport

OSCs are typically disordered materials. This is particularly the case with polymeric OSCs, which can be envisaged as 'spaghetti-like' in that the backbone can experience kinks and bends, fold back on itself and entangle with other chains. Together with rotations between monomer units, impurities and structural defects, such effects can reduce the spatial overlap between wavefunctions and introduce energy barriers as a consequence of changing conjugation lengths (see figure 1.2c). Coupled with the structural relaxations incurred by the presence of charge, hole and electrons therefore move through the bulk OSC under the action of an externally applied electric field with low mobilities, typically a few orders of magnitude less than $1 \text{ cm}^2 \text{ V}^{-1} \text{ s}^{-1}$. Compounding this, carrier concentrations available for conduction are typically in the range of 10^5 - 10^{10} cm^{-3} for OSCs^[31] (versus $\sim 10^{23} \text{ cm}^{-3}$ in, for example, copper) preventing the flow of large current densities. However, due to continued improvements in the understanding of the relationship between the OSC structure and charge transport, mobilities of OSCs have recently begun to outperform those of amorphous silicon (0.5 - $1.0 \text{ cm}^2 \text{ V}^{-1} \text{ s}^{-1}$) by quite a margin as recently reviewed by Sirringhaus^[32] and demonstrated by Yuan *et al.* ($43 \text{ cm}^2 \text{ V}^{-1} \text{ s}^{-1}$ for a solution processed thin film transistor)^[33]. Furthermore, the deposition of layers in the range of $\sim 100 \text{ nm}$ thick can give rise to large internal electric fields ($\sim 10^6 \text{ V cm}^{-1}$) that can permit the injection of charge and hence practical current densities in the order of 1 A cm^{-2} ^[31].

The ability of a material to allow charges to flow through it under the influence of an externally applied electric field F is measured as the conductance σ :

$$\sigma = \frac{J}{F} \tag{1.4}$$

where J (in A cm^{-2}) is the current density. However, it is the mobility μ ($\text{cm}^2 \text{ V}^{-1} \text{ s}^{-1}$) which is traditionally used to quantify the ability of an OSC to conduct charge. The mobility can be

viewed as the dependence of a charge's drift velocity v on the applied electric field and can be expressed as:

$$\mu = \frac{v}{F}. \quad 1.5$$

As reviewed by Coropceanu *et al.*, many factors can influence μ , including molecular packing, disorder, temperature and the applied electric field^[25]. Transport in OSCs is typically described as proceeding through a mixture of band transport and thermally activated tunnelling ('*hopping*'). The former is more likely to take place along the conjugated backbone and in instances where the bulk material can pack into a tight regular crystalline lattice, i.e. in situations where there is sufficient spatial overlap of the charged state wavefunctions. Here, charge will travel in a general direction as defined by F , but since conjugated chains are finite in length and likely to not be aligned along the same direction as F , the charge will have to hop to a different segment of the chain, or to another chain altogether to continue to drift^[23]. The likelihood of this happening is dependent on the energy required to hop on to another site as well as the distance to it. The variation in site energies within the LUMO and HOMO levels is a consequence of conformational variations in the OSC structure which change the conjugation length (figure 1.2c) and is known as diagonal disorder; the variation in the hopping distances leads to varying degrees of electronic overlap in the between segments is known as off-diagonal disorder^[34]. Figure 1.6 illustrates these phenomena for both crystalline and amorphous regions. The nature of charge hopping means that it acts as a rate limiting step to conduction in OSCs, though increases in temperature may improve conduction by providing the charges with more activation energy (band transport, on the other hand is adversely affected by temperature increases due to increased phonon scattering)^[25].

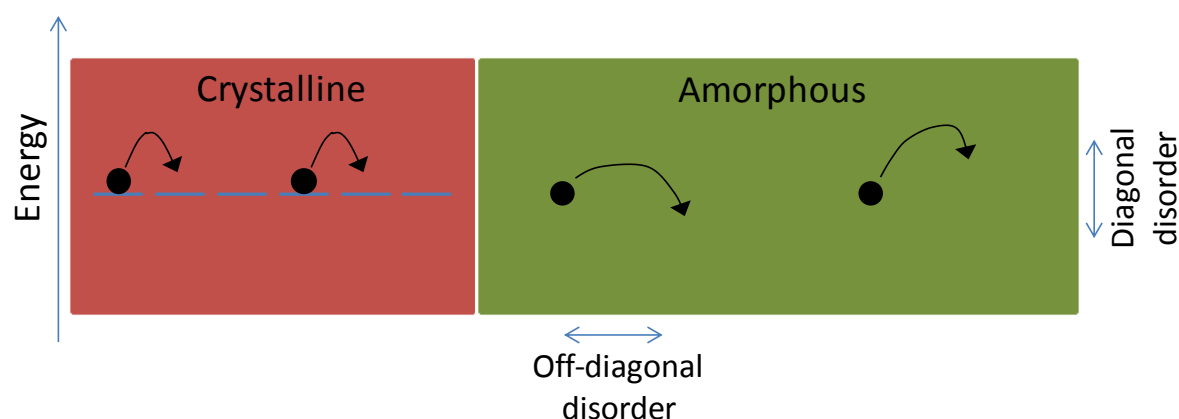


Figure 1.6: The nature of charge hopping in crystalline and amorphous regions for an electron travelling under the influence of an applied electric field.

The mobility itself may also be influenced by F as it distorts the potential well of a charge, lowering it in the direction of F similarly to the Poole-Frenkel effect^[35]. The mobility would then depend on F as

$$\mu = \mu_0 \exp(\beta\sqrt{F}) \quad 1.6$$

where μ_0 is the zero-field mobility and β is the experimentally determined field-dependent Poole-Frenkel coefficient. This will be further discussed in chapter 5 where it is also observed that the molecular weight (MW) of a polymer influences the charge transport through the bulk of the material due to variations in chain packing.

The transport of charge through an OSC is inextricably linked to its injection under an applied external voltage via an electrode; this is discussed next.

1.5. Charge Injection

Figure 1.7a considers an OSC sandwiched between two different metals each with its own work function ($\Phi_{m,1}$ and $\Phi_{m,2}$). The work function of a metal is the difference between the highest-energy occupied electron states at the Fermi Energy E_F and the vacuum energy (VE) which itself is the energy of the carriers removed from the solid and taken to infinity. One can also define the ionisation potential I_p as the energy required to remove an electron from the HOMO of the OSC to infinity, and the electron affinity χ as the decrease in energy in adding an electron to the LUMO levels from infinity. Thus, for a given Φ_m , there exists a barrier to electron injection ϕ^- and a barrier to hole injection ϕ^+ respectively defined as

$$\phi^- = \Phi_m - \chi \quad 1.7$$

$$\phi^+ = I_p - \Phi_m. \quad 1.8$$

Expected barrier values can deviate from that defined in equations 1.4 and 1.5 due to defects present in the OSC, the energetic disorder shown in figure 1.6 and the emergence of surface states and surface dipoles upon the creation of the interface between the two materials^[34,36]; indeed, in Chapter 5 it is observed that the in-built potential varies for a given polymer according to its MW and thermal processing. If at least one of the energetic barriers is small enough, electrons from the metal with the highest Φ_m can leak through the OSC to the other metal to lower the overall energy of the system. This will continue until an equilibrium is reached between both levels and the emergence of an internal electric field F_{BI} that acts to repel the leakage of further charges (figure 1.7b). The magnitude of this field is typically taken to be the difference between $\Phi_{m,1}$ and $\Phi_{m,2}$ over the thickness of the OSC layer d :

$$F_{BI} = \frac{V_{BI}}{d}, \quad 1.9$$

where $V_{BI} = \Phi_{m,1} - \Phi_{m,2}$. To inject further charge into the OSC, an applied forward bias V_{app} must exceed V_{BI} . At $V_{app} > V_{BI}$, the energy barrier spatially takes a triangular form. Should the barrier height exceed ~ 0.3 eV, charge transport through the OSC is injection limited, i.e. the resistance at the injection interface is greater than that of the bulk layer. In this case, charge injection occurs through a mixture of Schottky thermionic emission (figure 1.7c; more likely at higher temperatures and for thicker organic layers) and Fowler-Nordheim quantum tunnelling (figure 1.7d; more likely for thinner layers and higher voltages)^[34]. A full mathematical treatment for these injection modes is given in, for example, in reference ^[34], but figure 1.7 illustrates their physical significance.

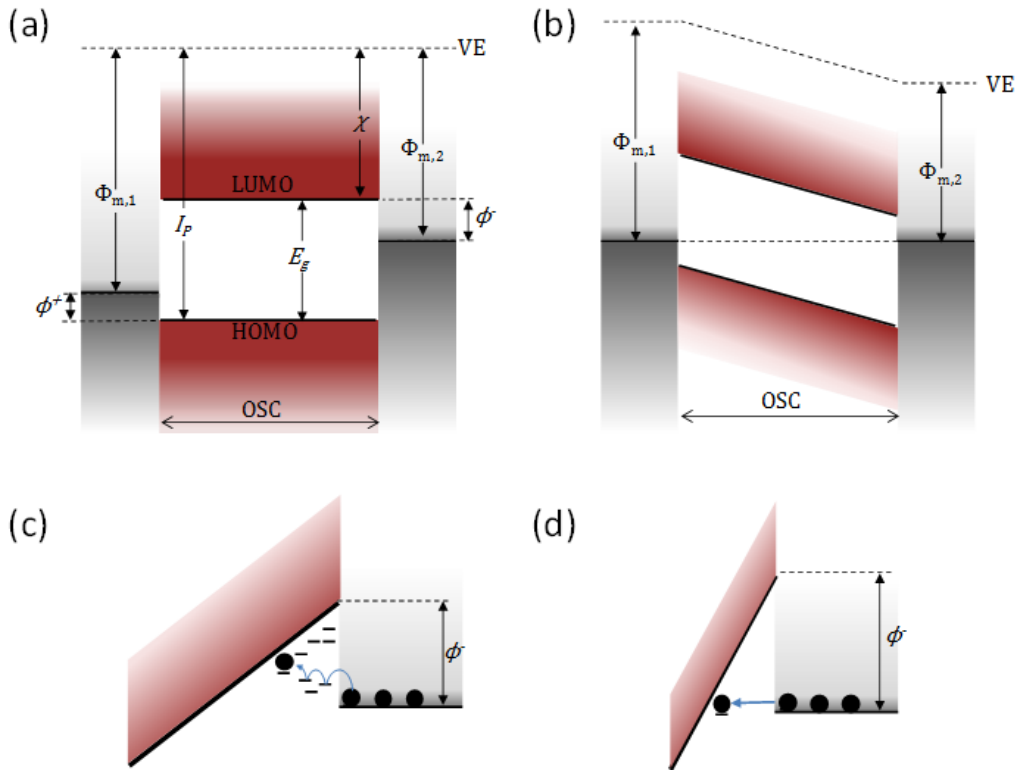


Figure 1.7: (a) Flat-band energy diagram of an OSC sandwiched between 2 metal contacts of different work functions. Shown are the relevant energy levels with respect to the VE position. (b) If the barriers to charge injection are small enough, the work functions will reach equilibrium at zero applied bias, preventing further injection. At forward bias, charge injection from the electrode into the metal will proceed via a mixture of (c) Schottky thermal emission into energetically disordered states at the interface, and (d) Fowler-Nordheim quantum tunnelling. Figures (c) and (d) have been adapted from reference ^[31].

Of great importance to device fabrication is the use of electrodes that closely match the HOMO and LUMO levels so as to reduce ϕ^+ and ϕ . At barrier values of $\lesssim 0.3$ eV, charge transport is no longer limited by the injecting interface, but by the low conductance of the bulk OSC, i.e. it is

bulk-limited. In this scenario, the contacts are said to be ohmic and charge is easily injected, but begins to accumulate in a region close to the injection interface. This wall of space charge enhances the internal electric field in the middle of the device, but also begins to screen newly injected charge at the interface to this internal field, reducing its effect. The device is now operating under the space charge limited current (SCLC) regime and the current is dependent on the thickness of the OSC d as well as its mobility μ , dielectric constant ϵ_r and V_{app} :

$$J_{SCLC} = \frac{9}{8} \mu \epsilon_0 \epsilon_r \frac{V^2}{d^3} \quad 1.10$$

where ϵ_0 is the permittivity of free space and $V = V_{app} - V_{Bl}$. Equation 1.10 is known as both Child's Law and the Mott-Gurney equation. The importance of SCLC for device performance is such that its derivation merits an overview; this is given in the next section.

1.5.1. Space Charge Limited Current

Equation 1.7 assumes the absence of trap states at the interface and in the bulk material. Furthermore, it assumes that μ is independent of F , i.e. it is not influenced by the Poole-Frenkel effect. Taking into account both of these effects was the subject of Murgatroyd's 1970 publication from which the following derivation follows^[37].

Given the presence of trap states, the proportion of the free charge density ρ_f over the trapped charge densities ρ_t is therefore:

$$\Theta = \frac{\rho_f}{\rho_f + \rho_t}, \quad 1.11$$

with the current density given by:

$$J = \mu \rho_f F. \quad 1.12$$

From Poisson's equation, the field due to the trapped and free charge densities is given by

$$\frac{dF}{dx} = \frac{\rho_f + \rho_t}{\epsilon_r \epsilon_0}. \quad 1.13$$

Combining equations 1.11-1.13 and integrating leads to

$$\frac{2Jx}{\Theta \mu \epsilon_r \epsilon_0} = F^2(x) - F^2(0), \quad 1.14$$

where x is the distance from the injecting interface. As $F(0) = 0$,

$$F = \left(\frac{2J}{\Theta \mu \epsilon_r \epsilon_0} \right)^{1/2} x^{1/2}, \quad 1.15$$

which, when both sides are integrated with respect to x , gives

$$J_{SCLC} = \frac{9}{8} \mu \epsilon_0 \epsilon_r \frac{V^2}{d^3} \Theta. \quad 1.16$$

where $d=x$. One sees that in the absence of traps, equation 1.16 reduces to equation 1.7. Charges will spend the majority of their time in trap states, reducing the overall mobility of the system which is expressed as an effective mobility^[34]:

$$\mu_{eff} = \Theta \mu. \quad 1.17$$

Equating μ_{eff} with equation 1.6 and substituting into equation 1.16 therefore gives the expected injected current in a system with trap states influenced by the Poole-Frenkel Effect, i.e. the Murgatroyd equation:

$$J_{M,SCLC} = \frac{9}{8} \epsilon_0 \epsilon_r \frac{V^2}{d^3} \mu_0 \exp(0.89\beta\sqrt{F}). \quad 1.18$$

Determination of the charge injection/transport regime that a system is operating under can be found by plotting $\log J$ against $\log V$ and determining the gradient m of the slope (corresponding to the voltage exponent of equation 1.1.8); e.g. $m = 2$ if operating under the trap-free SCLC condition (equation 1.10). Should μ be field-dependent, the gradient will increase exponentially with V and, given the disordered nature of OSC materials, this is a likely scenario. The presence of an exponential or Gaussian trap distribution in the energy gap will also increase the gradient. In fact, the nature of the traps states present (for instance whether they are discrete or follow some distribution^[34]) means that the dependence of J on V will not remain constant as V is increased during a device run and as different trap states are filled. This is observed in Chapter 5 in which the Murgatroyd equation is used to extract μ_0 and β for a set of polymer MW fractions.

These equations are usually only applied to one type of charge carrier (either holes or electrons) and they are particularly useful in assessing the quality of a charge injecting interface. Single carrier diodes are needed for this; for instance, if the charge injection capabilities of a potential hole injecting interface are being analysed, the opposite electrode must be chosen such that ϕ is very large to prevent electrons from being injected, too.

The appropriate use of electrical contacts for optimal charge injection is especially important for the efficient operation of OLEDs where it can lower operating voltages and improve charge balance. The next section deals specifically with how OLEDs work.

1.6. Organic Light-Emitting Diodes

1.6.1. Operating Principle

Fabricating and understanding how OLEDs work involves combining the theory discussed across sections 1.2-1.5. The most basic device resembles that shown in figure 1.7a in which a visible-light emitting OSC functions as the emissive layer (EML) sandwiched between two electrodes: one which operates as the anode with a work function Φ_A closely matched to the OSC HOMO and one which operates as the cathode with a work function Φ_C closely matched to the LUMO. These electrodes function to inject, respectively, holes and electrons into the OSC and hence an OLED must operate under an externally applied forward bias. As stated in Section 1.5, V_{app} must be greater than V_{BI} for injection to become energetically favourable. Figure 1.8a shows the effect of V_{app} on the energy levels of the materials and the ensuing injection of charge. Once in the EML, holes and electrons will travel under the action of the applied electric field via the mechanisms discussed in section 1.4. Electrons eventually interact with holes to form excitons which may either be in the S_1 or T_1 state (section 1.2). Once formed, excitons will diffuse (typically over 5-15 nm^[38-40]) to lower energy sites before they recombine, emitting light via EL as they do so (section 1.3). Of course, they may also recombine non-radiatively, lowering the efficiency of the overall device.

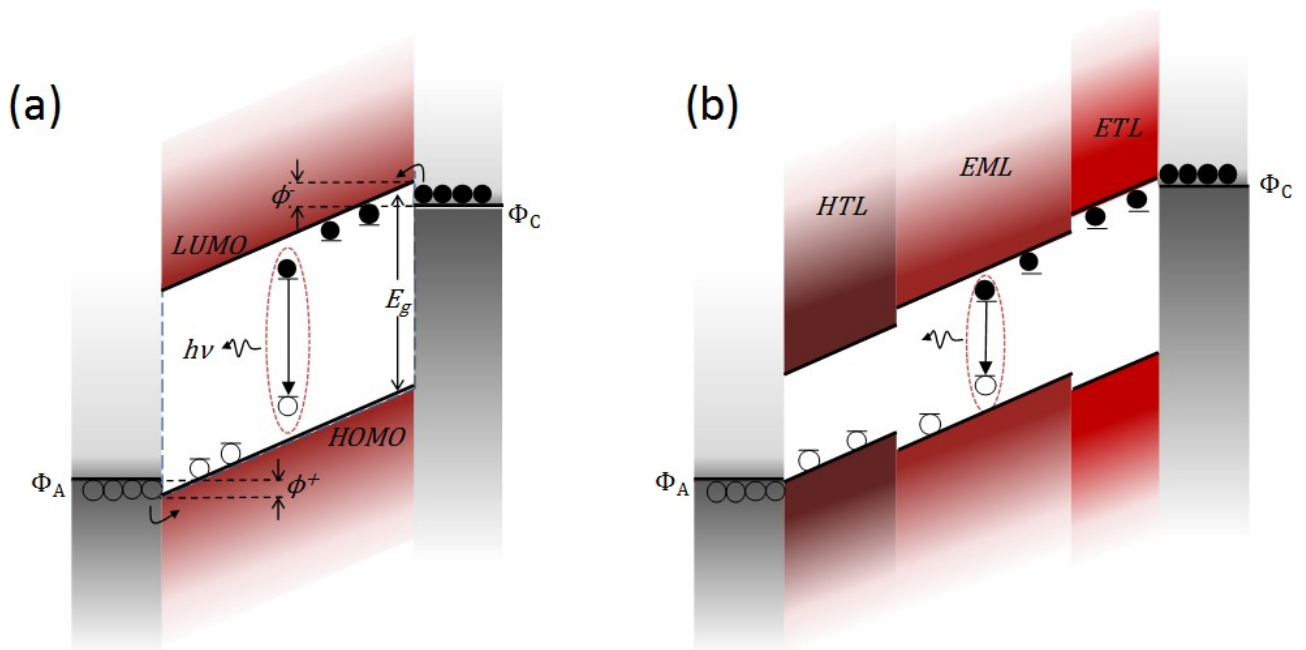


Figure 1.8: (a) Energy level schematic of an OLED under forward bias showing the injection of charges and the emission of a photon $h\nu$ following the recombination of an electron with a hole. (b) An OLED with multiple layers designed to optimise the charge injection and transport properties of the device. Adapted from reference [1].

There are in fact several routes by which the efficiency of an OLED can be reduced. To begin with, it is difficult to achieve efficient performance in an OLED consisting of just one OSC layer due to the challenge of finding appropriately energy-matched electrodes for charge injection. Furthermore, the EML will likely display asymmetric electron and hole mobilities which may result in one charge carrier reaching the opposite electrode before it can partake in recombination. OLEDs can therefore consist of several layers designed to facilitate charge transport and injection: hole transport and injection layers (HTLs and HILs) between the anode and the EML; electron transport and injection layers (ETLs and EILs) between the EML and the cathode. These can also serve as electron and hole blocking layers, respectively. Multiple EMLs may also be present to tune for a desired emission colour (for instance, white OLEDs may contain red, green and blue EMLs), but this function may also be shared with any of the transport layers. An example of such a device is shown in figure 1.8b. The deposition of such multilayer devices can be easily accomplished using vacuum-deposited small molecule OSCs; more difficult is attempting such devices using solution-processed OSCs as will be further discussed in Chapter 4. The next section considers the factors influencing the efficiency of an OLED.

1.6.2. OLED Efficiency

The internal quantum efficiency (IQE) of an OLED η_{IQE} is the product of the fraction of injected charges that are able to interact to form excitons η_{exc} , the fraction of these excitons that form in the singlet state η_S , and the fraction of these singlet excitons that decay radiatively via fluorescent light emission η_{fl} .

$$\eta_{IQE} = \eta_{exc}\eta_S\eta_{fl} \quad 1.19$$

Note that this is the case for fluorescent emitters only as emission from the T_1 state is not being considered. Equation 1.19 essentially describes the number of photons created given the number of carriers injected. However, various optical effects (such as reabsorption, internal waveguiding and so on) may prevent these photons from successfully exiting the device. The external quantum efficiency (EQE) η_{EQE} describes the fraction of photons coming out of the LED given the amount of charge injected into it:

$$\eta_{EQE} = \eta_{out}\eta_{IQE} \quad 1.20$$

where η_{out} is the fraction of photons created that have been extracted out the front of the device.

Both η_S and η_{fl} are material dependent, though they can be affected by other organic species and impurities that enable alternative decay pathways. It is generally assumed, using simple spin statistics, that $\eta_S \sim 25\%$. Chapter 5 shows that η_{fl} can be also affected by the processing

conditions of the material as well as the polymer chain length. However, η_{exc} and η_{out} are more dependent on the overall combination of materials and device design used^[23]. Both of these variables form part of the discussion throughout this thesis and so will now be discussed individually in more detail.

1.6.2.1. Charge Balance

In equation 1.19, η_{exc} is also known as the charge balance factor of an OLED. A device that exhibits balanced charge transport is one in which there is one electron injected for every hole, and where both hole and electron mobilities are similar. In this way each injected charge can recombine in the centre of the device. Any imbalances would otherwise result in excess (or higher mobility) charge reaching the opposite electrode without taking part in exciton formation as shown in figure 1.9^[31]. Here, the current density involved in recombination is given as J_r . The total injected electron and hole current densities, J_e and J_h are therefore given by:

$$J_e = J_r + J_e' \quad 1.21$$

$$J_h = J_r + J_h' \quad 1.22$$

where J_e' and J_h' are the electron and hole current densities not involved in exciton formation. The total current density J at each electrode is given by^[31]:

$$J = J_h + J_e' = J_e + J_h' \quad 1.23$$

and the charge balance factor can be expressed as:

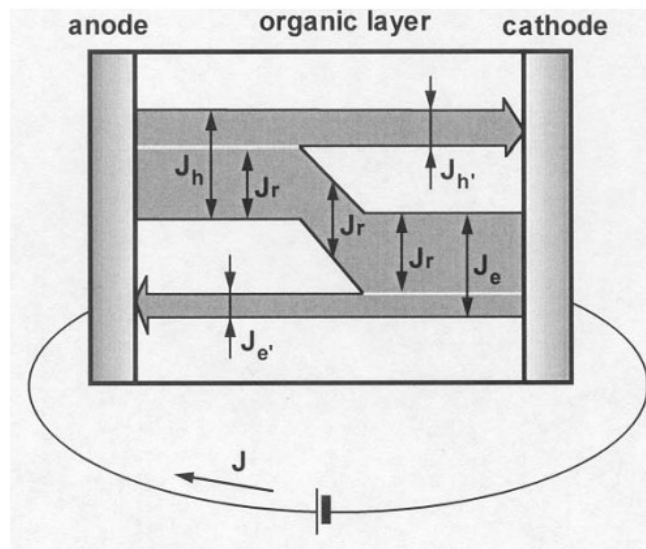


Figure 1.9: Schematic showing the potential paths of injected charge carriers highlighting the proportion that are involved in recombination and those which continue on to the opposite electrode. Adapted from reference [31].

$$\eta_{exc} = \frac{J_r}{J}. \quad 1.24$$

Ideally, $\eta_{exc} = 1$. For HyLEDs, early device configurations indicated a poor $\eta_{exc} = 0.04$ due to inefficient electron injection^[41]. As will be discussed in section 1.8, poor charge balance is a significant issue across many HyLED device configurations with much of the initial research geared to increasing J_e to the level of J_h .

1.6.2.2. Outcoupling of Light

As will be discussed further in Chapter 4, the number of interfaces and refractive indices n_r present in OLEDs can lead to the emitted light being modulated by internal optical interference effects. Along with successfully being emitted out of the front of the device in the intended direction, the internally generated photons can also become trapped, waveguided, edge-emitted or coupled to plasmons due to proximity to the metallic electrodes^[42]. Even assuming isotropic emission with no optical interference effects, Kim *et al.* calculated that the proportion of outcoupled light could be approximated by:

$$\eta_{out} \approx 0.5n_{r,OSC}^{-2} \quad 1.25$$

which, for a typical OSC refractive index $n_{r,OSC}$ of ~ 1.7 , means that $\sim 20\%$ of all internally generated light is able to escape the device stack^[43]. Demonstrations of devices with $\eta_{IQE} \sim 100\%$ are now commonplace due to the use of materials that encourage the conversion of S_1 excitons to the T_1 state for phosphorescence, or vice-versa for 100% fluorescent emission^[44–47]. This means that η_{out} has become *the* limiting factor, particularly where η_{IQE} is 100%. Efforts to improve η_{out} have involved employing nanostructured layers to disrupt internal reflection, hemispherical layers, and influencing the direction of emitting dipoles through molecular alignment^[28,42,48,49]. This latter method provides a convenient way of improving η_{out} without the need for extra layers; encouraging the emission dipole to be parallel to the substrate plane (as would be the case for polymers who have their chains parallel to the substrate) was calculated to increase η_{out} by 50%^[43,50]. However, while inclusion of extra layers leads to greater device – and, hence fabrication – complexity, the end results are striking: Reineke *et al.* report increasing the η_{EQE} of a phosphorescent device from 14.4% (33 lm/W) to 34% (90 lm/W) with the addition of an index-matched glass substrate and hemispherical extractor outcoupling lens^[28]; importantly for HyLED devices Lu *et al.* similarly showed increases in EQE from 8.9 to 15.1% with the addition of a hemispherical lens^[48].

Equation 1.20 offers one way in which the operating efficiency of an OLED can be characterised, but, as it does not weigh the wavelength of the emitted light according to the sensitivity of the

human eye, it is perhaps not the most practical measure. The next section briefly reviews the various metrics used in characterising the performance of an OLED.

1.7. Characterisation of Light Emission

The human eye exhibits a non-linear sensitivity to light in the wavelength range of 400-700 nm, being most sensitive at 555 nm and less so as the wavelengths extend into the UV and IR regions. This is demonstrated by the photopic response curve (figure 1.10a) and the degree of overlap between this and the spectrum of a light source provides an alternative, more useful, measure of the source's *lighting* efficiency. The optical power of a light source is also called the luminous flux $\varphi_{v,F}$ and describes the rate of flow of luminous energy in all directions. It is measured in lumens (lm) which takes into account the sensitivity of the eye according to the photopic curve and 1 lm is defined as having a power output of 1/683 W at 555 nm. In the case of directional light sources, it becomes more useful to describe the amount of flux travelling through a given solid angle Ω_v from the emission source. Such a quantity is the luminous intensity $\varphi_{v,I}$ and is measured in candelas (cd), defined as the flux emitted per steradian. The luminous flux can therefore be expressed as:

$$\varphi_{v,F} = \varphi_{v,I} \Omega_v. \quad 1.26$$

These optical quantities can then be combined with the electrical performance of the emitting OLED pixel to give efficiencies in terms of both characteristics. The power efficiency η_{PE} describes the light emitted over all solid angles per unit of electrical power, measured in lm/W. From the definition of the lumen, the maximum possible η_{PE} equals 683 lm/W corresponding to a perfect overlap of the emitted spectrum and the photopic curve (though as the sole peak wavelength of such a source would be 555 nm, it would be of limited use)^[51]. One could also describe the current efficiency η_{CE} as the light emitted in a unit solid angle per unit of current, measured in cd/A. These efficiencies are related as follows:

$$\eta_{PE} = \frac{\pi}{V_{app}} \eta_{CE}. \quad 1.27$$

A final useful measure is the amount of luminous intensity emitted per unit of surface area of the source - the luminance L_v , measured in cd/m². This is analogous to the brightness of a source and two figures of merit are 100 cd/m² and 1000 cd/m²; the first being the minimum required luminance for displays and the second for general lighting applications. The experimental set-up used for the characterisation of the diodes throughout this thesis measures the luminance from which the efficiencies are then derived.

Finally, it is useful to define absolute values for the *colour* of the emitted EL. A system was devised by the Commission Internationale d'Eclairage (CIE) which assigns an x - y coordinate for every visible wavelength. By definition, the response to the three-colour-sensitive human eye photoreceptors across the red (X), green (Y) and blue (Z) parts of the spectrum are shown in figure 1.10b. How colour is then perceived is due to the degree of overlap between the emitted spectrum $\gamma_v(\lambda)$ and each of these functions^[30]:

$$\begin{aligned} X_\gamma &= \int \gamma_v(\lambda) X(\lambda) d\lambda \\ Y_\gamma &= \int \gamma_v(\lambda) Y(\lambda) d\lambda \\ Z_\gamma &= \int \gamma_v(\lambda) Z(\lambda) d\lambda, \end{aligned} \tag{1.28}$$

which are then used to calculate the chromaticity coordinates:

$$\begin{aligned} x &= \frac{X_\gamma}{X_\gamma + Y_\gamma + Z_\gamma} \\ y &= \frac{Y_\gamma}{X_\gamma + Y_\gamma + Z_\gamma}. \end{aligned} \tag{1.29}$$

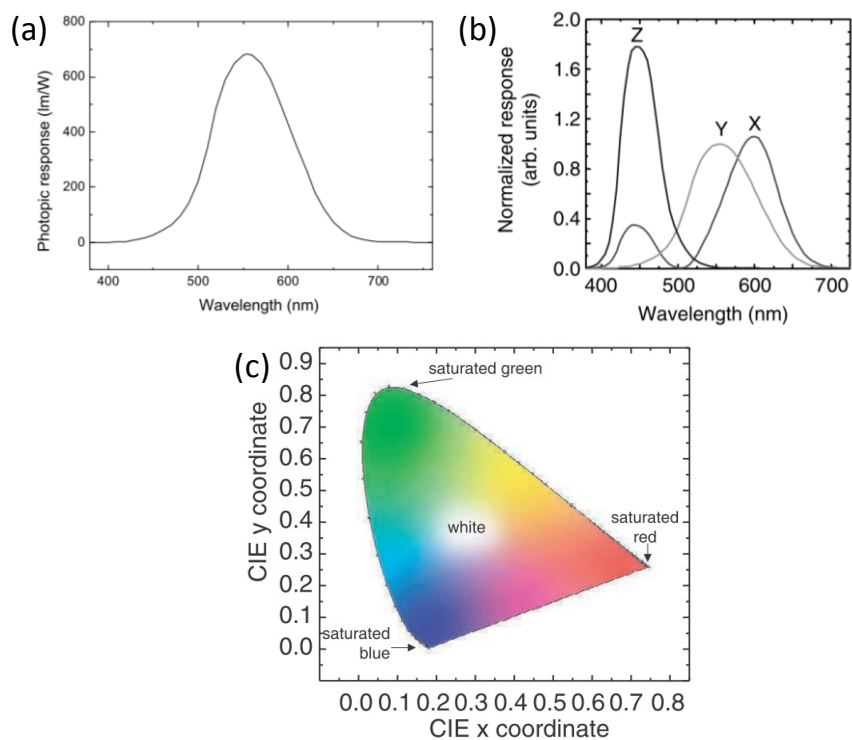


Figure 1.10: (a) The human eye photopic response curve. (b) Human eye photoreceptor responses to red, green and blue light. (c) The x - y chromaticity plot with important regions for white, red, blue and green light indicated. All figures are adapted from reference [30].

These coordinates can then be plotted on the CIE's x - y chromaticity plot (figure 1.10c). Knowledge of the chromaticity coordinates is vital when considering the applications of a light source. For example, perfect white light has the coordinate (0.33, 0.33) with deviations from this making the light redder and 'warmer' (typical of incandescent bulbs) or bluer and 'cooler'. In Chapter 4, shifts to the EL are quantified using the x - y chromaticity system.

Having reviewed the optoelectronic processes of OSCs, the working principles of OLEDs and the methods used to characterise them, we can now consider the development of HyLEDs as reported in literature. The current state of the technology and the challenges that it faces will now be considered in the next section.

1.8. HyLEDs

The initial motivation for HyLEDs was to create diodes that were more resistant to ambient conditions than the standard diode structure. A source of instability in OLEDs comes from needing a low Φ metal as the cathode in order to efficiently inject electrons into the OSC LUMO. These metals, e.g. Ca ($\Phi = -2.9$ eV), Mg ($\Phi = -3.7$ eV), Ba ($\Phi = -2.5$ eV) and Cs ($\Phi = -2.1$ eV), are highly reactive and therefore easily oxidise under ambient conditions. As most devices employ indium-doped tin oxide (ITO) coated glass as the anode, the cathode forms the 'top' electrode and therefore must be capped with a thick layer (100-200 nm) of a higher Φ metal - typically Al ($\Phi = -4.1$ eV) or Ag ($\Phi = -4.3$ eV) - to prevent corrosion. Unfortunately, this does not fully prevent the ingress of oxygen and moisture through the cathode^[52]. OLEDs can be further hermetically sealed with various types of encapsulants, but these add to the processing complexity of the OLED, hinder the flexibility of the device and ultimately still have a degree of permeability to both oxygen and water^[53,54]. The resulting degradation leads to the formation of non-emissive areas ('blackspots') across the pixel which drastically impair device performance.

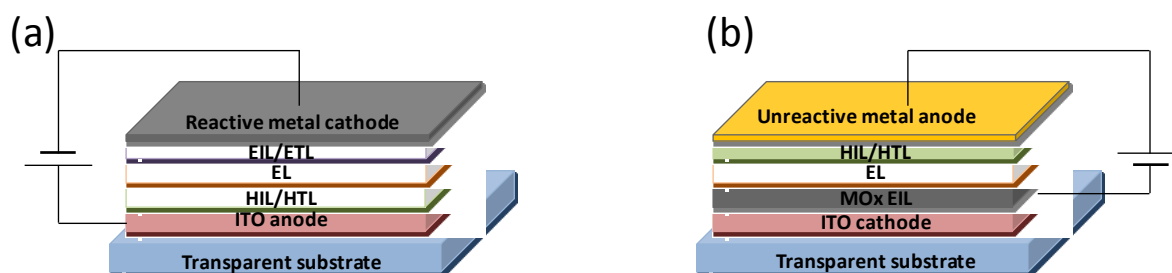


Figure 1.11: Device schematics of (a) a standard top-cathode OLED and (b) an inverted HyLED.

It has been shown that HyLEDs can reduce the need for rigorous encapsulation layers by replacing the low Φ EILs with more environmentally stable metal oxide layers. In the majority of cases, the layer order of HyLEDs is inverted with respect to most standard OLEDs, i.e. the ITO becomes the cathode with the top electrode now serving as the anode (figure 1.11). The latter needs to consist of higher Φ materials - e.g. Au ($\Phi = -5.1$ eV) - to inject holes into the OSC HOMO, but this feature also makes them more inert to ambient conditions. The HIL is also typically a metal oxide thus doing away with the frequently used poly(ethylenedioxythiophene) :poly(styrenesulfonate) (PEDOT:PSS) whose acidic nature is also suspected to be detrimental to long-term device stability^[55].

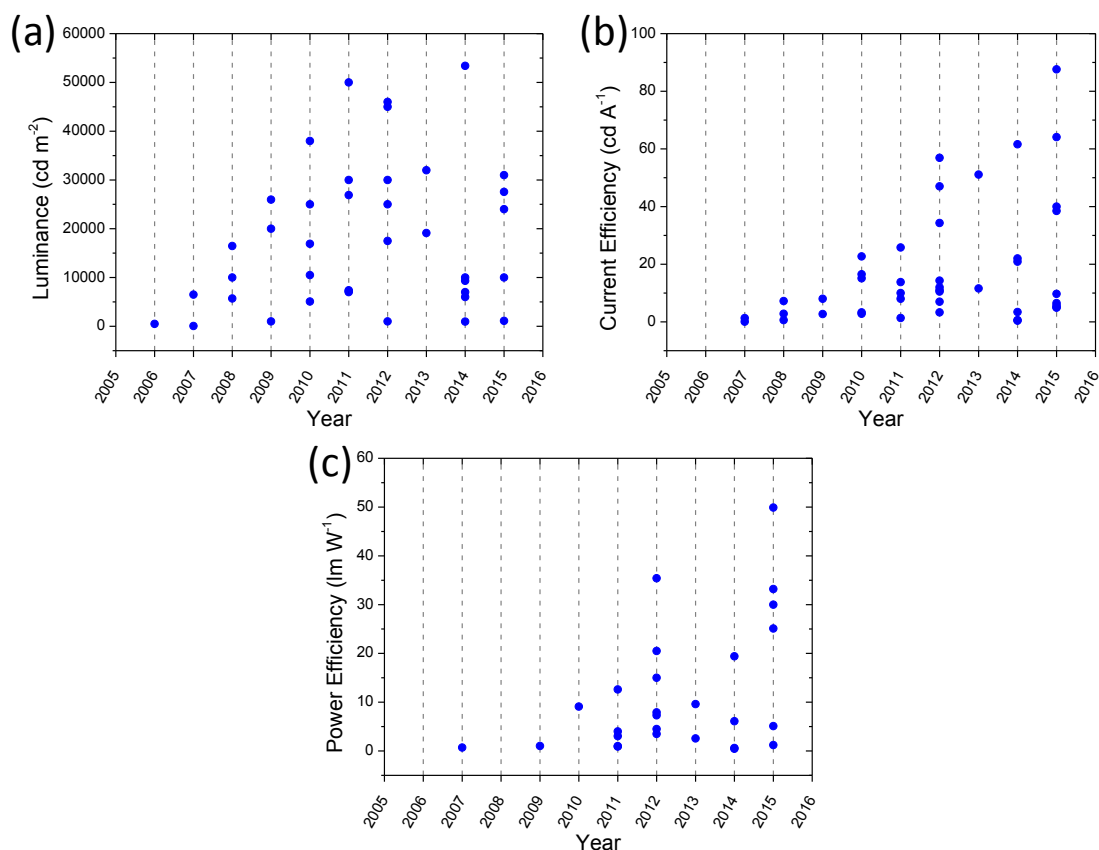


Figure 1.12: Reported performance trends for HyLEDs between 2006-2015: maximum (a) luminance, (b) η_{CE} and (c) η_{PE} . Note that there is no standard for reporting device metrics, so these figures only include those that have been reported^[41,56-96].

The advantage of using the inverted structure together with metal oxide injection layers (ILs) was demonstrated by de Bruyn *et al.* who compared the appearance of a standard device of

structure ITO/PEDOT:PSS/PF10TBT/Ba/Ag to an inverted device consisting of ITO/ZnO/PF10TBT/MoO₃/Au, i.e. where the PF10TBT was the LEP in both cases, but with the PEDOT:PSS HIL replaced with MoO₃ and the Ba EIL replaced with ZnO^[20]. Both devices were operated continuously under ambient conditions and it took 19 hours for black spot formation to manifest itself in the inverted devices; for the standard devices black spots were already visible within 8 minutes of operation. Fukagawa *et al.* recently went further with their lifetime comparison by also encapsulating both their standard and HyLED devices; after being stored in air for 250 days, the HyLED showed no dark spot formation whereas these were already visible in the standard device after 15 days^[56]. These demonstrations of improved stabilities very much show the benefits of inserting metal oxide layers into OLEDs.

Figure 1.12 shows how luminance and efficiency values for HyLEDs have increased since the first device was reported by Morii *et al.* in 2006^[96]. Luminance values have gone up from 500 cd/m²^[96] to 53,400 cd/m² ^[57], η_{CE} values up from 0.05^[94] to 87.6 cd/A with the aid of phosphorescent small molecules^[63], and reported η_{PE} values from 0.7^[95] to 49.9 lm/W^[63]. These values compare very well with recent industry reports which put η_{CE} values in the range of 75-85 cd/A for green emitters^[97].

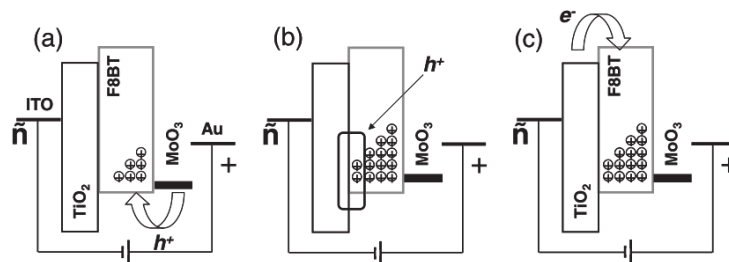


Figure 1.13: The mechanism of hole-assisted electron injection in HyLEDs as proposed by Bolink *et al.*^[41]. (a) Holes are efficiently injected at the F8BT/MoO₃ interface and then (b) accumulate at the EIL/F8BT interface. (c) The increase in the potential drop across this interface allows for electrons to then be injected. This figure is taken from reference [19].

Between 2006 and 2012 the main objective in HyLED research was to correct the highly unbalanced charge transport found in most of the diodes. As the most popular HIL, evaporated MoO₃ had been shown to efficiently inject holes into the organic layer^[41,88]. On the other hand, the poor energetic alignment between commonly used oxide EILs and OSCs would lead to large (> 0.5 eV) electron injection barriers at the EIL/OSC interface. Consequently, simple HyLEDs consisting of only one OSC layer sandwiched between an EIL and HIL are hole dominated devices. Bolink *et al.* proposed the HyLED operating mechanism shown in figure 1.13 in which hole charges flood the device when $V_{app} > V_{BI}$ and consequently build up at the EIL/OSC

interface^[19,41]. At the same time, electrons accumulate on the other side of this interface and as a result a large potential field forms across it. This reduces the width of the barrier allowing electrons to finally tunnel into the OSC where they may recombine with holes. Having the recombination zone (RZ) this close to an interface is not ideal; the large differences in energy levels across interfaces as well as the likely presence of discrete trap levels and the nature of excitons to diffuse to lower energy sites all increase the likelihood of non-radiative recombination and dissociation. During this period then, different metal oxides were investigated with the most successful being those that minimised ϕ whilst *also* blocking holes from leaking through to the ITO cathode. Bolink *et al.* demonstrated this through the use of oxides with different E_g values: ZnO (3.3 eV), HfO₂ (6.0 eV) and MgO (7.8 eV)^[87]. With increasing E_g , the VB would deepen (thus improving hole blocking) and the CB would move closer to VE, and consequently η_{CE} increased from 1.3 cd/A for devices with ZnO to 3.3 cd/A for those with MgO as the EIL. An alternative method to reduce ϕ was to modify the oxide surface with chemical species that would induce dipoles pointing in the direction of the OSC. This would effectively deepen the OSC LUMO with respect to the EIL CB and thus reduce ϕ . Examples of such modifiers include Cs₂CO₃^[79,88,90], self-assembled monolayers^[80,84] and Ba(OH)^[48].

Much of the current interest in HyLEDs follows the demonstration of significantly improved device efficiencies as a result of simply modifying the oxide surface with organic solvents^[57,60] as well as inserting thin insulating polymer layers such as polyethylenimine (PEI) and polyethylenimine ethoxylated (PEIE)^[61,63]. Their use has resulted in the highest luminance and efficiencies recorded in figure 1.12 over the 2014-15 period.

Beyond the insertion of multiple extra layers to achieve the highest efficiencies possible, there is also much research being done on simple HyLED devices to investigate how the basic layer properties and deposition conditions also influence the overall diode efficiencies. For example, lower EIL deposition temperatures will improve efficiencies in the case of a nanoparticle ZnO layer deposited via spin coating^[75], but worsen them in the case of spray-pyrolysis deposited ZnO layers^[81]. Throughout this thesis HyLEDs are employed in this manner to investigate the effects of a nanostructured EIL (Chapter 3), as well as the effects of polymer layer thicknesses (Chapter 4) and polymer chain length (Chapter 5) on overall device performance. The most common metal oxide EIL throughout literature is ZnO whilst the green light -emitting polymer poly(9,9'-dioctylfluorene-co-benzothiadiazole) (F8BT) is frequently used as the OSC layer; though these materials do not lead to the most impressive efficiencies, HyLEDs with a basic structure of ITO/ZnO/F8BT/MoO₃/Au are used as a standard. In the next section, the properties of these materials will be discussed along with those of poly[(9,9-dioctylfluorenyl)-2,7-diyl]-co-

(4,4'-(N-(4-sec-butylphenyl)diphenylamine)] (TFB) - another polymer used throughout this thesis.

1.9. Materials

1.9.1. ZnO

Initial HyLEDs used TiO_2 as the EIL^[94,96], based on the success of the material in dye sensitised solar cells. However, when both Bolink *et al.*^[95] and Kabra *et al.*^[93] separately showed superior device performance with ZnO as the EIL (η_{CE} increased from 0.18 to 0.34 cd/A and L_v from 3021 to 9370 cd/m²), this quickly became the standard to which all other EILs and device variables were tested against. TiO_2 and ZnO both have similar E_g values of 3.2-3.3 eV as well as similarly quoted CB and VB values of circa -4.0 and -7.3 eV, respectively. However, the improved device performance as suggested by Kabra *et al.* might be due to the lower n_r of ZnO which may allow for better light extraction, and its more polar surface compared to that of TiO_2 which resulted in more homogeneous F8BT film formation^[93].

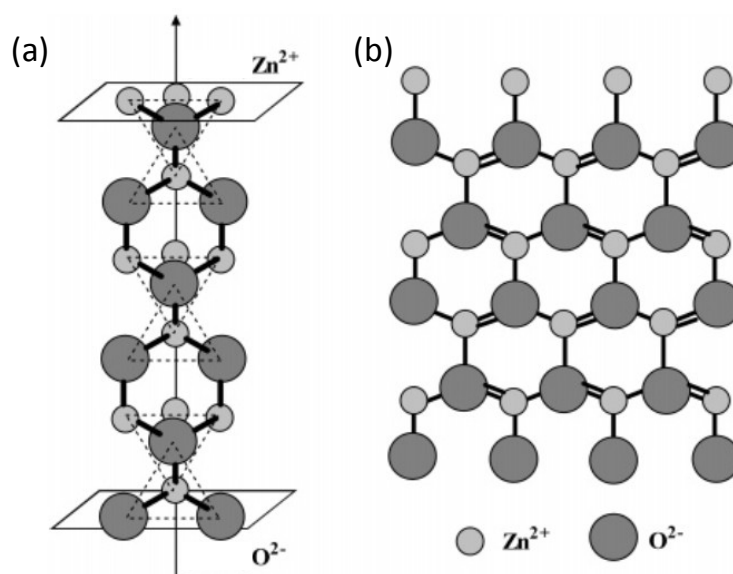


Figure 1.14: The crystal structure of ZnO showing (a) the terminating (002) planes and (b) the hexagonal arrangement as seen from side on. Adapted from reference [98].

ZnO is a non-toxic and versatile material that may be deposited using a range of techniques, with low temperature solution-processing from cheap precursor chemicals being a major draw. The polarity mentioned by Kabra *et al.*^[93] is a consequence of the material's wurtzite crystal structure in which Zn^{2+} and O^{2-} ions are arranged hexagonally in alternating planes (figure 1.14). This gives rise to crystallographic surfaces of different energies and by adjusting the ZnO growth environment, this property has been exploited to yield ZnO nanostructures with a wide

range of morphologies (further discussed in Chapter 3)^[99]. Its interest for optoelectronic applications is due to the material's inherent n-type conductivity arising from intrinsic defects such as oxygen vacancies and zinc interstitials, but also as a result of accidental doping with hydrogen during formation in chemical environments^[100]. The electronic properties of ZnO are therefore highly dependent on the growth conditions. For example, the electron mobility has been demonstrated to reach 205 cm²/Vs in hydrothermally deposited ZnO bulk crystals, whereas this was observed to be 130 cm²/Vs in thin films deposited via molecular beam epitaxy^[101].

In this thesis, all ZnO films are solution processed from solgels. A solgel consists of organometallic colloids dispersed in a solvent that over time, through hydrolysis and condensation reactions, crosslink to form a solid network through the solution (a gel)^[102]. Through the appropriate choice of precursors, it provides a method of creating high quality, crystalline oxide thin films using low temperature processing^[103,104]. Here, zinc acetate is used as the metal precursor with 2-methoxyethanol as the hydrolysing solvent to create a dispersion of Zn(OH)₂. A stabiliser of 2-aminoethanol is used to prevent the rapid precipitation of Zn(OH)₂ to ZnO when it is still in solution. Instead, this happens during the spin coating procedure (Chapter 2) and the subsequent annealing step which also serves as a densification step and removes the volatile organic components. The ability of forming highly oriented ZnO films along the (002) direction is vital for the orientation of the nanostructures discussed in Chapter 3.

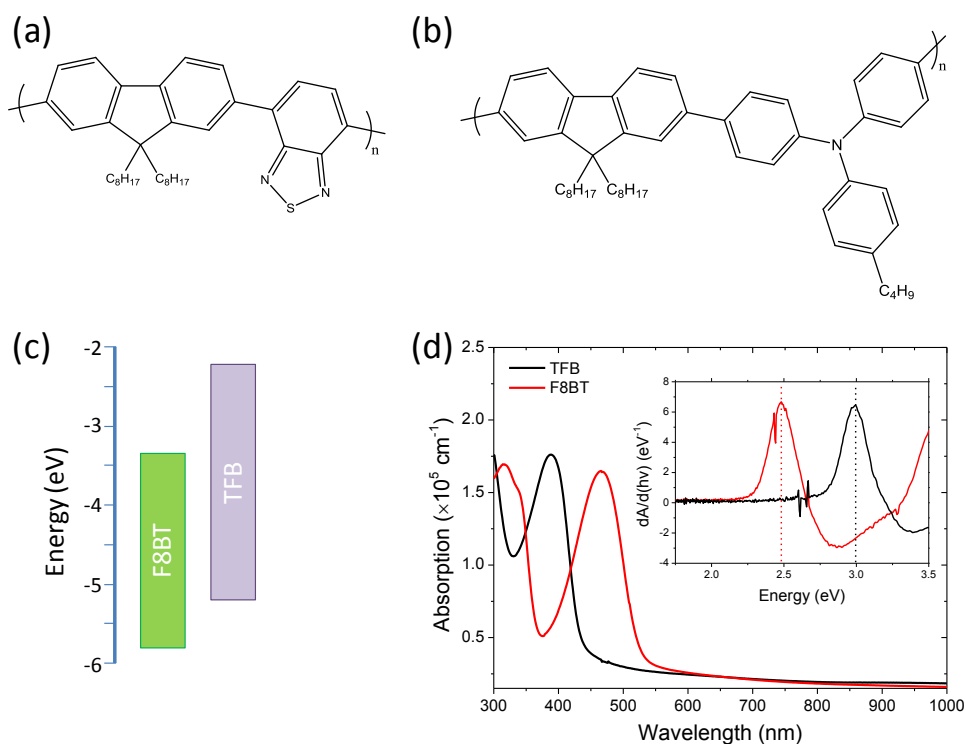


Figure 1.15: The chemical structures of (a) F8BT and (b) TFB. (c) The optical energy levels of F8BT and TFB. (d) The measured absorption spectra of F8BT and TFB (see Chapter 2). Inset: the derivative of the absorption with respect to the photon energy to yield E_{op} from the peak positions as indicated by the dashed lines.

1.9.2. Conjugated Polymers

Both F8BT and TFB are block co-polymers derived from the blue-emitting LEP, poly(9,9-dioctylfluorene) (PFO; also abbreviated to F8) - itself the subject of much research attention due in part to the optoelectronic changes induced when the material transitions from a disordered glassy phase to a more ordered phase where the backbone chains are parallel to the substrate (the β -phase). F8BT contains a benzothiadiazole (BT) unit along the backbone, while TFB contains a triarylamine group (figure 1.15a and b). Both are extensively used in device fabrication as the EML and HTL, respectively, and frequently combined within the same device for superior results^[38,93,105,106]. Along with their chemical structure, figure 1.15 also compares their energy levels and absorption spectra.

1.9.2.1. F8BT

Concepts in HyLEDs have been predominantly tested using the green emitter F8BT, but it is also widely used in PLEDs thanks to its high η_{II} of $\sim 75\%$ and solubility in many common organic solvents. Charge transport studies initially seemed to suggest that, unlike many polymers, F8BT exhibited superior electron mobilities over hole mobilities^[107], but more recent work suggests that it, in fact, exhibits ambipolar charge transport^[108]. This finding has made F8BT further attractive for light-emitting thin-film transistors where mobilities for both holes and electrons were found to be in the range of $0.7\text{-}2 \times 10^{-3} \text{ cm}^2/\text{Vs}$ ^[109,110]. Initial assumptions about its superior electron transporting properties might have been due to poor hole injection into the F8BT layer as a result of its deep HOMO level of -5.8 eV , which would give $\phi^+ \sim 0.6 \text{ eV}$ with an ITO/PEDOT:PSS contact.

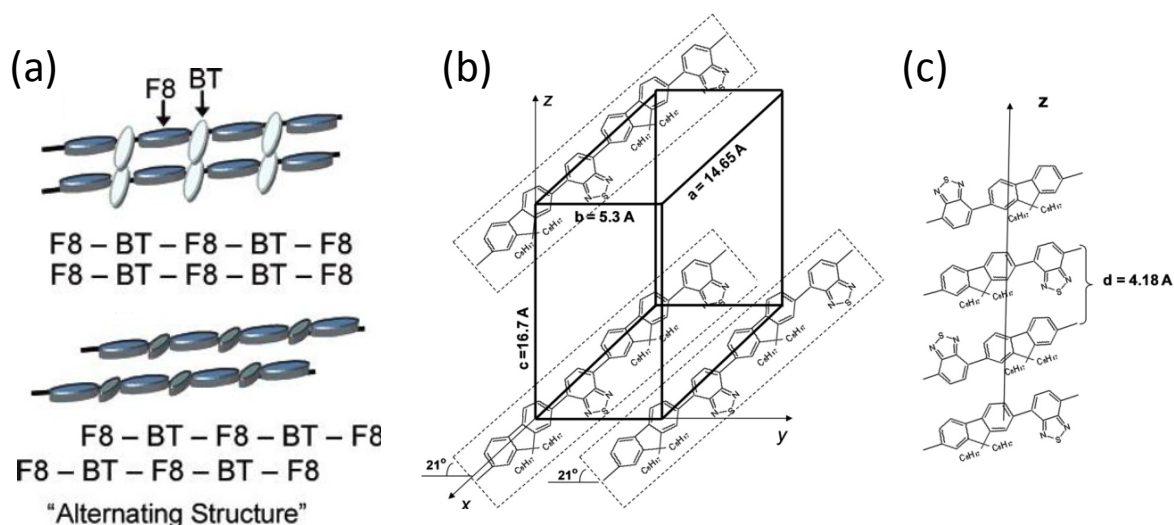


Figure 1.16: (a) Adjacent F8BT chains may pack such that identical units are side-by-side or such that F8 units are next to BT units. Adapted from reference [111]. (b) The monoclinic unit cell of crystalline F8BT highlighting the significance of the parameters with respect to the F8BT units. (c) The c lattice direction consists of four F8BT chains stacked on top of each other with a separation of 4.18 Å. Adapted from reference [112].

Due to its widespread use F8BT has been the focus of intensive fundamental research into the origin of its optoelectronic properties. Computational studies have shown that electrons are strongly localised on the BT unit as it has a LUMO 1.56 eV deeper than that of the F8 unit^[113]. This leads to highly anisotropic charge transport with holes being able to travel relatively efficiently along the backbone, whereas electrons have to hop between units on adjacent chains^[114]. Experimental studies have shown that the polymer exhibits distinct crystallisation and melting temperatures, and is stable against degradation during prolonged periods of heating up to 300 °C^[115]. Furthermore, X-ray diffraction (XRD) studies have indicated a monoclinic unit cell consisting of four chains preferentially arranged with their backbones parallel to the substrate plane^[111]. Based on the localisation of electrons on the BT unit, whether adjacent chains are aligned such that identical units are adjacent to each other, or whether BT units are adjacent to F8 units (and whether the units are pointing in the same direction) has been shown to have significant impacts on the transport and emission properties of the polymer (figure 1.16a)^[111,114]. For instance, Li and Lagowski show that electron mobility is enhanced when the electric field is parallel to the π -stacking distance and reduced when parallel to the monomer plane^[112]. Considering the hole-dominated nature of HyLEDs, encouraging the formation of F8BT morphologies with enhanced electron mobility (i.e. with the π -stacking perpendicular to the substrate plane), may result in improved device performance by shifting the RZ away from the EIL/F8BT interface once electrons have been injected.

Lattice Parameter, (hkl)	Significance	Donley <i>et al.</i> , Å	Eslamibidgoli and Lagowski	
			Lamellar, Å	'Hexagonal', Å
a (100)	Monomer length	14.65	12.9	12.9
b (010)	Side-chain spacing	5.3	15.8	11.3
c (004)	π -stacking	4.18	4.7	12.0

Table 1.1: The dimensions for the monoclinic crystalline phase as reported experimentally by Donley *et al.*^[111], and those calculated by Eslamibidgoli and Lagowski^[116].

Throughout this thesis, XRD is used to investigate the structure of F8BT under different experimental conditions and so this will be reviewed in detail. The unit cell proposed by Donley *et al.* consists of a , b and c lattice dimensions of 14.65, 5.3 and 16.7 Å, respectively^[111]. The

physical significance of these dimensions is shown in figures 1.16b and c and given in table 1.1 which gives the (hkl) notation for each and lists the π -stacking distance as a quarter of the c -axis length. However, the structure is still not clearly understood; upon annealing to the glass transition temperature (T_g i.e. the point at which the material transitions from glass-like to rubber-like as the chains gain enough kinetic energy to rearrange themselves in the solid state) Donley *et al.* noted that lower MW batches display an additional, larger unit cell not present in higher MW material. Furthermore, the authors themselves acknowledge that the side-chain spacing of 5.3 Å is unexpectedly small. In modelling the charge transport through F8BT using density functional theory (DFT) Li and Lagowski had to orient adjacent chains 21° with respect to each other to match the previously reported experimental results (figure 1.16b)^[112]. Later, the same group applied DFT analysis to confirm that the most energetically favourable manner for F8BT to pack is with the polymer backbone parallel to the substrate (lamellar packing). However, they also show that a second triclinic ‘nearly-hexagonal’ crystal structure is also possible^[116]. Interestingly, for both arrangements, their simulations show that the b -spacing is considerably larger than that recorded by Donley *et al.* (table 1.1). The existence of a second phase is confirmed from wide-angle X-ray diffraction measurements by Faria *et al.* who note the appearance of a helical phase at temperatures $> T_g$, though the authors do not assign physical parameters to the observed peaks^[117]. They, however, do report reflections corresponding to spacings of 16.0, 9.8 and 5.6 Å in which the last value is assigned as the interplanar distance in the lamellar phase, which is larger than that reported by previous groups. Faria *et al.* compare films of 4 µm and 250 nm thickness showing a higher degree of structural complexity in the former attributed to slower solvent evaporation, and hence different structural kinetics. This highlights how variability in experimental procedure may lead to a commensurate variability in lattice spacing values and peak assignment across literature and casts some ambiguity over the XRD discussion of Chapter 3.

Figure 1.15 shows that typical absorbance spectra for F8BT with the peak at ~465 nm attributed to the main π - π^* transition. Chapter 5 provides a further in-depth review of F8BT’s optoelectronic properties with respect to its MW.

1.9.2.2. TFB

The importance of TFB lies in its use as a HTL/HIL in OLED devices due to its shallow HOMO level of -5.3 eV and reported high hole mobilities of ~ 0.01 cm²/Vs^[118]. From figure 1.15, it has a peak absorbance at ~390 nm and an $E_{op} = 2.99$ eV (whereas F8BT $E_{op} \sim 2.48$ eV). Its high LUMO value of -2.25 eV^[105] provides a significant barrier to electrons leaking to the anode when it is combined with F8BT whose own LUMO value is deeper at -3.3 eV^[38]. This large offset in LUMO energies also acts as a buffer to non-radiative exciton decay and dissociation at the

electrode/LEP interface and it is this particular property that Bailey *et al.* recently identified as being the likely reason for the significant increases in devices containing a TFB interlayer^[119]. For a standard device of ITO/PEDOT:PSS/F8BT/Ca/Al, Kim *et al.* reported an increase in η_{CE} (η_{PE}) from 0.9 cd/A (0.7 lm/W) to 6 cd/A (6 lm/W) when a thin TFB interlayer was inserted at the PEDOT:PSS/F8BT interface^[38]. TFB is also commonly used as a blend with F8BT^[120,121] and this has yielded very high reported η_{PE} values of 10-18 lm/W^[105,122]. In HyLED devices, where it is cast at the F8BT/MoO₃ interface, it too has yielded improved device performances as reported by Kabra *et al.* (0.34 to 0.93 cd/A)^[93].

TFB was initially used in this thesis in order to mitigate a perceived charge imbalance in the nanostructured HyLEDs discussed in Chapter 3. However, the difficulty in casting the TFB directly onto the F8BT in these inverted devices proved challenging and Chapter 4 details the steps undertaken to overcome this. The use of thick TFB layers as an optical tuning layer in HyLED devices is also discussed in Chapter 4.

1.10. Summary

It is now 30 years since Tang and Van Slyke's groundbreaking work, OLEDs are quickly becoming an ubiquitous technology particularly in the arena of handheld devices and display monitors. They offer several advantages over traditional LEDs including more facile means of achieving the desired display characteristics, better outcoupling of light and, importantly, deposition of large areas using low cost, solution-processed means. The next few years will see ongoing developments geared towards the general lighting market, potentially with a focus on improving the lifetimes of each OLED component. In this way, the introduction of oxide interlayers makes HyLEDs great contenders for achieving stable, longer lifetime devices with simplified fabrication runs.

This chapter focused on the origin of the optical and electronic behaviour of OSCs and how it applied to OLED design, operation and characterisation. A general overview of the main challenges and developments in HyLEDs was presented along with a focus on the materials whose properties are investigated throughout this thesis. However, as each of the results chapters concern a specific investigation, a more focused literature review is given in the introductions to Chapters 3-5.

1.11. References

- [1] J. Costa Dantas Faria, M. A. McLachlan, In *Advanced Materials for a Sustainable Energy Future*, Edwards, P. P.; Kuznetsov, V. L.; Payne, D., Eds.; John Wiley & Sons, Inc.:

- Chichester; p. In Press.
- [2] H. J. Round, *Electr. World* **1907**, *19*, 309.
- [3] O. V. Losev, *Telegr. i Telef. bez Provodov (Wireless Telegr. Teleph.* **1927**, *44*, 485.
- [4] O. V. Losev, *London, Edinburgh, Dublin Philos. Mag. J. Sci.* **1928**, *6*, 1024.
- [5] N. Zheludev, *Nat. Photonics* **2007**, *1*, 189.
- [6] N. Holonyak, S. F. Bevacqua, *Appl. Phys. Lett.* **1962**, *1*, 82.
- [7] E. F. Schubert, *Light-Emitting Diodes*; Second Edi.; Cambridge University Press: New York, 2006.
- [8] S. Nakamura, M. Senoh, N. Iwasa, S. Nagahama, *Jpn. J. Appl. Phys.* **1995**, *34*, 797.
- [9] A. Bernanose, M. Comte, P. Vonaux, *J. Chim. Phys.* **1953**, *50*, 64.
- [10] J. H. Burroughes, D. D. C. Bradley, A. R. Brown, R. N. Marks, K. Mackay, R. H. Friend, P. L. Burns, A. B. Holmes, *Nature* **1990**, *347*, 539.
- [11] J. Kido, K. Hongawa, K. Okuyama, K. Nagai, *Appl. Phys. Lett.* **1994**, *64*, 815.
- [12] R. Mertens, Konica Minolta break their own record with world's most efficient OLED panel (139 lm/W). *OLED-info* **2014**.
- [13] en.lighten: Efficient Lighting for Developing and Emerging Countries.
- [14] US Department of Energy, *Solid-State Lighting Research and Development: Multi-Year Program Plan*; 2013.
- [15] European Commission, *Lighting the Cities: Accelerating the Deployment of Innovative Lighting in European Cities*; 2013.
- [16] N. Bardsley, S. Bland, L. Pattison, M. Stober, F. Welsh, M. Yamada, *Multi-Year Program Plan: Solid-State Lighting Research and Development*; 2014.
- [17] R. Mertens, UBI: OLED will be the dominant interior lighting technology in 2025. *OLED-info* **2015**.
- [18] *OLED Lighting Annual Report*; 2015.
- [19] M. Sessolo, H. J. Bolink, *Adv. Mater.* **2011**, *23*, 1829.
- [20] P. de Bruyn, D. J. D. Moet, P. W. M. Blom, *Org. Electron.* **2012**, *13*, 1023.
- [21] A. Ajayaghosh, *Chem. Soc. Rev.* **2003**, *32*, 181.
- [22] G. Klaerner, R. D. Miller, *Macromolecules* **1998**, *31*, 2007.
- [23] M. Geoghegan, G. Hadziioannou, *Polymer Electronics*; 1st ed.; Oxford University Press: Oxford, 2013.
- [24] J. L. Bredas, G. B. Street, *Acc. Chem. Res.* **1985**, *18*, 309.
- [25] V. Coropceanu, J. Cornil, D. A. da Silva Filho, Y. Olivier, R. Silber, J.-L. Brédas, *Chem. Rev.* **2007**, *107*, 926.
- [26] M. Knupfer, *Appl. Phys. A Mater. Sci. Process.* **2003**, *77*, 623.
- [27] M. A. Baldo, S. R. Forrest, **1998**, *395*, 151.

- [28] S. Reineke, F. Lindner, G. Schwartz, N. Seidler, K. Walzer, B. Lüssem, K. Leo, *Nature* **2009**, *459*, 234.
- [29] S.-J. Su, E. Gonmori, H. Sasabe, J. Kido, *Adv. Mater.* **2008**, *20*, 4189.
- [30] M. A. Baldo, S. R. Forrest, M. E. Thompson, In *Organic Electroluminescence*; Kafafi, Z. H., Ed.; Taylor & Francis Group: Boca Raton, 2005; pp. 267–305.
- [31] C. Adachi, T. Tsutsui, In *Organic Light-Emitting Devices: A Survey*; Shinar, J., Ed.; Springer-Verlag: New York, 2004; pp. 43–69.
- [32] H. Sirringhaus, *Adv. Mater.* **2014**, *26*, 1319.
- [33] Y. Yuan, G. Giri, A. L. Ayzner, A. P. Zoombelt, S. C. B. Mannsfeld, J. Chen, D. Nordlund, M. F. Toney, J. Huang, Z. Bao, *Nat. Commun.* **2014**, *5*, 3005.
- [34] A. J. Campbell, In *Functional Organic and Polymeric Materials*; Richardson, T. H., Ed.; John Wiley & Sons, Inc.: Chichester, 2000; pp. 201–232.
- [35] J. Frenkel, *Phys. Rev.* **1938**, *54*, 647.
- [36] Y. Nakayama, K. Morii, Y. Suzuki, H. Machida, S. Kera, N. Ueno, H. Kitagawa, Y. Noguchi, H. Ishii, *Adv. Funct. Mater.* **2009**, *19*, 3746.
- [37] P. Murgatroyd, *J. Phys. D. Appl. Phys.* **1970**, *151*.
- [38] J.-S. Kim, R. H. Friend, I. Grizzi, J. H. Burroughes, *Appl. Phys. Lett.* **2005**, *87*, 023506.
- [39] J. Wünsche, S. Reineke, B. Lüssem, K. Leo, *Phys. Rev. B* **2010**, *81*, 245201.
- [40] J. J. M. Halls, K. Pichler, R. H. Friend, S. C. Moratti, A. B. Holmes, *Appl. Phys. Lett.* **1996**, *68*, 3120.
- [41] H. J. Bolink, E. Coronado, D. Repetto, M. Sessolo, E. M. Barea, J. Bisquert, G. Garcia-Belmonte, J. Prochazka, L. Kavan, *Adv. Funct. Mater.* **2008**, *18*, 145.
- [42] W. Brütting, J. Frischeisen, T. D. Schmidt, B. J. Scholz, C. Mayr, *Phys. Status Solidi* **2013**, *210*, 44.
- [43] J.-S. Kim, P. K. H. Ho, N. C. Greenham, R. H. Friend, *J. Appl. Phys.* **2000**, *88*, 1073.
- [44] W. Li, Y. Pan, R. Xiao, Q. Peng, S. Zhang, D. Ma, F. Li, F. Shen, Y. Wang, B. Yang, Y. Ma, *Adv. Funct. Mater.* **2014**, *24*, 1609.
- [45] F. B. Dias, K. N. Bourdakos, V. Jankus, K. C. Moss, K. T. Kamtekar, V. Bhalla, J. Santos, M. R. Bryce, A. P. Monkman, *Adv. Mater.* **2013**, *25*, 3707.
- [46] Q. Zhang, D. Tsang, H. Kuwabara, Y. Hatae, B. Li, T. Takahashi, S. Y. Lee, T. Yasuda, C. Adachi, *Adv. Mater.* **2015**, *27*, 2096.
- [47] V. Jankus, P. Data, D. Graves, C. McGuinness, J. Santos, M. R. Bryce, F. B. Dias, A. P. Monkman, *Adv. Funct. Mater.* **2014**, *24*, 6178.
- [48] L. P. Lu, D. Kabra, R. H. Friend, *Adv. Funct. Mater.* **2012**, *22*, 4165.
- [49] M. Flämmich, M. C. Gather, N. Danz, D. Michaelis, A. H. Bräuer, K. Meerholz, A. Tünnermann, *Org. Electron.* **2010**, *11*, 1039.

- [50] J. Frischeisen, D. Yokoyama, A. Endo, C. Adachi, W. Brütting, *Org. Electron.* **2011**, *12*, 809.
- [51] A. R. Duggal, In *Organic Electroluminescence*; Kafafi, Z. H., Ed.; Boca Raton, 2005; pp. 437–466.
- [52] H. Aziz, Z. Popovic, C. P. Tripp, N.-X. Hu, A.-M. Hor, G. Xu, *Appl. Phys. Lett.* **1998**, *72*, 2642.
- [53] A. B. Chwang, M. Hack, J. J. Brown, *J. Soc. Inf. Disp.* **2005**, *13*, 481.
- [54] J. Greener, K. C. Ng, K. M. Vaeth, T. M. Smith, *J. Appl. Polym. Sci.* **2007**, *106*, 3534.
- [55] M. P. de Jong, L. J. van IJzendoorn, M. J. a de Voigt, *Appl. Phys. Lett.* **2000**, *77*, 2255.
- [56] H. Fukagawa, K. Morii, M. Hasegawa, Y. Arimoto, T. Kamada, T. Shimizu, T. Yamamoto, *Appl. Phys. Express* **2014**, *7*.
- [57] B. R. Lee, E. D. Jung, J. S. Park, Y. S. Nam, S. H. Min, B.-S. Kim, K.-M. Lee, J.-R. Jeong, R. H. Friend, J.-S. Kim, S. O. Kim, M. H. Song, *Nat. Commun.* **2014**, *5*, 4840.
- [58] C.-Y. Huang, C.-C. Yang, H.-C. Yu, Y.-C. Chen, *J. Appl. Phys.* **2014**, *115*, 083109.
- [59] H. Alehdaghi, M. Marandi, A. Irajizad, N. Taghavinia, *Org. Electron.* **2014**, *16*, 87.
- [60] S. Lee, B. R. Lee, J.-S. Kim, M. H. Song, *J. Mater. Chem. C* **2014**, *2*, 8673.
- [61] S. Höfle, A. Schienle, M. Bruns, U. Lemmer, A. Colmann, *Adv. Mater.* **2014**, *26*, 2750.
- [62] L. P. Lu, C. E. Finlayson, R. H. Friend, *Semicond. Sci. Technol.* **2014**, *29*, 025005.
- [63] R. Wang, C. Fan, Z. Xiong, X. Yang, G. E. Jabbour, *Org. Electron.* **2015**, *19*, 105.
- [64] J. Xu, L. Yu, L. Hu, R. He, W. Yang, J. Peng, Y. Cao, *J. Mater. Chem. C* **2015**, *3*, 9819.
- [65] X. Li, F. Xie, S. Zhang, J. Hou, W. C. Choy, *Light Sci. Appl.* **2015**, *4*, e273.
- [66] J. Lee, H. Youn, M. Yang, *Org. Electron.* **2015**, *22*, 81.
- [67] R. L. Z. Hoye, K. P. Musselman, M. R. Chua, A. Sadhanala, R. D. Raninga, J. L. MacManus-Driscoll, R. H. Friend, D. Credgington, *J. Mater. Chem. C* **2015**, *3*, 9327.
- [68] C. Fan, Y. Lei, Z. Liu, R. Wang, Y. Lei, G. Li, Z. Xiong, X. Yang, *ACS Appl. Mater. Interfaces* **2015**, *7*, 20769.
- [69] H. Lee, C.-M. Kang, M. Park, J. Kwak, C. Lee, *ACS Appl. Mater. Interfaces* **2013**, *5*, 1977.
- [70] B. R. Lee, W. Lee, T. L. Nguyen, J. S. Park, J.-S. Kim, J. Y. Kim, H. Y. Woo, M. H. Song, *ACS Appl. Mater. Interfaces* **2013**, *5*, 5690.
- [71] M. Vasilopoulou, A. M. Douvas, D. G. Georgiadou, L. C. Palilis, S. Kennou, L. Sygellou, A. Soultati, I. Kostis, G. Papadimitropoulos, D. Davazoglou, P. Argitis, *J. Am. Chem. Soc.* **2012**, *134*, 16178.
- [72] M. Vasilopoulou, L. C. Palilis, D. G. Georgiadou, S. Kennou, I. Kostis, D. Davazoglou, P. Argitis, *Appl. Phys. Lett.* **2012**, *100*, 013311.
- [73] M. Vasilopoulou, G. Papadimitropoulos, L. C. Palilis, D. G. Georgiadou, P. Argitis, S. Kennou, I. Kostis, N. Vourdas, N. a. Stathopoulos, D. Davazoglou, *Org. Electron.* **2012**, *13*, 796.
- [74] J. Chen, C. Shi, Q. Fu, F. Zhao, Y. Hu, Y. Feng, D. Ma, *J. Mater. Chem.* **2012**, *22*, 5164.
- [75] M. Sessolo, H. J. Bolink, H. Brine, H. Prima-Garcia, R. Tena-Zaera, *J. Mater. Chem.* **2012**, *22*,

- 4916.
- [76] J. S. Park, J. M. Lee, S. K. Hwang, S. H. Lee, H.-J. Lee, B. R. Lee, H. Il Park, J.-S. Kim, S. Yoo, M. H. Song, S. O. Kim, *J. Mater. Chem.* **2012**, *22*, 12695.
- [77] L.-P. Lu, D. Kabra, K. Johnson, R. H. Friend, *Adv. Funct. Mater.* **2012**, *22*, 144.
- [78] M. Vasilopoulou, L. C. Palilis, D. G. Georgiadou, P. Argitis, S. Kennou, L. Sygellou, I. Kostis, G. Papadimitropoulos, N. Konofaos, A. a. Iliadis, D. Davazoglou, *Appl. Phys. Lett.* **2011**, *98*, 123301.
- [79] D.-Y. Chung, D.-S. Leem, D. D. C. Bradley, A. J. Campbell, *Appl. Phys. Lett.* **2011**, *98*, 103306.
- [80] C.-Y. Li, Y.-N. Chou, J.-R. Syu, S.-N. Hsieh, T.-D. Tsai, C.-H. Wu, T.-F. Guo, W.-C. Hsu, Y.-J. Hsu, T.-C. Wen, *Org. Electron.* **2011**, *12*, 1477.
- [81] J. W. Ryan, E. Palomares, E. Martínez-Ferrero, *J. Mater. Chem.* **2011**, *21*, 4774.
- [82] J. S. Park, B. Ram Lee, E. Jeong, H.-J. Lee, J. Min Lee, J.-S. Kim, J. Young Kim, H. Young Woo, S. Ouk Kim, M. Hoon Song, *Appl. Phys. Lett.* **2011**, *99*, 163305.
- [83] E. Martínez-Ferrero, A. Forneli, C. Boissière, D. Grosso, C. Sanchez, E. Palomares, *Appl. Mater. Interfaces* **2011**, *3*, 3248.
- [84] J. S. Park, B. R. Lee, J. M. Lee, J.-S. Kim, S. O. Kim, M. H. Song, *Appl. Phys. Lett.* **2010**, *96*, 243306.
- [85] H. Lee, I. Park, J. Kwak, D. Y. Yoon, C. Lee, *Appl. Phys. Lett.* **2010**, *96*, 153306.
- [86] H. J. Bolink, H. Brine, E. Coronado, M. Sessolo, *Adv. Mater.* **2010**, *22*, 2198.
- [87] H. J. Bolink, H. Brine, E. Coronado, M. Sessolo, *J. Mater. Chem.* **2010**, *20*, 4047.
- [88] D. Kabra, L. P. Lu, M. H. Song, H. J. Snaith, R. H. Friend, *Adv. Mater.* **2010**, *22*, 3194.
- [89] K. Morii, *Synth. Met.* **2009**, *159*, 2312.
- [90] H. J. Bolink, E. Coronado, J. Orozco, M. Sessolo, *Adv. Mater.* **2009**, *21*, 79.
- [91] N. Tokmoldin, N. Griffiths, D. D. C. Bradley, S. A. Haque, *Adv. Mater.* **2009**, *21*, 3475.
- [92] K. Morii, T. Kawase, S. Inoue, *Appl. Phys. Lett.* **2008**, *92*, 213304.
- [93] D. Kabra, M. H. Song, B. Wenger, R. H. Friend, H. J. Snaith, *Adv. Mater.* **2008**, *20*, 3447.
- [94] S. A. Haque, S. Koops, N. Tokmoldin, J. R. Durrant, J. Huang, D. D. C. Bradley, E. Palomares, *Adv. Mater.* **2007**, *19*, 683.
- [95] H. J. Bolink, E. Coronado, D. Repetto, M. Sessolo, *Appl. Phys. Lett.* **2007**, *91*, 223501.
- [96] K. Morii, M. Ishida, T. Takashima, T. Shimoda, Q. Wang, M. K. Nazeeruddin, M. Grätzel, *Appl. Phys. Lett.* **2006**, *89*, 183510.
- [97] R. Mertens, UDC's evaporable emitters still outperform the best soluble materials. *OLED-info* **2016**.
- [98] L. Xu, Y. Guo, Q. Liao, J. Zhang, D. Xu, *J. Phys. Chem. B* **2005**, *109*, 13519.
- [99] Z. L. Wang, X. Y. Kong, Y. Ding, P. Gao, W. L. Hughes, R. Yang, Y. Zhang, *Adv. Funct. Mater.* **2004**, *14*, 943.

- [100] A. Janotti, C. G. Van de Walle, *Reports Prog. Phys.* **2009**, *72*, 126501.
- [101] U. Özgür, Y. I. Alivov, C. Liu, A. Teke, M. A. Reshchikov, S. Doğan, V. Avrutin, S.-J. Cho, H. Morkoç, *J. Appl. Phys.* **2005**, *98*, 041301.
- [102] L. L. Hench, J. K. West, *Chem. Rev.* **1990**, *90*, 33.
- [103] M. Ohyama, H. Kozuka, T. Yoko, S. Sakka, *J. Ceram. Soc. Japan* **1996**, *104*, 296.
- [104] L. Znaidi, *Mater. Sci. Eng. B* **2010**, *174*, 18.
- [105] J.-S. Kim, L. Lu, P. Sreearunothai, A. Seeley, K.-H. Yim, A. Petrozza, C. E. Murphy, D. Beljonne, J. Cornil, R. H. Friend, *J. Am. Chem. Soc.* **2008**, *130*, 13120.
- [106] J. C. D. Faria, A. J. Campbell, M. A. McLachlan, *J. Mater. Chem. C* **2015**, *3*, 4945.
- [107] A. J. Campbell, D. D. C. Bradley, H. Antoniadis, *Appl. Phys. Lett.* **2001**, *79*, 2133.
- [108] Y. Kim, S. Cook, S. a. Choulis, J. Nelson, J. R. Durrant, D. D. C. Bradley, *Chem. Mater.* **2004**, *16*, 4812.
- [109] J. Zaumseil, C. L. Donley, J. S. Kim, R. H. Friend, H. Sirringhaus, *Adv. Mater.* **2006**, *18*, 2708.
- [110] M. C. Gwinner, Y. Vaynzof, K. K. Banger, P. K. H. Ho, R. H. Friend, H. Sirringhaus, *Adv. Funct. Mater.* **2010**, *20*, 3457.
- [111] C. L. Donley, J. Zaumseil, J. W. Andreasen, M. M. Nielsen, H. Sirringhaus, R. H. Friend, J.-S. Kim, *J. Am. Chem. Soc.* **2005**, *127*, 12890.
- [112] Y. Li, J. B. Lagowski, *Comput. Theor. Chem.* **2011**, *977*, 157.
- [113] J. Cornil, I. Gueli, a. Dkhissi, J. C. Sancho-Garcia, E. Hennebicq, J. P. Calbert, V. Lemaury, D. Beljonne, J. L. Brédas, *J. Chem. Phys.* **2003**, *118*, 6615.
- [114] A. Van Vooren, J.-S. Kim, J. Cornil, *ChemPhysChem* **2008**, *9*, 989.
- [115] M. J. Banach, R. H. Friend, H. Sirringhaus, *Macromolecules* **2004**, *37*, 6079.
- [116] M. J. Eslamibidgoli, J. B. Lagowski, *J. Phys. Chem. A* **2012**, *116*, 10597.
- [117] G. C. Faria, E. R. DeAzevedo, H. von Seggern, *Macromolecules* **2013**, *46*, 7865.
- [118] A. Buckley, D. Pickup, C. Yates, Y. Zhao, D. Lidzey, *J. Appl. Phys.* **2011**, *109*, 084509.
- [119] J. Bailey, E. N. Wright, X. Wang, A. B. Walker, D. D. C. Bradley, J.-S. Kim, *J. Appl. Phys.* **2014**, *115*, 204508.
- [120] J. Kim, P. Ho, C. Murphy, N. Baynes, R. H. Friend, *Adv. Mater.* **2002**, *14*, 206.
- [121] Y. Hou, M. Koeberg, D. D. C. Bradley, *Synth. Met.* **2003**, *139*, 859.
- [122] A. C. Morteani, A. S. Dhoot, J.-S. Kim, C. Silva, N. C. Greenham, C. Murphy, E. Moons, S. Ciná, J. H. Burroughes, R. H. Friend, *Adv. Mater.* **2003**, *15*, 1708.

Chapter 2 – Experimental Methods

This chapter details the materials, experimental techniques and characterisation methods used throughout the investigations in Chapters 3-5 including the general device fabrication procedure. Procedures or particular steps that were only carried out under certain investigations are also mentioned here, but are discussed in greater detail in the relevant chapter. All chemicals were purchased from Sigma Aldrich unless otherwise stated.

2.1. Spin Coating

All solution processed films in this thesis were cast via spin coating. In this process, a substrate fixed onto a chuck is coated with a solution and is then made to spin at speeds from 100s to 1000s of rpm. Excess solution is ejected from the substrate whilst the remaining solution thins and dries to leave a film of the dissolved solid. This is a readily available, facile manner in which to create thin, uniform films reliably. The control of film thickness may be achieved by varying a number of parameters and the evolution of the liquid film thickness h during the spinning process is given as^[1]:

$$\frac{dh}{dt} = \frac{-2\rho\omega^2 h^3}{3\eta} - e, \quad 2.1$$

where ρ is the solution density (% w/v), ω is the angular speed (rpm), η is the viscosity ($\text{m}^2 \text{s}^{-1}$) and e ($\text{m}^1 \text{s}^{-1}$) is the evaporation rate. This last parameter highlights the importance of constant day-to-day laboratory conditions when performing this technique. Though related to ρ , it is seen in Chapter 5 (figure 5.4) that the MW of a polymer specifically also influences the film thickness. Throughout this thesis, however, control of film thickness was achieved by varying the solution concentration (section 2.6.1).

2.2. General Device Fabrication

2.2.1. Substrate Cleaning

All devices were fabricated onto $12 \times 12 \text{ mm}^2$ glass substrates patterned with a $12 \times 8 \text{ mm}^2$ strip of 150 nm thick ITO in the middle. Substrates were purchased already patterned from Psiotec ($\sim 14 \text{ } \Omega/\text{sq}$; used exclusively in experiments in chapters 3 and 4), and Thin Film Devices (TFD) Inc. ($\sim 17 \text{ } \Omega/\text{sq}$; used exclusively in experiments in chapter 5) and were cleaned prior to film deposition. Psiotec ITO was first rinsed in acetone to remove the photoresist before undergoing successive 10 minute ultrasonication runs in acetone, isopropan-2-ol (IPA) and de-ionised (DI) water (14-18 M Ω). Substrates were dried under flowing N_2 and subjected to a final 10 minute UV- O_3 treatment. Concerns with potential water contamination lead to changes in

substrate cleaning for the last project involving the TFD substrates. These did not come packaged with a layer of photoresist. Therefore, films were first rinsed in DI water, sonicated for 10 minutes in DI water:detergent solution followed by a DI water rinse. Successive 10 minute sonications in acetone and IPA followed and the films were finally dried under flowing N₂ and treated with UV-O₃ for 10 minutes. In all cases, the substrates were used immediately.

2.2.2. Planar ZnO Deposition

All light-emitting diodes and electron-only devices discussed, consisted of a planar ZnO EIL. These films were cast from a sol-gel using an in-house procedure and published by Downing *et al.*^[2]. This procedure was as follows:

- 1) Equal molar amounts of zinc acetate dihydrate and 2-aminoethanol (as the stabiliser) were dissolved in 2-methoxyethanol and made up to 0.75 M solutions.
- 2) The solution was sonicated until the solid precursors had completely dissolved. The sol-gel was then aged for 24 hours before being used.
- 3) The solutions were then cast under ambient conditions onto just-cleaned substrates via spin coating with the following parameters:
 - a) 12s wetting step at 500 rpm, followed by
 - b) 30s spinning at 2000 rpm.
- 4) Substrates were then annealed at 300 °C to remove volatile organic precursors for 10 minutes.
- 5) Steps 3 and 4 were repeated a further 2 times for a total of 3 coatings to reduce the presence of pinholes.
- 6) A final anneal of 450 °C for 1 hour was applied with a Carbolite furnace in ambient conditions to encourage film crystallinity predominantly along the (001) direction.
- 7) Finally, substrates were allowed to cool down within the furnace to 300 °C to prevent shattering of the glass substrate and then removed to cool completely to room temperature.

At these concentrations, the films exhibited thicknesses of ca. 130 nm. To obtain thinner films, volumes from the stock 0.75 M sol-gel were diluted with 2-methoxyethanol according to

$$c_i V_i = c_f V_f \tag{2.2}$$

where c and V are the concentration and volume, respectively, of the initial i and final f solutions. Film thickness was observed to give a linear relationship with sol-gel concentration (Appendix A, figure A.1(a)). Sol-gel solutions were discarded after one week.

2.2.3. Polymer Solutions

Vials and magnetic stirrers used for polymer solutions were first cleaned using successive double rinses of DI water, acetone and IPA and a final UV-O₃ treatment of 10 minutes; they were used immediately. Polymers were weighed out in air and solutions were made up to the required concentrations with anhydrous solvents in a glovebox with water and oxygen levels maintained at <0.01 ppm. F8BT was dissolved in toluene whereas TFB was dissolved in cyclohexanone. Solutions were left to stir overnight in the glovebox prior to thin film preparation. All polymers were purchased from American Dye Source (ADS).

2.2.4. HyLEDs

Prior to casting any further layers onto the ITO/ZnO substrate, a small spot of the ZnO would be etched away with 10% dilute nitric acid so as to allow electrical contact to be made to the ITO anode. The spot would be immediately wiped with DI water to remove any excess acid which may otherwise damage the ITO. From this point on, devices were completed in a glovebox with water and oxygen levels maintained at <0.01 ppm. Here, the ITO/ZnO substrates would then be annealed at 150 °C to remove any physisorbed surface water^[3]. Depending on the project and the device required, the general steps towards completed devices were followed:

1. F8BT would then be spin coated onto the ZnO from solution in toluene; spin parameters and solution concentrations varied from project to project depending on the polymer thickness desired.
2. Films would then undergo either a drying step at 90 °C for 20 minutes, or would be annealed for a particular time above the polymer's T_g or T_m temperature. Those annealed above the T_m would then be quenched or slow-cooled at 5 °C/min back to room temperature.
3. For polymer bilayer devices, the TFB layer would then be cast directly onto the F8BT-coated substrates with spin parameters of 2000 rpm for 40s. The concentration would be 10 mg/ml to give a ~40 nm thick film; this is varied in chapter 4.
4. After casting the polymer layer/s, the substrates would be transferred to an MBraun thermal evaporator system for contact deposition. MoO_x (10 nm) and Au (80 nm) would be deposited at rates of 0.2 Å/s and 0.1-0.6 Å/s, respectively, at base pressures of 0.5-1×10⁻⁶ mbar. A boron-nitride crucible was used as the source for the MoO₃ powder (> 99.5%), whereas a tungsten boat was used for the Au (99.99%, Testbourne). Deposition occurred via a shadow mask to give 6 pixels of 0.45 cm² on each substrate.

The polymer layer over the etched ITO would be mechanically etched and the substrates would be stored in the glovebox during the testing period, typically within 24 hours of device completion. Final device structures would generally be ITO/ZnO/F8BT/MoO_x/Au for single

polymer diodes, or ITO/ZnO/F8BT/TFB/MoO_x/Au for polymer bilayer diodes. A schematic showing the overlap of the evaporated electrodes with the patterned ITO is shown in figure 2.1.

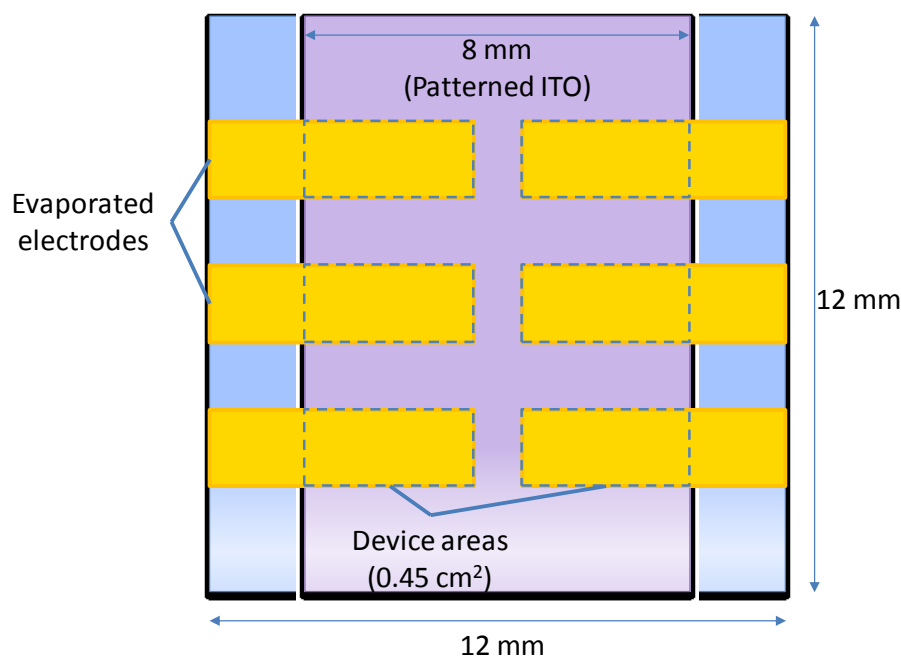


Figure 2.1: Top-view schematic of the device substrates used throughout illustrating the spatial overlap of the evaporated electrodes with the patterned ITO layer.

2.2.5. Single-Carrier Devices

Fabricating single-carrier devices involves replacing one of the injection layers with another material whose properties (ideally) completely prevent the flow of the charge facilitated by the original layer. For example, an EIL would be replaced with an HIL meaning that the LEP is now sandwiched by two HILs. By eliminating the injection of one sign of carrier, single carrier devices provide a means to investigate the injection and transport of holes and electrons through the device in the absence of recombination with the other carrier sign and thus assess the quality of a given injection layer/OSC interface and the mobility (Chapter 1, Section 1.5).

Pre-cleaned ITO substrates were used for all single-carrier devices

2.2.5.1. Electron-only Devices

For electron-only devices, the MoO_x/Au contact was replaced with a Ca(20 nm)/Al(150 nm) electrode to give an ITO/ZnO/F8BT/Ca/Al diode structure. Ca (99 %) was evaporated from a boron-nitride crucible at 0.2 Å/s and Al (99.99 %, Kurt J. Lesker) from an alumina-coated tungsten basket at 0.3-1.0 Å/s.

2.2.5.2. Hole-only Devices

Here, the ZnO EIL was removed and replaced with a 25 nm PEDOT:PSS interlayer to give an ITO/PEDOT:PSS/F8BT/MoO_x/Au diode structure. The PEDOT:PSS (Heraeus Clevios P VP Al 4083, Ossila), was passed through a 0.45 µm PTFE filter prior to use and dynamically cast by pipetting directly onto the substrate spinning at 4000 rpm for 30 s. The films were dried at 150 °C for at least 5 minutes to remove residual water and then transferred to the glovebox to deposit all other layers from F8BT onwards as in section 2.4. This PEDOT:PSS casting procedure was guided by the supplier instructions^[4].

2.3. Device Characterisation

2.3.1. Efficiency and Luminance Measurements

The completed devices were loaded into testing chambers and connected to an OLED testing rig consisting of a Keithley 236 Source Measure Unit (SMU) and a Minolta luminance meter. The voltage sweep was set from -4 V with the upper voltage limit selected to coincide to just after a decrease in current efficiency was recorded; this would vary between device types, and would prevent premature device burnout. The voltage sweep, light detection and efficiency calculations were automated by a LabView programme written by Dr Xuhua Wang at the Blackett Laboratory, Imperial College London.

2.3.2. Electroluminescence and Chromaticity Measurements

The EL spectra, where discussed, were always recorded after electrical testing. Diodes connected to the SMU would be manually set to a voltage or current particular to the experiment and positioned in front of an Ocean Optics S2000 Fibre Optic Spectrometer. The distance between the emitting diode and the spectrometer was adjusted to give a strong signal without saturating the detector. The spectra were recorded using the Ocean Optics software which, based on the data recorded, automatically calculated the *xy* chromaticity values. Since the set-up did not allow for fixed distance between the emitter and detector, all spectra were normalised. In Chapter 4 (section 4.3.2), the EL spectrum is recorded as a function of angle from the surface normal.

2.4. Optical Characterisation

2.4.1. UV-vis Spectra

A Bentham single-beam UV-vis system was used to measure the UV-vis response of thin films cast on pre-cleaned substrates. The spectra were obtained in transmission mode using air as a reference which was then converted to give the absorbance *A*:

$$A = -\ln\left(\frac{\%T}{100}\right) \quad 2.3$$

where %*T* is the transmission recorded as a percentage. If the film thickness *d* is known, the absorption coefficient α can then be calculated:

$$\alpha = \frac{A}{d}. \quad 2.4$$

For organic materials, extracting the optical band gap E_g from the onset of absorption is common practice. Alternatively, as *A* shows an exponential dependence on the photon energy $h\nu$ below E_g (the Urbach region), but a square-root dependence above E_g (the Kane region) then plotting the derivative of *A* with respect to the photon energy $h\nu$ (i.e. $dA/dh\nu$) allows one to easily identify E_g as the maximum gradient at the lowest energy^[5]. This latter method does not determine E_g based on arbitrarily drawn tangents like the former method (or the more commonly used Tauc plot method), has been previously applied to poly(arylenephylene)s^[6], and hence was the preferred manner to extract E_g for TFB and F8BT here, and previously ZnO during the Masters Report. Figure 1.15b (Chapter 1), shows that the polymer E_g values correspond exactly to those reported throughout literature.

2.4.2. Photoluminescence Spectra and PLQE

Photoluminescence (PL) spectra of polymer films were measured using a Horiba Scientific FluoroMax 3 spectrofluorimeter. Substrates were positioned within an integrating sphere with a holder fixing the substrate in the path of the excitation beam. The excitation wavelength λ_{ex} would be set at the sample's peak absorption wavelength and direct detection of emitted photons prevented with a baffle. Photoluminescence quantum efficiency (PLQE) measurements were conducted according to the method detailed by de Mello *et al.*^[7] and is defined as the total number of photons emitted given the number of photons that have been absorbed:

$$\eta = \frac{\sum(emitted)}{\sum(absorbed)} \quad 2.5$$

In order to calculate these parameters three separate readings must be taken: measurement (*a*) records the spectrum of the empty sphere with no sample present (figure 2.2a); the second (*b*) measures the spectrum of the sphere with the sample present, but away from the excitation beam path (figure 2.2b); and the third (*c*) measures the spectrum with the sample present and directly placed in the excitation beam path (figure 2.2c). Scans are taken to also include the peak due to the set λ_{ex} as shown in the examples for each of the three readings in figures 2.2d-f. Note that the spectra is then plotted with the product of the intensity at each λ and is proportional to

the number of photons at a given wavelength interval, i.e. the area under the graph. Thus the area under the excitation peak represents the total number of *unabsorbed* photons in each experiment, respectively Λ_a , Λ_b and Λ_c . The area under the broader emission peak represents the number of emitted photons in the indirect and direct measurements, respectively, ξ_b and ξ_c .

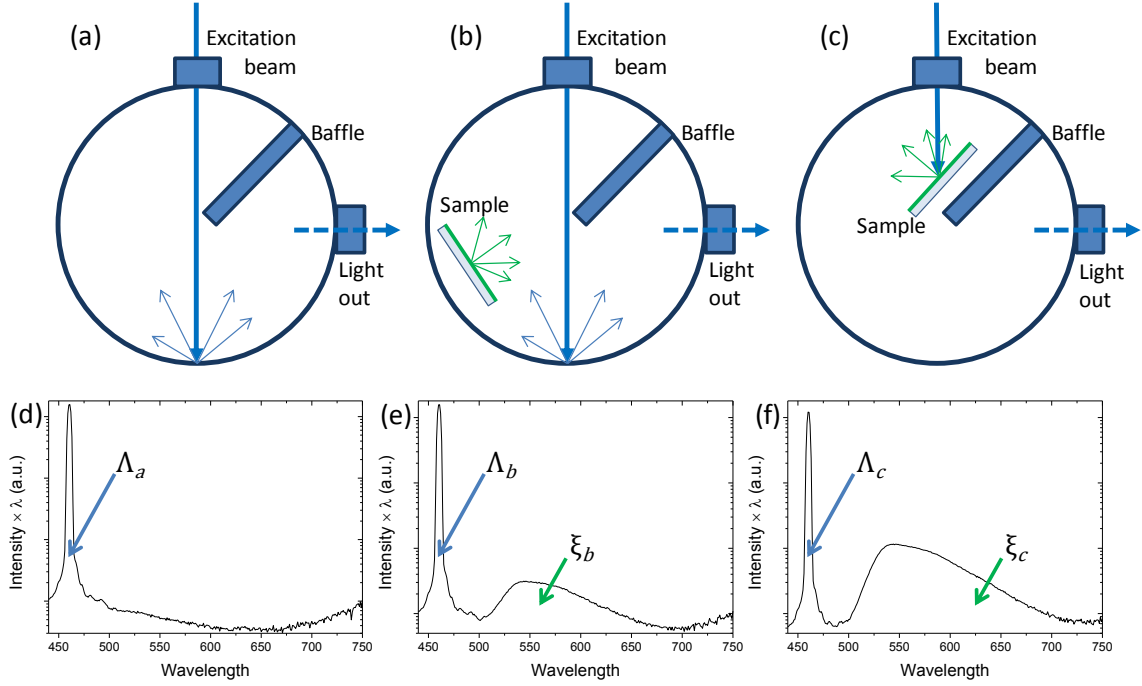


Figure 2.2: Schematics of the integrating sphere set-up for PLQE measurements. (a) measurement of the sphere response. (b) Indirect sample measurement. (c) Direct sample measurement. Also shown are example recorded spectra for F8BT in case of (d) no sample present, (e) indirect excitation and (f) direct excitation.

In experiments (b) and (c), Λ is reduced due to photon absorption by the sample; one then defines μ as being the fraction of the incident light which is scattered from the sphere wall and subsequently absorbed by the sample and A as the fraction of incident light which is directly absorbed by the sample. Therefore,

$$\Lambda_b = \Lambda_a(1 - \mu) \quad 2.6$$

$$\Lambda_c = \Lambda_a(1 - A)(1 - \mu) \quad 2.7$$

$$A = \left(1 - \frac{\Lambda_c}{\Lambda_b}\right). \quad 2.8$$

In the third experiment the total number of photons detected is the sum of the contributions from Λ_c and ξ_c and is given by,

$$\Lambda_c + \xi_c = (1 - A)(\Lambda_b + \xi_b) + \eta\Lambda_a A. \quad 2.9$$

Given that the total photon count in measurement (b) is given by $\Lambda_b + \xi_b$, the first term on the right hand side of equation 2.9 is therefore the contribution due to scattered laser light from incident light that was transmitted or reflected from the sample. The second term on the right is the light emitted as a result of direct absorption. Thus the PLQE efficiency can be calculated using,

$$\eta = \frac{\xi_c + \xi_b(A-1)}{A\Lambda_a}. \quad 2.10$$

These measurements were done for F8BT and in all cases Λ was found by integrating between 440-480 nm. ξ values were calculated by integrating between 490-750 nm. Each cycle of measurements was repeated three times for reliability.

2.4.3. Reflectance

In Chapter 4 reflectance spectroscopy was performed to confirm the presence of weak micro-cavity effects in polymer bilayer HyLEDs. Measurements were performed on completed device stacks following their electrical characterisation using a Shimadzu 2600 UV-Vis system. The beam width was reduced to ensure that only reflection through the device stack from the gold anode was detected. A quartz baseline was used as a reference and the actual reflectance R_{eff} of the measured samples R_{exp} calculated using:

$$R_{eff} = \frac{R_Q R_{exp}}{100} \quad 2.11$$

where R_Q is the measured reflectance of the quartz calculated from its measured transmittance T_Q :

$$R_Q = 100 - T_Q \quad 2.12$$

i.e. using the assumption that no absorption has taken place.

2.5. Material Characterisation

2.5.1. Thickness Measurements

Clean glass substrates (VWR) were cleaned as discussed in section 2.2.1 and the film to be tested cast as it would be in device preparation. In the case of polymer films, several scratches would be made to the film and their depth measured using a Veeco DekTak 150 surface profilometer; the results of the relationship between the measured thickness and solution concentration for the polymer batches used are shown in figure 2.3. The thickness of ZnO films had already been previously measured during the Masters Report (Appendix A)^[8].

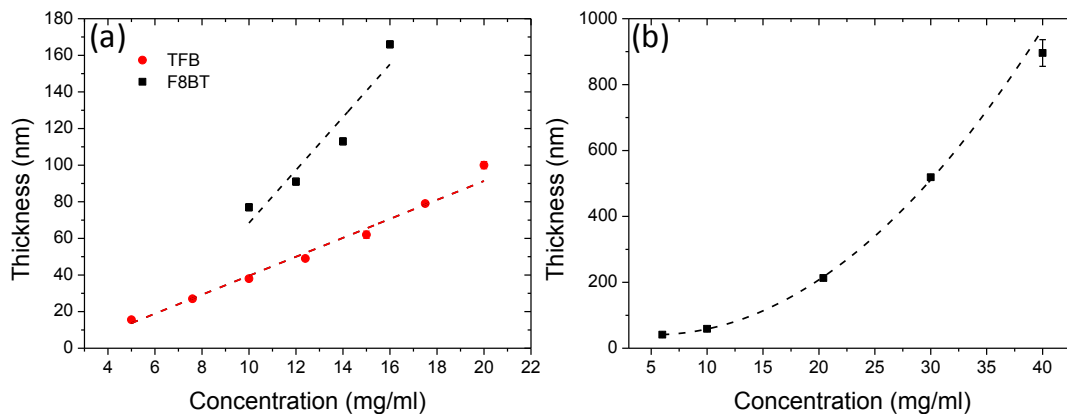


Figure 2.3: Thickness vs. Concentration for polymer films used throughout this thesis. (a) Thickness variation of TFB (Chapters 3-5) and 46K* F8BT (Chapters 4 and 5). (b) Thickness variation of $M_w \sim 115$ kg/mol F8BT (Chapter 3). These films were all cast at 2000 rpm for 40s (section 2.1). The fitted lines were used for interpolation only.

2.5.2. Scanning Electron Microscopy

SEM was used to study the surface morphology of thin films, nanostructures as well as entire HyLED device stacks. A FEGSEM Leo1525 was used for this purpose. In this technique, electrons are emitted from a field-emission gun, accelerated through an electric field and then focused by objective lenses to be then rastered over the sample under analysis using scanning coils. These measurements are conducted at pressures $< 2 \times 10^{-5}$ mbar. The electron beam interacts with the sample producing backscattered, secondary and Auger electrons as well as X-rays; the images presented in this thesis were produced from secondary electron (SE) detection. SEs are the result of a valence electron being knocked out of its orbital by an incoming electron and typically have energies of less than 50 eV as a result of inelastic collisions. They originate from a shallow layer at the sample surface and hence give high topographical detail with variations in the surface morphology resulting in contrasts between different areas^[9].

In preparation for SEM imaging, all samples would be coated with a thin Cr layer to improve their conduction for better image quality. Cross-sectional imaging of the substrates was used to assess the uniformity of the NRAs as well as the extent of polymer infiltration. For these, substrates would be scored with a diamond pen on the reverse side and then cleaved along the line to obtain a cross-section of the layers in the middle of the substrate. Polymer-coated substrates would first be submerged in liquid nitrogen; this would serve to make the polymer brittle and therefore more likely to give a 'clean' break during the cleaving step. Several examples of cross-sectional SEM images following this procedure are presented in Chapter 3.

2.5.3. Atomic Force Microscopy

Like SEM, AFM also provides topographical information on a sample, but also provides height, spatial and chemical information. Furthermore, the sample does not need to be conductive. This technique involves the interaction of a tip with the sample (figure 2.4). The tip is attached to a cantilever and is rastered over the sample. The back of the cantilever is used to reflect a laser onto a photodiode. Thus, as the cantilever is deflected due to surface features, the location of the laser on the photodiode changes, which in turn feeds back into the system to change how the tip interacts with the surface building an image of the sample as it does so^[10].

A Bruker Multimode Nanoscope AFM was used in these studies under tapping mode which lowers the probability of both contaminating the tip and damaging the surface (particularly important for soft materials like polymers) as the tip and sample contact only intermittently. The cantilever is made to oscillate (~ 100 s of kHz), but changes in force between the tip and the sample lead to phase shifts between the set oscillation frequency and that actually achieved. Such an effect is sensitive to the materials composition of the surface and so one can therefore extract information about different material phases that may be present^[11].

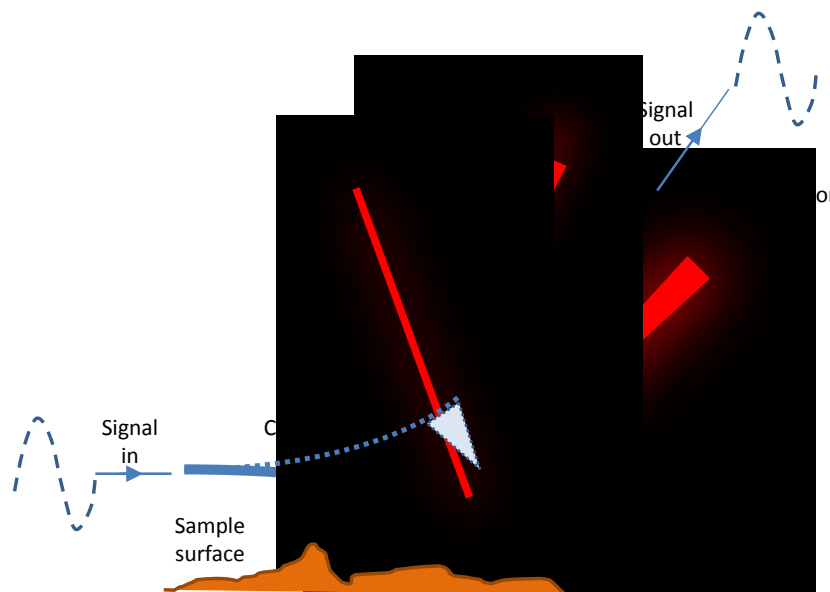


Figure 2.4: Schematic of how an AFM functions with deflections to the cantilever resulting in deflections to the reflected laser beam incident on a photodetector.

Given that layer thicknesses in devices are typically < 100 nm, AFM is a popular tool used to assess the homogeneity of these layers. Lack of homogeneity through, for example, pinholes and height differences can lead to deleterious effects during the operation of organic devices particularly in PLEDs where the higher voltage operation can lead to localised high current densities and blackspot formation. AFM can be used to quantify the surface roughness and this

is frequently done in literature to explain device behaviour^[12-14]. This is typically expressed as the root-mean-squared roughness, given as:

$$R_{rms} = \sqrt{\frac{1}{n} \sum_{i=1}^n y_i^2} \quad 2.13$$

where, for n number of points, y is the height of the i^{th} value. To ensure that the comparison of roughness values is valid, all images were processed identically and done so using Gwyddion^[11,15].

2.5.4. X-ray Diffraction

This technique was used to gather information regarding the crystal structure of polymer thin films and ZnO nanostructured layers to reveal, in particular, the preferred crystal orientation. Diffraction arises as a result of the constructive interference between X-rays as they are scattered from adjacent lattice planes in an ordered medium as shown in figure 2.5. More precisely, this scattering is an elastic process in which the incoming radiation causes a valence electron to oscillate at the same frequency as that of the radiation and then re-emitting it again at the same energy (Thomson Scattering)^[16]. For constructive interference to take place, the path difference between the two rays must equal an integer number of wavelengths, i.e. $n\lambda = n\lambda$. Given that this path difference can be expressed in terms of the angle between the plane and the incoming beam, one then arrives at the Bragg equation:

$$n\lambda = 2d \sin \theta \quad 2.14$$

which allows for the distance between lattice places d to be determined. Here, n is the order and λ is the wavelength of the Cu K_{α} (L to K) state transition used as the X-ray source (0.15418 nm). From figure 2.5, it is clear that the X-ray detector must also move at the same angular rate as the X-ray source to detect the reflections from all planes that are parallel to the substrate. Such a setup is known as the 2θ configuration. A Panalytical X'Pert Pro diffractometer was used for XRD measurements here with scan durations set in accordance to the expected overall crystallinity of the sample being analysed:

- Polymers: 30-45 minute scans over 2θ angles of 3-30°,
- Oxide layers: 7 minute scans between 20-80°.

Subsequent diffractograms were analysed with the program HighScore Plus to remove the $K_{\alpha 2}$ transition, but background removal of the polymer diffractograms was accomplished with a script written in Matlab.

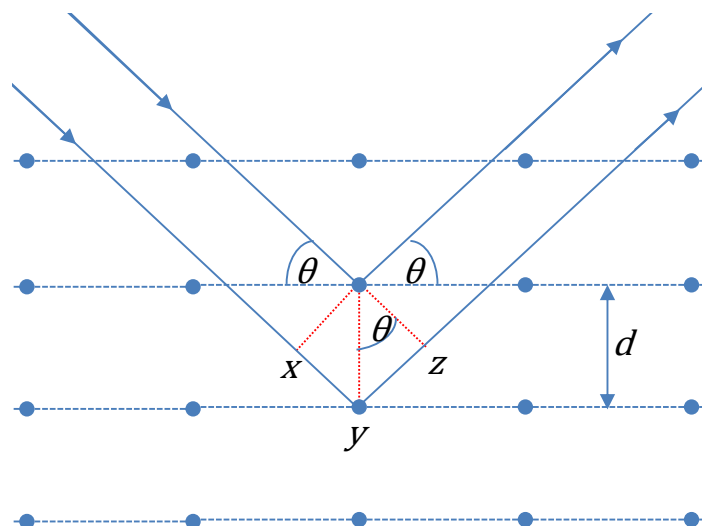


Figure 2.5: Two incoming parallel X-rays scattering off adjacent crystallographic planes and interfering constructively.

If one assumes that the crystallites giving rise to the observed diffraction peaks are of the same shape, the Debye-Scherrer equation may be used to calculate their size^[16]:

$$D = \frac{0.9K_S \lambda}{FWHM \cos \theta} \quad 2.15$$

in which the constant of 0.9 is a result of basing the calculation on the full width at half maximum (*FWHM*) of a peak centred at the Bragg angle θ . The value of the factor K_S is dependent on the shape of the crystallite being assumed. For spherical crystallites $K_S \approx 1$ and is the assumption that will be made in this thesis even if it does reduce equation 2.15 to just a comparative tool between samples.

2.5.5. Differential Scanning Calorimetry

This technique was applied to all polymer batches in order to determine key phase transitions, particularly T_g , T_c and T_m if they are present. The technique works by supplying energy to two separate pans so that both heat at the same rate as each other. One pan contains a small amount of the material under investigation while the second is a reference pan and is left empty. More energy is required in the first pan to maintain it at the same temperature as the second due to the material held inside; DSC plots this heat flow against temperature. As the material goes through phase transitions, its specific heat capacity will change and consequently the amount of energy required to raise its temperature by 1 °C will also change causing the plotted heat flow to vary against temperature. The heat flow will increase during endothermic phase transitions, such as the glass transition and melting; it will decrease during exothermic transitions, e.g.

crystallisation. Thus T_g , T_c and T_m can all be identified as shifts to the curve baseline (in the case of T_g) or peaks (for T_c and T_m) when the measured heat flow is plotted against the temperature. Figure 2.6 shows an example of a thermal analysis curve for poly(ethylene terephthalate) (PET) with the positive y -axis representing exothermic heat flow^[17]. As shown, a common practice is to define the temperature of these transitions at the intersection of the onset of heat-flow change and the baseline. However as the heat capacity of the material can vary through a measurement, the baseline will vary, too, and is itself user defined. More pertinent to this thesis is the return of the curve to the 'baseline' as that signifies the conclusion of the transition. As this temperature is also difficult to pinpoint precisely^[17], all thermal procedures applied to polymer films throughout this thesis were conducted at least 10 °C above the transition temperature being analysed – this was particularly important in chapter 3 for the complete wetting of NRA substrates with F8BT via thermal annealing.

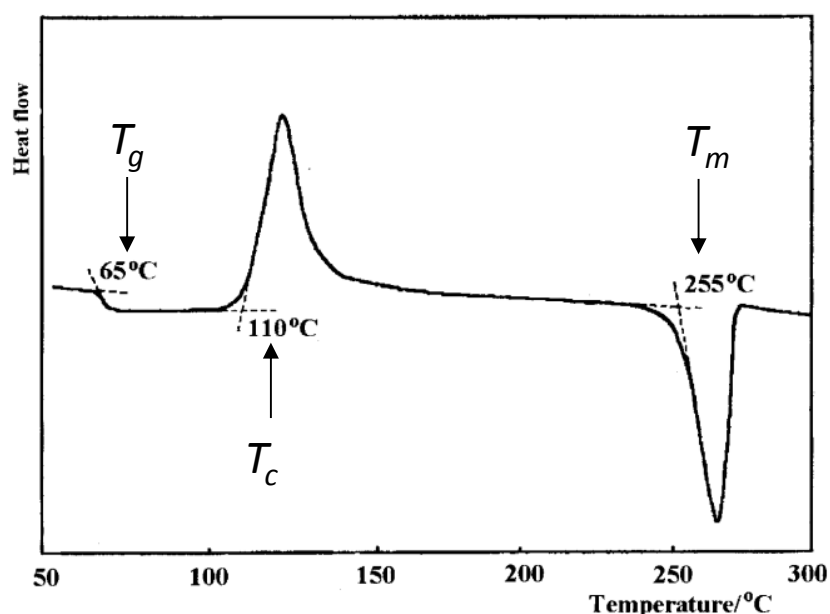


Figure 2.6: Example of a thermal analysis curve (an 'endotherm') for PET with the key phase transitions labelled. Adapted from reference [17].

It is possible to use DSC to extract an estimate of the fractional crystallinity of a sample by considering the energies needed to crystallise and then melt the sample – both of these quantities may be found by integrating the area under each respective peak and then dividing the values by the heating rate to give the enthalpy change per unit mass ΔH . This is discussed further in Chapter 5.

Due to the limited amount of polymer in some instances, 2-3 mg of each sample was loaded into Al pans and subjected to 3 heating/cooling cycles between temperatures of 50-300 °C at a rate

of 10 °C/min; all analyses were done according to the third cycle. These measurements were carried out with a Mettler Toledo DSC1 using an empty Al pan as a reference. Baseline fittings and peak integrations were conducted in OriginLab.

2.5.6. Contact Angle

Contact angle measurements were made to assess the wetting behaviour of solution droplets on differently processed surfaces. These measurements were carried out using a homemade setup positioned in fume hood with images captured via a USB microscope. ImageJ was then used to extract the contact angle θ_c from the captured images as shown in figure 2.7. Given the simple nature of the set-up, multiple droplets across multiple substrates were analysed to obtain at least a relative measure of θ_c between different samples in a series.

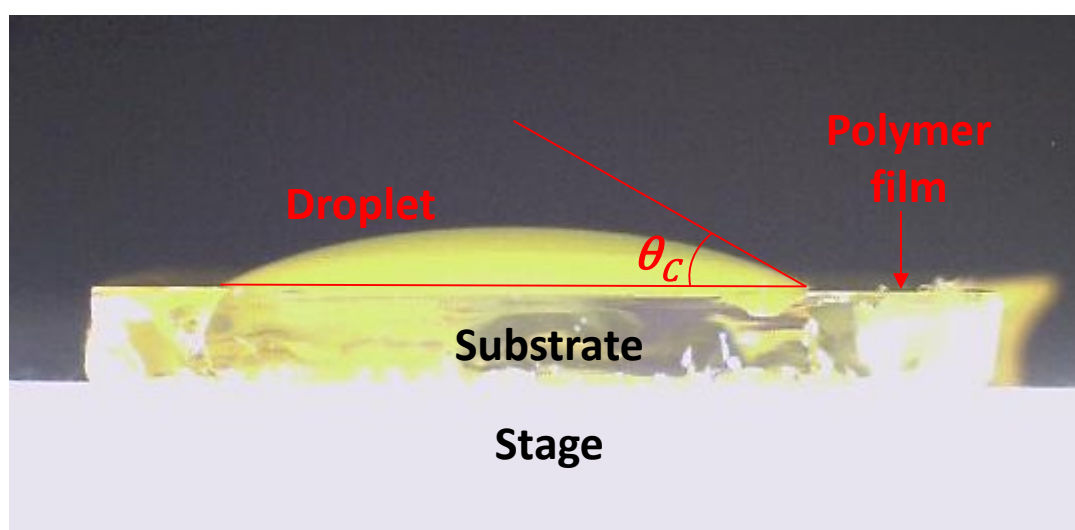


Figure 2.7: Example of a contact angle measurement with θ_c indicated.

2.6. References

- [1] D. Meyerhofer, *J. Appl. Phys.* **1978**, *49*, 3993.
- [2] J. Downing, M. P. Ryan, N. Stingelin, M. A. McLachlan, *J. Photonics Energy* **2011**, *1*, 011117.
- [3] D. C. Olson, Y.-J. Lee, M. S. White, N. Kopidakis, S. E. Shaheen, D. S. Ginley, J. A. Voigt, J. W. P. Hsu, *J. Phys. Chem. C* **2008**, *112*, 9544.
- [4] Ossila, *Organic Photovoltaic (OPV) and Organic Light Emitting Diode (OLED) Fabrication Manual*.
- [5] V. Ariel, V. Garber, D. Rosenfeld, G. Bahir, *Appl. Phys. Lett.* **1995**, *66*, 2101.
- [6] M. Losurdo, M. M. Giangregorio, P. Capezzuto, G. Bruno, F. Babudri, D. Colangiuli, G. M. Farinola, F. Naso, *Macromolecules* **2003**, *36*, 4492.

- [7] J. C. de Mello, H. F. Wittmann, R. H. Friend, *Adv. Mater.* **1997**, *9*, 230.
- [8] J. Costa Dantas Faria, A. J. Campbell, M. A. McLachlan, *Optimisation of Zinc Oxide as a Charge Injection Layer for Hybrid Organic-Inorganic Light Emitting Diodes*, 2012.
- [9] K. D. Vernon-Parry, *III-Vs Rev.* **2000**, *13*, 40.
- [10] M. Geoghegan, G. Hadziioannou, *Polymer Electronics*, 1st ed.; Oxford University Press: Oxford, 2013.
- [11] P. Eaton, P. West, *Atomic Force Microscopy*, Oxford University Press: Oxford, 2010.
- [12] Y.-P. Zhao, G.-C. Wang, T.-M. Lu, G. Palasantzas, J. De Hosson, *Phys. Rev. B* **1999**, *60*, 9157.
- [13] H. Alehdaghi, M. Marandi, A. Irajizad, N. Taghavinia, *Org. Electron.* **2014**, *16*, 87.
- [14] C. Jonda, a B. R. Mayer, U. Stolz, A. Elschner, A. Karbach, *J. Mater. Sci.* **2000**, *35*, 5645.
- [15] D. Nečas, P. Klapetek, *Cent. Eur. J. Phys.* **2012**, *10*, 181.
- [16] M. Birkholz, *Thin Film Analysis by X-Ray Scattering*, Wiley-VCH Verlag GmbH & Co. KGaA: Weinheim, FRG, 2005.
- [17] P. G. Laye, In *Principles of Thermal Analysis and Calorimetry*, Haines, P. J., Ed.; The Royal Society of Chemistry: Cambridge, 2002; pp. 55–93.

Chapter 3 – ZnO Nanorod Arrays as an Electron Injection Layers for Hybrid Light-Emitting Diodes.

This Chapter concerns the use of ZnO NRAs as EILs within HyLEDs. Traditionally, HyLEDs already possess a planar oxide EIL; a ZnO EIL can therefore serve as a seed layer for the growth of high quality ZnO NRAs. Much of the initial characterisation of such NRAs, including the influence of growth time and ZnO seed layer thickness on the NRA, was carried out in the Masters research phase of this project from which the work in this Chapter continued; those results can be found in reference [1] as well as Appendix A. The research detailed in this Chapter involves the application of such ZnO NRAs as a non-planar EIL in hybrid organic/inorganic LEDs for lighting and displays; the main results of this chapter have been published in *Adv. Funct. Mater.* **2015**, *25*, 4657^[2].

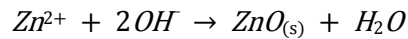
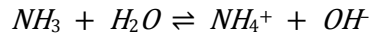
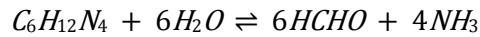
3.1. ZnO Nanorods in Literature

Depending on the growth conditions and techniques, ZnO can express a wide range of morphologies including nanoflowers^[3], tubes^[4], ribbons^[5], and propellers^[6] all possessing their own unique optoelectronic properties^[7,8]. NRs, in particular have seen a significant uptake for a variety of optoelectronic applications, in wholly inorganic devices, or combined with OSCs to create hybrid devices. In the latter field, the ability to deposit NRAs using low (< 100 °C) temperature techniques which are compatible with flexible substrates is an added attraction and there has been particular interest in incorporating them into hybrid OPVs. The development of NRAs with OSCs for light emission is significantly behind that of NRAs for OPVs where there has been a greater exploration of, for example, processing techniques for device optimisation. This section gives an overview of the growth and the factors affecting the morphology of ZnO NRAs and its current implementation in light-emitting devices, but also considers the use of NRAs in OPVs.

3.1.1. Growth and Characterisation

Solution-based growth methods of a ZnO NRA have been favoured as they require relatively low temperatures and only ambient pressures, considerably simplifying and reducing the costs of

their deposition. Vayssieres showed that it was possible to grow a ZnO NRA using hydrothermal methods using zinc nitrate hexahydrate $[Zn(NO_3)_2 \cdot 6H_2O]$ and hexamethylenetetramine (HMT) $[(CH_2)_6N_4]$ as precursors^[9]. The HMT reacts with water to produce ammonia which further reacts with water to release OH^- ions. These react with Zn^{2+} and the resulting thermal decomposition results in ZnO precipitating out of the solution, thus:



This initial report demonstrated nanorods of lengths 0.5-1.5 μm , randomly orientated with respect to the substrate. Subsequent research has been focused on identifying the variables which affect the morphology of the array to improve its uniformity and reproducibility. A major breakthrough in achieving this goal was made by Greene *et al.* who demonstrated that the alignment of the array could be considerably improved if it was grown on a thin textured ZnO seed layer^[10]. The crystallite orientation of the ZnO seeds was found to directly influence the orientation of the NRs, in particular the alignment of the (001) lattice plane parallel to the substrate resulted in the NRA aligning perpendicularly to the substrate as growth along the *c*-axis is energetically preferred. Changing the orientation of the seed layer crystallites by varying the post-deposition annealing temperature resulted in more randomly aligned rods with respect to the substrate. Importantly, this work showed that the crystalline orientation of the seed layer was substrate independent and that zinc acetate appeared to be unique amongst zinc oxide precursors in creating alignment in this way. Subsequent work by others has shown the effects on the NRA morphology due to a wide range of variables including the pH of the growth solution^[4,11] as well as growth duration and temperature^[12-15]. For example, the Masters' research conducted prior to this report^[1] highlighted the effect on the NRA caused by changing the concentration of the sol-gel from which the seed layer was cast from: varying the concentration between 0.1-0.75 M led to a change in the thickness of the seed layer between 20-130 nm over which the rods would become more ordered and aligned perpendicularly to the substrate with thicker films (Appendix A). Their diameter would also increase and so too would the number of rods per unit area^[1]. This work largely supported the findings by Ma *et al.* who similarly recorded a drop in density and alignment in thinner films, though with rods instead *increasing* in diameter^[16].

The ZnO NRA procedure followed here uses a pre-cast ZnO seed layer to aid in NRA alignment, but also includes additives to attain the desired morphology for specific optoelectronic

applications; as discussed in Section 3.1.2. Additives can affect the NRA morphology by altering the concentration of Zn^{2+} and OH^- present in the solution or by encouraging growth along certain planes through adsorption to particular ZnO crystal surfaces. For instance, it is well known that increasing the concentration of the reactants leads to the supersaturation of the Zn^{2+} and OH^- ions and therefore the rapid formation of ZnO precipitate *within* the solution (homogenous nucleation). The addition of ammonia, however, lowers the concentration of OH^- by slowing down the degradation of HMT allowing nucleation of ZnO to take place on a substrate surface (heterogenous nucleation); the result is a longer NRA for a given growth duration^[17]. The additives used in this work are polyethylenimine (PEI) and KCl. The effects of PEI are well documented and show that the addition of PEI reduces rod diameter whilst simultaneously increasing their length, i.e. the aspect ratio of the rods is increased dramatically. Mahmood *et al.* showed increased rod lengths from 3 to 7 μm and reduced rod diameters from ~ 330 to 150 nm giving an overall factor 5 increase in aspect ratio^[18]. Zhou *et al.* explain that the PEI selectively adsorbs onto the sides of the NRs due to the electrostatic attraction between the $-\text{NH}_2$ groups on the PEI and non-polar lateral rod facets: (100), (110) and (010)^[19]. The polar (001) facet, however, remains exposed to Zn^{2+} ions; coupled with the fact that this facet exhibits the highest surface energy, growth is therefore strongly encouraged along the *c*-axis.

Conversely, Downing *et al.* suggested that KCl interacts primarily with the (001) facet. A strong correlation between NR length and KCl concentrations between 0-500 mM was observed coupled with a very weak increase in rod diameter up to 400 mM^[20]. Specifically, increasing KCl concentration stabilises the rod terminations causing the disappearance of pointed tips to flat hexagonal facets.

Therefore, the use of PEI and KCl addresses different aspects of rod growth and their combined application together with the use of a textured ZnO seed layer has been shown to yield reproducible and highly uniform arrays^[21].

3.1.2. Applications: Organic Photovoltaics

Within the field of plastic electronics, it is OPVs that have seen the greatest uptake of NRA devices. In fact, a large proportion of the advances in ZnO NRA morphology control have been carried out by teams aiming to utilise them for harvesting solar energy. Here, by filling the gaps between the NRs with an OSC, it is possible to create a large interpenetrating network between donor and acceptor materials with a significantly enhanced interfacial surface area for exciton separation and charge collection. It is therefore important to have an array with: (i) high aspect ratio rods to increase the surface area of the layer (though not so thin as to compromise

electron transport through the layer); (ii) an inter-rod spacing corresponding to twice the exciton diffusion length of the OSC so excitons can reach the OSC:ZnO interface; (iii) an open and well aligned morphology to improve material infilling; and (iv) uniformity of length to prevent device shorting through the OSC material on top of the array.

For example, for their ZnO NRA DSSC devices, Mahmood *et al.* show that the increased aspect ratio due to the addition of PEI gives PCEs of 2.8 ± 0.1 % versus 1.13 ± 0.01 % in devices without PEI^[18]. Length is a clear influential factor as it would increase the available surface area for charge collection and indeed Olson *et al.* noted an increase in J_{sc} in devices with rods 500 nm versus those with 250 nm^[22]. Wu *et al.* demonstrated that the advantage of longer rods exists only up to a point: beyond 500 nm there was little increase in efficiency due to the attenuation of light through the active layer^[23]. Baeten *et al.*, even noted a decrease in device efficiencies beyond lengths of 600 nm; this was attributed to the increasing distance that charges (particularly those travelling in the polymer) would have to travel to be collected by the electrodes^[24]. This same group later showed that the best device efficiencies were unexpectedly obtained from those possessing a highly disordered array with a low rod density^[25]. In this way, they were able to report an improved power conversion efficiency (PCE) of 0.82 % using a poorly aligned array of 300 nm rods against their 0.76 % recorded with an aligned array of 600 nm rods. The density of the layer is likely to impact the morphology of the polymer layer itself as well as its wetting behaviour with more closed arrays being harder to infiltrate^[22].

Unfortunately, the PCE achieved by incorporating NRs into hybrid OPVs are frequently lower than that recorded by either planar heterojunction OPVs or those with other nanostructured ZnO layers, such as nanoparticles^[26]. This could be due to difficulties in achieving polymer infiltration as well as the right polymer morphology to aid the transport of dissociated charges. Nevertheless, research into ZnO NR OPVs remains popular and is proceeding along many lines. For instance, passivation of the NRA surface with SAMs was observed to lead to efficiencies of 2.1% compared to 1.6% in untreated arrays^[27]; making use of the rods' piezoelectric properties by exposing the array to acoustic vibrations led to a 45% efficiency increase to 1.75%^[28]; and patterning the NRA via stamp-processing improved the light harvesting of the layer increasing efficiencies to 5.95%^[29]. Finally, ZnO NRAs were recently combined with a perovskite layer to create a solar cell exceeding 11% efficiency^[30].

3.1.3. Applications: Light-Emitting Diodes

The amount of research devoted to the development of NR OPVs far exceeds that given to the development of these structures when combined with OSCs for light emitting purposes. This is

somewhat understandable: given that the role of the array in OPVs is to increase the surface area for exciton dissociation and charge collection, it therefore seems counterintuitive to combine an array with an OSC and expect efficient light-emission – surely a high degree of non-radiative exciton decay is likely to occur? The frequently low OPV efficiencies reported from devices with a ZnO NRA acceptor layer suggests that, amongst the other factors already listed, the ZnO/polymer interface may be a poor one for exciton dissociation. Indeed, Lloyd *et al.* have shown that the concentration of photogenerated polarons is nearly identical in P3HT films cast either on glass or ZnO showing that ZnO does not appear to promote additional exciton dissociation^[31]. Recently, Musselman *et al.* demonstrated that this behaviour is likely due to the existence of a high density of trapped electron states which serve to raise the WF of ZnO at the surface; lowering the concentration of these states through nitrogen doping lowered the WF causing an increase in J_{sc} from 0.22 to 0.50 mA/cm²^[32]. The same appears to be true of ZnO NR OPVs: in their review, Huang *et al.* compared a range of results from ZnO NR/P3HT devices and ZnO NR/P3HT:PCBM devices; the former demonstrated efficiencies below 0.5%, whilst the latter, (in which the NRA acts a buffer layer and exciton dissociation occurs at the P3HT:PCBM interface instead), efficiencies were at 1.8-3.90%^[26].

The LUMO of F8BT as quoted across literature is slightly lower than that of P3HT (cf. -3.3 eV vs. -3.1 eV), putting it even closer to the potential WF of the ZnO. All else being equal, it is therefore assumed that the impact of non-radiative exciton dissociation at the ZnO NR/F8BT interface to be low.

The earliest report in which a ZnO NRA was used in conjunction with an organic layer for light-emission was published in 2004 by Könenkamp *et al.*: here, the ZnO NR layer was grown using electrodeposition from a SnO₂ substrate, coated with an insulating polystyrene layer followed by PEDOT:PSS and an Au anode^[33]. The recorded emission originated from the ZnO layer itself, namely due to band edge transitions at ~380 nm, and a broad emission centred at ~600 nm attributed to defect states. Like this initial device, those that were reported soon after also used an insulating polymer infiltrated into the array to prevent device shorting^[34]; this is particularly true of the work published by Willander's group who have used high M_w polymers for this purpose^[35-37].

Earlier reports merely used an OSC as a hole transporting layer for charge recombination at the NR/polymer interface with the diodes mainly functioning as UV-emitters^[33,34,38,39]. Polymers such as MEH-PPV^[40] and PFO^[41] have also been employed in dual roles as hole transporters and visible light emitters; in these reports light emission occurs from both the polymer and the ZnO

giving rise to broad EL spectra and frequent claims of white light emission^[41], though many deviate considerably from the (0.33, 0.33) chromaticity coordinate ^[35,37].

Claims stating that these devices can be used for display and lighting purposes seem premature as the EL spectra reported are often very noisy reflecting a weak emission intensity and emission colour is strongly dependent on the applied forward bias. This might explain why prior to our research into these devices, there were no reported measures of efficiency or luminance values. Furthermore, the literature cited thus far shows the NRA in a variety of different diode geometries with no clear reference to an ideal NR morphology for light-emitting applications. Aside from the device stacks which cover the array with an insulating polymer, there are those, too, which infiltrate the array with the OSC, but few experimental details are given and complete infiltration is usually presumed^[40,42]. A third approach sees the OSC cast onto the substrate with the NRA subsequently hydrothermally grown on top of it^[36,41]. All of these factors make it difficult to compare devices and to understand the exact role of the ZnO NRA.

Only recently have reports started to be published detailing the role of ZnO NRAs within hybrid LEDs with accompanying quantitative efficiency measurements. Yang *et al.* were first to give detailed EQE calculations for a ZnO NR UV-emitter in which they took advantage of the piezoelectric properties of the material to generate efficiencies of 5.92 %^[43]. These, however, had unusual geometries in which the NRs were individually cast parallel to the substrate with PEDOT:PSS/Au electrodes at both ends^[43]. Beyond NRAs of ZnO, great success has been found by casting a self-aligned horizontal layer of NRs as shown by Nam *et al.* who used double heterojunction ZnSe/CdS NRs as emission centres to generate an EQE of 12% along with efficiencies of 27.5 cd/A and 34.6 lm/W^[44]. There also appears to be some interest in utilising polymers as downconverters in inorganic LEDs as shown by Smith *et al.* who successfully infiltrated a vertical InGaN/GaN NRA with F8BT to generate white light^[45]. Generally, nanostructured layers have been used in OLEDs to improve device efficiency by enhancing the outcoupling of generated photons^[46]. Such layers are typically composed of low aspect ratio periodic grating structures onto which the active layers are cast. There is theoretical work which shows, too, that nanostructured contacts can also improve charge injection through enhancement of the internal electric field^[47,48]. However, as stated by Gerken (2013), with IQEs of 100% being frequently reported as a result of other, perhaps simpler, experimental procedures, nanostructuring in OLEDs has largely been used to address the issue of poor photon outcoupling^[46].

At the time of starting our investigations, the viability of a vertically aligned ZnO NRA infiltrated with a light emitting polymer such as F8BT for lighting and display purposes had yet to be determined. The remainder of the Chapter details the results and experimental routes taken in the creation of such a diode.

3.2. Growth and Characterisation of the ZnO Nanorod Array

Growth of the NRA was carried out on pre-prepared ZnO seed layer-covered substrates (Chapter 2) using the hydrothermal method described by Downing *et al.*^[21]. The ZnO substrates were fixed onto mounts, rinsed with DI water to remove any particulates which may have settled on the surface and dried with a N₂ gun before being submerged into the hydrothermal growth solution at 95 °C in a 1L Pyrex glass flask. The precursors in the solution consisted of zinc nitrate hexahydrate and KCl dissolved in 980 ml DI water. To avoid a delay between the start of the reaction and the exposure of the substrates to the reaction environment, the HMT and the PEI were dissolved separately in 20 ml of DI water and added to the main solution after the substrates have been submerged in the flask. This would bring the combined volume to 1L. The duration of the substrates within the reaction mixture dictated the length of the rods as previously shown (Appendix A)^[1]. The reaction was stopped by the removal of the substrates from the mixture and the substrate surface rinsed with DI water to wash off any reactants. Substrate preparation was completed with a final drying step at 60 °C.

SEM images show a highly uniform array consisting of rods aligned perpendicularly to the substrate^[1]. To supplement the array characterisation previously conducted, the increase to the surface area as a function of different NR lengths was analysed. Plane-view SEM images of arrays grown between 0.5-2.0 hours (~170-750 nm lengths) were taken and 1 × 1 μm² quadrats were processed with ImageJ. The software was used to calculate the percentage (i.e. the surface area) of the image consisting of the top nanorod facets, as well as the circumference around these tip areas. The surface area of the exposed side facets was then the product of this circumference and the NR length. Finally, the total surface area of the ZnO was the sum of the area due to the side facets plus that corresponding to the exposed area of the base and tips (1 μm²). Alternatively, multiplying the total area *between* NRs by the height of the array gives an estimate of the total volume within the array that is available for material infilling. These are ball-park calculations with the assumption that *all* of the nanorods are perfectly aligned perpendicular to the substrate. Figure 3.1a-b shows an example of the image processing steps and the results of these calculations for the lengths grown. It can be seen that the surface area increases by a factor of ~17 between a planar surface and a 750 nm high array. Should the extra

surface area be providing extra pathways for electron injection, one would expect the electron current density J_e to correlate with these results.

The main device work was carried with arrays 750 nm thick for which we see a distribution of NR diameters of around 70 nm (figure 3.1c). For such an array, XRD measurements confirm the highly crystalline nature of the layer with an intense reflection from the (002) plane indicating predominant orientation of the c -axis perpendicular to the substrate plane (figure 3.1d).

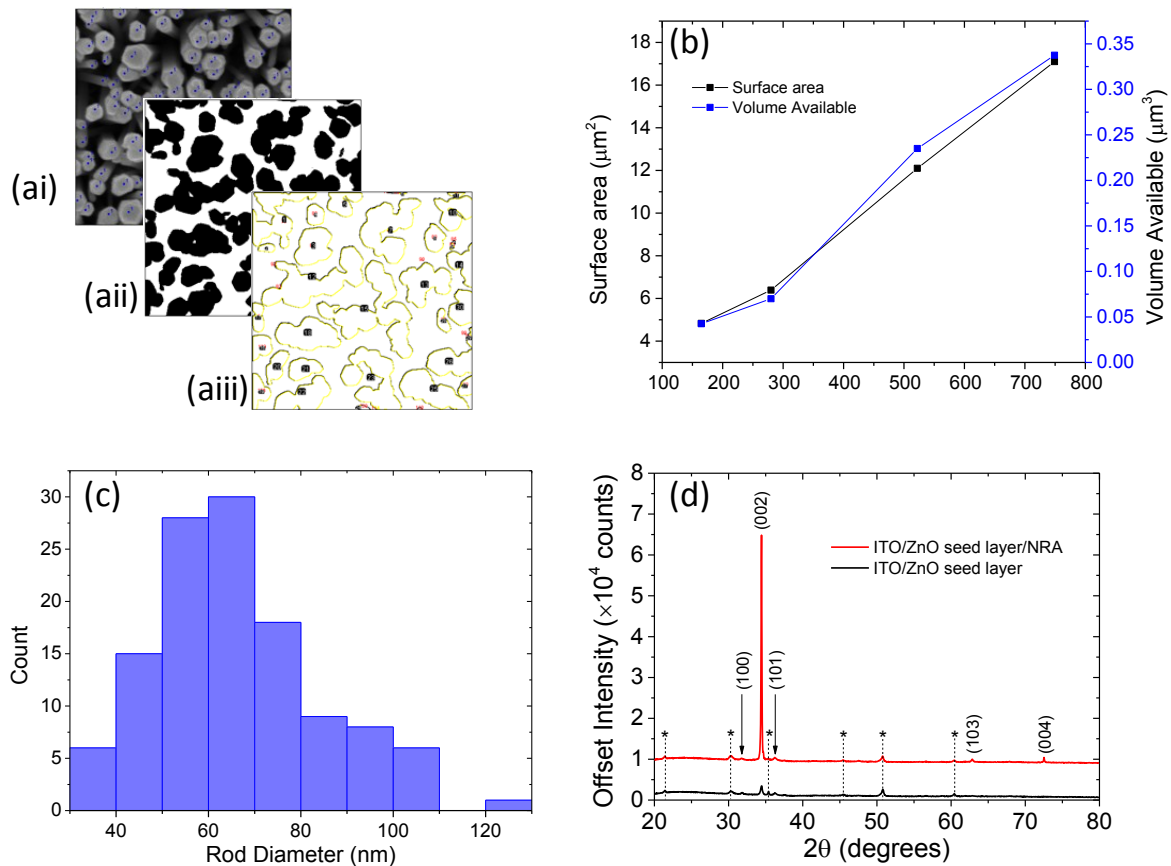


Figure 3.1: (a) Analysis of a typical $1 \times 1 \mu\text{m}^2$ quadrat: (ai) the NRs, (aii) calculation of the surface area due to the NR tips and (aiii) the circumference of these regions. (b) Variation of surface area and infiltration volume available as a function of NR length. (c) Variation of rod diameter for a 750 nm thick array. (d) XRD patterns for ITO/ZnO and ITO/ZnO/NRA.

3.3. ZnO NRA HyLED Devices

3.3.1. Device Preparation

For the batch of F8BT used for these experiments (American Dye Source, $M_w \sim 116$ kg/mol and dispersity 3.4) the DSC measurements (figure 3.2) showed a T_g of 125 °C and a broad T_m from 220-260 °C; this compares well with DSC measurements by others for F8BT of similar M_w and indicates the presence of multiple polymorphs^[49]. Like the planar (seed) ZnO thin films, the NRA substrates were heated at 150 °C for 30 minutes to remove potentially physisorbed surface

water once transferred into the glovebox^[50]. F8BT was then spin-cast from a concentration of 30 mg/ml in toluene corresponding to a thickness of ~ 450 nm on planar substrates. The substrates were then dried at 90 °C or underwent the post-deposition thermal treatments outlined in Chapter 2 for twenty minutes at temperatures just above either the measured T_g or T_m . TFB was spin-cast only onto the substrates that were annealed above the F8BT T_m and slow-cooled back to room temperature to encourage the adherence of the TFB layer (Chapter 4). Following the deposition of the polymer layer/s, the contacts were evaporated as discussed in Chapter 2 to give an overall device structure ITO/ZnO (130 nm)/ZnO NRA (750 nm)/F8BT (nominal pre-infiltration thickness 450 nm)/TFB (0 or 50 nm)/MoO_x (10 nm)/Au (80 nm). Devices without TFB will be referred to as 'preliminary', whilst those with TFB will be referred to as 'optimised.'

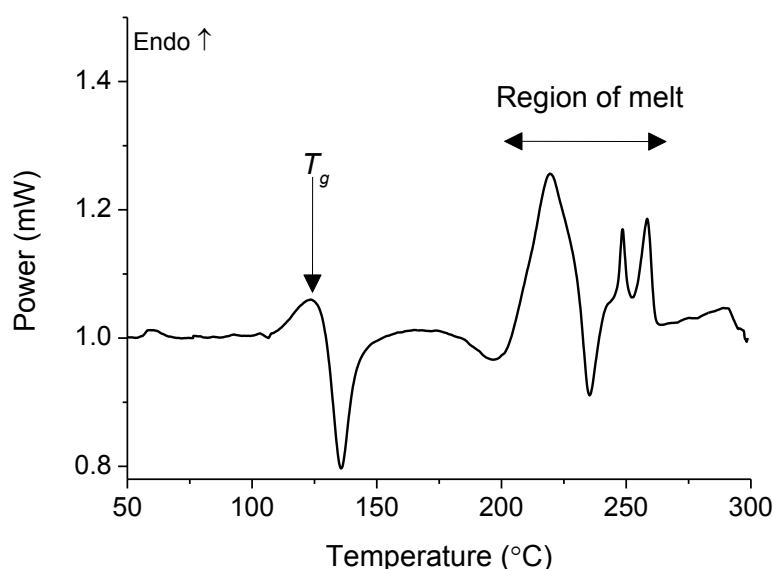


Figure 3.2: DSC measurements for the batch of F8BT used in this Chapter's experiments with the relevant thermal transitions highlighted.

3.3.2. Preliminary Devices

Figure 3.3 shows that full infiltration of the polymer into the array was possible following a thermal anneal of the polymer layer above its T_m whilst still leaving a 150-200 nm thick F8BT layer on top of the array. We note that the calculated available infiltration volume (Figure 3.1(b)) for a 750 nm high array would be expected to reduce the F8BT thickness of a 450 nm thick film to 100 nm; these measured values therefore indicate a high degree of polymer infiltration. The lack of any thermal treatment leaves a thick organic layer on top of the array while some uptake was observed when the polymer was annealed just above T_g . The need to melt the OSC to achieve wetting of the NRA is widely reported in OPV literature. This is in sharp

contrast to NR HyLED literature to date, Smith *et al.* reporting the need to cast F8BT four successive times from a standard 10 mg/ml solution to infiltrate their InGaN/GaN NRA^[45].

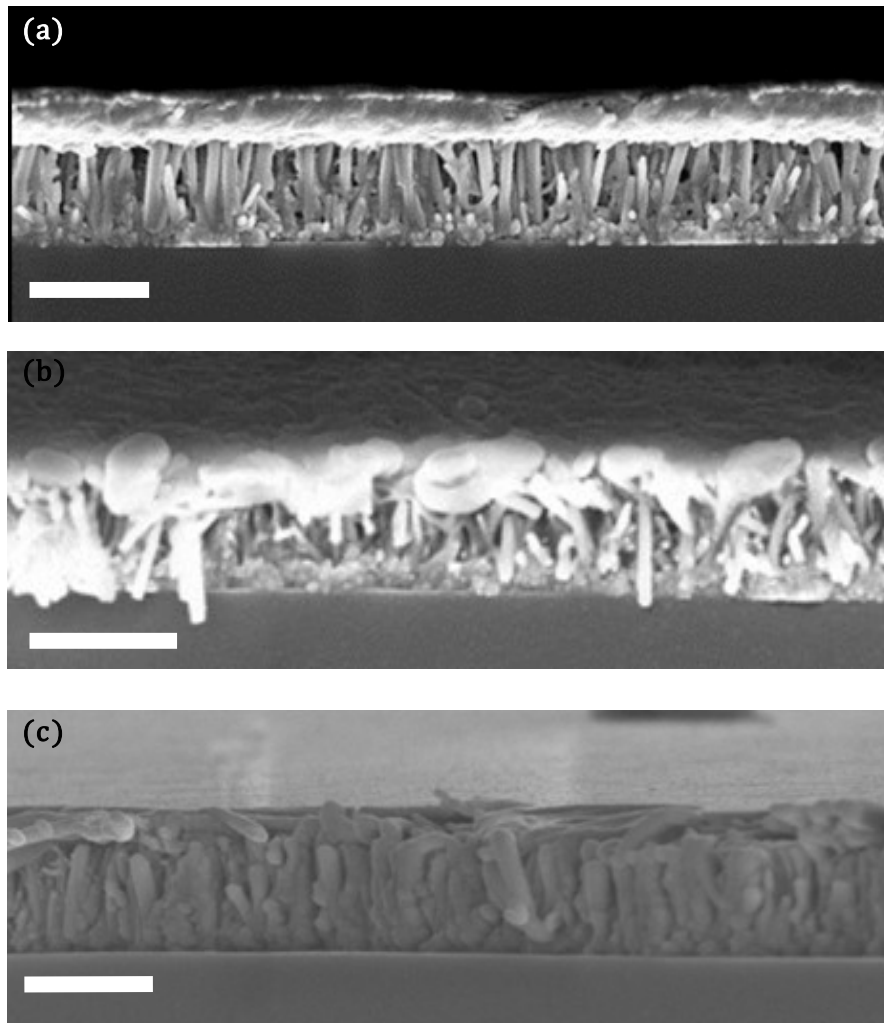


Figure 3.3: Cross sectional SEM images of the NRA with F8BT a) as-cast, b) annealed just above T_g and c) annealed just above T_m . Scale bar = 1 μm .

J - V characteristics clearly show the effect of annealing the F8BT above T_m versus those that were as-cast (figure 3.4a). Whilst both demonstrate diode behaviour, the ratio of the forward/reverse currents at ± 4 V is 8 times higher in melt devices (20.3) compared to the as-cast devices (2.60), most likely due to the increase in interfacial contact between the NRA and the F8BT. Light detected from the as-cast devices was considerably lower than < 1 cd/m^2 attributed to the high resistance due to the thick polymer layer contacting only the tips of the array. With considerably more pathways for charge injection available, the melt devices show a current almost 1000 times greater at 10 V in comparison. Despite such a large current density repeat measurements only led to one instance of strong light emission being detected (figure

3.4b); this device demonstrated a light turn-on voltage V_{L-on} of 3.2 V, max luminance of 878 cd/m^2 and a current efficiency of 0.047 cd/A . Though this efficiency was very low, the luminance almost reached the 1000 cd/m^2 required for general lighting and in any case, these represented the first quantifiable performance metrics for this class of LED.

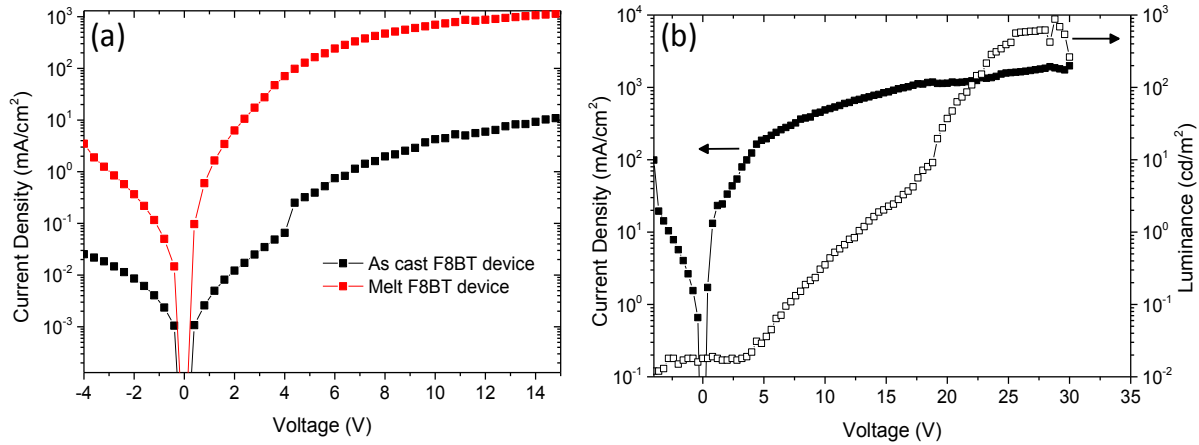


Figure 3.4: (a) J - V characteristics comparing NRA HyLEDs in which the F8BT was left as-cast or annealed above T_m . (b) J - V - L characteristic of the only 'preliminary' device to show significant light emission.

3.3.3. Optimisation with Electron Blocking Layer

Consideration of the energy levels of the materials (figure 3.5) involved might explain the poor yield of these devices. It can be seen that the F8BT/ MoO_x interface is likely to be a poor barrier to electron transport due to the large negative barrier ϕ_e between the F8BT LUMO and the oxide CB. Therefore if the NRA is flooding the device with negative charge, it might be the case that it will be efficiently extracted if there are insufficient holes for recombination. This would assume that the NRA turns a traditionally hole-dominated HyLED into an electron-dominated one - electron-only NRA devices (see section 5 of this Chapter) suggest that this might be the case. Furthermore, in Chapter 5 we observe that the hole injection from the MoO_x/Au anode in our systems may be subject to significant trapped charge effects which would add weight to this argument. If electron injection is improved by the NRA, there would also be a shift in the RZ away from the $\text{ZnO}/\text{F8BT}$ interface towards the $\text{F8BT}/\text{MoO}_x$ interface. The large difference in energy levels at $\text{F8BT}/\text{MoO}_x$ interface would lead to substantial exciton quenching and minimal light emission.

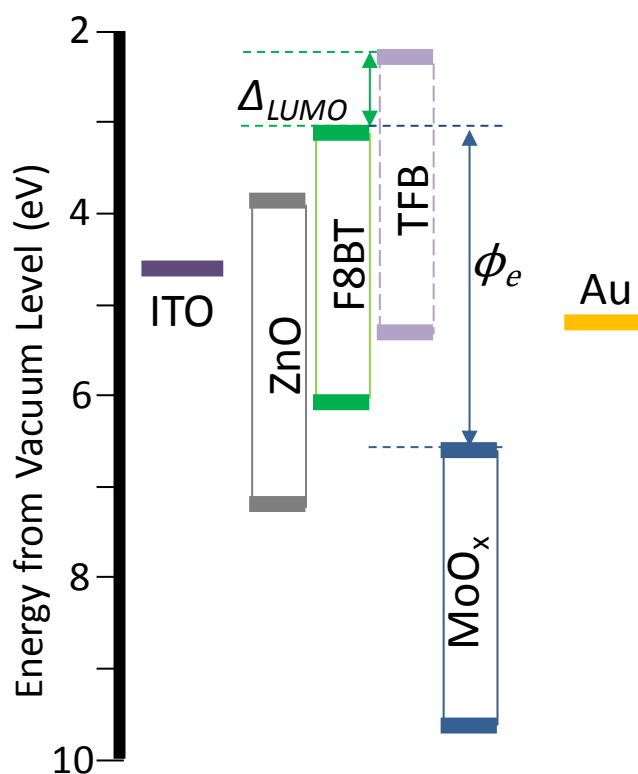


Figure 3.5: Energy-band diagram of all the materials discussed in this Chapter. Note that 'preliminary' devices do not contain the TFB layer.

TFB (see Chapter 1) has traditionally been used in conjunction with F8BT to reduce both electron transport to the anode and exciton dissociation at the PEDOT:PSS/F8BT interface in PLEDs due to the ~ 0.7 eV difference in LUMO levels Δ_{LUMO} between the two polymers^[51,52]. Therefore, a 50 nm layer of TFB was introduced at the F8BT/MoO_x interface to confine electrons within F8BT and/or reduce potentially non-radiative exciton decay here. The procedure of casting the TFB layer onto the F8BT using solution-based methods is discussed in Chapter 4. Cross-sectional SEM (figure 3.6) shows the complete structure for these 'optimised' devices, with an overlayer of TFB now present.

Device yield, luminance and efficiency all improved dramatically upon the addition of TFB supporting the hypothesis that unfavourable charge processes were indeed occurring at the F8BT/MoO_x interface. Figure 3.7 shows a sample of five pixels all of which managed to exceed the luminance barrier of 1000 cd/m². The highest recorded luminance was 8602 cd/m² while the η_{CE} was 1.66 cd/A. However, as indicated by figure 3.7, there is a large spread across the recorded metrics. A total of 23 pixels were analysed (figure 3.8) and maximum luminance values exceeding 1000 cd/m² were observed in 87% of these devices with 75% falling in the 1000-3000 cd/m² range. 22% exceeded 1 cd/A, though over half (56%) recorded efficiencies

below 0.3 cd/A. Despite a low V_{L-on} of 2.5-3V, the luminance increases slowly with voltage, so significant brightness values are not reached until 15-20 V. The maximum power efficiency recorded was therefore rather low at 0.26 lm/W. Nevertheless, with a large percentage of devices exceeding 1000 cd/m² these metrics represented the first to show that hybrid LEDs consisting of a vertical ZnO NRA together with a light-emitting OSC could have applications for general lighting and, indeed, display purposes. As a step towards device optimisation, it is clear that the TFB layer has had a significant, positive impact.

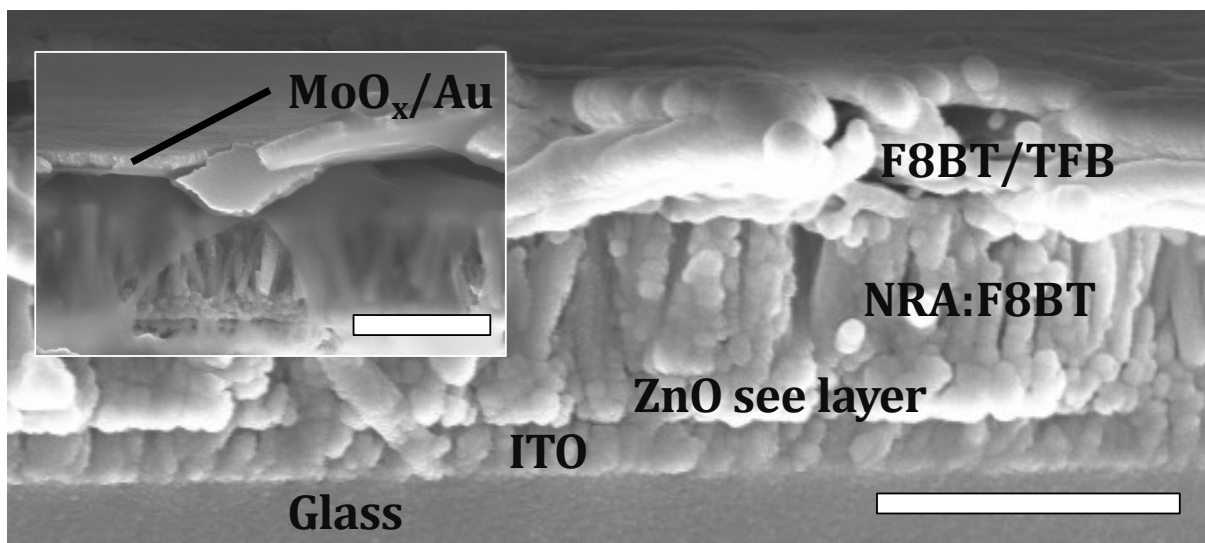


Figure 3.6: SEM cross-section of the 'optimised' device with all of the non-organic layers clearly distinguishable. Inset: a cross-section of the same substrate also showing the evaporated top contact. Scale bars: 1 μ m.

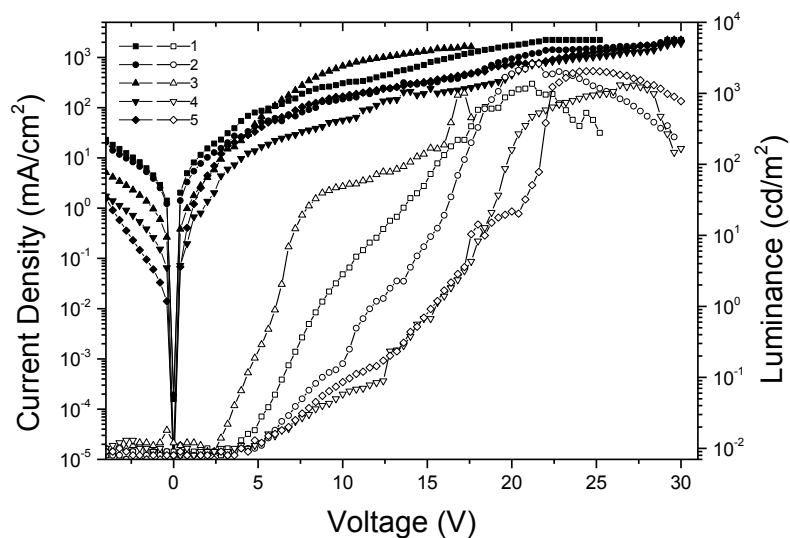


Figure 3.7: J - V - L characteristics for a sample of NR HyLEDs following the introduction of TFB. Closed symbols represent J and open symbols represent L .

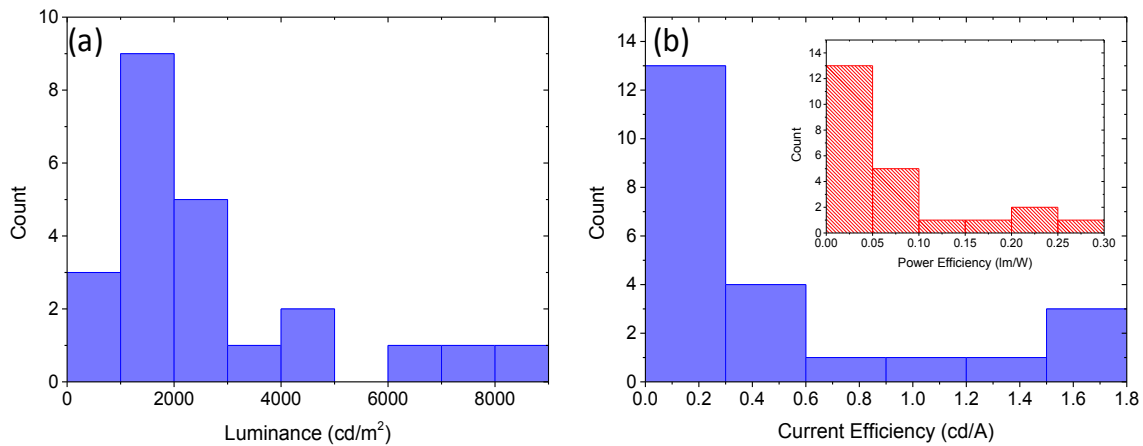


Figure 3.8: Frequency charts for a sample of 23 ('optimised') devices showing the maximum recorded (a) luminance and (b) current efficiency with power efficiency shown inset.

EL measurements suggest that all detected emission appears to originate from exciton recombination within the F8BT layer (figure 3.9a). This is in sharp contrast to the NR HyLEDs reported in literature which show that the most intense emission is due to the ZnO band-edge transition at 380 nm - this is not observed at all here. This peak does lie in the high absorbance regions of the two polymer layers (figure 3.9b), but if isotropic emission is assumed, at least some light at this wavelength should be have been detected. Emission due to ZnO defect states would coincide with the F8BT emission range over 500-600 nm; this is always reported to be considerably weaker than the 380 nm peak and since that peak isn't observed, it is unlikely that these states are contributing to the EL either. F8BT normally exhibits a broad emission profile with a peak at 550 nm and a shoulder at ~580 nm, but three distinct peaks are instead observed. Optical interference effects are likely to take place as a result of the thick device geometry giving rise to multiple peaks. Such interference effects are also observed in transmission measurements (figure 3.9b) through the device stack (without the evaporated contacts) and a separate EL measurement from a different pixel shows again three distinct peaks, but at different wavelengths with different relative intensities; this is expected if there are slight differences in layer thicknesses between pixels.

We now consider some of the issues which may be causing the observed large spread in data.

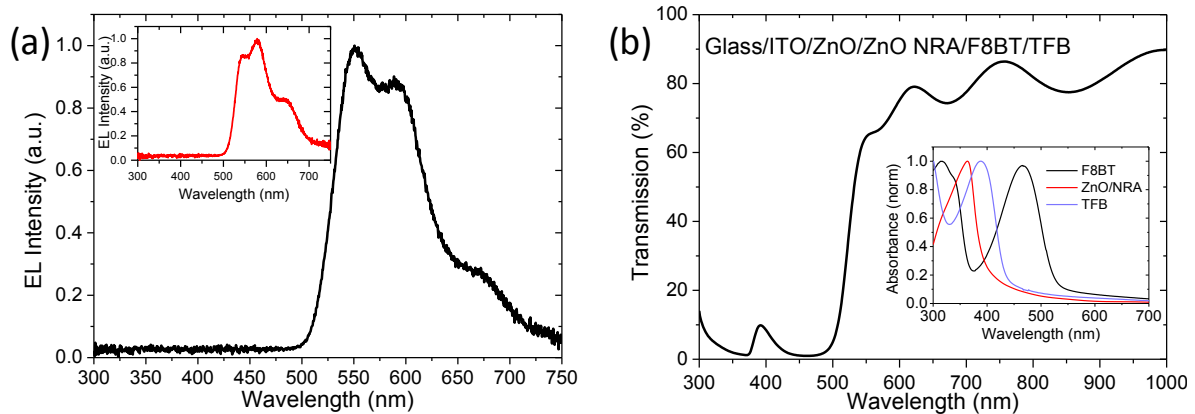


Figure 3.9: (a) 'Optimised' device EL with an EL from a second pixel inset. (b) Transmission spectra of a device stack showing interference fringes in the high transmission (> 500 nm) region. Inset: absorbance spectra the ZnO/ZnO NRA and polymer layers.

3.4. Causes of Device Variability

It is clear from top-view SEM images of completed device stacks that local variations in nanorod length as well as that of the F8BT layer thickness on top of the array may be contributing to the spread in data observed in figures 3.7 and 3.8. For instance, whilst the average pre-infiltration thickness of the F8BT was observed to be 450 nm, a range of measurements from 409 to 483 nm was recorded. This would lead to variations in the distance between the NR tips and the evaporated anode after infiltration. Any variations in the inter-rod spacing would further compound this effect through changes to the volume of infiltrated material. These distance variations would, at the very least, lead to a non-uniform electric field across a pixel and, at worst, direct physical contact between a NR and the anode; both cases would lead to device instability and reduced lifetimes. Figure 3.10 shows a collection of these non-ideal layer variations with SEM images of the top polymer and electrode surfaces of tested devices.

3.5. Further Work

Beyond the fabrication of the LEDs, further experiments were attempted to clarify the operation of these devices. Specifically, these involved measuring: 1) J_e in single carrier NRA devices; 2) the XRD pattern of the infiltrated polymer layer to assess the impact of the NRA on polymer packing and; 3) the influence of NR length on device performance. Due to time constraints and the frequent unstable device performance encountered with NRA devices, the work discussed in this section is very much at a preliminary stage, but present several promising avenues for further research.

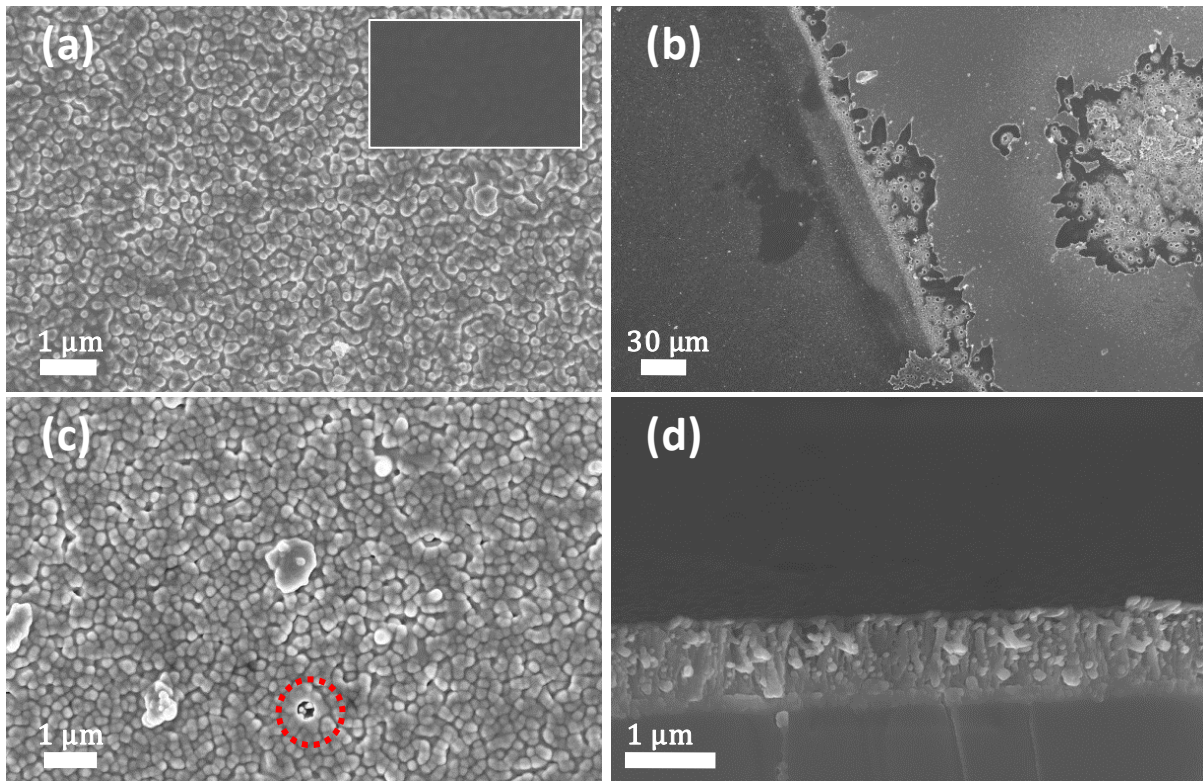


Figure 3.10: SEM images of tested devices with non-ideal layers. (a) SEM of the top electrode suggesting a surface morphology influenced by the underlying NRA as a result of a thinner polymer layer. Inset: for a 'good' electrode the surface is observed to be largely featureless. (b) Image showing both polymer and electrode surfaces; the electrode has undergone significant delamination as a result of unstable operation exposing the underlying layers. (c) A magnified image of the top polymer surface showing clear NR exposure (red circle) and a morphology heavily influenced by the NRA. (d) A cross-section confirming the otherwise complete polymer infiltration of the NRA in (c) leading to NRs punching through the top polymer layer.

3.5.1. Electron-Only Devices

To confirm whether the array was enhancing J_e , electron-only devices with the structure ITO/ZnO/ZnO NRA/F8BT/Ca/Al were fabricated. These were compared to planar devices lacking the NRA, but with all other layers cast and processed in the same way, including the same volume of F8BT. Measurements were averaged over multiple pixels across at least 2 substrates for each device type. Figure 3.11a shows that the electron current of devices with a NRA is on average 20 times greater over the measured voltage range compared to the device with the planar ZnO seed layer as the EIL. The gradients of these $\log J_e$ - $\log V$ plots (extracted from the linear regime; higher voltages show a decrease in current suggesting device breakdown), show that the gradient of the NRA device data has a value of 2.00 ± 0.06 whereas the planar device data gives a gradient of 1.76 ± 0.04 . This suggests that the presence of the NRA is allowing the electron current to reach the SCLC operating regime, i.e. the array is acting as an

ohmic injector of electrons (Chapter 1). This is somewhat surprising given that literature values indicate a barrier in the order of 0.5 eV between the ZnO CB and the F8BT LUMO; this is reflected by the lower gradient of the second device confirming the non-ohmic injection of planar ZnO. In their report, Fina *et al.* demonstrated that the internal electric field enhancement due to their nanostructured injection layers acts to lower the effective Schottky barrier height by 0.1 eV^[48]. Their structures measured 50 nm wide with a height of 20 nm to give an aspect ratio of 0.4; with aspect ratios ca. 9 for the NRs here, the electric field enhancement, and therefore the barrier-lowering, is likely to be even greater in these devices^[53].

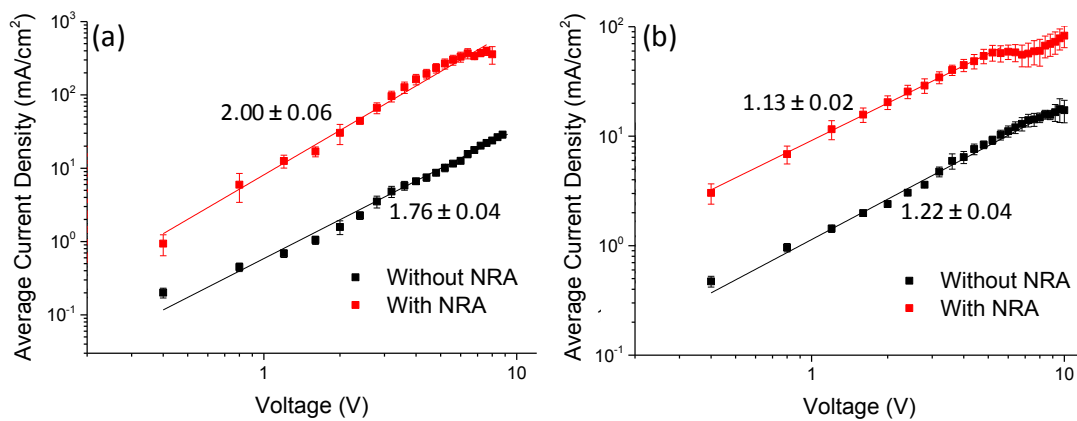


Figure 3.11: $\log I$ - $\log V$ characteristics of electron-only devices for electron injection from (a) the ZnO NRA and (b) the Ca/Al contact. Gradient values are shown next to each fitted line.

Fina *et al.*'s calculations show that the enhanced internal electric field would also improve (to a lower extent) the injection of charge from the opposite, non-structured electrode. To confirm this, the electron current due to the Ca/Al electrode in both types of device was also measured. Like figure 3.11a, breakdown in the NRA devices appears to occur as the voltage approaches 10V possibly due to polymer degradation and the issues highlighted in section 3.4, but the gradients (again, extracted from the linear region) are curiously lower than expected for what should be a good electron-injecting electrode (figure 3.11b). This may reflect some issues related to the evaporation procedure. However, across the measured voltage range, the electron current is indeed an order of magnitude greater in the NRA devices, implying that the hole carrier concentration is also likely to be increased in the NRA HyLED devices.

While the same volume of F8BT was used in order to ensure as fair a comparison between structured and planar device as possible, one important aspect has been neglected in this analysis: the distance between the nanorod tips and the top electrode is ~ 200 nm in the NRA

devices while that between the ZnO seed layer and the top electrode in the planar devices is ~ 450 nm. Therefore, electrons injected from the NR tip region would experience a smaller resistance which would provide an alternative explanation for the larger current in the NR devices. This might be particularly true for the Ca/Al electron-injection observations given that $\log J_e$ has a similar dependence on $\log V$ across planar and NRA devices.

Nevertheless this should not detract from the observation that electron injection from the NRA appears to be ohmic - an improvement over the planar ZnO EIL. Therefore, the lack of ZnO emission in the EL data together with this preliminary electron-only device data suggests that the NRA is primarily acting as a charge injection layer only.

To better determine the precise nature of the NRA on the current, different lengths of NR should be investigated for a given polymer volume. It would then be interesting to note whether J_e then scales with the surface area recorded in figure 3.1b. Given the arguments presented by Fina *et al.*, it would be important to decouple the current contribution due to the increase in surface area from enhancements due to the electric field. This would involve wetting the NRA with an insulating material, such as polystyrene, but leaving the NR tips exposed as the electric-field enhancement occurs primarily from these regions^[48].

3.5.2. F8BT Chain Packing Due to the NRA

As discussed in Chapter 1 (section 3.4.1), the manner in which polymer chains pack will directly influence the optoelectronic behaviour of the layer and, consequently, the overall device. As has been suggested by XRD studies done on P3HT NR-OPVs, the array will influence the chain arrangement of the organic layer^[54]. Naturally, this is expected to also be the case for an F8BT layer infiltrated into a NRA. Donley *et al.* demonstrated that significant changes in the F8BT structure occurred at the polymer's T_g and T_m with further changes induced by slow-cooling or quenching the polymer from these temperatures back to room temperature. Therefore, given the annealing treatments needed to fabricate the NRA HyLEDs, the polymer here was subjected to these same processes.

Glass substrates were cleaned and were either left bare or coated with a ZnO/NRA layer. The same volume of F8BT was then cast across all samples and subjected to different post-deposition annealing procedures, with the bare-glass samples used as a control. For the XRD measurements, all scans were 31 minutes in duration.

No F8BT-related peaks were detected in both control and NRA as-cast samples (figure 3.12a and b) indicating an amorphous material. Figure 3.12a shows that annealing the control

samples above T_g for 15 minutes and then quenching or slow-cooling however, induces a degree of crystallinity in the layer with the emergence of peaks corresponding to the (001) and (004) planes attributed to the c - and π -stacking directions as reported by Donley *et al.* (see Chapter 1, table 1.1)^[49]. For the discussion which follows, we attribute the peak at 15° to the (010) plane, i.e. the side-chain spacing. Quenching from the T_m results in a significant reduction in intensity of each of these peaks, but also in the emergence of peaks at roughly 8.06 and 11.59° corresponding to d -spacings of 11.0 and 7.6 Å, respectively. Slow-cooled from T_m samples show all of these peaks with a greater intensity compared to all of the other samples with one significant difference: the disappearance of the (010) peak and the emergence of two peaks on either side with spacings of 6.1 and 5.3 Å. The latter values exactly matches the side chain spacing reported by Donley *et al.*^[49]. This value, however, varies considerably between reports possibly due to the variations in the angle of the alkyl groups relative to the a - b plane, as well as variations in the adjacency between functional groups as discussed in Chapter 1. The disappearance of the peak at 15.03° coinciding with the emergence of peaks at 14.56 and 16.77° might therefore indicate that the chains are given time to orient towards more stable configurations in the slow-cooled from T_m samples.

The control samples indicate that crystalline regions in F8BT will preferably orient with the chain backbone parallel to the substrate plane as indicated by the intensity of the (001) and (004) peaks, agreeing with reports elsewhere. Quenching from the melt leads to a predominantly amorphous layer. Slow-cooling, however, leads to a more mixed orientation with evidence of edge-on packing. Indeed the appearance of a peak at 8.06° corresponds to a d -spacing of 11.0 Å - almost exactly the same as the theoretical side-chain spacing of 11.3 Å given by Legowski's group. However, given the general ambiguity of the F8BT crystal structure, only the peaks identified by Donley *et al.* are labelled in figure 3.12a; all others are indicated by an asterisk.

The effect of the NRA on the arrangement of the F8BT chains is stark (figure 3.12b). Note that exactly the same amount of polymer material is in the beam path in both the control and NRA sample experiments, and scan times are also identical. As indicated by the SEM images, samples annealed to the T_g are not expected to show significant infiltration of the polymer into the array. Nonetheless, the peaks related to the c -axis direction are considerably more intense than those of the control samples for the same thermal conditions indicating that the array has further encouraged the packing of the chain backbone parallel to the substrate, i.e. a greater proportion of the material is crystalline. The higher intensity of the slow-cooled peaks suggest a greater degree of crystallinity as the polymers are given more time to orient to this arrangement, though also observed is the only instance of the (100) plane, corresponding to the monomer

length. The (001) and (004) peaks are the only ones observed in the slow-cooled from T_m sample showing the NRA has suppressed the perpendicular growth of other crystallite orientations.

Experiment	2 θ Angle, degrees	Possible hkl	d-spacing, Å
Post-deposition thermal treatments on glass	4.33	-	20.4
	5.45	001	16.2
	8.06	-	11.0
	11.59	010	7.6
	14.56	010	6.1
	15.03	010	5.9
	16.77	-	5.3
	21.46	004	4.1
Post-deposition thermal treatments on ordered NRA	5.45	001	16.2
	6.21	100	14.2
	21.55	004	4.1
F8BT Slow-cooled from the melt on misaligned NRA of different lengths.	4.83	-	18.3
	5.82	001	15.2
	8.33	-	10.6
	11.56	010	7.7
	14.30	010	6.2
	15.98	010	5.5

Table 3.1: d -spacings calculated from the Bragg equation and their associated 2θ angles for each experiment discussed in text. The possible Miller indices are taken from both experimental and computational literature sources, notably those proposed by Donley *et al.* and Eslamibidgoli and Lagowski (see Chapter 1, table 1.1)^[49,57].

The effect of the NRA on the polymer packing was further observed by infiltrating F8BT into a poorly aligned array created by growing from a seed layer cast from a three-month aged sol-gel (figure 3.13a-d show bare SEM images of these arrays). The F8BT here was slow-cooled from T_m and the NR growth time varied to give lengths between 0-750 nm. All the peaks observed in the slow-cooled from T_m glass/F8BT sample are observed here but with different relative intensities, and all are lower in intensity compared to those in figure 3.12 as indicated by the more prominent background noise level (figure 3.13e). This is true even on the planar substrate which sees the peak at $\sim 8.0^\circ$ at the same intensity as the (001) peak. We note a change to the

latter peak with respect to the control study with a reduction of ~ 1 Å in spacing. The F8BT packing morphology therefore seems to be dependent on the substrate. An initial increase in intensity of the $\sim 8.0^\circ$ peak was observed with the 170 nm sample, but with increasing NR length, the polymer becomes more amorphous, possibly as crystallite formation is disrupted by the misaligned NRA.

This study shows that the NRA morphology heavily influences the packing of F8BT chains. The NRA greatly increases semiconducting polymer crystallinity, even when it sits on top of the nanorods. This is expected to have consequences on the optoelectronic behaviour of the devices. For instance, with the backbone parallel to the substrate plane the emitting dipoles are instead perpendicular to the plane. Hence, the ordered NRA should demonstrate improved light outcoupling. Furthermore, in a diode structure the electric field would be parallel to the c -axis, and hence the carrier mobility through the F8BT should be enhanced by both better chain alignment to the substrate and better chain packing due to the enhanced overall crystallinity (Chapter 1)^[55]. Further experiments here would involve decoupling the XRD pattern of the infiltrated F8BT from the F8BT which caps the NRA so as to clarify the morphology of just the infiltrated material. Near edge X-ray absorption fine structure (NEXAFS) spectroscopy can be used to elucidate the alignment of chains relative to a substrate as well as the extent of such alignment; this technique was recently used for this purpose to determine the molecular orientation of the conjugated polymer PCDTPT, albeit on planar substrates^[56].

All discernible peaks with their corresponding d -spacings are listed by experiment in table 3.1.

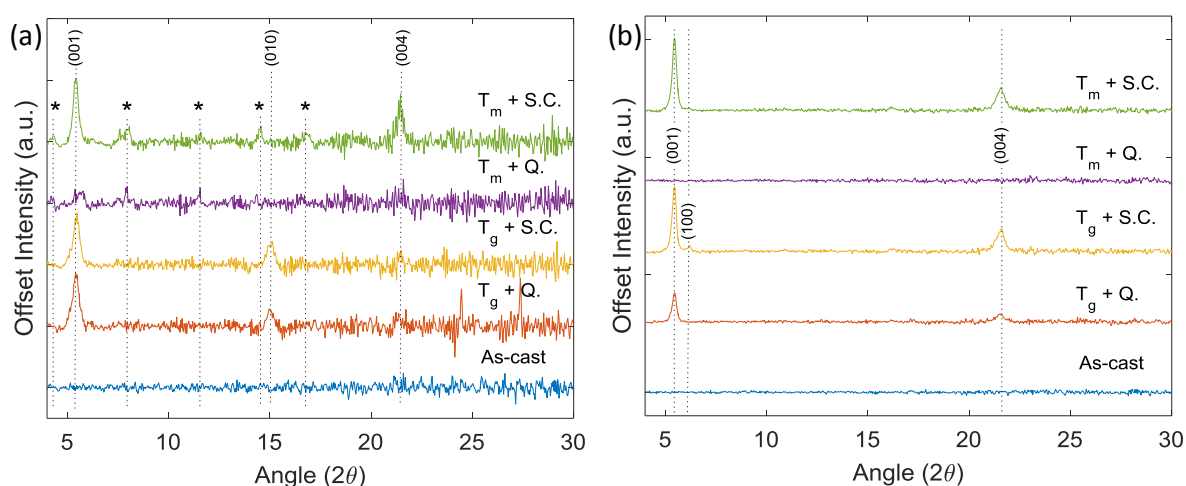


Figure 3.12: (a) Diffractogram of F8BT on glass and (b) on an NRA following different post-deposition annealing temperatures where Q = quenched, S.C. = slow-cooled.

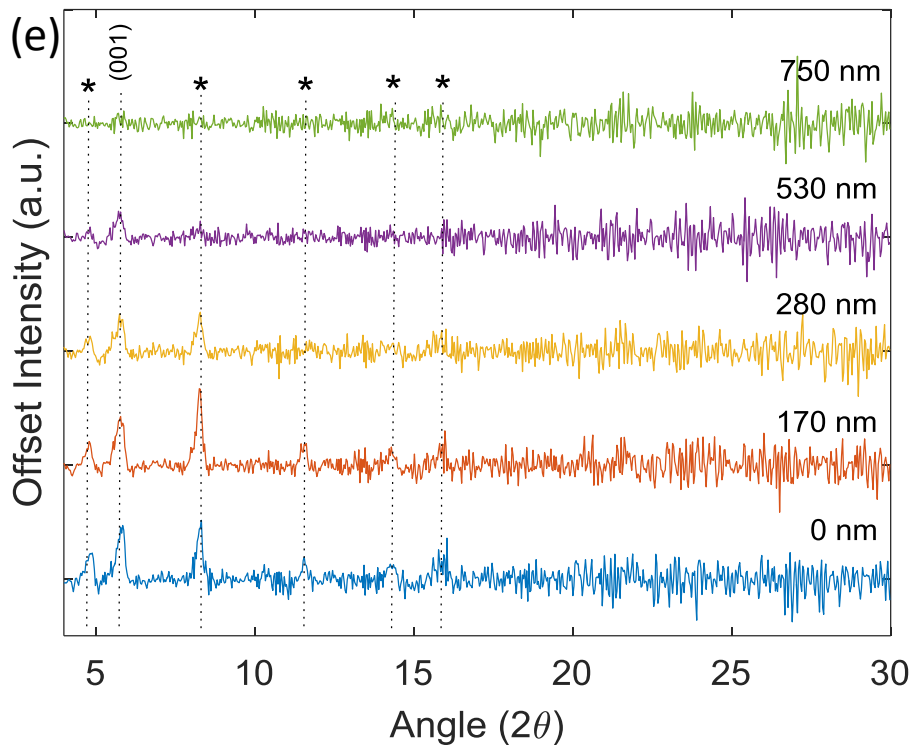
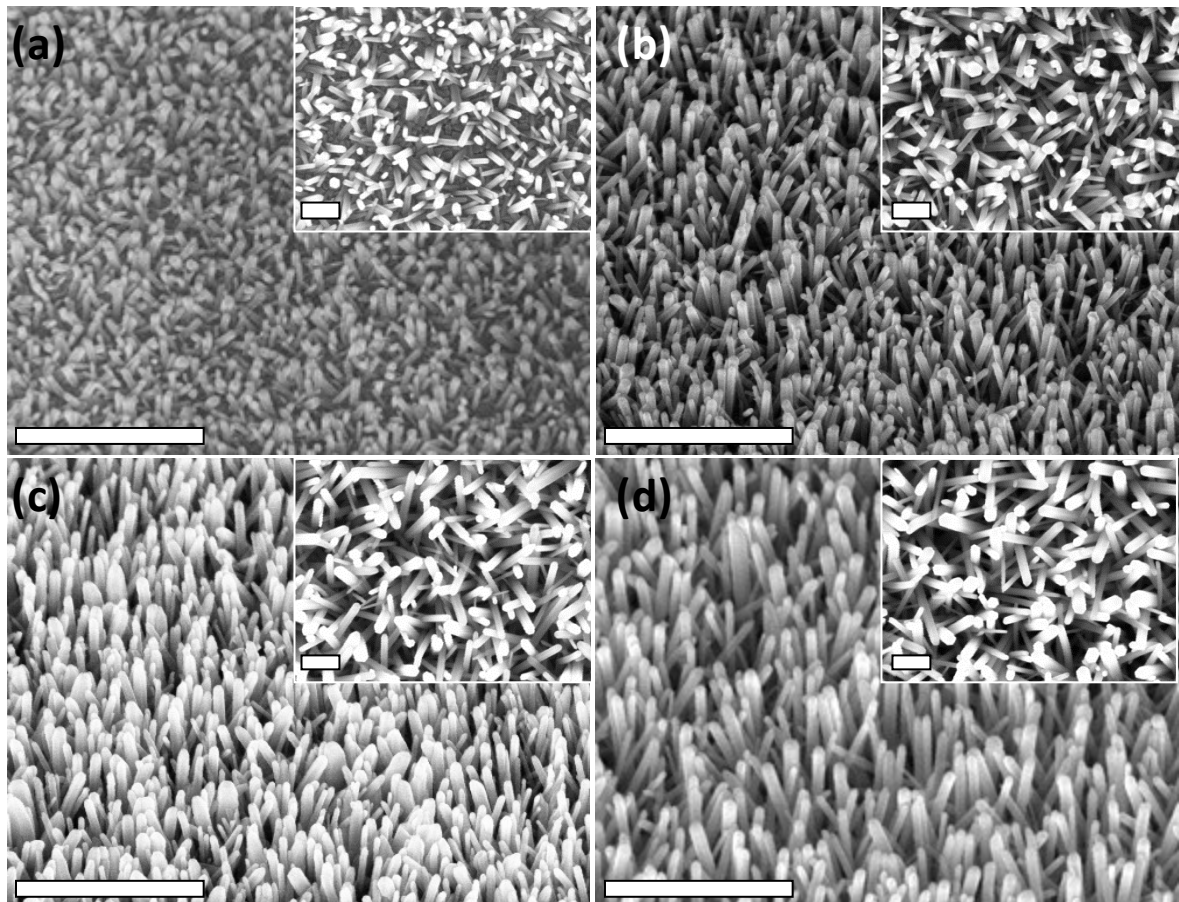


Figure 3.13: a)-d) 45° SEMs of misaligned NRAs with top view insets for lengths 170, 280, 530 and 750 nm, respectively. Scale bar: 1 μm (200 nm, insets). e) XRD of infiltrated F8BT on misaligned NRAs with planar ZnO as control (0 nm).

3.5.3. Effect of Nanorod Length on Devices

Several attempts were made to determine the optimal NR length for the HyLED devices for a fixed volume of F8BT. Unfortunately, this was hampered by several experimental issues at the time and also by the broad spread in data that was generally observed throughout (see figure 3.8, for example). Thus, it was not possible to draw definite conclusions from these studies. Nonetheless, figure 3.14 shows the 'best' devices recorded for lengths of 170, 280, 530 and 750 nm for one experiment and justifies the use of a 750 nm array; it was the brightest and had the steepest rise in light output with increasing voltage along with the 530 nm device. Compared to the JVs reported elsewhere in this thesis, those of figure 3.14 exhibit highly non-ideal behaviour. It is clear that greater attention must be given to understand the effect of the NR length on device performance, particularly whether a correlation can be identified between their length, the surface area (figure 3.1b) and J .

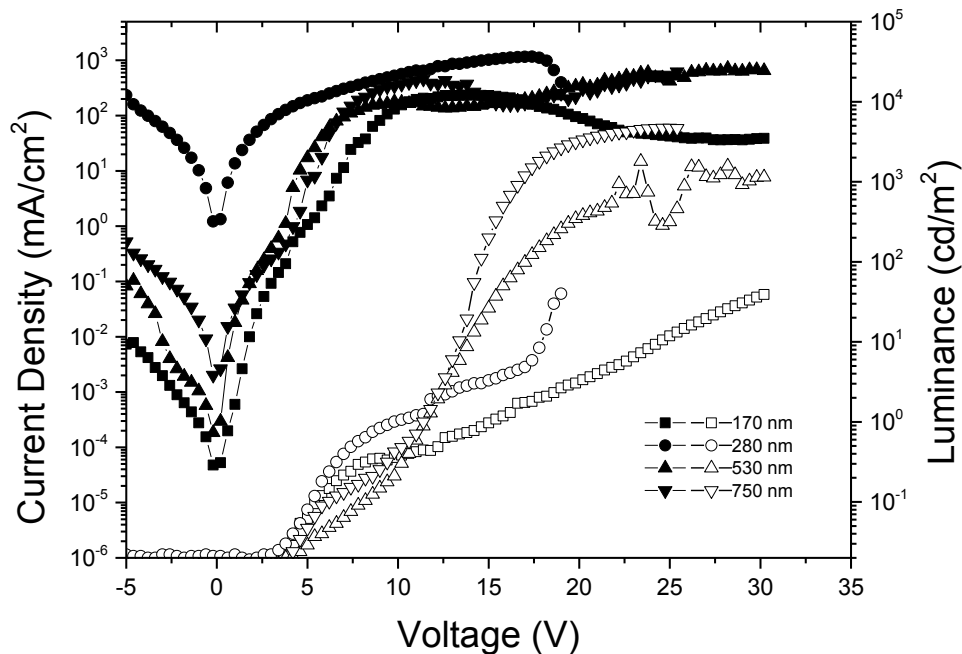


Figure 3.14: Current density (filled shapes) and luminance (open shapes) for devices of different NR lengths.

3.6. Conclusions

The use of ZnO NRAs for light-emitting applications with an OSC was described in this Chapter. The standard planar ZnO HyLED device structure was used as a basis from which the already-present planar ZnO was used as a seed layer to grow a highly ordered NRA. F8BT, as the OSC, was then used to infiltrate the array via thermal annealing above its T_m . Devices exhibiting a high yield of luminances exceeding 1000 cd/m² were only made possible with the insertion of

an electron-blocking/exciton blocking layer of TFB between the F8BT and the MoO_x contact. Together with preliminary electron-only devices, this suggests that the NRA has increased the J_e , pushing the recombination zone closer to the anode interface - a change from the hole-dominated planar HyLEDs reported in literature.

By recording the efficiencies and luminance metrics it was shown, for the first time, that NR HyLEDs have the potential to be used for display and general lighting applications. Furthermore, the lack of ZnO-related emission shows that the array is acting purely as a charge injection layer. Beyond device fabrication, efforts were made to understand the role of the NRA on performance. In particular, XRD measurements show that a well-ordered array encourages the packing of the F8BT chains such that the backbone is parallel to the substrate. This should lead to benefits in the outcoupling of light due to the favourable orientation of emitting dipoles as well as improved electron transport in the vertical direction.

In order for these devices to compete with their planar hybrid counterparts, the variation in performance must be reduced and the device stability needs to improve. These issues can be traced to variations in the polymer coverage of the NRA leading to poor top morphologies as evidenced by SEM measurements. To this end, alternative methods may be used to deposit the polymer. As has been reported by others, multiple coatings of lower concentration solutions could be used to achieve the required thickness^[45]. Dip-coating, through variation of solution concentration, substrate withdrawal and drying temperatures may allow a greater control over the final film morphology and hence provide more uniform substrates^[58].

The extra fabrication time of these devices as well as their increased complexity must be justified by the final device performance if they are to be attractive to further development. The general lack of interest in comparison to NR OPVs means that there is a wealth of potential research to be carried out in the field of NRA HyLEDs. Given the variety of device geometries published to date, it is hoped that the structure presented here will be used as a standard for this further work. Ultimately, as Gerken (2013) stated, the use of a nanostructure layer such as a NRA, is “a promising alternative to additional polymer layers for control of the carrier injection and the turn-on voltage in solution processed devices.”^[46]

3.7. References

- [1] J. Costa Dantas Faria, A. J. Campbell, M. A. McLachlan, *Optimisation of Zinc Oxide as a Charge Injection Layer for Hybrid Organic-Inorganic Light Emitting Diodes*, 2012.
- [2] J. C. D. Faria, A. J. Campbell, M. a. McLachlan, *Adv. Funct. Mater.* **2015**, *25*, 4657.
- [3] C. Y. Jiang, X. W. Sun, G. Q. Lo, D. L. Kwong, J. X. Wang, *Appl. Phys. Lett.* **2007**, *90*, 263501.

- [4] M. Ashfold, R. Doherty, N. Ndiforangwafor, D. Riley, Y. Sun, *Thin Solid Films* **2007**, *515*, 8679.
- [5] H. Yan, R. He, J. Pham, P. Yang, *Adv. Mater.* **2003**, *15*, 402.
- [6] P. X. Gao, Z. L. Wang, *Appl. Phys. Lett.* **2004**, *84*, 2883.
- [7] A. B. Djurišić, Y. H. Leung, *Small* **2006**, *2*, 944.
- [8] A. B. Djurišić, X. Chen, Y. H. Leung, A. Man Ching Ng, *J. Mater. Chem.* **2012**, *22*, 6526.
- [9] L. Vayssieres, *Adv. Mater.* **2003**, *15*, 464.
- [10] L. E. Greene, M. Law, D. H. Tan, M. Montano, J. Goldberger, G. Somorjai, P. Yang, *Nano Lett.* **2005**, *5*, 1231.
- [11] Y. Tak, K. Yong, *J. Phys. Chem. B* **2005**, *109*, 19263.
- [12] Y. Tong, Y. Liu, L. Dong, D. Zhao, J. Zhang, Y. Lu, D. Shen, X. Fan, *J. Phys. Chem. B* **2006**, *110*, 20263.
- [13] M. Guo, P. Diao, S. Cai, *J. Solid State Chem.* **2005**, *178*, 1864.
- [14] Y. I. Jeong, C. M. Shin, J. H. Heo, H. Ryu, W. J. Lee, J. H. Chang, C. S. Son, J. Yun, *Appl. Surf. Sci.* **2011**, *257*, 10358.
- [15] S. Xu, N. Adiga, S. Ba, T. Dasgupta, C. F. J. Wu, Z. L. Wang, *ACS Nano* **2009**, *3*, 1803.
- [16] T. Ma, M. Guo, M. Zhang, Y. Zhang, X. Wang, *Nanotechnology* **2007**, *18*, 035605.
- [17] J.-H. Tian, J. Hu, S.-S. Li, F. Zhang, J. Liu, J. Shi, X. Li, Z.-Q. Tian, Y. Chen, *Nanotechnology* **2011**, *22*, 245601.
- [18] K. Mahmood, B. S. Swain, G.-S. Han, B.-J. Kim, H. S. Jung, *ACS Appl. Mater. Interfaces* **2014**, *6*, 10028.
- [19] Y. Zhou, W. Wu, G. Hu, H. Wu, S. Cui, *Mater. Res. Bull.* **2008**, *43*, 2113.
- [20] J. M. Downing, M. P. Ryan, M. A. McLachlan, *Thin Solid Films* **2013**, *539*, 18.
- [21] J. Downing, M. P. Ryan, N. Stingelin, M. A. McLachlan, *J. Photonics Energy* **2011**, *1*, 011117.
- [22] D. Olson, S. Shaheen, R. T. Collins, D. S. Ginley, *J. Phys. Chem. C* **2007**, *111*, 16670.
- [23] F. Wu, W. Shen, Q. Cui, D. Q. Bi, W. J. Yue, Q. Y. Qu, M. T. Wang, *J. Phys. Chem. C* **2010**, *114*, 20225.
- [24] L. Baeten, B. Conings, H.-G. Boyen, J. D'Haen, A. Hardy, M. D'Olieslaeger, J. V Manca, M. K. Van Bael, *Adv. Mater.* **2011**, *23*, 2802.
- [25] L. Baeten, B. Conings, J. D'Haen, C. De Dobbelaere, A. Hardy, J. V Manca, M. K. Van Bael, *ChemPhysChem* **2012**, *13*, 2777.
- [26] J. Huang, Z. Yin, Q. Zheng, *Energy Environ. Sci.* **2011**, 3861.
- [27] L. Whittaker-Brooks, W. E. McClain, J. Schwartz, Y.-L. Loo, *Adv. Energy Mater.* **2014**, *4*.
- [28] S. Shoaee, J. Briscoe, J. R. Durrant, S. Dunn, *Adv. Mater.* **2014**, *26*, 263.
- [29] S. Kim, J. H. Koh, X. Yang, W. S. Chi, C. Park, J. W. Leem, B. Kim, S. Seo, Y. Kim, J. S. Yu, J. H. Kim, E. Kim, *Adv. Energy Mater.* **2014**, *4*.
- [30] D. Son, J. Im, H. Kim, N. Park, *J. Phys. Chem. C* **2014**, *118*, 16567.
- [31] M. T. Lloyd, R. P. Prasankumar, M. B. Sinclair, A. C. Mayer, D. C. Olson, J. W. P. Hsu, *J. Mater. Chem.* **2009**, *19*, 4609.
- [32] K. P. Musselman, S. Albert-Seifried, R. L. Z. Hoyer, A. Sadhanala, D. Muñoz-Rojas, J. L. Macmanus-Driscoll, R. H. Friend, *Adv. Funct. Mater.* **2014**, *24*, 3562.
- [33] R. Könenkamp, R. C. Word, C. Schlegel, *Appl. Phys. Lett.* **2004**, *85*, 6004.

- [34] H. Guo, J. Zhou, Z. Lin, *Electrochem. commun.* **2008**, *10*, 146.
- [35] M. Willander, O. Nur, S. Zaman, a Zainelabdin, N. Bano, I. Hussain, *J. Phys. D. Appl. Phys.* **2011**, *44*, 224017.
- [36] N. Bano, S. Zaman, a. Zainelabdin, S. Hussain, I. Hussain, O. Nur, M. Willander, *J. Appl. Phys.* **2010**, *108*, 043103.
- [37] S. Zaman, A. Zainelabdin, G. Amin, O. Nur, M. Willander, *J. Appl. Phys.* **2012**, *112*, 064324.
- [38] M. Willander, O. Nur, Q. X. Zhao, L. L. Yang, M. Lorenz, B. Q. Cao, J. Zúñiga Pérez, C. Czekalla, G. Zimmermann, M. Grundmann, a Bakin, a Behrends, M. Al-Suleiman, a El-Shaer, a Che Mofor, B. Postels, a Waag, N. Boukos, a Travlos, H. S. Kwack, J. Guinard, D. Le Si Dang, *Nanotechnology* **2009**, *20*, 332001.
- [39] X. W. Sun, J. Z. Huang, J. X. Wang, Z. Xu, *Nano Lett.* **2008**, *8*, 1219.
- [40] S.-L. Zhao, P.-Z. Kan, Z. Xu, C. Kong, D.-W. Wang, Y. Yan, Y.-S. Wang, *Org. Electron.* **2010**, *11*, 789.
- [41] C. Y. Lee, J. Y. Wang, Y. Chou, C. L. Cheng, C. H. Chao, S. C. Shiu, S. C. Hung, J. J. Chao, M. Y. Liu, W. F. Su, Y. F. Chen, C. F. Lin, *Nanotechnology* **2009**, *20*, 425202.
- [42] D.-W. Wang, S.-L. Zhao, Z. Xu, C. Kong, W. Gong, *Org. Electron.* **2011**, *12*, 92.
- [43] Q. Yang, Y. Liu, C. Pan, J. Chen, X. Wen, Z. L. Wang, *Nano Lett.* **2013**, *13*, 607.
- [44] S. Nam, N. Oh, Y. Zhai, M. Shim, *ACS Nano* **2015**, *9*, 878.
- [45] R. Smith, B. Liu, J. Bai, T. Wang, *Nano Lett.* **2013**, *13*, 3042.
- [46] M. Gerken, In *Organic light-emitting diodes (OLEDs): Materials, devices and applications*; Buckley, A., Ed.; Woodhead Publishing: Cambridge, 2013; pp. 235–261.
- [47] L. Deang, M. Fina, C. Zhaoyang, C. Xiaobo, L. Gao, S. Johnson, S. S. Mao, *Appl. Phys. Lett.* **2007**, *91*, 93513.
- [48] M. Fina, S. S. Mao, *J. Appl. Phys.* **2012**, *112*, 024512.
- [49] C. L. Donley, J. Zaumseil, J. W. Andreasen, M. M. Nielsen, H. Sirringhaus, R. H. Friend, J.-S. Kim, *J. Am. Chem. Soc.* **2005**, *127*, 12890.
- [50] D. C. Olson, Y.-J. Lee, M. S. White, N. Kopidakis, S. E. Shaheen, D. S. Ginley, J. A. Voigt, J. W. P. Hsu, *J. Phys. Chem. C* **2008**, *112*, 9544.
- [51] J.-S. Kim, R. H. Friend, I. Grizzi, J. H. Burroughes, *Appl. Phys. Lett.* **2005**, *87*, 023506.
- [52] J.-S. Kim, L. Lu, P. Sreearunothai, A. Seeley, K.-H. Yim, A. Petrozza, C. E. Murphy, D. Beljonne, J. Cornil, R. H. Friend, *J. Am. Chem. Soc.* **2008**, *130*, 13120.
- [53] R. Smith, J. Carey, R. Forrest, S. Silva, **2005**, *632*, 632.
- [54] J. M. Downing, Control and Characterisation of Metal Oxide/Polymer Morphologies for Hybrid Photovoltaic Devices, Imperial College London, 2013.
- [55] Y. Li, J. B. Lagowski, *Comput. Theor. Chem.* **2011**, *977*, 157.
- [56] S. N. Patel, G. M. Su, C. Luo, M. Wang, L. a. Perez, D. a. Fischer, D. Prendergast, G. C. Bazan, A. J. Heeger, M. L. Chabinyc, E. J. Kramer, *Macromolecules* **2015**, *48*, 6606.
- [57] M. J. Eslamibidgoli, J. B. Lagowski, *J. Phys. Chem. A* **2012**, *116*, 10597.
- [58] P. Yimsiri, M. R. Mackley, *Chem. Eng. Sci.* **2006**, *61*, 3496.

Chapter 4 – Copolymer Fluorene Bilayers for Colour Tuning in Inverted HyLEDs

Achieving high yields of bright NRA HyLED devices (Chapter 3) was made possible through the insertion of a TFB layer at the F8BT/MoO_x interface to block the transport of electrons to the anode and/or reduce possible exciton dissociation at this interface. The inclusion of this layer required a series of optimisation steps to overcome the wetting issues which frequently hinder the formation of solution-processed polymer bilayers. Those steps are detailed in this Chapter. To simplify the process, this work was carried out on planar F8BT-coated substrates with an objective of determining the experimental procedures and surface morphologies which lead to a high yield of F8BT/TFB bilayer formation, and in turn, reproducible inverted polymer bilayer HyLED devices. Although this Chapter was motivated by the work on NRA HyLEDs, the large spread in data encountered with those devices made it difficult to determine the influence of the properties of the polymer layers; the devices here are therefore planar. The final procedure does not make use of multiple substrates or 'lift-off' techniques to create the bilayer, relying instead on post-deposition solvent processing and thermal annealing of the F8BT layer. A surprising observation was made when changing the thickness of TFB that it allowed the electroluminescent emission from F8BT to be easily tuned from green to orange whilst maintaining brightness levels appropriate for lighting and display applications. This particular observation is discussed with respect to microcavity effects. The main results of this Chapter have been published in *J. Mater. Chem. C* **2015**, *3*, 4945^[1].

4.1. Relevant Background

This section provides the reader with a brief overview of the challenges affecting the deposition of multilayer devices from solutions and the efforts to overcome these issues. Given the optical observations recorded from the completed devices, a brief theoretical background of microcavity effects is also provided.

4.1.1. Deposition of Multilayer Devices

As discussed in Chapter 1 (Section 1.6.1.), the deposition of multiple layers in devices enables the user to rectify poor charge balance and optimise recombination, emission and light out-coupling. This is routine for molecular OLEDs in which layers are deposited using high-vacuum thermal evaporation techniques. However, the creation of multilayer devices using solution-based deposition methods, particularly spin-coating, is far from trivial. This process may dissolve already-cast organic layers and unfavourable surface energies may prevent the formation of uniform, high-quality films. In the utilisation of low-cost deposition alternatives to high-vacuum processes there are other methods by which different polymers can be combined to achieve the desired optical and operational properties, namely through blends and block-

copolymers. In the former, optimisation is achieved through adjusting the ratio of the blend components, while the latter achieves this through the synthesis of polymer chains with the desired functional groups; these methods have been found to be particularly attractive for the creation of single-layer, white-light PLEDs^[2,3]. However, controlling the morphology of the films created via these two methods is difficult and phase separation of the individual components is a common problem with negative consequences on long-term device performance^[4-7]. Multilayers clearly do not face these issues and have the significant benefit of allowing each layer (and hence the function associated with it) to be individually optimised whilst also allowing for optimised exciton formation and light-emission.

In their review Newby *et al.* identify the two most promising methods that may help to overcome the issue of layer redissolution during the fabrication of multilayer stacks: the use of orthogonal solvents and inducing crosslinking^[8]. Having cast the first organic layer from a particular solvent, the former technique then deals with identifying a solvent from which the following layer can be cast with, but does not damage the already cast layer. This generally involves the synthesis of polymers that are soluble in highly polar solvents such as ethanol and water. For example, Sax *et al.* synthesised PFO with ethylene glycol side chains to make the polymer soluble in ethanol to create multilayer PLEDs with efficiencies of 1.23 cd/A^[9]. Trattinig *et al.*, too, used ethanol-soluble PFO to create a PLED with three solution processed layers with a maximum efficiency of 1.46 cd/A and brightness of 16540 cd/m²^[10]. While the use of orthogonal solvents makes polymers resistant to one type of solvent, inducing crosslinking within a layer would make it resistant to many types of solvent^[8]. In their review, Zuniga *et al.* define crosslinking as 'a process whereby the formation of new covalent bonds leads to insolubilization of an organic layer'^[11]. As they discuss, certain functional groups are able to readily achieve this once exposed to hard-baking or UV-radiation. Aizawa *et al.* demonstrated the ability to thermally crosslink a carbazole derivative by the addition of styrene groups^[12]. DSC scans of the material are featureless after the first cycle indicating that crosslinking has indeed taken place and the material is now thermally stable, while AFM studies show no change in film thickness following the application of solvent rinses. The location of the crosslinks in the chemical structure may interfere with the conjugation length of a polymer thereby altering its intrinsic optoelectronic properties and this can manifest in the material's absorption and emission spectra. This is not always the case; for instance upon thermally crosslinking their 'SuperYellow' (SY) layer Köhnen *et al.* show that no changes were observed in the polymer's optical properties^[13]. Ultimately, as stated by Newby *et al.*, given that these techniques can be material specific, it is likely that solution processing of multilayer devices may require a combination of techniques to be successful.

4.1.1.1. TFB/F8BT and F8BT/TFB Bilayers

As detailed in Chapter 1 (Section 1.9.2.), the insertion of a thin TFB layer at the PEDOT:PSS/F8BT interface of standard devices leads to a significant enhancement in device efficiencies. In standard PLEDs, a TFB/F8BT bilayer is created using the following process as first reported by Kim *et al.*^[14]:

1. The TFB is cast onto the PEDOT:PSS and is then subjected to a 'hard-bake', i.e. annealed above the T_g for a period of time to insolubilise a fraction of the material.
2. The layer then undergoes a solvent rinse to remove any still soluble material. This leaves thin (~10 nm) insoluble TFB layer.
3. F8BT can then be cast from a non-orthogonal solvent onto the insoluble TFB layer.

However, for inverted devices in which the F8BT is cast first, washing away such a significant fraction of the layer responsible for light emission is not ideal. A different approach is therefore necessary. At the time of writing, only two reports were available detailing devices with a F8BT/TFB (inverted) bilayer and each used different approaches to achieve their device stacks:

1. Kabra *et al.* utilised a lift-off method in which a 60 nm TFB layer was cast on a separate substrate from the ITO/ZnO/F8BT device substrate. The TFB layer was delaminated from its substrate by submerging in water. The F8BT substrate was finally used to lift-off the TFB film on its dry side^[15].
2. Chung *et al.* used an orthogonal solvent approach, reporting TFB to be soluble in cyclohexane, whereas F8BT is not^[16].

In the wider context of scaling up device fabrication, the complexity of the former therefore seems undesirable; simplifying the process by using just one substrate would remove the need for having to use any lift-off techniques. Casting from orthogonal solvents was therefore the more attractive option. However, as will be detailed later in this Chapter, the batch of TFB used in this work was completely insoluble in cyclohexane, even when stirring at 100 °C for a period of 3 days. Even upon finding an appropriate solvent, poor wetting of the TFB onto the underlying F8BT led to irreproducible results. Ultimately, the final procedure (section 4.2.4) consisted of a combination of appropriate solvents, thermal processing of the F8BT and the application of a solvent rinse to enable the successful deposition of the F8BT/TFB bilayer.

4.1.2. Optical Interference Effects in OLEDs

An OLED/PLED naturally contains a number of interfaces due to the different functional layers typically contained within. As each material possesses its own optical behaviour, the light generated within the LEP may be subjected to reabsorption as well as refraction and reflection as it crosses through layers of different refractive index n_r . Consequently, the inherent EL

spectrum of the emitting layers can be significantly altered due to the optical response of the entire device stack. As this would also influence the operating efficiency of the device, these optical effects should therefore be considered when designing a device stack^[17].

Reflections at layer interfaces are major contributors to these so-called microcavity effects (MCEs). The proportion of reflected light for *s*- and *p*-polarised waves travelling through two adjacent media (*a* and *b*) with refractive indices $n_{r,a}$ and $n_{r,b}$, is, respectively:

$$R_s = \left(\frac{n_{r,a} \cos\theta_i - n_{r,b} \cos\theta_t}{n_{r,a} \cos\theta_i + n_{r,b} \cos\theta_t} \right)^2 \quad R_p = \left(\frac{n_{r,a} \cos\theta_t - n_{r,b} \cos\theta_i}{n_{r,a} \cos\theta_t + n_{r,b} \cos\theta_i} \right)^2 \quad 4.1$$

where θ_i and θ_t are the angles of incidence and refraction, respectively. Note that for unpolarised light, the reflection R is the average of R_s and R_p . As these equations show, the more significant the difference between the refractive indices of adjacent media, the greater the reflection. Within a device the greatest amount of reflection typically occurs from the evaporated metal contact and, to a much lesser extent, the glass/ITO boundary. Emitted photons will undergo multiple reflections leading to interference effects which may be constructive or destructive depending on the geometry of the device. The optical path length $O_L(\lambda)$ for a given wavelength λ of the device cavity is given by

$$O_L(\lambda) = \sum_i n(\lambda)_{r,i} d_i \cos\theta + \left| \frac{\Phi_m}{4\pi} \lambda \right| \quad 4.2$$

where the first term is the sum of the individual optical path lengths (given as the product of the $n_{r,i}$ and thickness d_i of each layer) and Φ_m is the phase shift caused by reflection from the metal contact defined as:

$$\Phi_m = \arctan\left(\frac{2n_{r,m}k_m}{n_{r,s}^2 - n_{r,m}^2 - k_m^2} \right). \quad 4.3$$

Here, $n_{r,m}$ and k_m are the refractive index and extinction coefficient of the metal and $n_{r,s}$ is the refractive index of the layer adjacent to the contact (MoO_x in the case of the HyLEDs here). The resonant wavelength λ_{res} of the cavity is then given by

$$m\lambda_{res} = 2O_L(\lambda) \quad 4.4$$

where m is the mode number. Changing the cavity length therefore changes λ_{res} ; for instance, increasing $O_L(\lambda)$, by increasing the thickness of some layer d_i would lead to a redshift in the emission wavelength. On the other hand, equation 4.2 shows that if the angle of incidence θ is

increased, the change in $O_L(\lambda)$ decreases λ_{res} to smaller values resulting in a hypsochromic shift in the EL when the device is observed at wider viewing angles.

These effects are widely reported in the literature and can be exploited in order to increase the intensity of emission, select for particular emission wavelengths and reduce the large spectral width inherent to organic emitters to improve colour purity^[18-24]. To achieve these effects, the reflections within the device must be amplified and this is accomplished through the use of either two reflective metal electrodes sandwiching the device stack (one of which must be thin enough to allow light to escape)^[18,25,26], or inserting a dielectric mirror between the glass substrate and the device stack to manipulate $O_L(\lambda)$ ^[20,22,27-29]. This is the case for 'strong' MCEs. Standard device structures otherwise demonstrate 'weak' MCEs^[30], though the device structure can be such that stable interference effects may not exist and the inherent EL will not be affected. Weak MCEs can typically be detected through small changes in the peak emission wavelength λ_{peak} by changing the d_i such that the distance between the RZ and the metal contact also changes, but so too through measurements of the angular dependency of the EL spectra^[30-34].

Throughout the cited literature of this section, the presence of MCEs is experimentally deduced through reflectance measurements from the metallic top contact and through the device stack. Of interest are any dips present in the high reflectance region due to the metallic electrode/dielectric mirror; as absorption effects are significantly minimised here, dips in the reflection therefore indicate wavelengths which would be preferentially transmitted through the device stack during operation. Reflectance measurements are therefore employed here to confirm the presence of weak MCEs in these devices.

4.2 Bilayer Deposition

4.2.1. Contact Angle and Film Thickness

As cyclohexane did not dissolve the batch of TFB used in these experiments, cyclohexanone was instead identified as a potentially suitable solvent as it was found to readily dissolve TFB, but F8BT only to a small extent. Initial use of TFB was carried out within the context of the NRA HyLED work (Chapter 3) in which the TFB solution would be cast directly onto the substrates after thermally processing the F8BT. Such a procedure was highly unreliable resulting in good TFB layers just as often as poor, irregular ones - figure 4.1 is indicative of the latter. In the creation of a multilayer PLED, Trattnig *et al.* report on applying a pure methanol spin rinse on already cast organic layers prior to casting the subsequent polymer from a methanol solution^[10]. This was reportedly carried out in order to "reduce the possibility of wetting issues"

and the AFM analysis of the rinsed layer shows “perfect morphological stability”. Application of solvent rinses has been widely shown to significantly change the behaviour of polymer surfaces. Draper *et al.*, for instance, have shown that rinsing an immiscible polymer blend with polar (e.g. ethanol) and non-polar (toluene) solvents can select for hydrophilic or hydrophobic groups to the layer surface^[35]. Xiao *et al.* show that a spin rinse of methanol onto InGaZnO transistors can chemisorb onto the surface whilst removing adsorbed water and oxygen species^[36]. Several different groups have also measured changes to the surface potential due to the application of solvent (particularly alcohol) spin rinses demonstrating that this procedure is a highly effective and facile way to dramatically improve the performance of organic devices^[36-40].

Likewise, in an attempt to improve the wetting behaviour of the TFB being cast here, a spin rinse of cyclohexanone was applied to the F8BT-coated substrates prior to casting the TFB solution under the same spin-coating parameters as the polymer solutions (2000 rpm for 40s).

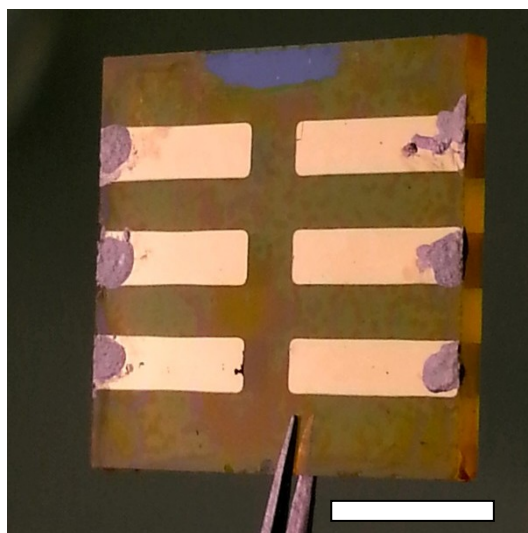


Figure 4.1: Photograph of a NRA HyLED substrate showing poor wetting of the TFB layer on the F8BT. Scale bar: 5 mm.

To test the effect of the solvent rinse on the F8BT, thickness and contact angle measurements were carried out. Both of these measurements were carried out on clean glass substrates coated with a *ca.* 480 nm thick F8BT film. Samples were annealed above the T_m of F8BT and then slow-cooled or quenched back to room temperature to emulate experimental conditions during device preparation.

For contact angle measurements (Chapter 2, Section 2.6.6.), Figure 4.2a shows that the wetting angle of TFB solution droplets is smaller by ~30 % on F8BT films that have undergone the solvent rinse indicating improved wetting behaviour that should translate to improved bilayer

formation. This was observed in both types of thermally processed films and the application of a second spin rinse did not result in significant further changes. This is in line with reports showing that the surface morphology of the film is not changed with multiple rinses and hence only one rinse of cyclohexanone was used hereafter^[10].

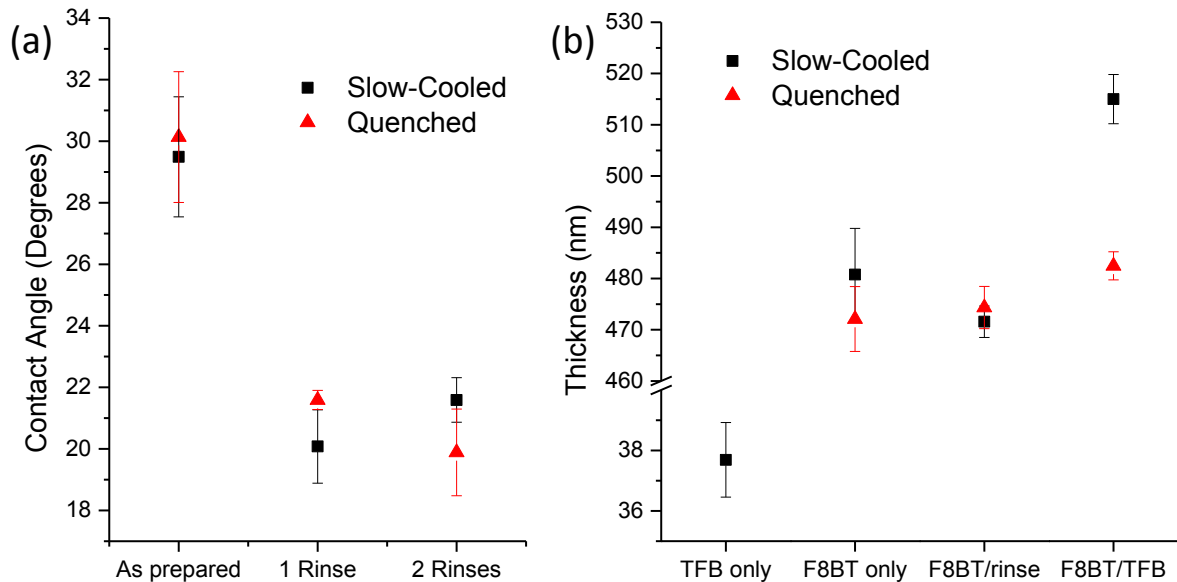


Figure 4.2: (a) Contact angle measurements of TFB solution droplets on quenched or slow-cooled from T_m F8BT films as a function of the number of cyclohexanone solvent rinses. (b) Thickness measurements of F8BT films as a result of the thermal and solvent processes. Also shown are the thickness of the TFB as well as the combine F8BT/TFB bilayer thicknesses.

Figure 4.2b shows that the thickness of either film is barely changed following the spin rinse with all film thicknesses measured between 470-480 nm. There is, however, a reduction in the spread of data indicating that the rinse may help to planarise the layer to an extent. Most importantly, there is no dissolution of the F8BT due to the cyclohexanone in either case. A distinct difference between slow-cooled and quenched F8BT is observed upon spin-casting the TFB solution. In the former case, an average thickness of 515 nm was measured and closely corresponds to the addition of the TFB and rinsed F8BT film thicknesses, thus providing encouraging confirmation of successful F8BT/TFB bilayer formation with minimal layer dissolution. This appears to not be the case for the quenched F8BT sample which sees an increase of only ~10 nm upon the addition of TFB indicating that it has not adhered well to the substrate despite similar wetting behaviour according to the contact angle measurements. Based on these measurements, all the NRA device work in Chapter 3 involved slow-cooling F8BT layers from T_m .

4.2.2. F8BT/TFB Bilayer for Planar Devices

Following the results shown in figure 4.2, the solvent rinse step was implemented into the NRA HyLED deposition procedure with improved yields (Chapter 3, Section 3.3.3.). However, further optimisation of the TFB layer - namely, in varying the layer's thickness to maximise device performance - was hampered by the large spread in data of the NRA HyLEDs making it difficult to draw any firm conclusions in this respect. Optimisation of the TFB layer thickness was therefore carried out on planar HyLEDs of structure ITO/ZnO/F8BT/TFB/MoO_x/Au with the intention of transferring the results back to the NRA HyLEDs. The thickness of the F8BT was reduced to 75 nm whereas that of the ZnO seed layer was kept at 130 nm to maintain some consistency with the NRA HyLEDs. In any case, the preceding Masters report component of this research^[41] demonstrated that device performance varied little across 15-160 nm of ZnO layer thickness; increasingly thicker F8BT, on the other hand, lead to a considerable increase in operating voltage and peak power efficiency values at 80 nm (Appendix A). With no obvious need to anneal the F8BT above T_m for planar devices (no melt phase infilling required), F8BT films in this initial work were cast with just a 20 minute 90°C drying step before applying the solvent rinse and TFB-casting steps. However, the TFB did not form a layer on these substrates.

Knowing that the packing of the F8BT chains changes on annealing of the layer (Chapter 3), it was suspected that the simple drying step may have been insufficient to create a suitable surface morphology to enable the formation of the TFB layer. To test this, F8BT was cast on ZnO-coated glass substrates (knowing, too, that the substrate will influence the packing of polymer chains), and subject to different thermal processes with and without a solvent rinse prior to TFB deposition. Casting TFB onto substrates heated to 90 °C resulted in the TFB completely failing to adhere to the substrate (figure 4.3a). This, too, was the case if these F8BT films were then subjected to the solvent rinse. A strong purple colour is indicative of a TFB layer adhering to F8BT substrates annealed at 155 °C ($T_g \sim 140$ °C) for 20 minutes, but the films show many discontinuities (figure 4.3b). Annealing the F8BT film for 60 minutes at this temperature shows further improvements in the resulting TFB layer, but still with an unacceptable amount of defects (figure 4.3c). Finally slow-cooling the F8BT from 260 °C ($T_m \sim 250$ °C), and applying the solvent rinse once again gave uniform, defect-free TFB layers; removing the solvent rinse from these substrates resulted in discontinuous films again, highlighting the continued importance of this particular step (figure 4.4d). To determine why this might be the case, the effect of the solvent rinse and the F8BT surface morphology under different annealing conditions was investigated.

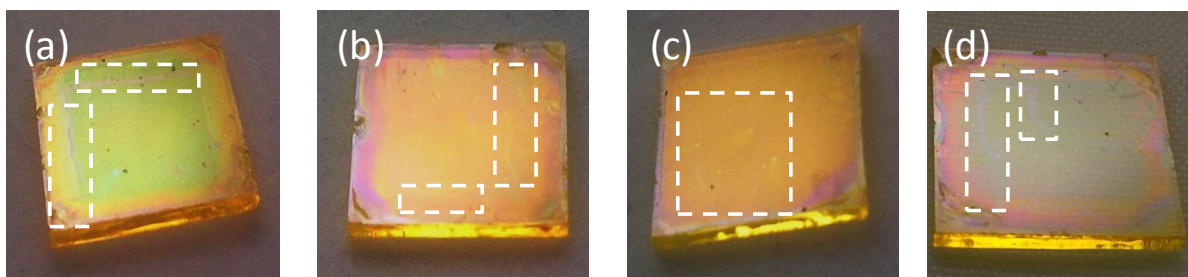


Figure 4.3: Poor TFB film formation with undesirable features shown by dotted white boxes. (a) Traces of TFB residue on an F8BT film dried at 90 °C for 20 minutes. (b) The purple colouration indicates that TFB coats an F8BT film annealed above T_g for 20 minutes, though with several discontinuities present. (c) Defects still present on a F8BT film annealed above T_g for 60 minutes. (d) Without the solvent rinse, TFB films on slow-cooled from the melt F8BT also show discontinuities.

4.2.3. Impact of F8BT Morphology on Bilayer Formation

AFM was used to assess the effect of the post-deposition thermal and solvent treatments on the F8BT surface morphology in the hope of drawing a correlation between surface features and successful bilayer formation. Once again, F8BT was cast on substrates coated with 130 nm of ZnO and subjected to different post-deposition conditions. All images shown were taken over an area of $2 \times 2 \mu\text{m}^2$.

Films that were slow-cooled from the melt exhibit a homogenous and granular surface with an RMS roughness of 2.27 nm (figure 4.4a). Applying the solvent rinse smooths the surface with a slight drop in RMS roughness to 1.97 nm (figure 4.4b) and a loss in the sharp projections from the surface as highlighted by the extracted line profiles of both films (figure 4.4e). Given that high quality film formation was more likely to occur on the latter films, this initially seemed to indicate that smoother F8BT films might be a requirement to the process. However, the measured roughness of F8BT films that were just dried at 90 °C or quenched from the melt were similar at 1.78 nm and 1.70 nm, respectively (to be expected given the lack of features in their diffractograms in Chapter 3). The former is shown in figure 4.4c. Applying the solvent to the former resulted in an *increased* roughness to 2.52 nm (figure 4.4d) accompanied by an increased granularity and the appearance of surface projections (figure 4.4f). The solvent spin rinse (and by extension the casting of the TFB solution) onto these amorphous films appears to destabilise and restructure the polymer surface.

It is well known that particular surface features may discourage effective surface wetting due to the formation of air-pockets between the solid surface and the material being deposited^[42,43]. However, the references cited here show projections in the order of hundreds of nanometres; the roughness values measured here - as well as their differences from film to film - are small

indicating that, while surface roughness may play a role, it is likely that there other more significant factors involved. As was reported by others, the solvent may chemisorb or otherwise leave a thin layer of residue on the F8BT surface^[36]. AFM phase images of slow-cooled from melt and pristine samples exposed or left unexposed to the solvent rinse were analysed (figure 4.5). Over the scan area, all images are very homogenous with deviations related to changes in topography (by comparing with figures 4.4a-d) since phase imaging is also sensitive to the slope of the surface. A large difference was observed between the pristine samples with little change observed between the annealed ones; again the former could be due to the considerable roughening of the surface caused by the solvent rinse. It is therefore difficult to ascertain if the chemistry of the polymer surface has changed due to the solvent rinse.

Now, the chain rearrangement associated with annealing the layers may lead to the exposure of certain functional groups that may affect the wetting properties of the layer. For instance, alkyl side chains are known to be hydrophobic. Sohn *et al.* showed that longer alkyl chains lead to more ordered surface structures and therefore higher contact angles for separate water and hexadecane droplets as compared to more disordered surfaces from short alkyl chains^[44]. Rangwalla *et al.*, too, showed that the melting of crystallites associated with alkyl groups resulted in better wetting of their polymer films^[45]. Though evidence of increased chain backbone planarity in F8BT was observed in XRD measurements upon annealing (Chapters 3 and 5), Winfred *et al.* use Raman spectroscopy to deduce that these thermal processes also result in a decrease in torsion angle between the BT and F8 units which would therefore reduce the protrusion of alkyl side chains at the surface^[46]. Furthermore, this would be more likely in samples slow-cooled from the melt which would have more time and energy to achieve this arrangement.

Given the ambiguity of the AFM results, it is hypothesised from literature that the thermal annealing of the F8BT discourages the presence of groups at the polymer surface which would negatively impact the formation of the TFB film, while the solvent rinse further stabilises the surface of annealed films.

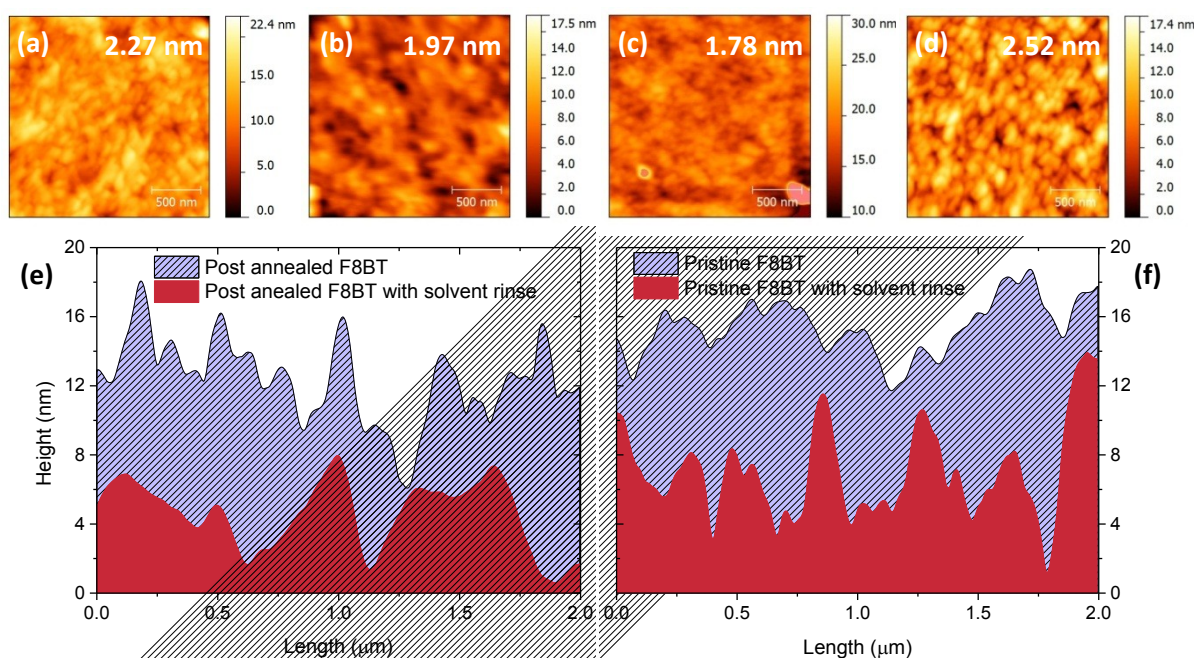


Figure 4.4: AFM topology images of F8BT films that have been slow-cooled from the melt (a) without, and (b) with a solvent treatment, as well as a pristine film (c) without and (d) with solvent treatment. RMS surface roughness is indicated at the top right of each image. (e) Line profiles extracted from (a) and (b). (f) Line profiles extracted from (c) and (d).

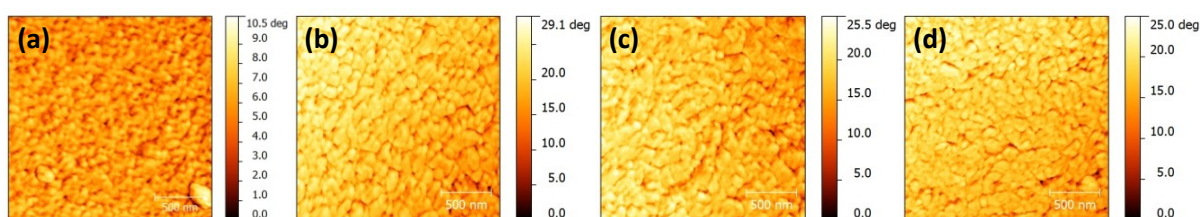


Figure 4.5: AFM phase images of (a) pristine, (b) pristine with solvent rinse, (c) slow-cooled from the melt and, (d) as (c) but with the solvent rinse.

4.2.4. Bilayer Casting Procedure

To summarise, of the permutations attempted the most successful procedure for creating the F8BT/TFB bilayer was as follows:

1. The solution cast F8BT thin film was annealed for 15 minutes above its T_m as determined by DSC measurements.
2. The film was then slow-cooled at a rate of 5 °C/min back to under 100 °C. Since DSC measurements show no thermal transitions below this temperature, the films were then immediately quenched back to room temperature.
3. A spin rinse of cyclohexanone was then applied to these F8BT-coated substrates.

4. Finally, the TFB in solution with cyclohexanone was spin cast onto the processed F8BT layers.

As shown in figure 4.3, deviations from this procedure resulted in either poor or no film formation. Though much still needs to be done in order to fully understand why this should be the case - a more rigorous analysis of contact angle variation across all films verified by the use of different solvents, for instance - the procedure was applied to create inverted bilayer HyLED devices. Figure 4.6 shows photos of completed devices as a result of following these steps using TFB solutions with concentrations of 7.5 – 20 mg/ml to give a series of inverted bilayer devices with TFB film thickness between 25-100 nm. The films are highly uniform and free from defects or discontinuities. A general device schematic is also shown. Furthermore, in Chapter 5 we show that this procedure works across different molecular weights of F8BT.

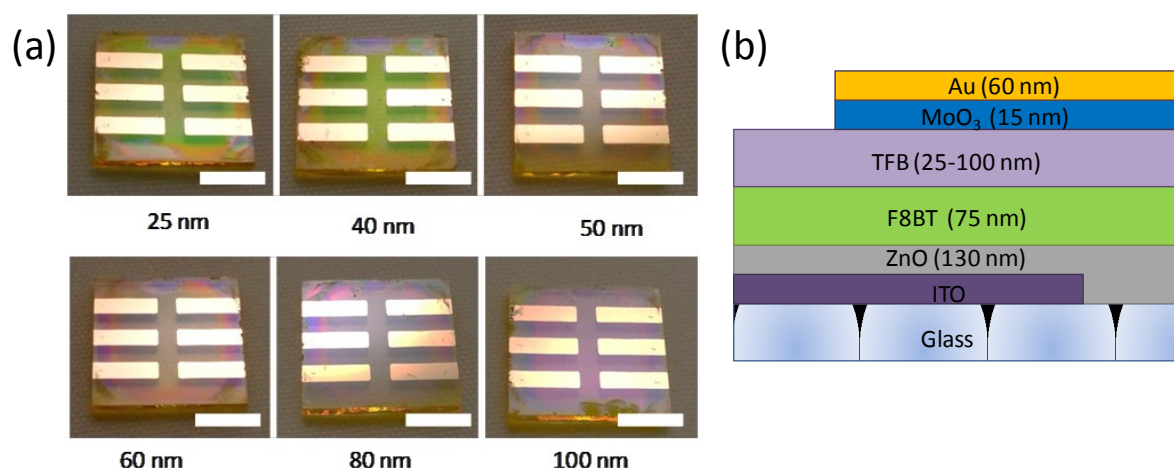


Figure 4.6: (a) Completed inverted bilayer HyLED devices following the procedure outlined in section 2.1. The increasingly purple colouration is indicative of the increasing thickness of the TFB layer (noted beneath each photo) as a result of increasing the TFB solution concentration. Scale bar = 5 mm. (b) Bilayer HyLED device schematic showing all thickness ranges used.

4.3. Device Characterisation

As previously stated, varying the TFB thickness for inverted polymer bilayer HyLEDs was initially chosen as an optimisation step to then incorporate into other devices reported in this thesis. Bilayer devices had structures of ITO/ZnO (130 nm)/F8BT (75 nm)/TFB (25-100 nm)/MoO_x (15 nm)/Au (80 nm) and were compared to F8BT-only devices in which the polymer thickness was varied over 75-170 nm, i.e. comparable to the total polymer thickness of the bilayer devices. To ensure that only the influence of the TFB was being tested, the F8BT of these

single layer devices was subjected to the same thermal and solvent conditions to those of the bilayer devices. Along with variations noted in device efficiencies, a more immediate change was noted in the emission spectra across devices of different TFB thickness. This is commented on first.

4.3.1. Emission Spectra

Over the 75 nm range in TFB thickness a comparable bathochromic shift of ~ 60 nm was recorded for the normalised peak wavelength λ_{peak} (figure 4.7a). At 25 nm of TFB, the green EL spectrum strongly resembles that of F8BT with $\lambda_{peak} \sim 550$ nm. By increasing the TFB thickness, the intensity at 550 nm falls until it reaches ~ 50 % at 100 nm of TFB with $\lambda_{peak} \sim 610$ nm giving strong orange emission. The spectra are highly saturated as indicated by the calculated chromaticity coordinates all of which lie close to the locus of the CIE plot and show the steady transition from green (0.43, 0.56) to orange (0.52, 0.46) emission.

Bilayers are prone to the formation of charge transfer states at the buried polymer interface and exciplex states were first observed in polymer bilayer devices as reported by Gebler *et al.*^[47]. For standard TFB/F8BT PLEDs, the presence of a weakly emissive low-energy exciplex state at the polymer/polymer interface has been identified in both bilayer and polymer blend devices^[48,49]. Shakutsui *et al.* also noted the prominent appearance of a peak at 575 nm in their standard TFB/F8BT PLEDs to which they speculated as not only being due to exciplex formation, but also due to interference effects; no studies were reported in support of either, however^[50]. Prior to considering the presence of weak MCEs, it was therefore hypothesised that the lowering of the emission energy commensurate with the increasing TFB thickness might be due to an increase in exciplex emission relative to exciton emission at the F8BT/TFB interface. As exciton emission is responsible for the 550 nm state, a change to the proportion between emissive states may account for the decreased emission at this λ .

This behaviour was compared to that of the control devices (figure 4.7b). Should exciplex states be responsible for the changes to the EL, these should not be observed in F8BT-only devices as they are charge transfer states formed between two different organic species. However, subtle shifts to the EL are also observed, though these shifts do not vary linearly in step with the device thickness. For instance, while there is a significant broadening of the emission between 90 nm to 110 nm of F8BT, that of the 170 nm device strongly resembles the 75 nm device EL. The measured colour range is also narrower, from yellow-green (0.46, 0.53) to yellow (0.48, 0.51). Figure 4.8 shows the calculated colour coordinates for each device.

That changes to the EL are also observed in single layer diodes suggests that exciplex states are not likely to be responsible for these changes across both device types.

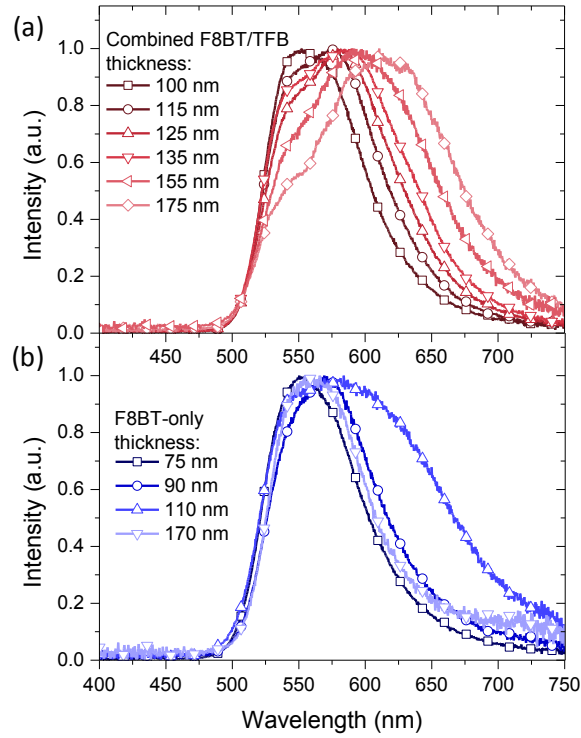


Figure 4.7: EL spectra for (a) F8BT/TFB bilayer and (b) F8BT-only HyLEDs for indicated device thicknesses.

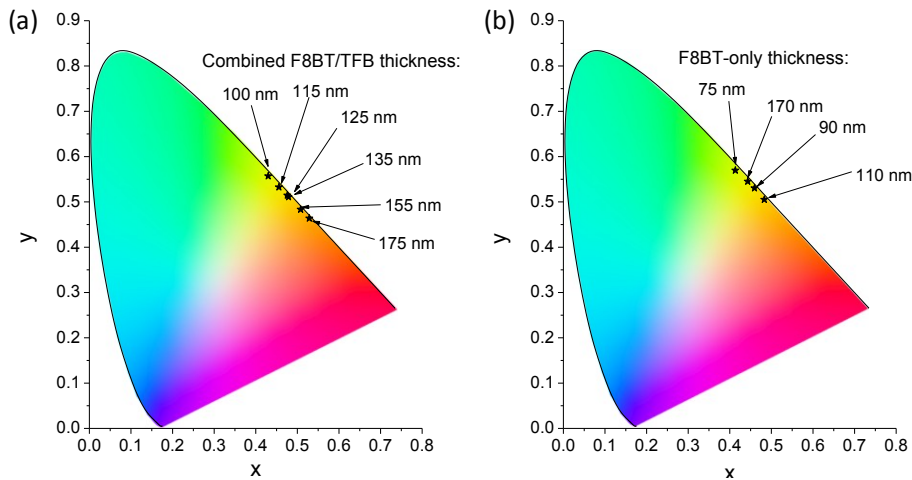


Figure 4.8: Chromaticity plots indicating the colour of the EL spectra for different thicknesses of (a) F8BT/TFB bilayer and (b) F8BT-only devices.

4.3.2. Evidence of Weak Microcavity Effects

Reflectance measurements were carried out as described in Chapter 2 through the glass substrate side of the device and the results for bilayer and F8BT-only devices are shown in figure 4.9. Both figures show dips at 470 nm corresponding to the absorption of the F8BT A_{F8BT} while the distinct dip at 390 nm in the bilayer devices is likely due to TFB A_{TFB} . The increasing

reflectance from 500 nm is due to the MoO_3/Au contact, confirmed by taking measurements with only the ITO/ZnO/polymer layers as shown in the inset to both plots. For the bilayer devices, thinner TFB layers result in a slight plateau in reflectance in the region of 520-560 nm. This slight resonance begins to weaken in intensity, whilst also broadening out and shifting to higher λ . This becomes particularly prominent in the thickest device with a flattening of the spectra between 600-650 nm. This behaviour is mirrored in the EL spectra in figure 4.7a with the plateaus coinciding with the λ that are preferentially outcoupled as would be expected with weak microcavity effects. Reflectance from the F8BT-only devices confirm this; the 75, 90 and 170 nm devices show similar behaviour around 550 nm, but the 110 nm device shows a broad depression between 570-650 nm which, again, mirrors the EL spectra from these devices (figure 4.7b).

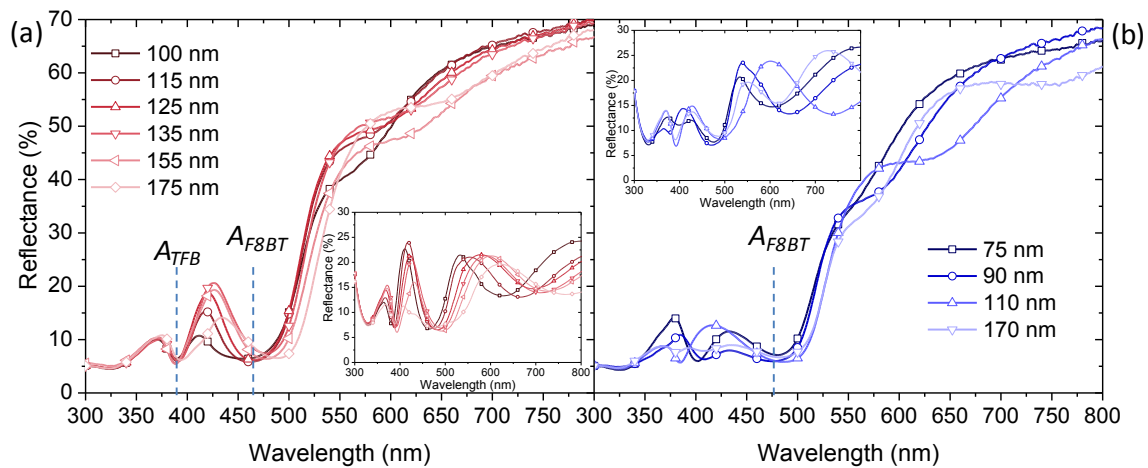


Figure 4.9: Reflectance measurements taken through the glass substrate side the device of (a) F8BT/TFB bilayer (b) F8BT-only devices for different thickness of TFB and F8BT, respectively. Indicated are the total polymer layer thicknesses. Insets show the reflectance spectra of an equivalent device without a MoO_x/Au anode.

Other features observed in these spectra are likely to be due to reflections at interfaces where the refractive indices of the layers differ by significant amounts as a result of Fresnel back reflection (equations 4.1). For example, at ~ 410 nm, the $n_r = 2.10$ for TFB and $n_r = 1.48$ for F8BT^[51] may explain the reflection peak observed at this wavelength and why it is not seen in the F8BT-only devices.

Further analysis of these weak microcavity effects were made using angle dependent EL measurements using the set-up shown in figure 4.10. A rotating stage was designed by the author for this purpose and then built by the mechanical workshop in the Blakett Laboratory at Imperial College London. The arm of the stage would hold the fibre optic spectrometer and the illuminating pixel would be positioned at the centre of the arc swept by the arm. Recordings

would be made at every 5° intervals between $\pm 40^\circ$ of the substrate normal (due to the shape of the sample chamber the EL was obstructed at higher viewing angles). Furthermore, in order to reduce potential effects due to the edge of the substrate, only the pixels located in the middle of the substrate were used in the orientation showed in figure 4.10. The designs for the stage are shown in Appendix B.

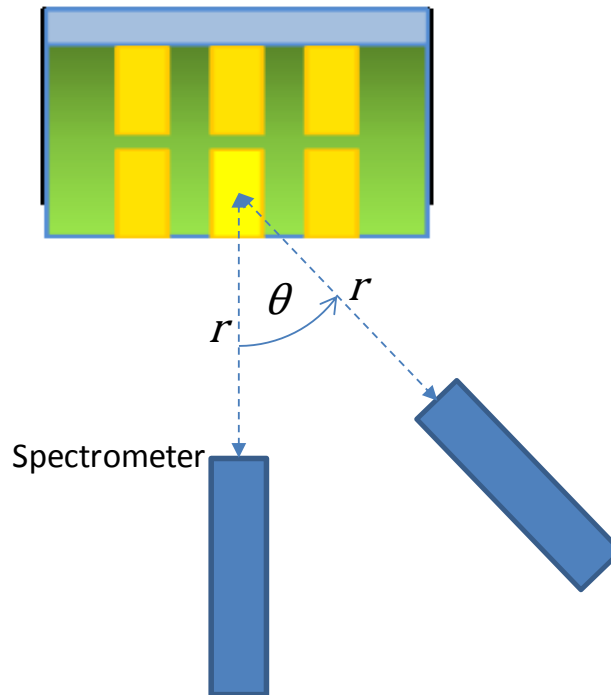


Figure 4.10: A top-view schematic of the measurement set-up used to extract EL at specific angles θ . As the spectrometer swept out an arc, the distance to some fixed point on the illuminated pixel was kept constant at r .

The angle-dependent EL measurements were carried out for devices with 40, 50, 60 and 100 nm of TFB. Figure 4.11 shows the EL extracted at 5° increments in viewing angle from the substrate surface normal against λ . In each case, the EL was normalised to the λ_{peak} with the whitest regions indicating the most intense wavelengths (i.e. a value of 1). Across all measured samples, it is clear that increasing the viewing angle away from the substrate normal, results in greener emission; the 40 nm TFB device, for example, sees a shift from 573 to 553 nm between 0 and $\pm 40^\circ$. These observations are in line with equation 4.2: they are due to a decrease in the optical path length with viewing angle and indicates that the thicknesses used in these devices lead to a lower extraction efficiency for shorter wavelengths at the normal viewing angle^[52].

Though the role of exciplex emission cannot be ruled out, that the reflectance measurements show behaviour which is clearly in step with that observed in the EL spectra is a strong indicator that the shifts in colour are related to the presence of weak microcavity effects. Finally,

it was also noted that all devices were spectrally stable with the measured EL independent of the forward bias; figure 4.12 shows examples for the 40 and 100 nm TFB devices.

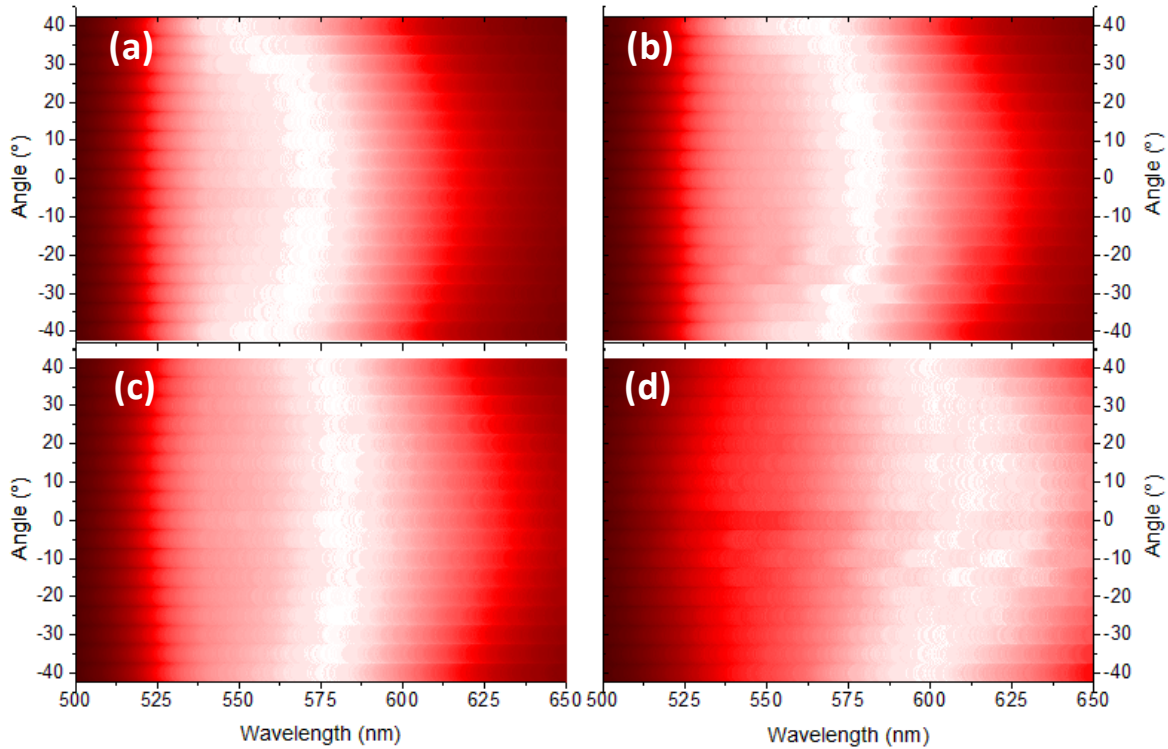


Figure 4.11: Normalised EL intensity measured with changing viewing angle ($\pm 40^\circ$) for bilayer devices with a TFB thickness of (a) 40 nm, (b) 50 nm, (c) 60 nm and (d) 100 nm of TFB. White regions indicate the most intense wavelengths, whilst redder regions are least intense. Interference fringes are observed in (b) and (d) indicating the high quality of the interfaces present in the devices.

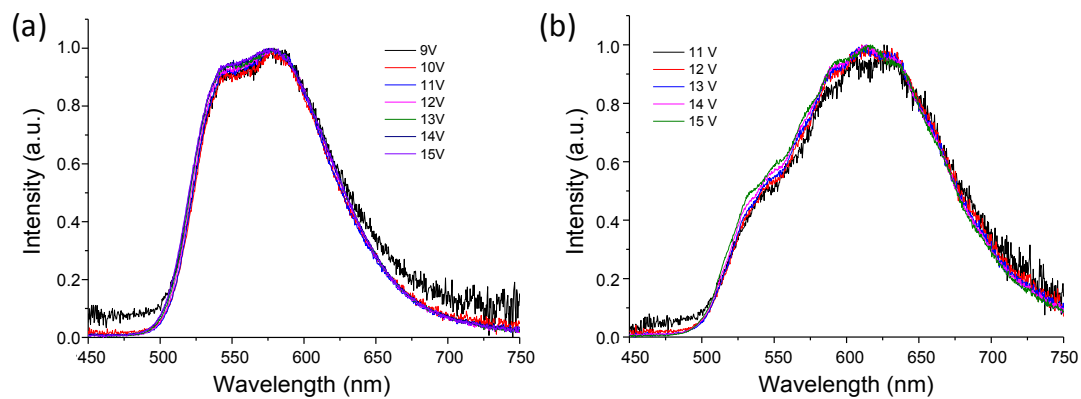


Figure 4.12: EL spectra at different forward voltages for (a) 40 nm and (b) 100 nm of TFB in the bilayer devices. The noisy nature of the 9V reading in (a) results in a higher baseline compared to the higher voltages.

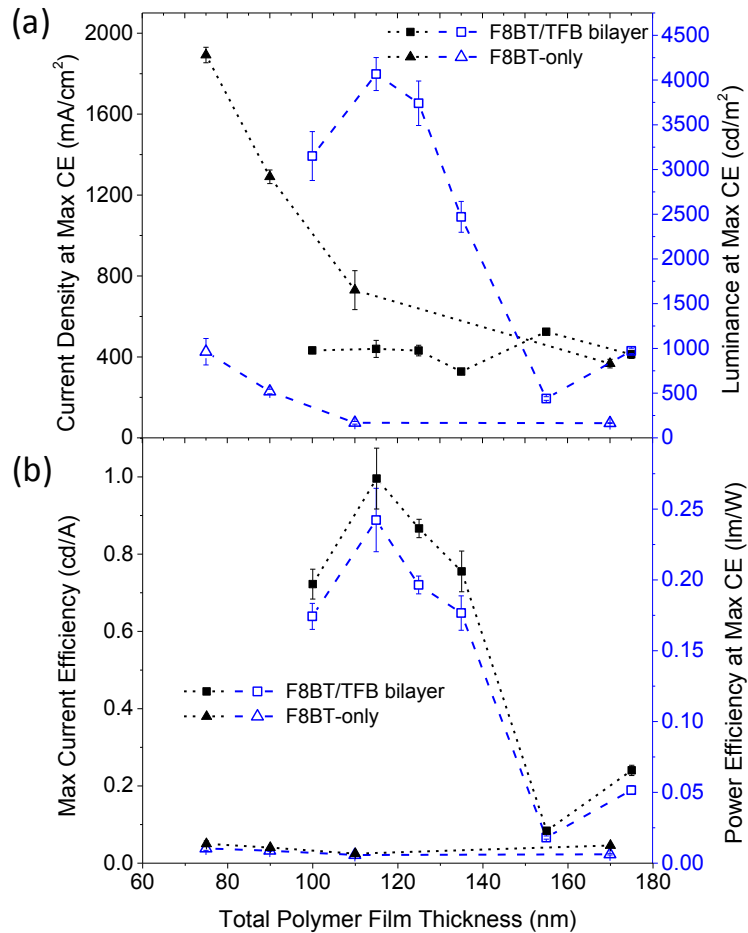


Figure 4.13: (a) Current density (dotted line) and luminance (dashed line) measured at maximum η_{CE} , and (b) Maximum η_{CE} (dotted line) and $\eta_{PE,CE}$ (dashed line) for polymer bilayer (squares) and F8BT-only (triangles) devices.

4.3.3. Efficiency and Luminance Characterisation

The EL measurements reported up to this point were made possible by the fact that the devices were highly stable under operation; no decrease in EL intensity was observed even for the angle-dependent EL experiments where a period of time was required to extract all 17 readings for each measured pixel. This is reflected in the J - V - L measurements in which devices were stable to multiple test runs. A testing cycle consisted of applying the voltage from -4 V and ramping up to a bias just after the current efficiency η_{CE} peaked. The data presented in this section was extracted from the third test cycle of each pixel with the few devices that failed in the first or second test cycle being excluded altogether. The data from the 25 nm TFB device and the 170 nm F8BT device were obtained from one 6-pixel substrate. Data for all other device structures was obtained from 2-3 substrates so that information could be processed from up to 18 pixels to ensure accuracy of results. The 80 nm TFB is the exception to this as, across

separate device batches, it consistently gave low yields; here, the data was averaged from just 2 pixels.

Current density J , luminance L_v , operating voltage and power efficiency η_{PE} values were all extracted at the point of maximum and denoted by the subscript CE . For the bilayer devices, figure 4.13 shows that efficiencies and L_v peak at a TFB thickness of 40 nm to give a η_{CE} of 1.00 ± 0.08 cd/A, a $\eta_{PE,CE}$ of 0.24 ± 0.02 lm/W and a $L_{v,CE}$ of 4070 ± 180 cd/m². These values decrease steadily with further increases in TFB thickness. J_{CE} shows little variation throughout though the increasing device thickness does show a slight increase in the voltage required to record the peak η_{CE} (13.0 to 14.7 V) reflecting an increase in electrical resistance.

Overall, these values compare favourably with the inverted F8BT/TFB HyLEDs fabricated using lift-off techniques reported by Kabra *et al.*^[15]. That report used similarly thick ZnO and MoO_x layers (respectively, 120 and 20 nm versus 130 and 15 nm here) to give a higher max η_{CE} of 2.81 cd/A, though with a maximum luminance $L_{v,max}$ of only 2150 cd/m²; though $L_{v,max}$ was not measured for the devices discussed here in order to not accelerate their degradation, continuing to measure L_v just beyond V_{CE} nonetheless gave values in excess of 11,000 cd/m² (40 nm of TFB). A higher L_v coupled with a lower max η_{CE} does highlight a greater amount of current that does not contribute to light emission, however.

Compared to F8BT-only devices the inclusion of a TFB layer leads to considerable improvements in device performance with a maximum increase by a factor of ~ 41 in max η_{CE} at similar total polymer thicknesses of ~ 110 nm. Unlike the bilayer devices, a clear decrease is observed in J_{CE} as thickness is increased with the trend in L_{CE} mirroring this behaviour. Whereas changes to $L_{v,CE}$ in the F8BT-only devices appear to be dominated by electrical effects, those in the bilayer devices appear to be dominated by optical effects as the $L_{v,CE}$ shows a significant variation with thickness despite J_{CE} remaining fairly constant around 400 mA/cm². Different thicknesses of TFB are therefore changing the overall light extraction efficiency (for the F8BT-only devices, too, the slight uptick in efficiencies at 170 nm coincides with the shift in EL spectra back to shorter and more efficient wavelengths).

Overall, the averaged bilayer device data shows tremendous consistency as indicated by the small standard deviation of each data point. Figures 4.14ai-ei show the recorded J - V - L s for a random sample of tested devices at each thickness verifying this small spread in data. The light turn-on voltage V_{L-on} is consistently observed to be 3.6-4 V regardless of the TFB thickness and is very similar to the F8BT/TFB devices reported by Kabra *et al.*^[15]. Extracting the η_{CE} variation with J for this device sample shows that all TFB devices exhibit an incredibly low efficiency roll-off despite the typical high current densities observed for HyLEDs (figure 4.14aii-eii) implying a

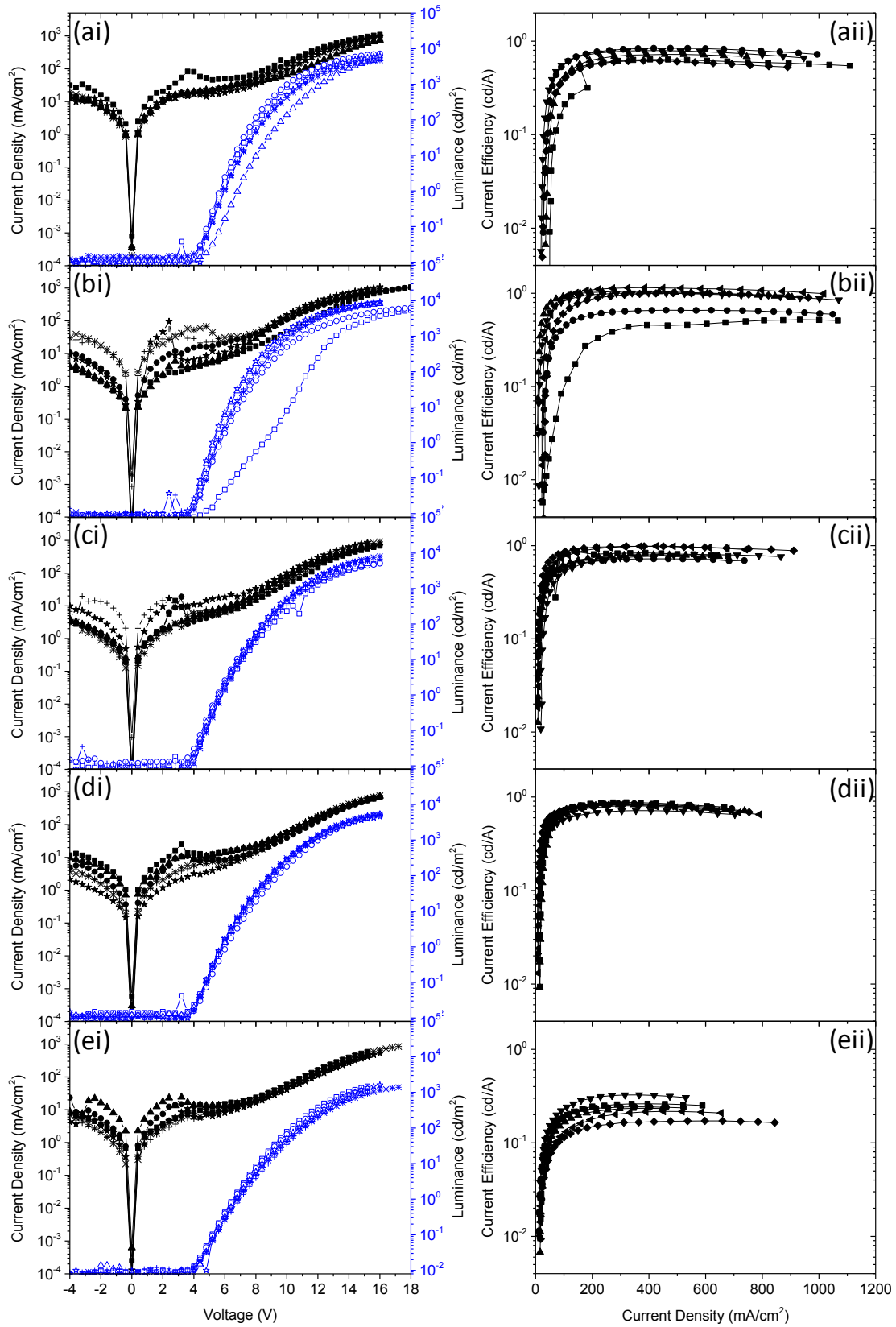


Figure 4.14: Electrical, luminance and efficiency data for a random sample of bilayer devices at TFB thickness of (a) 25, (b) 40, (c) 50, (d) 60 and (e) 100 nm. J - V - L characteristics are the left hand column (i series) and η_{CE} variation with J on the right (ii series).

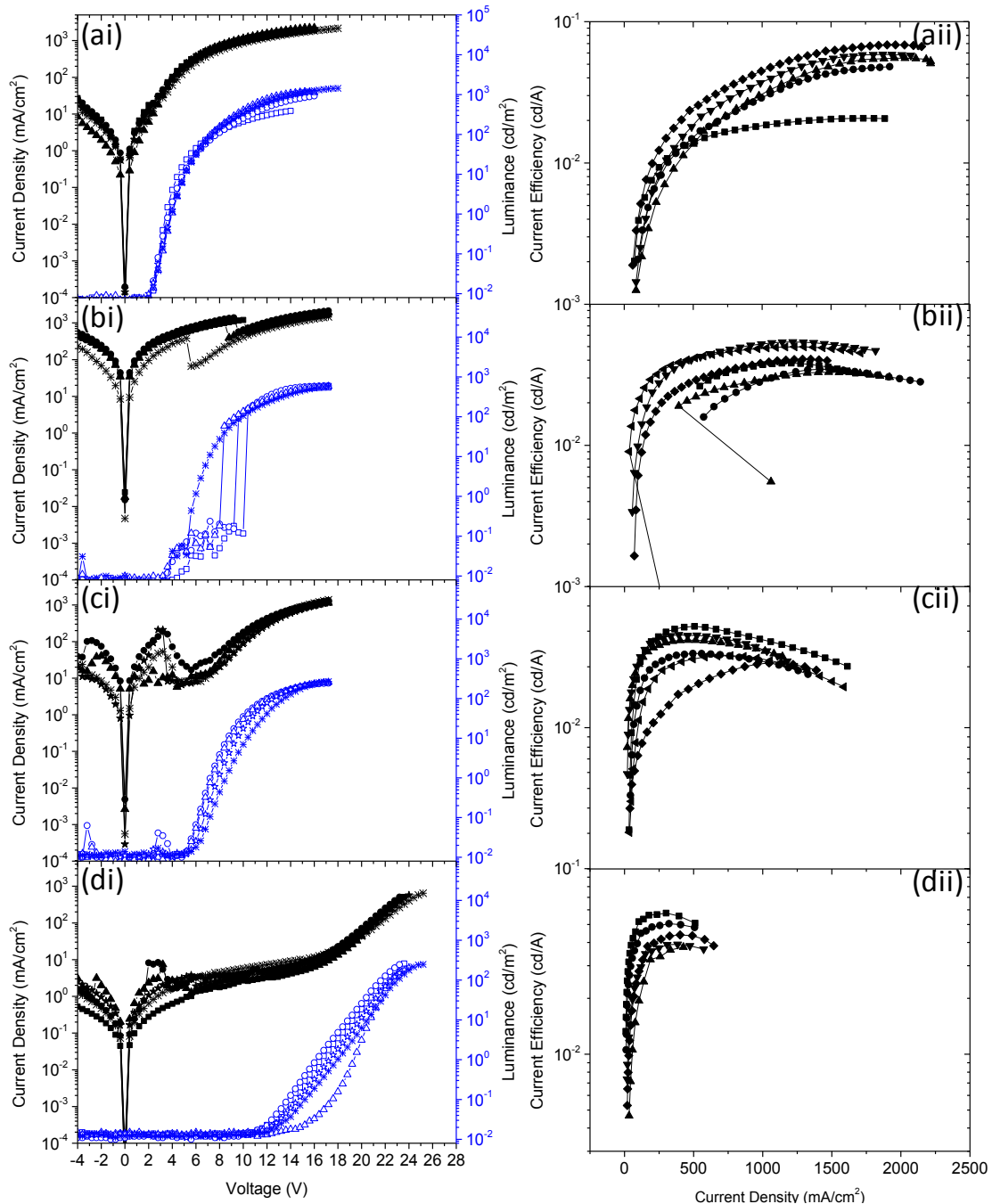


Figure 4.15: Electrical, luminance and efficiency data for a random sample of F8BT-only devices at F8BT thickness of (a) 75, (b) 90, (c) 110, AND (d) 170. J - V - L characteristics are the left hand column (i series) and η_{CE} variation with J on the right (ii series).

fairly constant current balance over this range of J . The 75 nm F8BT-only HyLEDs, too, show consistent measurements with the clearest diode behaviour in its J - V characteristic of all devices (figure 4.15ai); at 2.0 V, it also demonstrated the lowest V_{L-on} . At greater thicknesses, however (figure 4.15b-d), F8BT-only HyLEDs typically showed non-ideal diode behaviour with poor rectification and a larger data spread. V_{L-on} increases to 11.6 V for the 170 nm devices and the

charge balance quickly worsens after η_{CE} peaks with respect to J . The TFB layer has therefore also improved the stability and consistency of the devices whilst allowing them to be operated at higher, more practical luminance values whilst maintaining η_{CE} values close to their maximum.

4.4. Device Operation

Unlike the procedure for standard TFB/F8BT layers the process described in this Chapter removes the need to induce cross-linking within the TFB layer. Shakutsui *et al.* reported that the hole current of TFB begins to decrease at the temperatures needed to insolubilise it (> 180 °C)^[50]. Therefore, the procedure detailed here should preserve the transport properties of TFB. Equally, annealing the F8BT to such temperatures is not expected to adversely affect its performance in devices; the stability of the polymer at highly elevated temperatures has been commented on by others^[53], while an increase in PLQE has been reported following such thermal treatment (Chapter 5)^[54]. It is not expected that the resistance of F8BT to cyclohexanone is due to crosslinking of the layer; throughout this thesis DSC scans of the polymer have been performed that continue to show distinct thermal transitions even after 3 heating/cooling cycles above T_m ; the T_g would be non-existent in the case of induced crosslinking.

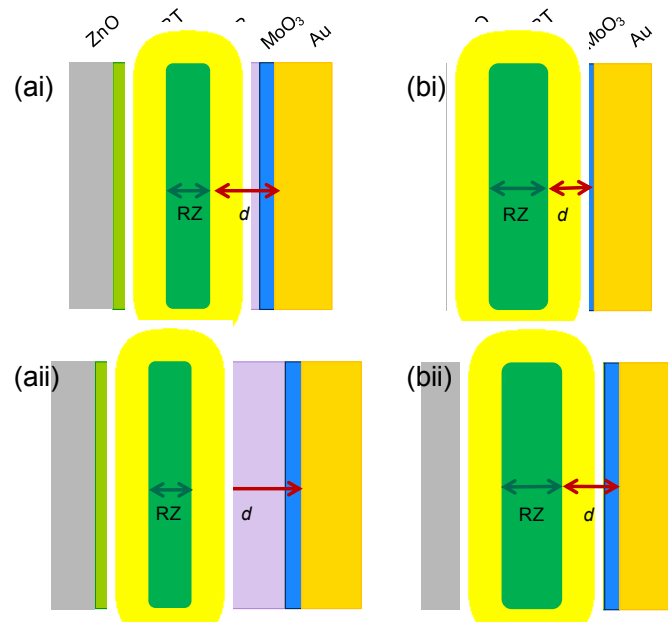


Figure 4.16: schematics of (ai) bilayer and (bi) F8BT-only diodes showing the presumed location of the RZ with respect to the device layers, particularly the distance d to the Au electrode. (a) and (b) show the bilayer and F8BT-only diodes respectively, with a thinner TFB and F8BT layer. (a) and (b) show the bilayer and F8BT-only diodes respectively, with a thicker TFB and F8BT layer.

With no evidence of emission taking place within the TFB layer (figure 4.7), the large LUMO offset between the F8BT and the TFB is likely to confine the RZ to within the F8BT layer near the F8BT/TFB interface (figure 4.16ai)^[31]. Consequently, any changes to the TFB thickness (figure 4.16aii) would lead to a direct change in the distance between the emitter species and the reflective back contact and hence the preferential outcoupling of different wavelengths and the gradual bathochromic shift in the EL^[52]. This is not likely to be the case in the F8BT-only devices; it has been previously reported that increasing the thickness of F8BT in inverted HyLEDs will likely reposition the RZ away from the cathode/F8BT interface (figures 4.16bi-ii)^[55]. With the RZ less defined, the emitter-contact distance will not be a simple linear dependence on the F8BT thickness. The confinement of emissive species due to the TFB layer therefore allows it to be used as an effective optical tuner.

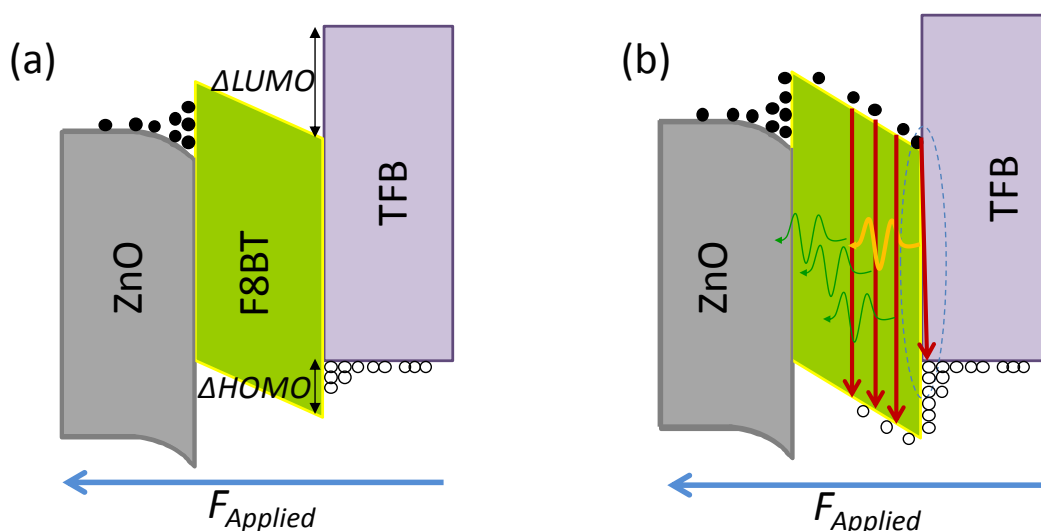


Figure 4.17: (a) The energy offsets at the F8BT interfaces act as barriers to the injected charges under the applied electric field $F_{applied}$. This separation of charges would lead to the build-up of an electric field across the F8BT. (b) Eventually, charges are able to tunnel into the F8BT where they recombine. A transition from the F8BT LUMO to the TFB HOMO is also shown illustrating any contribution due to excimer emission.

It is known that HyLEDs based on materials with similar CB-LUMO offsets to ZnO/F8BT are hole-dominated devices with electron injection occurring due to the build-up of holes at the EIL/LEP interface (Chapter 1)^[56]. Kabra *et al.* have reported on observing an increase in the efficiency of single-polymer devices with increased F8BT thickness, though such devices contained a Cs_2CO_3 interlayer at the ZnO/F8BT interface to improve electron injection^[55]; here an increase in F8BT thickness is observed to worsen device performance. This is assumed to be due to an increase in resistance to the hole current as well as due to a smaller electric field across the increasingly thick F8BT. The combination of both affects will lead to fewer holes

building up at the ZnO/F8BT interface and a wider triangular barrier for electrons to tunnel through. Fewer electrons are therefore present in the F8BT to contribute to light emission.

If HyLEDs are hole-dominated, at first regard it makes little sense to include an efficient hole transporter like TFB in such devices. However, the increase in device performance proves otherwise and it is likely to be due to the 0.7 eV HOMO offset (ΔHOMO) between TFB and F8BT providing a barrier to injected holes (figure 4.17a). This would have a further effect of repositioning the RZ away from the ZnO/F8BT interface and as discussed above, would not change with the thickness of TFB. Given that an ohmic contact should form between the TFB and the MoO_x, the rapid increase in J from 0 V should be due to holes flooding the device assuming a very low device turn-on voltage V_{on} (this has previously been attributed to, for example, electrons overcoming their energetic barrier at the ITO/oxide EIL interface^[57] or to the difference between the metal contact work functions^[58]). Holes would then begin to accumulate at the F8BT/TFB interface leading to a decrease in the proportion of the applied bias dropped across the TFB layer and a slowing down of the current rise. From HyLED literature values, the barrier to electron injection at the ZnO/F8BT interface is likely to be very similar to ΔHOMO . Therefore, charges will accumulate on either side of the F8BT until the forward bias allows the triangular energy barriers at the interfaces to become narrow enough for both signs of charge to tunnel through into the F8BT layer. Injected electrons also get blocked at the F8BT/TFB interface, helping hole injection from TFB into F8BT. Radiative recombination then takes place at the F8BT/TFB interface. The delay between V_{on} and V_{L-on} is most likely due to the period of charge accumulation at the ZnO/F8BT and F8BT/TFB interfaces. Such a delay is not ideal given that it may lead to detrimental effects such as Joule heating due to a unipolar hole current, but over the period of time tested the devices showed highly stable behaviour with no decrease in brightness or efficiency with multiple measurements.

4.5. Conclusions and Outlook

The initial aim of the work discussed in this Chapter was to develop a procedure that would allow for a layer of TFB to be cast onto an F8BT-coated substrate using simple solution-based processing without needing to employ multiple substrates and lift-off techniques. Considering device fabrication, such a technique would need to give consistent high yields of defect-free, uniform bilayers. Upon identifying the best procedure, however, the initial work was developed further to optimise the TFB layer in planar HyLED devices by exploring its thickness beyond the typical ~ 10 nm used in standard PLEDs. In doing so, it was demonstrated that not only can TFB be employed as a hole transporting/electron blocking/exciton buffer layer to boost device efficiencies, but that it can also be used as an optical tuning layer to easily alter the colour of the

EL spectrum. Such an effect had not been previously reported for inverted HyLED devices. Reflectance measurements indicate that changes to the EL might be a consequence of weak microcavity effects and further indicates the presence of high quality interfaces present in these devices. Following the publication of these results, Xu *et al.* used single polymer layer HyLEDs to vary the emission colour of other polyfluorene derivatives, though this time by varying the thickness of the emissive layer^[32]. They noted a cyclical change in λ_{em} coordinates over a thickness range of 100-700 nm as well as a spectral narrowing in the EL spectra with increasing viewing angle. Furthermore, they suggest that HyLEDs are well suited to investigations of weak MCEs due to the location of the RZ typically being far from the metal electrode and therefore more likely to lead to stable optical interference.

The bilayer devices were very stable and all thicknesses (and consequently, emitted colours from green to orange) were able to achieve luminance values in excess of 1000 cd/m². As such, though efficiencies are modest, there is potential for these devices to be used for display purposes. Angle-dependent emission as observed in figure 4.11 is not ideal in such a case, but the use of nanostructured layers has been shown to rectify this problem in other devices^[59,60].

The creation of multilayers from solution processes is extremely challenging though there is much progress being made in this regard particularly with the development of alcohol-soluble OSCs. After exploring various approaches in this work, annealing the F8BT to above its T_m and then applying a solvent spin rinse of cyclohexanone from which to then cast the TFB is the procedure which worked the most consistently. However, it is hoped that the procedure could be simplified further. For example, IPA is known to wet F8BT extremely well, so dissolving TFB in a IPA-cyclohexanone co-solvent may be sufficient to remove some of the steps in the procedure. Furthermore, it would be ideal to test the generality of these procedures by applying them to other polymers to test whether side-chain exposure at the surface is having an effect. PFO, in particular, might prove insightful given its identical side-chain structure to F8BT.

The procedure discussed in Section 4.2 of this Chapter was successfully applied across to other bilayer device fabrications in this project as discussed in Chapters 3 and 5.

4.6. References

- [1] J. C. D. Faria, A. J. Campbell, M. A. McLachlan, *J. Mater. Chem. C* **2015**, *3*, 4945.
- [2] C. Tang, X. D. Liu, F. Liu, X. L. Wang, H. Xu, W. Huang, *Macromol. Chem. Phys.* **2013**, *214*, 314.
- [3] X. Yang, G. Zhou, W.-Y. Wong, *J. Mater. Chem. C* **2014**, *2*, 1760.
- [4] X. He, D. Cai, D.-Y. Kang, W. Haske, Y. Zhang, C. a. Zuniga, B. H. Wunsch, S. Barlow, J. Leisen,

- D. Bucknall, B. Kippelen, S. R. Marder, *J. Mater. Chem. C* **2014**, *2*, 6743.
- [5] B. Ma, B. J. Kim, L. Deng, D. A. Poulsen, M. E. Thompson, J. M. J. Fréchet, *Macromolecules* **2007**, *40*, 8156.
- [6] C. Pan, K. Sugiyasu, M. Takeuchi, *Chem. Commun. (Camb)*. **2014**, *50*, 1.
- [7] S. Dailey, W. J. Feast, R. J. Peace, I. C. Sage, L. Wood, **2001**, 4.
- [8] C. Newby, J.-K. Lee, C. K. Ober, *Macromol. Res.* **2013**, *21*, 248.
- [9] S. Sax, N. Rugen-Penkalla, A. Neuhold, S. Schuh, E. Zojer, E. J. W. List, K. Müllen, *Adv. Mater.* **2010**, *22*, 2087.
- [10] R. Trattnig, L. Pevzner, M. Jäger, R. Schlesinger, M. V. Nardi, G. Ligorio, C. Christodoulou, N. Koch, M. Baumgarten, K. Müllen, E. J. W. List, *Adv. Funct. Mater.* **2013**, *23*, 4897.
- [11] C. a. Zuniga, S. Barlow, S. R. Marder, *Chem. Mater.* **2011**, *23*, 658.
- [12] N. Aizawa, Y.-J. Pu, H. Sasabe, J. Kido, *Org. Electron.* **2013**, *14*, 1614.
- [13] A. Köhnen, M. Irion, M. C. Gather, N. Rehmman, P. Zacharias, K. Meerholz, *J. Mater. Chem.* **2010**, *20*, 3301.
- [14] J.-S. Kim, R. H. Friend, I. Grizzi, J. H. Burroughes, *Appl. Phys. Lett.* **2005**, *87*, 023506.
- [15] D. Kabra, M. H. Song, B. Wenger, R. H. Friend, H. J. Snaith, *Adv. Mater.* **2008**, *20*, 3447.
- [16] D.-Y. Chung, D.-S. Leem, D. D. C. Bradley, A. J. Campbell, *Appl. Phys. Lett.* **2011**, *98*, 103306.
- [17] Y.-G. Ju, In *Organic Light Emitting Diode - Material, Process and Devices*; Ko, S. H., Ed.; InTech, 2011.
- [18] R. Liu, C. Xu, R. Biswas, J. Shinar, R. Shinar, *Appl. Phys. Lett.* **2011**, *99*, 093305.
- [19] L. G. Connolly, D. G. Lidzey, R. Butté, a. M. Adawi, D. M. Whittaker, M. S. Skolnick, R. Airey, *Appl. Phys. Lett.* **2003**, *83*, 5377.
- [20] D. P. Puzzo, M. G. Helander, P. G. O'Brien, Z. Wang, N. Soheilnia, N. Kherani, Z. Lu, G. A. Ozin, *Nano Lett.* **2011**, *11*, 1457.
- [21] A. Dodabalapur, L. J. Rothberg, R. H. Jordan, T. M. Miller, R. E. Slusher, J. M. Phillips, *J. Appl. Phys.* **1996**, *80*, 6954.
- [22] a. Dodabalapur, L. J. Rothberg, T. M. Miller, E. W. Kwock, *Appl. Phys. Lett.* **1994**, *64*, 2486.
- [23] D. Poitras, C.-C. Kuo, C. Py, *Opt. Express* **2008**, *16*, 8003.
- [24] S. Chen, L. Deng, J. Xie, L. Peng, L. Xie, Q. Fan, W. Huang, *Adv. Mater.* **2010**, *22*, 5227.
- [25] C. L. Lin, H. W. Lin, C. C. Wu, *Appl. Phys. Lett.* **2005**, *87*, 3.
- [26] J. Tischler, M. Bradley, V. Bulović, J. Song, A. Nurmikko, *Phys. Rev. Lett.* **2005**, *95*, 036401.
- [27] R. B. Fletcher, D. G. Lidzey, D. D. C. Bradley, M. Bernius, S. Walker, *Appl. Phys. Lett.* **2000**, *77*, 1262.
- [28] S. Tokito, T. Tsutsui, Y. Taga, *J. Appl. Phys.* **1999**, *86*, 2407.

- [29] T. Shiga, H. Fujikawa, Y. Taga, *J. Appl. Phys.* **2003**, *93*, 19.
- [30] V. Bulović, V. Khalfin, G. Gu, P. Burrows, D. Garbuzov, S. Forrest, *Phys. Rev. B* **1998**, *58*, 3730.
- [31] H. Becker, S. Burns, R. H. Friend, *Phys. Rev. B* **1997**, *56*, 1893.
- [32] J. Xu, L. Yu, L. Hu, R. He, W. Yang, J. Peng, Y. Cao, *J. Mater. Chem. C* **2015**, *3*, 9819.
- [33] C. H. Cheung, A. B. Djurišić, C. Y. Kwong, H. L. Tam, K. W. Cheah, Z. T. Liu, W. K. Chan, P. C. Chui, J. Chan, A. D. Rakić, *Appl. Phys. Lett.* **2004**, *85*, 2944.
- [34] J. D. Shore, *Appl. Phys. Lett.* **2005**, *86*, 186101.
- [35] J. Draper, I. Luzinov, S. Minko, I. Tokarev, M. Stamm, *Langmuir* **2004**, *20*, 4064.
- [36] P. Xiao, L. Lan, T. Dong, Z. Lin, L. Wang, H. Ning, J. Peng, *ECS J. Solid State Sci. Technol.* **2014**, *3*, Q3081.
- [37] Q. Wang, Y. Zhou, H. Zheng, J. Shi, C. Li, C. Q. Su, L. Wang, C. Luo, D. Hu, J. Pei, J. Wang, J. Peng, Y. Cao, *Org. Electron. physics, Mater. Appl.* **2011**, *12*, 1858.
- [38] J. Lee, Y. K. Jung, D. Y. Lee, J.-W. Jang, S. Cho, S. Son, J. Jeong, S. H. Park, *Synth. Met.* **2015**, *199*, 408.
- [39] H. Du, Z. Deng, Z. Lü, Y. Yin, L. Yu, H. Wu, Z. Chen, Y. Zou, Y. Wang, H. Liu, Y. Li, *Synth. Met.* **2011**, *161*, 2055.
- [40] H. Zhou, Y. Zhang, J. Seifert, S. D. Collins, C. Luo, G. C. Bazan, T.-Q. Nguyen, A. J. Heeger, *Adv. Mater.* **2013**, *25*, 1646.
- [41] J. Costa Dantas Faria, A. J. Campbell, M. A. McLachlan, *Optimisation of Zinc Oxide as a Charge Injection Layer for Hybrid Organic-Inorganic Light Emitting Diodes*, 2012.
- [42] C. Ran, G. Ding, W. Liu, Y. Deng, W. Hou, *Langmuir* **2008**, *24*, 9952.
- [43] M. Miwa, A. Nakajima, A. Fujishima, K. Hashimoto, T. Watanabe, *Langmuir* **2000**, *16*, 5754.
- [44] E. H. Sohn, J. Ahn, B. G. Kim, J. C. Lee, *Langmuir* **2011**, *27*, 1811.
- [45] H. Rangwalla, A. D. Schwab, B. Yurdumakan, D. G. Yablon, M. S. Yeganeh, A. Dhinojwala, *Langmuir* **2004**, *20*, 8625.
- [46] J. M. Winfield, C. L. Donley, R. H. Friend, J.-S. Kim, *J. Appl. Phys.* **2010**, *107*, 024902.
- [47] D. D. Gebler, Y. Z. Wang, J. W. Blatchford, S. W. Jessen, D. K. Fu, T. M. Swager, A. G. MacDiarmid, A. J. Epstein, *Appl. Phys. Lett.* **1997**, *70*, 1644.
- [48] J.-S. Kim, R. H. Friend, I. Grizzi, J. H. Burroughes, *Appl. Phys. Lett.* **2005**, *87*, 023506.
- [49] A. C. Morteani, A. S. Dhoot, J.-S. Kim, C. Silva, N. C. Greenham, C. Murphy, E. Moons, S. Ciná, J. H. Burroughes, R. H. Friend, *Adv. Mater.* **2003**, *15*, 1708.
- [50] M. Shakutsui, H. Matsuura, K. Fujita, *Org. Electron.* **2009**, *10*, 834.
- [51] C. M. Ramsdale, N. C. Greenham, *J. Phys. D. Appl. Phys.* **2003**, *36*, L29.
- [52] J. Lee, N. Chopra, F. So, *Appl. Phys. Lett.* **2008**, *92*, 033303.

- [53] M. J. Banach, R. H. Friend, H. Sirringhaus, *Macromolecules* **2003**, *36*, 2838.
- [54] C. L. Donley, J. Zaumseil, J. W. Andreasen, M. M. Nielsen, H. Sirringhaus, R. H. Friend, J.-S. Kim, *J. Am. Chem. Soc.* **2005**, *127*, 12890.
- [55] D. Kabra, L. P. Lu, M. H. Song, H. J. Snaith, R. H. Friend, *Adv. Mater.* **2010**, *22*, 3194.
- [56] H. J. Bolink, E. Coronado, D. Repetto, M. Sessolo, E. M. Barea, J. Bisquert, G. Garcia-Belmonte, J. Prochazka, L. Kavan, *Adv. Funct. Mater.* **2008**, *18*, 145.
- [57] H. J. Bolink, H. Brine, E. Coronado, M. Sessolo, *J. Mater. Chem.* **2010**, *20*, 4047.
- [58] H. J. Bolink, E. Coronado, J. Orozco, M. Sessolo, *Adv. Mater.* **2009**, *21*, 79.
- [59] W. C. H. Choy, C. Y. Ho, *Opt. Express* **2007**, *15*, 13288.
- [60] W. Gaynor, S. Hofmann, M. G. Christoforo, C. Sachse, S. Mehra, A. Salleo, M. D. McGehee, M. C. Gather, B. Lüssem, L. Müller-Meskamp, P. Peumans, K. Leo, *Adv. Mater.* **2013**, *25*, 4006.

Chapter 5 – Effects of Polymer Molecular Weight on Device Performance

Here, the effect of molecular weight (MW) on the properties of F8BT and, consequently, on the performance of F8BT-based LEDs is discussed. Beyond oligomers, the effect of chain length on the characteristics of light-emitting polymer based optoelectronic devices is poorly discussed, often failing to link the material properties in the solid state to the resulting device performance. In this chapter, optical, thermal and structural measurements are made to first compare the properties of each F8BT MW fraction to those in the literature. They are then used to explain the general improvement in device performance that is observed with increasing MW, as well as the changes which occur with annealing F8BT above its key phase transition temperatures. Importantly, the MW fractions here have been obtained via soxhlet purification and gel permeation chromatography (GPC) from a single commercial batch to ensure that all possess the same chemical history and chain end groups. Finally, hole-only devices are analysed with possible injection regimes discussed to explain diode behaviour for each MW fraction across the three annealing procedures.

5.1. Literature

5.1.1. Polymer Properties as a Function of Molecular Weight

One of the most fundamental features of a polymer is its chain length and varying it will often lead to significant alterations to a polymer's physical properties. Early empirical work on well established polymers, e.g. polystyrene, pointed to a general expression that can be used to model the behaviour of a polymer as a function of its MW; for a given property P ,

$$P = P_{\infty} - \frac{A}{M} \quad 5.1$$

where P_{∞} is the value of the property for an infinitely long chain, A is a polymer-dependent constant and M is some molecular weight average^[1,2]. Thus, the value of P will increase rapidly with M , but, after converging asymptotically towards some value, essentially becomes independent of chain length. The relation shown by equation (5.1) is very general and does not necessarily always apply; for example, while Fox and Flory showed that equation (5.1) could model the T_g of polystyrene as a function of M^2 , Merz et al found that it didn't vary at all^[1]. Another noted trend is one in which the property reaches a peak for some MW and is then seen to decrease before levelling off with increasing chain length. These variations are linked to the way in which individual chains arrange themselves in the solid state with the influence of entanglements growing along with MW, changing the extended chain crystalline order of low

molecular weight (LWM) samples through to folded chain crystals before resulting in a complex structure in which crystalline regions are surrounded by amorphous ones in high molecular weight (HMW) samples. Figure 5.1 shows examples of these relations. The desired MW very much depends on the end application and often a compromise must be struck between the good physical properties offered by high MW and the ease of processability offered by lower MW^[3].

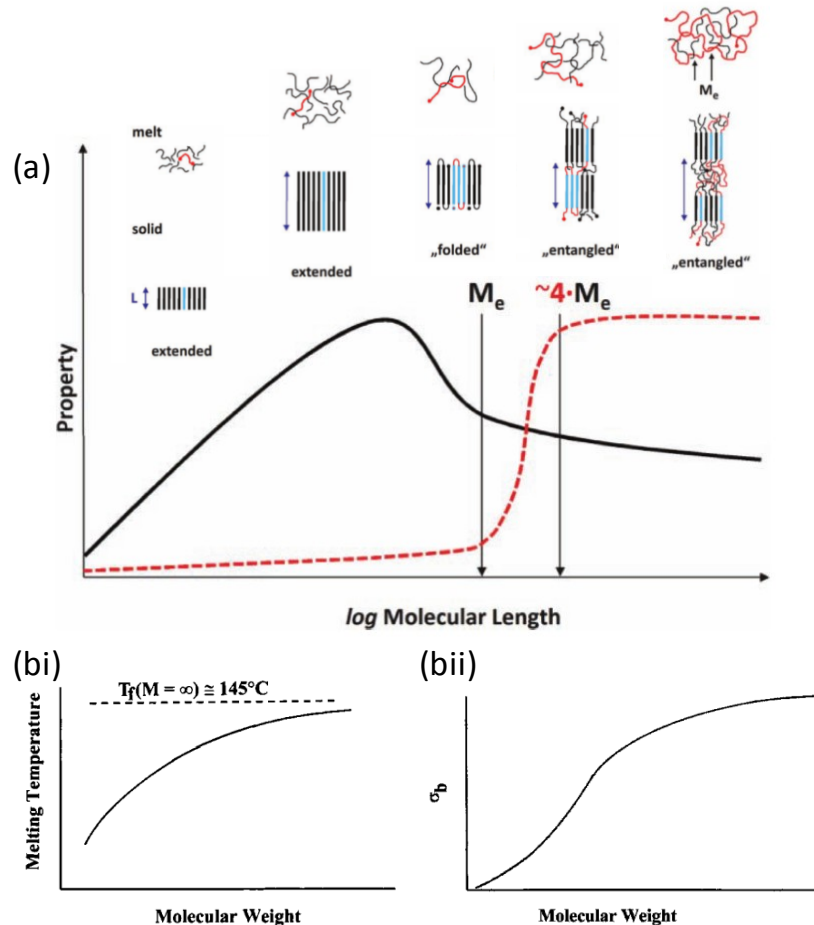


Figure 5.1: (a) Illustration of two general trends often observed for certain properties as a function of polymer chain length. These trends are related to the conformation of the chains and the influence of the weight between entanglements M_e , the influence of which increases with MW. Adapted from reference [4]. Examples of particular trends are the melting temperature of the (bi) alkane series and, (bii) generally, the tensile strength (adapted from reference [3]).

Due to the nature of the polymerisation techniques polymers are mainly mixtures composed of a distribution of different chain lengths. Throughout this thesis the term 'molecular weight' has been used generally to refer to the length of the polymer chain. However, since a given batch consists of a distribution of chain lengths there are many ways in which to quantify the 'molecular weight'. One can describe the *number average molecular weight* M_n which is simply the average of all of the molecular weights M_i present in a batch

$$M_n = \frac{\sum_i N_i M_i}{\sum_i N_i}, \quad 5.2$$

where N_i is the number of chains with molecular weight is M_i . *Mass average molecular weight* M_w , on the other hand, is weighted towards longer chains and can be understood by realising that, for a given distribution of different lengths, the most likely chains to be 'selected' are those which are also the longest^[5]. This is given by:

$$M_w = \frac{\sum_i N_i M_i^2}{\sum_i N_i M_i}. \quad 5.3$$

M_w will return a larger value than M_n which itself returns a value close to the middle of the weight distribution. The dispersity \mathcal{D} is defined as the ratio M_w/M_n and gives a measure of the spread in chain lengths in a given batch. It is generally considered that larger \mathcal{D} values lead to a worsening of properties with shorter chains, for example, acting as impurities through phase separation^[3].

5.1.2. Influence of Molecular Weight on Device Performance

In parallel to the device applications of ZnO NRAs, the OPV research community has extensively pursued investigations of device performance as a function of polymer MW as recently reviewed by Katsouras *et al.*^[6]; the PLED literature in this respect, however, is relatively scarce. An overview of the work carried out by the OPV community therefore gives some insight into the methods and interpretations used when analysing the dependence of device performance on MW.

5.1.2.1. Polymers for Organic Photovoltaics

The work reported by Kline *et al.* over 2003-2005 very much acted as an impetus to further investigations into the role polymer MW plays on device performance. Initially, they observed an increase in the field effect mobility of P3HT from 1.7×10^{-6} to $9.4 \times 10^{-3} \text{ cm}^2 \text{ V}^{-1} \text{ s}^{-1}$ as the MW increased from 3.2 to 36.5 kg/mol^[7]. These transport changes were accompanied by changes to the polymer morphology with AFM images showing LMW P3HT packing into domains consisting of nanorod-shaped crystals while HMW polymer gave a more isotropic and nodular structure (figure 5.2a-b). The authors suggested that the effects of MW could provide an explanation for the variety of device data as reported by different groups at the time. The same group went on to further explore how different MW batches were affected by processing conditions, noting in particular that LMW P3HT mobility was more easily affected by deposition

technique, solvent and annealing conditions than HMW P3HT^[8]. They noted that the difference in mobility was likely to be morphological in origin with the longer chains of HMW material acting as connectors that would allow charge to travel between crystalline domains; with the absence of these chains in LMW material, charge would be affected by trap sites at disordered grain boundaries^[8].

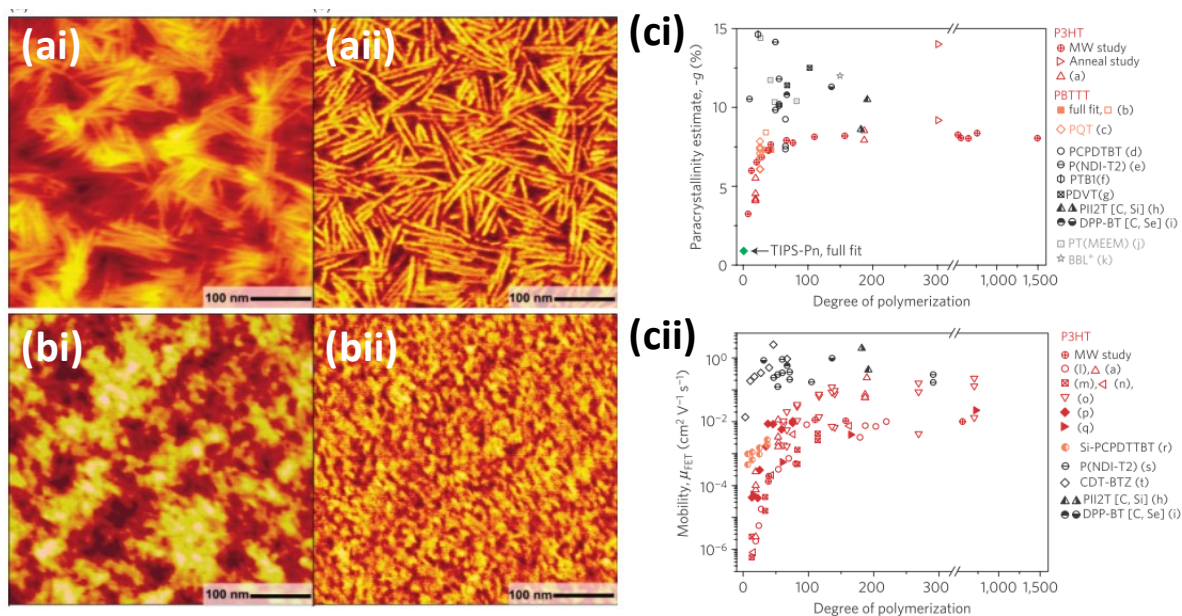


Figure 5.2: AFM scans of (ai) LMW P3HT morphology and (aai) the associated phase image. Similarly the morphology of (bi) HMW P3HT and (bii) its phase image. Reproduced from reference [7]. (ci) The effect on crystalline structural disorder across different polymers and (cii) the transistor mobility as a function of MW. Reproduced from reference [9].

Schilinsky *et al.* soon followed this research by testing BHJ OPVs in which the P3HT varied between 2.0-19.0 kg/mol^[10]. Here, they noted an impressive jump in PCE between the MW range extremes from ~ 0.1 to ~ 3.0 % mostly due to an order-of-magnitude increase in J_{SC} . This they attributed to improved π - π^* stacking enabling improved charge transport in the HMW material as well as to the increased absorption at longer wavelengths as a consequence of extended lamellar packing structures (aggregates) and increased conjugation lengths. More recent studies have cast further light on these processes^[6] which have been observed in other polymeric OPV materials; for instance, Kang *et al.* also noticed an increase in PCE as the MW of the donor polymer PPDT2FBT increased doing so for similar morphological reasons as those analysed in P3HT studies^[11]. Blends of HMW PPDT2FBT with an acceptor material gave a more intermixed morphology favourable to charge transport while shorter chain material would self-aggregate in the blend. While the LMW material was more crystalline as shown by GIXS measurements, these domains also exhibited a more random orientation, further impeding the

out-of-plane charge transport through the diode. Overall, Noriega *et al.* showed that short-range intermolecular aggregation is sufficient for effective transport and that bridging chains between ordered regions are needed for this to be the case^[9]. Therefore, crystallinity is not necessary for efficient transport, but ordered regions are responsible for charge transport due to the energetic barrier between these and amorphous regions (absorption is blueshifted in the latter due to the decreased conjugation length present). Impressively, the authors analyse several studies to show that the transistor mobility follows the same trend as the quantified disorder in crystalline regions (paracrystallinity) when both are plotted against MW (figure 5.2c). Much like the general trends shown in figure 5.1 and implied by equation (5.1), both the mobility and disorder become independent of MW after some value as the increased number of interconnects becomes limited by the increased disorder of the system^[9]. There is therefore a limit to how much an increase in MW is likely to improve the performance of OPVs; in their review Katsouras *et al.* note that there is an ideal chain length for P3HT beyond which PCE performance begins to degrade again to which they attribute to the increased distortions (and therefore reduced interchain overlap) in longer chains^[6]. Such an ideal length is shown to vary from group to group and thus shows that it is highly dependent on the processing conditions used.

Beyond investigations of the chain length, it is generally accepted that increased \mathcal{D} values will worsen device performance but only recently has its influence on OPV performance been reported; for three batches of similar M_w PTB7 (100, 118 and 103 kg/mol with $\mathcal{D} = 2.1, 3.5$ and 4.3 , respectively), Lu *et al.* observed a dramatic drop in PCE from 7.20 % to 2.48%^[12]. The authors note the existence of species that act as trapping centres in high \mathcal{D} samples which also contain a greater amount of structural defects that act as energy transfer centres as shown by a weakening PL emission towards longer wavelengths. Finally, Bruner and Dauskardt recently also showed that HMW P3HT was associated with the most mechanically robust devices^[13]. This was analysed through the spread of cracks in the P3HT layer using bending tests on glass substrates and reasoned that the entangled amorphous regions between crystalline domains are responsible for increasing the tensile strength of the material. They did, however, note that the most efficient devices did not necessarily correspond to the most robust. Repeating such studies using flexible substrates is likely to become more commonplace as device fabrication moves to high throughput methods like roll-to-roll printing.

5.1.2.2. Polymers for Light-Emitting Diodes

Like the OPV field, a range of techniques is employed to analyse the physical and optoelectronic properties of light-emitting polymers. For instance Knaapila *et al.* use AFM on polyfluorene derived PF2/6 polymer films with $M_n \sim 3$ -150 kg/mol aligned on polyimide substrates to show a sudden increase in surface roughness from which they define distinct LMW and HMW

ranges^[14]. They use GIXS measurements to reveal that LMW films have a more nematic morphology, but that this transitions to a hexagonal structure around 10^3 kg/mol. Lai *et al.* use DSC on four different vinyl-containing polymers each divided into LMW and HMW to show that each experiences an increase in T_g and that the latter are more spectrally stable when heated beyond this temperature, showing little loss in PL emission^[15]. For a range of $M_w \sim 10$ -1600 kg/mol Koynov *et al.* extracted optical coefficients of MEH-PPV films showing, for instance, an increased absorption coefficient with M_w to which they use waveguide experiments and infrared measurement techniques to be due to changes in the polymer chain orientation^[16]. They noted that HMW films have a greater degree of backbone alignment parallel to the substrate whereas chain segments are randomly oriented in LMW samples and that these particular properties are especially influenced by M_w below 400 kg/mol. The authors reason that HMW polymers should lead to better PLED performance as the in-plane alignment may improve intermolecular charge transport perpendicular to the substrate plane. Interestingly, the authors noted that one sample did not follow the trends because of a much higher \mathcal{D} value relative to all the other samples. An earlier study by Menon *et al.* had already stated that control of \mathcal{D} was paramount for extracting conclusive results when comparing different polymers or even the same polymer from different batches^[17]. Looking at monodisperse oligomers of PPV ($M_w \sim 1.0$ -5.8 kg/mol), the authors noted that doping a LMW sample with only 2 % HMW material significantly redshifted the PL and absorption spectra of the former so much that it resembled that of the latter. The longer chain dopants were found to act as trap sites causing the migration of charges and excited species to the lower energy longer chains (a consequence of increased conjugation length). Unlike the literature cited thus far, this study was significant in that it also included an analysis of PLED efficiencies. Briefly, the longer the oligomer chain, the higher the device EQE. This was also true of their PLQE values and the lower efficiencies of the LMW material was attributed to a greater tendency for chains to aggregate. Liu *et al.* later provided some confirmation of this using their own PFO-derived oligomers ($M_w \sim 0.9$ -8.8 kg/mol) with an increase in max CE from 0.08 cd/A (at 362 cd/m²) to 0.80 cd/A (1300 cd/m²)^[18]. As an explanation the authors merely state that this improvement is due to HMW polymers being able to "form more robust films" as a consequence of their chain lengths and high T_g . A particularly interesting aspect of this study was that the authors suggested a general relationship for T_g in the form of equation (5.1): $T_g = 88.0 - 200.2M^{-1}$. The asymptotic value for T_g is reached at the high end of these oligomers, significantly before such molecules can be considered 'polymers' as defined by Sperling ($M_w \sim 25$ kg/mol)^[3].

Beyond the use of oligomers, Hosoi *et al.* used PFO in the M_w range of 19.1-240 kg/mol, albeit with $\mathcal{D} \sim 3.4$ -17.6, and again noted improved efficiencies with HMW material^[19]. However,

drawing firm conclusions from this study is questionable given the potentially spurious effects of such large chain length distributions and particularly given the lack of any material characterisation on the part of the authors.

5.1.2.2.1. *Molecular Weight Studies of F8BT*

Of particular interest to this chapter are the results of Donley *et al.*^[20] and Martinez-Ferrero *et al.*^[21]. The former expanded upon the work of Banach *et al.*^[22] to elucidate the material and optoelectronic properties of F8BT as a function of MW through a systematic study of 8 separate batches over $M_n \sim 9\text{-}255$ kg/mol; the latter detailed specifically the influence of F8BT MW on HyLED device performance.

The polymer's structural properties have already been summarised in Chapter 1 (Section 1.9.2.1.). Despite the breadth of measurements conducted by both Donley *et al.* and Banach *et al.*, both studies came short of including any PLED device data, but the results of the former study suggest that higher MW material should lead to more efficient PLED devices. In particular, an increase in PLQE values was observed which increase further upon thermal annealing of the films across the studied MW range. AFM measurements showed films becoming smoother, too, which may be beneficial for device stability. The reasons for these observations are due to an increased planarity of F8BT chains parallel to the substrate at higher MW, the reduced influence of chain ends which may act as exciton dissociation sites, and the alignment of BT units across adjacent chains preventing exciton transfer to lower energy emissive sites^[20]. There is an uncertainty, however, in predicting the behaviour of HyLEDs as a function of F8BT MW: both annealing and increasing MW showed a decrease in electron mobility in F8BT films which may be a negative factor given the hole-transport dominated character of the standard HyLED device.

Martinez-Ferrero *et al.* attempted to investigate this issue by comparing the performance of 8 different batches of F8BT from four separate commercial suppliers with $M_w = 15.7 - 116$ kg/mol^[21]. Despite the authors concluding that longer chain samples lead to better devices, if one plots their tabulated data (figure 5.3), no trend is observed between M_w and $L_{v,max}$.

The groups cited in section 5.1.2.2. which reported device efficiencies all synthesised their own polymer and therefore had control of growth conditions and uniformity of synthesis routes. Comparing batches of the same polymer but from different suppliers is therefore likely to lead to the conflation of multiple experimental variables. For example, Martinez-Ferrero *et al.* do not account for the presence of different polymer chain end-capping groups which may be used by different suppliers. Such groups, depending on their nature, can act as non-radiative pathways and thus detrimentally effect PLQE^[23,24]. Adding to this, across all their batches \mathcal{D} varies from 1.9

(for their 60 kg/mol batch) to 5.6 (23 kg/mol) and it should be noted that even different batches from the same supplier have been shown to give wildly different results as recently reported with some anxiety by So's group^[25].

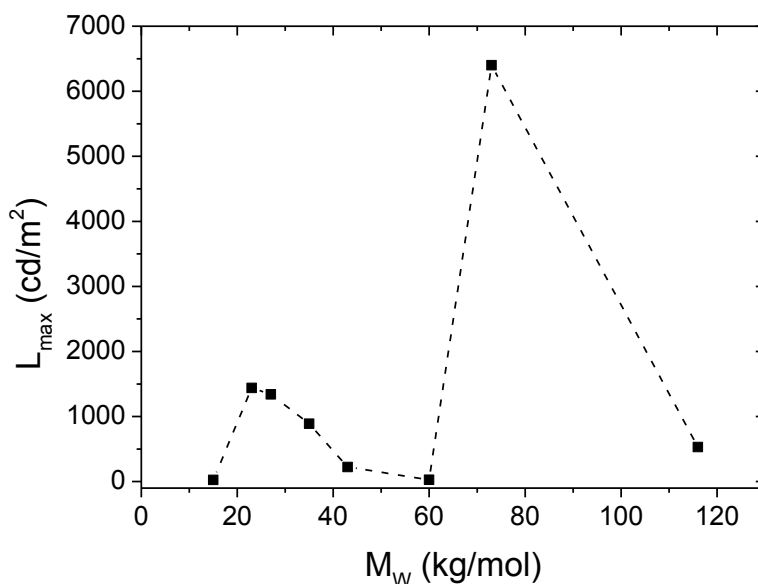


Figure 5.3: HyLED device data reported by Martinez-Ferrero *et al.* represented graphically^[21].

There is therefore significant scope in which to investigate the MW of an LEP such as F8BT on device performance. Furthermore, given the reported augmentations to PLQE and electron mobility^[20], diode behaviour as a combined function of post-deposition thermal treatment across a MW range warrants investigation.

The material used in this chapter was purchased in a single batch from American Dye Source (ADS), subsequently purified and separated into several different MW fractions. In this way, batch-to-batch variations would be circumvented and polymer chains across all fractions would be identically end-capped. The results and analysis of these fractions form the remainder of this chapter.

5.2. Experimental Methods

5.2.1. F8BT Purification and Fractionation

The purification of the commercially purchased F8BT was carried out by Bob C. Schroeder who was, at the time, in Iain McCulloch's group within the Imperial College London Chemistry Department. Approximately 1 gram of the material was first purified using soxhlet extraction

before undergoing further purification and fractionation via GPC. The experimental details are outlined in Appendix C. Briefly, the crude polymer was found to contain "catalytic impurities (mainly ligands) and insoluble material (colourless plastic bits)" with the large D value "caused by low molecular weight oligomers." It was not possible to recover these oligomers during the purification process resulting in a loss of approximately 500 mg of original material. Details of the final fractions, including the amount available, are shown in table 5.1. The molecular weight values were calculated in comparison to polystyrene standard samples.

Polymer Sample	M_n/M_w (kg/mol)	D	Amount (mg)
Crude (46K*)	46/172	3.7	~1000
After Soxhlet	67/177	2.6	~800
300K	300/400	1.3	28
160K	160/230	1.4	66
100K	100/180	1.8	82
67K	67/140	2.1	66
47K	47/124	2.6	53
36K	36/117	3.3	90
35K	35/123	3.5	14
Cut-off	55/176	3.2	102

Table 5.1: Details of the polymer fractions extracted following the purification of commercially obtained F8BT.

There is a reduction in D following purification and extraction procedures, though it is observed to increase as MW decreases and therefore may impact the shorter-chain fractions negatively. In any case fraction 35K was not used due to the low amount of material. The extracted 'cut-off' batch was similarly not used as solutions of this polymer were full of insoluble particulates. A small amount of the crude polymer (46K*) was available and so was used as a comparison in some of the studies.

5.2.2. Solution Concentration vs. Film Thickness

Efforts were made to deposit the same film thickness within these studies to enable fair comparisons across the different fractions. In order to determine the relationship between solution concentration and film thickness, a Mettler Toledo Analytical scale with precision up to 0.01 mg was employed here to measure < 1.0 mg amounts so as to preserve as much polymer

as possible for device and material characterisation. Toluene was used throughout to dissolve the polymer and solvent amounts added to achieve the required concentration. Solutions were left to stir overnight at 80 °C under an inert glovebox atmosphere. In order to achieve thicker films from more dilute concentrations, the spin coating speed was reduced to 1500 rpm (films from lower spin speeds exhibited an increasing amount of edge fringing); spin time was maintained at 40s. Solutions were *not* filtered on deposition seeing as they had already undergone purification. Film thicknesses were measured as discussed in Chapter 2 section 2.5.1.

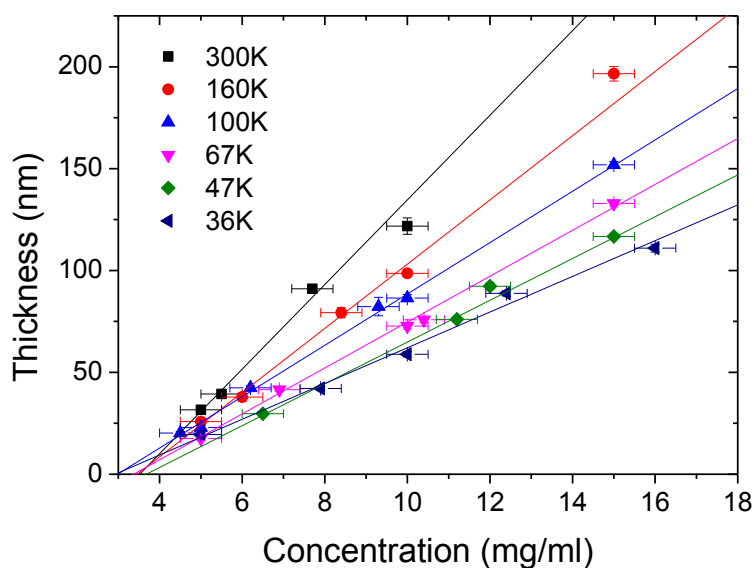


Figure 5.4: Relationship between film thickness and solution concentration for different MW fractions.

As expected, higher MW leads to thicker films for a given concentration (figure 5.4). The spread in data is larger than anticipated and this is likely due to the small amounts of material used; one can see that it becomes difficult to distinguish between points at lower concentrations. Nevertheless, the lines of best-fit were used in all subsequent experiments.

5.2.3. Device Fabrication

Device fabrication for bipolar and single carrier diodes follows the procedures outlined in Chapter 2, section 2. Throughout the literature the deposition of F8BT for LEDs is followed by a solvent drying step, or annealing to T_g ; films of F8BT are therefore annealed at either 90 or 150 °C for 20 minutes under an inert atmosphere. Additionally, in keeping with the device fabrication procedures of Chapters 3 and 4, a third set of substrates was annealed above their T_m (240 °C for 36K and 47K, and 275 °C for all others as defined by DSC measurements - Section

3.1) for 20 minutes and slow-cooled at 5 °C/min to 100 °C from which they were then quenched to room temperature.

5.2.4. Material Characterisation

Absorbance, X-ray, PL and PLQE measurements were all conducted on the same set of films all spin-cast under identical conditions. Films were spin-cast on 10 × 10 mm quartz substrates and dried as normal at 90 °C. In between measurements the substrates were kept wrapped in Al foil under an inert glovebox atmosphere. Once all four measurements were completed, the films were then annealed above T_g and the readings were repeated. The films were then subjected to the T_m procedure and all films characterised for a final time.

All procedures were otherwise carried out as explained in Chapter 2.

5.3. Results of Material and Optical Characterisation

In order to understand the behaviour of the devices reported in Section 4 of this chapter, the material and optical properties of the MW fractions were measured and compared to similar studies in literature, notably that of Donley *et al.*^[20]. For the optical, PLQE and XRD measurements in which the same films were used throughout (Section 5.2.4), the thicknesses of these films are noted in table 5.2. The films for the extracted MW samples all lie in the 75-90 nm range which should allow for a sufficiently fair comparison in their properties; due to little remaining material for the crude polymer, the thickness of its film is much lower despite an effort to reduce the spin coating speed to mitigate this. Nonetheless, as some properties have been shown to be insensitive to film thickness^[26] it is included in the discussions of sections 5.3.2 and 5.3.3 for completion.

Polymer	36K	46K*	47K	67K	100K	180K	300K
Thickness, nm	89.9 ± 2.2	46.3 ± 1.6	76.0 ± 0.6	75.8 ± 1.8	82.3 ± 5.4	79.3 ± 3.0	91.4 ± 1.8

Table 5.2: Thicknesses of films used in the characterisation techniques in Sections 5.3.2 and 5.3.3.

5.3.1. Thermal Analyses

Figure 5.5 shows the endotherms for the 36-300K fractions as extracted from the third DSC heating/cooling cycle. Also shown is that for the crude polymer (46K*). The heating curves show an exothermic transition peaking at 135 °C ($T_{c,1}$) which is prominent at LMW, but not discernible at 160 and 300K. The HMW batches instead show an exothermic peak at 205 °C ($T_{c,2}$), though there is a suggestion that this is also present in the LMW samples, albeit 5-10°C

lower. The fractions below 160K all show multiple endothermic peaks over broad temperature ranges; for the 36K sample, it extends over 210-230 °C, extending out to a peak at 259 °C for the 67K sample. There is a transition between the 67 and 100K samples with a decrease in features around 230 °C and an increase around 260 °C with a possible exothermic peak around 230 °C; by 160-300K, only one endothermic peak is observed at ~265 °C. Upon cooling at the same rate reveals a single exothermic peak ($T_{c,3}$) which increases from 125 to 145 °C with MW.

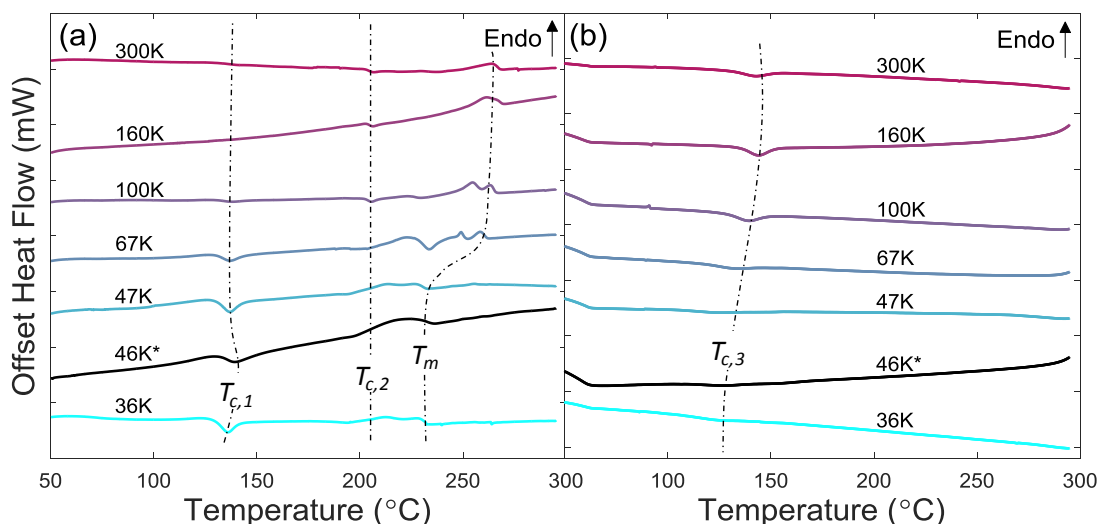


Figure 5.5: DSC (a) heating and (b) cooling curves for the crude polymer and its extracted M_w fractions.

These results are largely in line with that reported by others, though interpretation does differ slightly from author to author^[20,22,27]. T_g is usually taken to occur just before $T_{c,1}$ which itself is assumed to arise due to some crystallisation as the polymer transitions from the glassy to the rubbery state (the endothermic shift in the baseline associated with this transition is more clearly seen in figure 3.2, Chapter 3)^[22,27]. Banach *et al.*, however, see an isotropic film until 240 °C in their 129K film with the suggestion that $T_{c,1}$ is not related to crystallisation; the formation of spherulites is only apparent in films annealed to 250 °C^[22]. This is in contrast to XRD measurements in Chapter 3 which shows that annealing the batch of 116K F8BT just above T_g *did* induce some crystallinity (figure 3.12), probably due to the shorter, more mobile chains of that batch. In any case, T_g is typically further deduced from the cooling curves to be in the range indicated by $T_{c,3}$ in figure 5.5b^[20,27]. Out of interest, T_g (assuming $T_g = T_{c,3}$) was plotted against M_n^{-1} (figure 5.6) and was found to follow the form of the empirical formula defined in equation (5.1):

$$T_g = 148.0 - \frac{944.2}{M_n^{-1}}. \quad 5.4$$

In other words, this implies that for an infinitely long chain, the T_g of F8BT tends to 148.0 ± 1.7 °C.

The many endothermic transitions observed in the 210-260 °C range could be due to the melting of successive liquid crystalline phases^[3] before the nematic state is achieved^[22]. It should be said that despite the differing \mathcal{D} values, the endotherms presented here and across the cited literature are highly reproducible for a given MW range. The crude polymer does show less detail probably due to the large \mathcal{D} as well as the high concentration of impurities which tend to broaden transitions in DSC measurements. In conclusion, these results defined the annealing temperatures specified in section 5.2.3.

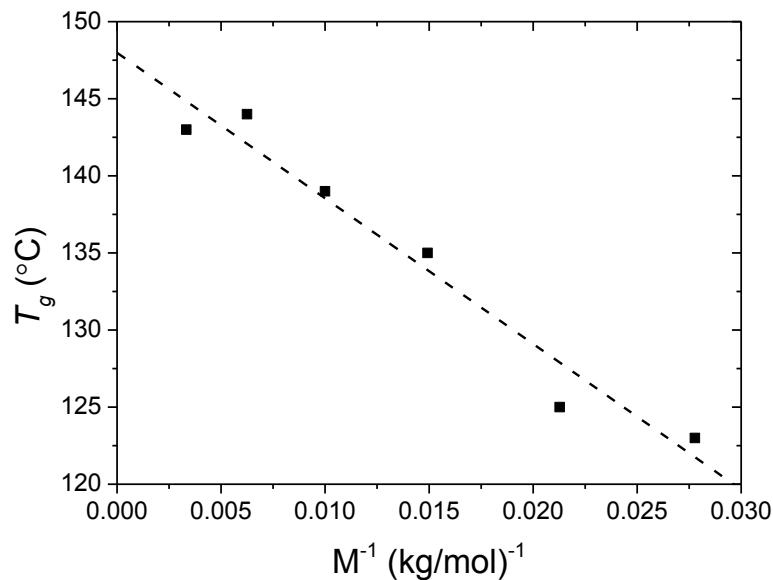


Figure 5.6: Variation of T_g with M_n^{-1} (not including the crude polymer).

5.3.1.1. Determination of Crystalline Fraction

It is possible to estimate the crystalline fraction of a polymer via DSC by finding the difference between the energy needed to melt the polymer ΔH_m and the energy given off during crystallisation ΔH_c , and then dividing it by the enthalpy of fusion ΔH_f^{∞} ^[28]:

$$X_C = \frac{\Delta H_m - \Delta H_c}{\Delta H_f^{\infty}}. \quad 5.5$$

ΔH_m and ΔH_c are respectively found by computing the areas of the melting and crystallisation peaks using an estimated baseline curve. These values are then divided by the heating rate. The

difference between these two quantities gives the energy needed to melt the fraction of the polymer that was already crystalline before further crystallinity was induced at T_c . Therefore, ΔH_f^∞ is the energy required to melt a 100% perfectly crystalline sample. Obtaining such a sample is difficult, however, and therefore determining ΔH_f^∞ equally so. Nevertheless, given a range of MWs, ΔH_f^∞ can be extrapolated by plotting the enthalpy of melt ΔH_m against M_n^{-1} as shown by Remy *et al.* who were able to extract ΔH_f^∞ for P3HT^[29]. Figure 5.7a shows 2 distinct regions in which ΔH_m increases with chain length up to $M_w \sim 140K$ (the LMW regime) and is then seen to decrease monotonically with further increases in length (HMW regime). This is a consequence of how the chains pack; as explained by Remy *et al.* the LMW regime adopts an extended chain conformation when crystalline ("like pencils in a box") and more energy is required as the chain length increases. However, with increasing length the polymer chain becomes more flexible allowing it to fold in on itself. Continuing beyond this in the HMW regime, parts of a chain are now entangled within amorphous regions between crystallites (figure 5.1) which lead to a lower ΔH_m ^[29]. In the LMW regime, the presence of chain ends lowers ΔH_m , but their effect becomes less and less significant as the chain length increases^[30]. Therefore, extrapolating from this region to infinite M_n would give ΔH_m for an infinitely long crystal, i.e. ΔH_f^∞ . Doing so in this case gives $\Delta H_f^\infty = 0.65 \pm 0.06$ J/g. This is almost two orders of magnitude smaller than the value for P3HT^[29]. Others have reported ΔH_m values of F8BT being an order of magnitude greater^[31], though the values reported here do compare similarly with those of PFO and other PFO-derived polymers^[32,33]. It should be said that Remy *et al.* do add a correction to their P3HT ΔH_f^∞ value by taking into account the area of the amorphous halo in their GIXS data. Nevertheless, to the best of the author's knowledge, this is the first time an estimate of ΔH_f^∞ has been calculated for F8BT.

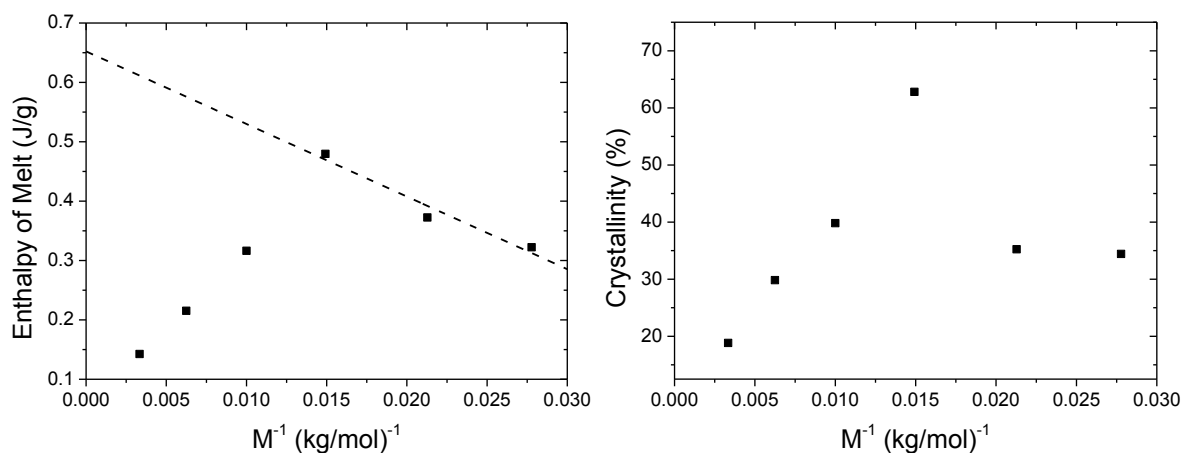


Figure 5.7: (a) Determination of ΔH_f^∞ by extrapolating from the ΔH_m of the LMW region. (b) The calculated crystalline fraction as a function of F8BT MW.

Utilising equation (5.5) it was now possible to obtain an estimate of the crystalline fraction across all samples (figure 5.7b). Balko *et al.* showed that crystallinity of P3HT varies between 68-80% depending on the MW^[34]; the 67K F8BT sample here matches quite well with those values, but otherwise all other samples exhibit crystallinities < 40%. The trend generally follows that of the ΔH_m which is expected given the increasingly entangled nature of the material at higher MW. Together with other material characterisation techniques, knowledge of the crystalline content of each sample should improve the understanding of the optoelectronic behaviour of these MW fractions.

5.3.2. X-ray Diffraction

XRD did not yield any information regarding the bulk morphology of as-cast or even T_g -annealed films (figure 5.8a-b). The latter should have shown some reflections (see Chapter 3), but it seems that even with a 45 minute scan, these films were too thin. This is especially the case with the crude polymer as only very weak reflections were resolved in the slow-cooled from T_m film whilst all other films exhibited more intense peaks under this procedure (figure 5.8c). The strongest reflections correspond to the unit cell spacing along the c -axis (001) which results in significant reflections due to the interchain π - π stacking distance (004). This verifies the observations made by others that aggregates in F8BT will preferentially align so that the chain backbone is parallel to the substrate plane. However, the presence of a notable (100) peak (corresponding to the monomer spacing) does suggest a significant amount of out-of-plane packing.

These results further suggest that LMW films exhibit the greatest proportion of chain alignment parallel to the substrate plane on slow-cooling from T_m with intensities peaking in the 47K sample and then generally decreasing thereafter in support of DSC crystallinity data. Further analyses of the relative intensities of the (100) peak to the (001) peak ($I_{(100)}/I_{(001)}$) was found to give noisy results and a trend with MW cannot be discerned (figure 5.9a). Likewise, calculation of the grain sizes (via Scherrer analysis - Chapter 2) associated with the (100) peak yielded no further information and this could be a consequence of the low intensities recorded. The (001) peak grain sizes are more consistent and suggest an asymptotic decrease with MW, but the difference in values is small.

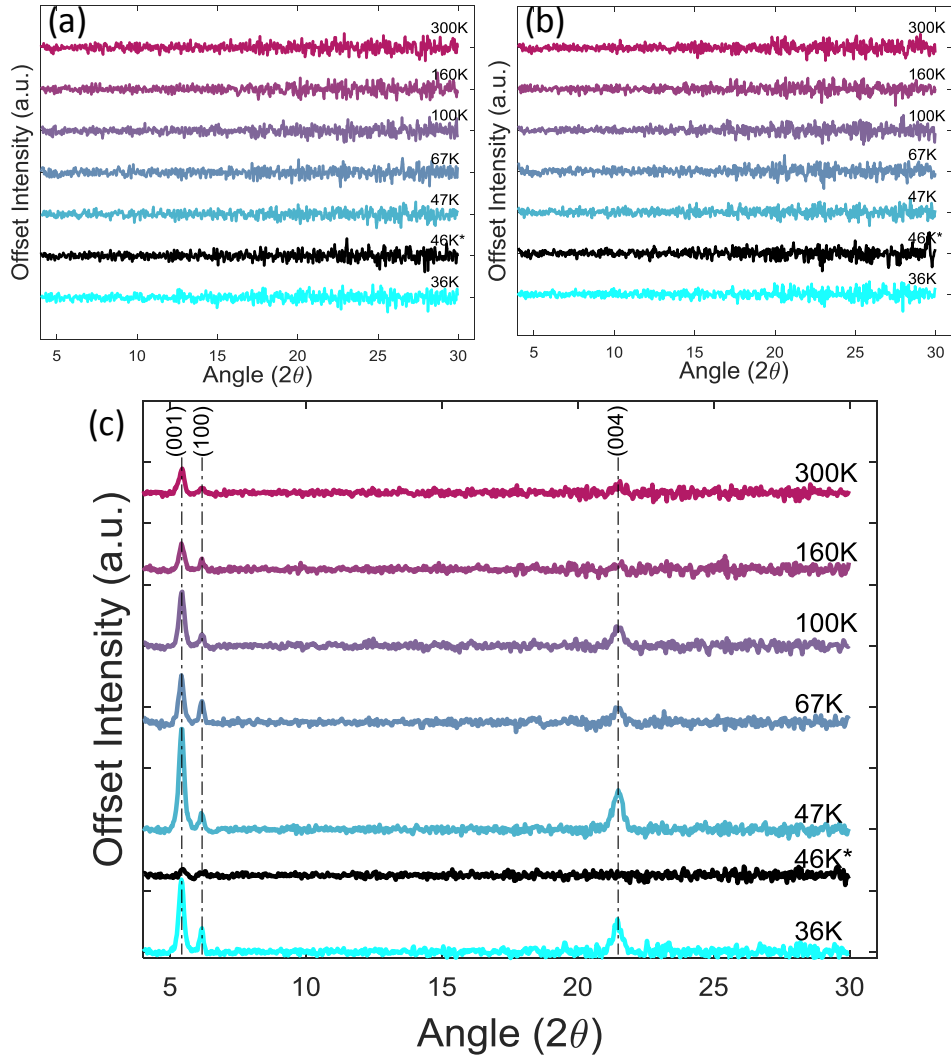


Figure 5.8: XRD diffractograms of (a) as-cast, (b) T_g -annealed and (c) slow-cooled from T_m F8BT films.

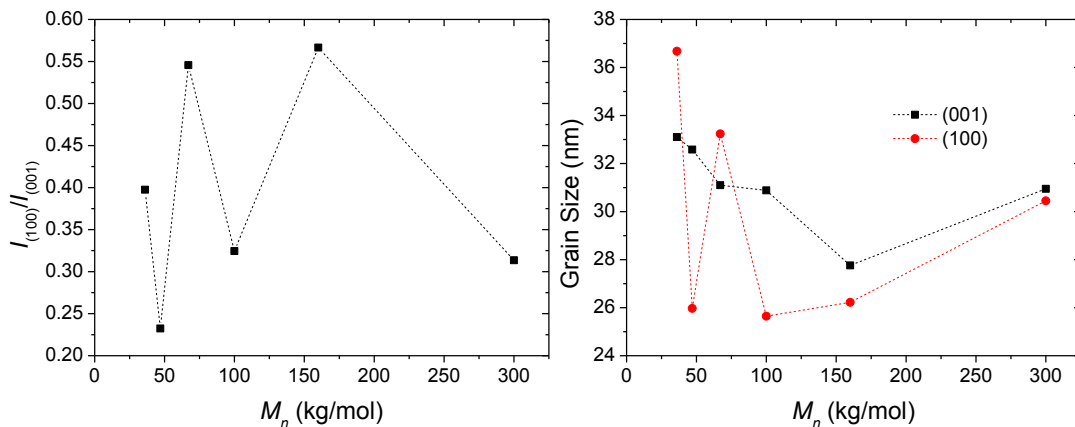


Figure 5.9: For slow-cooled from T_m F8BT films (a) Variation of the (100) peak intensity with respect to the (001) peak. (b) Grain size calculations of the (001) and (100) peaks.

5.3.3. Absorbance and Photoluminescence Spectra

In comparing the absorbance between their 9 and 255K F8BT samples, Donley *et al.* noted only a very small (< 5 nm) bathochromic shift in their as-cast samples^[20]. Upon annealing and slow-cooling from either T_g or T_m the absorption peak λ_{abs} of those films both shifted noticeably towards longer wavelengths with the spectra broadening out as a result. These shifts were more dramatic in the lower MW films. Likewise, there was no significant difference in the absorbance spectra of the as-cast films measured here suggesting a consistent conjugation length across the 35-300K range (figure 5.10). However, thermally processing only induced slight ($\Delta\lambda_{abs} < 5$ nm) peak shifts and in this case towards *shorter* wavelengths. The T_m -annealing process, in particular, resulted in noticeable broadening towards the blue, this being most pronounced in the HMW films. The crude sample (46K*) differs in that it does show a broadening to longer wavelengths instead, but this could be explained by the large presence of HMW chains that were subsequently removed by soxhlet extraction.

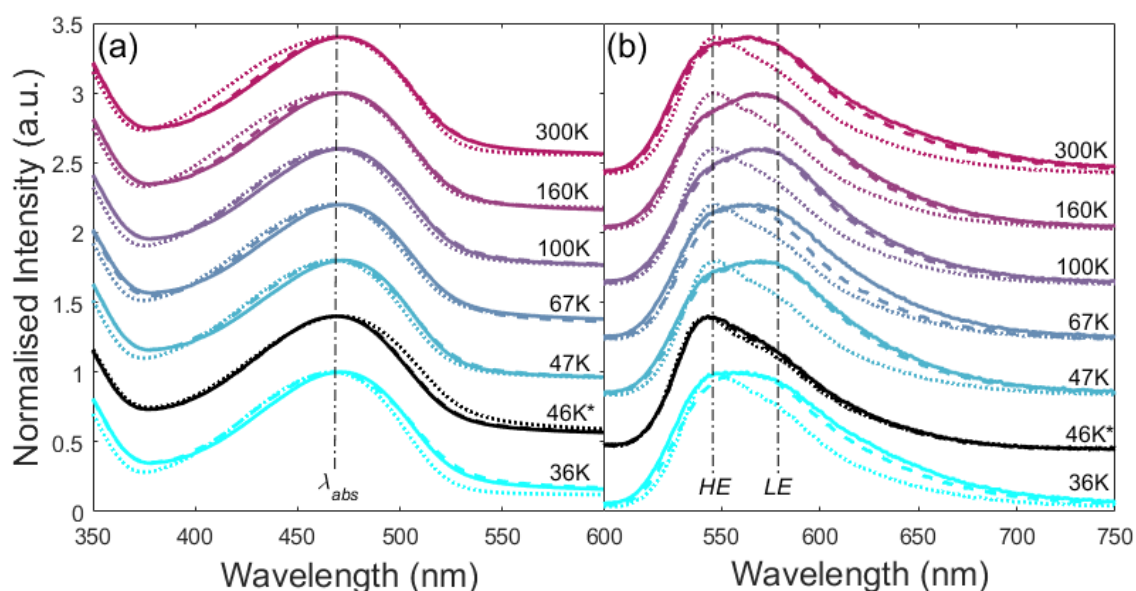


Figure 5.10: (a) Absorbance and (b) PL spectra for the fractionated and crude F8BT samples across different deposition conditions: as-cast (solid lines), T_g -annealed (dashed lines) and slow-cooled from T_m (dotted lines).

The PL spectra of these films (figure 5.10b) do follow closely what has been reported in literature^[20,35]. Two peaks can be identified at ~ 545 and ~ 580 nm, respectively the higher energy (HE) and lower energy (LE) emissive states. The latter becomes more prominent as the MW increases, exhibiting a hypsochromic shift from 580 to ~ 565 nm. Annealing to T_g does not considerably change their PL, but slow-cooling from T_m significantly enhances the HE state emission. The most intense emission comes from the HE state in the crude polymer and this

does not change with annealing. In this case, it appears that the smaller thickness of this film may have heavily influenced the spectra; Yim *et al.* confirm that spin cast thin films (<60 nm) across all MWs of F8BT do show more intense emission from the HE state due to a greater proportion of disordered material at the substrate/polymer interface^[35].

From the cited literature, the following points need to be considered in order to understand the results of figure 5.10^[20,26,35,36]:

- adjacent F8BT chains may align such that the F8 and BT units on separate chains are next to each other (the "aligned structure"). They may also align such that the F8 units are next to BT units (the "alternating structure"^[20]); see Chapter 1, figure 1.16a;
- annealing causes a translation from the aligned to the alternating structure;
- with increasing MW, the chains go from the alternating to the aligned structure,
- the chain orientation of as-cast LMW films have been shown to be more isotropic in nature, and those of HMW more oriented in parallel to the substrate plane,
- LMW film samples exhibit the smallest torsion average angle between the F8 and BT units. Annealing it reduces it further across all MWs with HMW film samples ultimately showing the highest degree of planarisation.

In the alternating structure the strong localisation of electrons on the BT unit^[37] restricts their movements reducing the flow of excitons to lower energy sites^[35]. Films with this structure therefore show higher energy transitions; as the HMW films adopt this structure on annealing, this may explain their hypsochromic broadening evident in the absorbance spectra, (the LMW samples already exhibit this conformation). As BT and F8 units reportedly show a smaller average torsion angle in HMW samples, the alkyl side-chain spacing would need to increase to accommodate them and thus increase the distance for some interchain charge transfer states. In light of the crystallinity results (figure 5.7b), this shift may also be explained in terms of a shortening in the effective conjugation length in these more amorphous HMW films. This may also explain why the LE emissive state shifts to shorter wavelengths in the as-cast films. With the adoption of the alternating structure on annealing, the emission from the HE state is therefore encouraged over that of the LE state. The exact nature of these emissive states remains somewhat unclear in the literature, but they are highly dependent on the complex interplay between the chain conformation and the wider morphology of these films.

The PLQE data for these samples across the different thermal treatments is also consistent with those measured elsewhere, though below the ~75% that is often quoted for F8BT in device papers (figure 5.11). Across all thermal treatments PLQE increases asymptotically with MW as the probability of excitons dissociating due to chain end groups decreases; this is an additional

mechanism alongside the conformational and morphological ones already discussed^[20]. Given a finite exciton diffusion length, this is consistent with PLQE tending to a limiting value as MW increases. Considering the 160K sample as an example, relative to the as-cast films annealing to T_g and then T_m induces a 22.7 and 43.4% increase in PLQE, again, likely due to the reduced migration of excitons to LE and other lower energy/non-radiative emission sites in the alternating F8BT structure. This is unlike the results reported by Donley *et al.* in that annealing to T_m led to a slight reduction in PLQE relative to the efficiencies recorded at T_g . These results imply that - all else being equal - HMW material should give the most efficient devices and that they should improve if the material is annealed. The T_g and T_m PLQEs of the crude F8BT sample are in line with those of the fractionated samples implying that the purification process has not had a significant impact on the radiative efficiency of the polymers. That the as-cast sample shows a higher efficiency of 40.5 ± 3.3 % versus the 33.4 ± 4.1 % shown by the similarly long 47K sample is in line with the more intense HE emission recorded in the PL spectra (figure 5.10b).

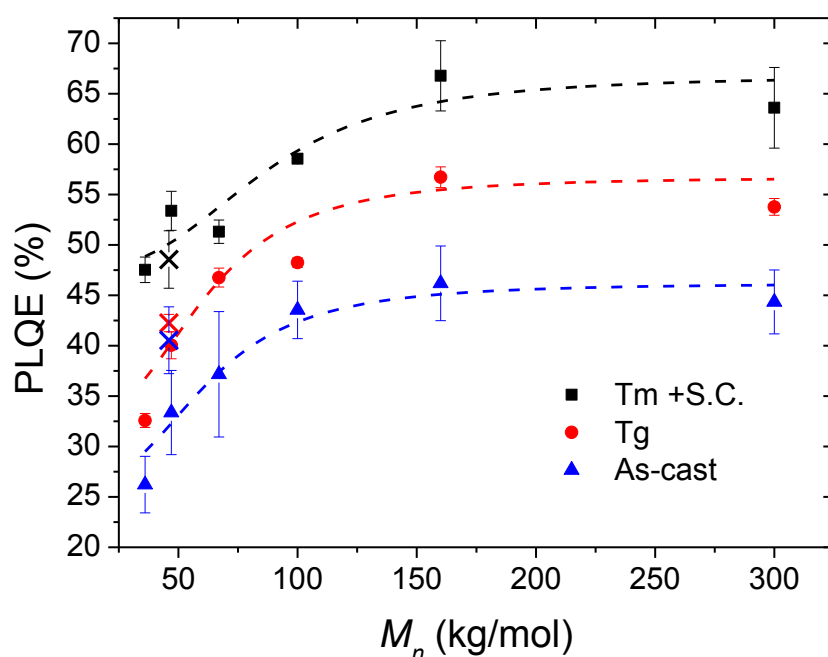


Figure 5.11: PLQE of F8BT as a function of M_n across the different thermal processes employed in this study. The crude polymer PLQE is indicated with an 'x' symbol. The dashed lines are guides for the eyes and reflect only the fractionated F8BT values.

5.4. Device Characterisation

This section presents the results of devices fabricated with each of the F8BT MW fractions. These devices are HyLEDs (both F8BT-only and bilayer) as well as PLEDs in an attempt to generalise these results to other device structures. Included in the batch of bilayer HyLED devices was a substrate fabricated with the remaining crude polymer. All F8BT thicknesses are assumed to be ~ 80 nm thick according to figure 5.4. Appendix D contains the raw data.

5.4.1. HyLEDs

5.4.1.1. F8BT-only HyLEDs

The results of the ITO/ZnO/F8BT/MoO_x/Au devices as a function of F8BT MW and thermal processing are shown in figures 5.12 (as-cast and annealed T_g) and 5.13 (slow-cooled from T_m). As in Chapter 4, parameters were extracted at CE_{max} and averaged across a number of pixels. Compared to the devices of Chapter 4, it was not possible to test a majority of pixels beyond a single run; the data in these figures is therefore for the first testing cycle only. In particular, the T_g 47K devices shorted or burned out at low forward biases and are therefore not represented.

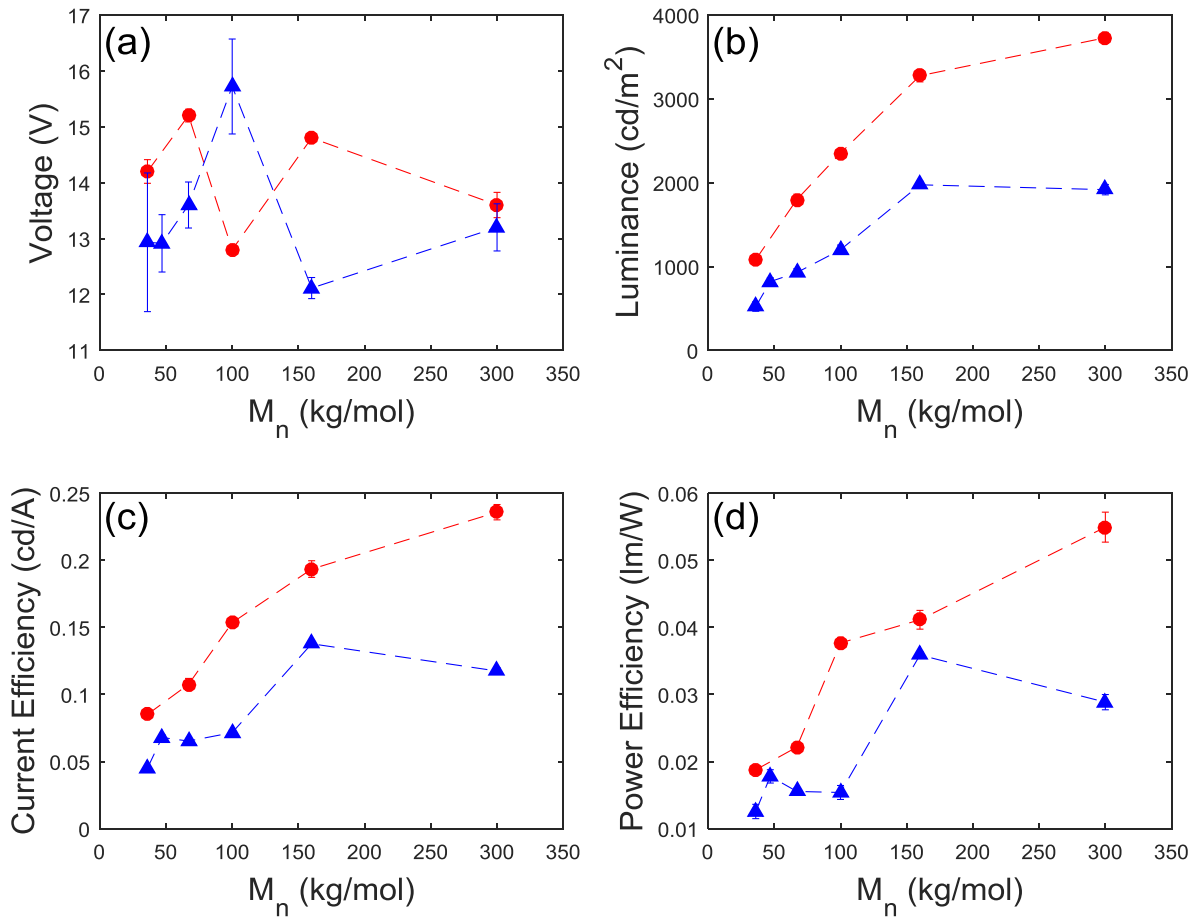


Figure 5.12: Device performance parameters extracted at maximum CE for as-cast (blue triangles) and T_g -annealed (red circles) HyLEDs as a function of F8BT MW. (a) V_{CE} (b) $L_{v,CE}$ (c) max CE itself, and (d) PE_{CE} .

There was no trend observed with respect to V_{CE} , but all other parameters showed general asymptotic increases with MW, unlike the data reported by Martinez-Ferrero *et al.*^[21]. Furthermore this data mirrors the trend observed for PLQE across MWs with an increase to efficiencies and brightness values upon annealing to T_g also observed.

Breaking from this trend are the devices in which the F8BT was slow-cooled from T_m . Despite these films showing the highest PLQE, there is a sharp reduction across efficiencies and brightness values (for clarity, these are shown separately from the other two sets of devices). Importantly, these values show a complete opposite trend in relation to these other device sets, *decreasing* asymptotically with MW. This is likely to be related to the morphological changes induced by the thermal processing as indicated by the XRD and PL measurements. Indeed, Donley *et al.* noted that electron transistor mobility dropped across all films when the same thermal procedure was applied to their substrates. If that is the case, that would significantly worsen the charge balance in a device structure that is already dominated by hole charges. This result has significant consequences within the context of the device results reported in Chapters 3 and 4.

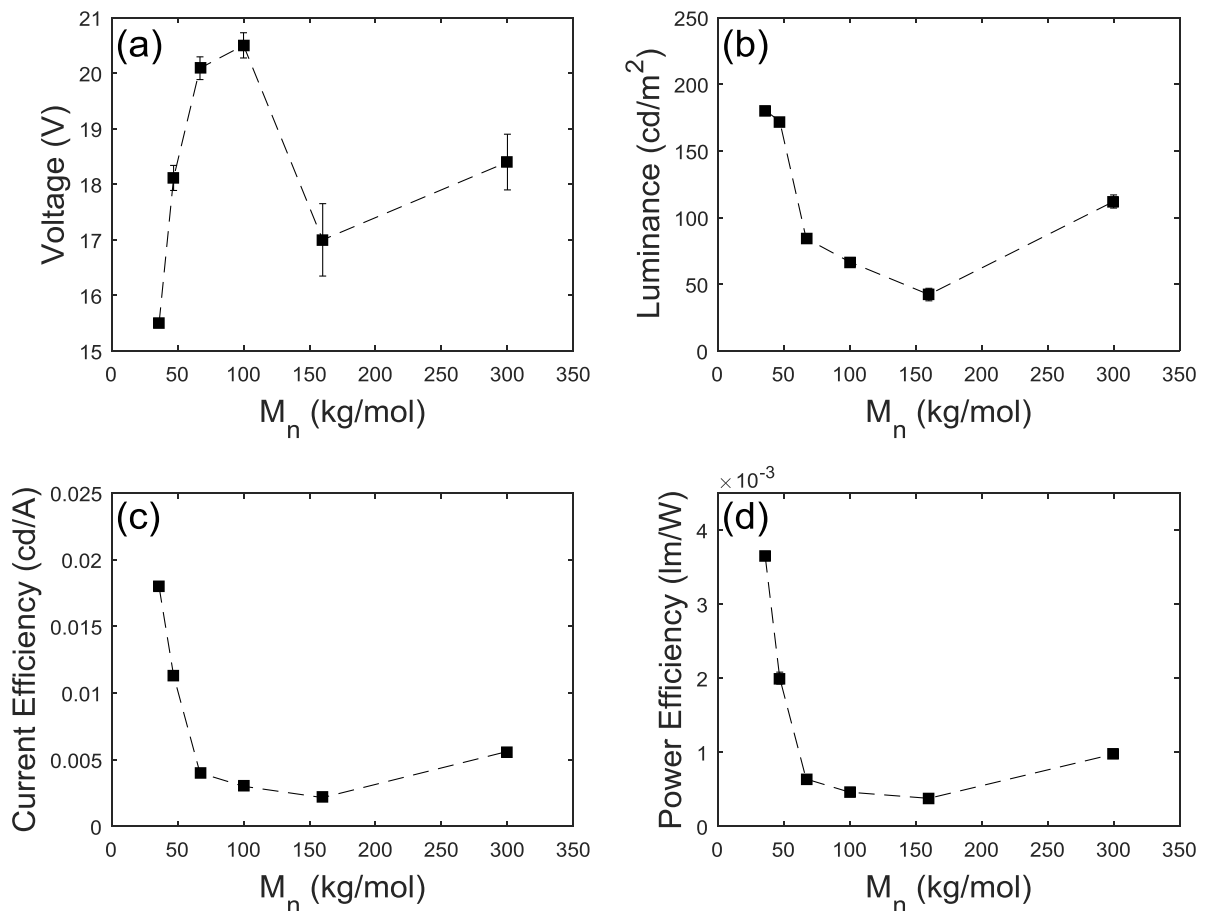


Figure 5.13: Device performance parameters extracted at maximum CE for F8BT slow-cooled from HyLEDs as a function of F8BT MW. (a) V_{CE} , (b) $L_{v,CE}$, (c) max CE itself, and (d) PE_{CE} .

5.4.1.2. Bilayer HyLED

To link the work here to other studies of this thesis, ITO/ZnO/F8BT/TFB/MoO_x/Au substrates, i.e. bilayer devices, were deposited as per the procedure outlined in Chapter 4 using a separate batch of substrates in which the F8BT films were slow-cooled from the melt (figure 5.14). The results of this experiment are very much in line with those of figure 5.13 in that a general decrease in device performance with MW is observed. As hoped, the inclusion of TFB has acted to improve all device parameters with an order of magnitude increase to $L_{v,CE}$ and CE increasing by a factor of 30 across the MW range. Here, the thickness of the crude F8BT film was comparable to that of all other F8BT films and thus it can be stated with confidence that it behaves similarly to other F8BT samples of similar MW. Again, this seems to imply that the purification has not improved the resulting emission properties of the material.

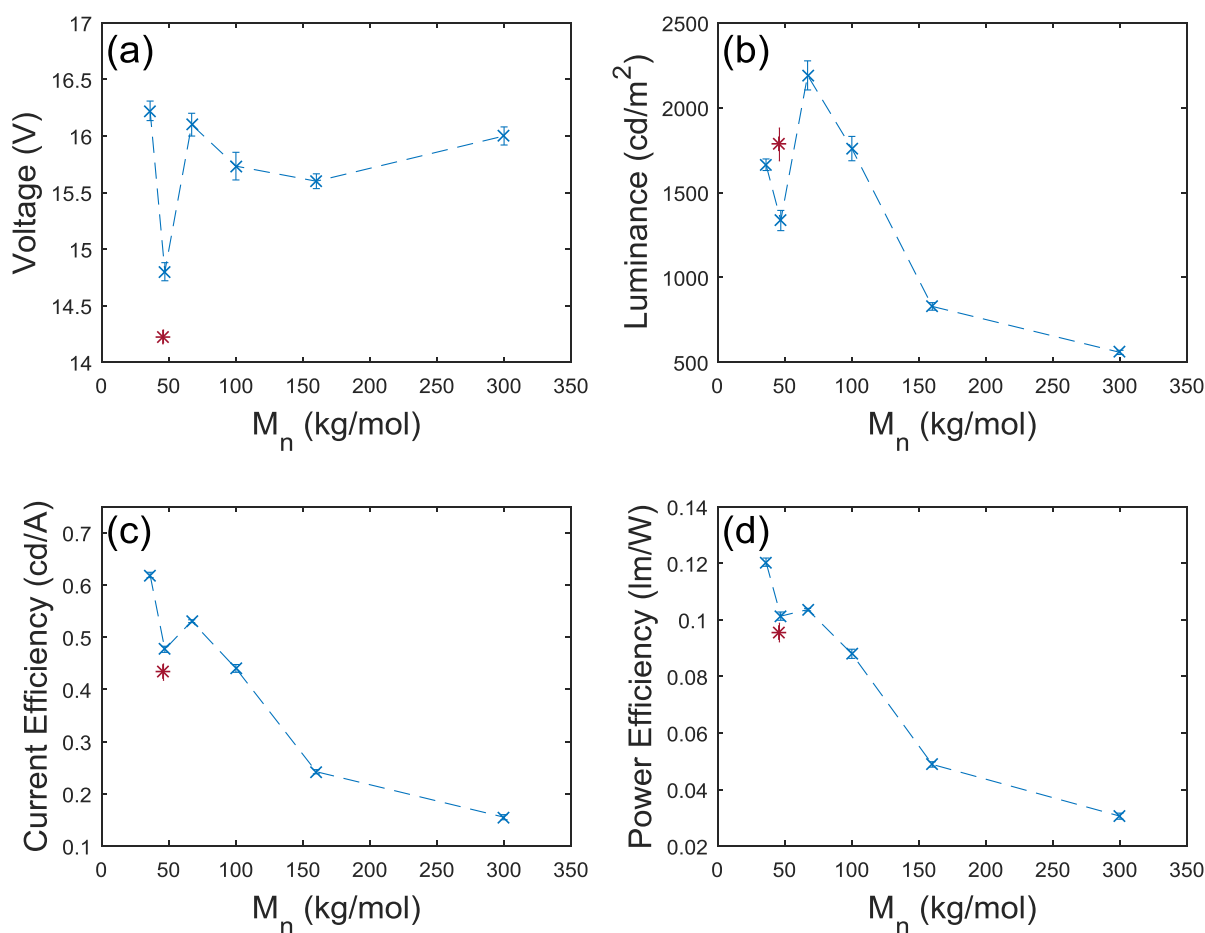


Figure 5.14: Device parameters for bilayer HyLEDs fabricated as a function of F8BT MW. (a) V_{CE} , (b) $L_{v,CE}$, (c) max CE itself, and (d) PE_{CE} . The behaviour of the device fabricated with the crude polymer is represented by the red data point in each plot.

5.4.2. PLEDs

Performance parameters extracted for PLED devices of structure ITO/PEDOT:PSS/F8BT/Ca/Ag are shown in figure 5.15. By this point, all of the 300K batch had been used up, so data is only present for devices of 36-160K F8BT. Due to time constraints, it was only possible to test substrates subjected to the as-cast and T_g -annealed procedures. The 160K $L_{v,CE}$ data point aside these pixels were remarkably consistent in their behaviour as could be seen from the small spread in data throughout. Like the HyLED devices, a considerable improvement in performance is seen upon annealing F8BT to T_g with average maximum PE_{CE} values increasing from 0.54 to 0.86 lm/W and CE_{max} from 1.24 to 1.77 cd/A and exceeding values from identical F8BT PLEDs reported by others^[38,39]. There is a slight difference in MW dependence compared to HyLEDs with values appearing to reach a peak between 67-100K rather than decreasing, although an additional data point beyond 160K would be needed to verify this. Unlike the HyLEDs, MW clearly influences the operating voltage with the 100K sample reaching maximum CE at approximately two-thirds of the voltage required by the 36K sample.

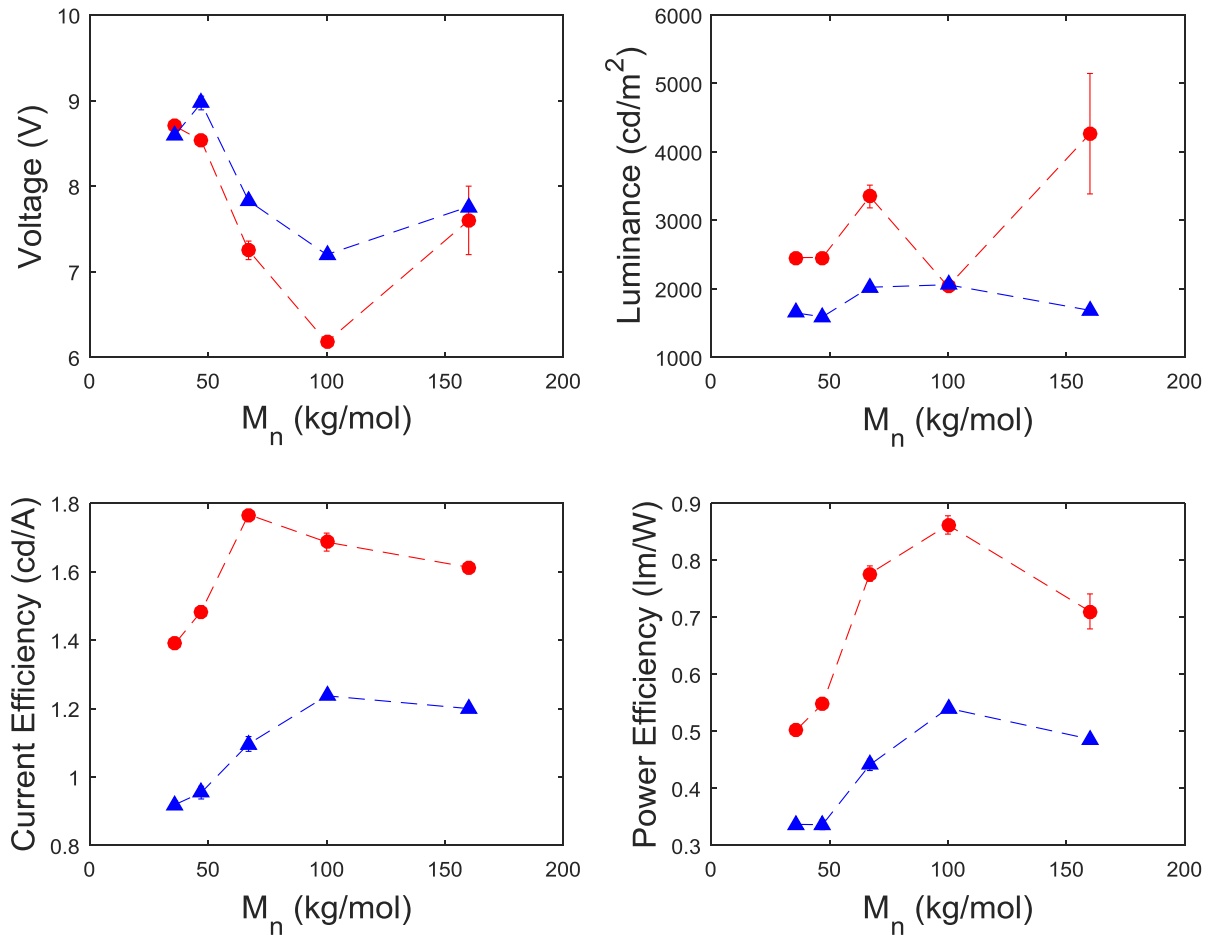


Figure 5.15: (a) V_{CE} , (b) $L_{v,CE}$, (c) max CE itself, and (d) PE_{CE} for a set of standard PLED devices as a function of F8BT MW with films as-cast (blue triangles) or T_g -annealed (red circles).

The results of figure 5.15 reflect the different operating mechanism of these PLEDs versus that of the HyLEDs. With the WF of Ca being closer to the vacuum level than the F8BT LUMO and a ~ 0.6 eV barrier to hole injection existing at the PEDOT:PSS/F8BT interface, F8BT PLEDs are electron dominated devices with the RZ considered close to the anode interface^[39] - a situation that is analogous to that of HyLEDs. The impact on exciton behaviour is likely to be different between the ZnO/F8BT and PEDOT:PSS/F8BT interfaces, however, and a comparison of the J - V s (Appendix D) of these different device types shows that the reverse current of HyLEDs can be up to five orders of magnitude greater indicating ZnO's poor charge blocking properties.

5.4.3. Summary of Device Results

Unlike recently published literature^[21], the device results here show clear trends with F8BT MW, with performance generally improving with chain length. These trends were observed in both HyLED and PLED devices in substrates that were as-cast or annealed to F8BT's T_g . Device performance worsened when substrates were slow-cooled from T_m with efficiencies falling further with increases in MW; this was observed in both F8BT-only and bilayer devices. So far, attempts to explain these observations have been in context of the material characterisation results of section 3. However, it is known that the charge transport properties of F8BT change across both MW and thermal annealing conditions; for instance, it has been shown that electron mobility increases asymptotically with MW, but that it decreases overall on annealing^[20]. The next section analyses single-carrier diodes to gain a further understanding of the results of this section.

5.5. Charge Transport

Here, an attempt to understand the results of section 5.4 is made by analysing the individual hole and electron currents through ITO/PEDOT:PSS/F8BT/MoO_x/Au and ITO/ZnO/F8BT/Ca/Ag diodes, respectively. With the knowledge of how F8BT chains pack, it was viewed that diode geometries would provide a more accurate picture of the charge transport behaviour in PLEDs and HyLEDs than, for instance, transistors. The charge injected from all four interfaces was measured, but the electron current was found to be highly unstable. Consequently, beyond the initial analyses, only the hole transport is subsequently studied. This proceeds with an analysis of the gradients of the J - V curves to confirm the nature of charge injection (SCLC or otherwise) taking place before using the Murgatroyd equation to extract parameters relevant to charge transport. After an undesirable amount of short-circuited HyLED

devices was observed in section 5.4, the thickness of the F8BT layers was increased slightly in an attempt to circumvent this; these values are shown in table 5.3.

Polymer	36K	47K	67K	100K	160K	300K
Thickness, nm	137.4 ± 1.4	137.2 ± 2.2	125.5 ± 3.5	122.4 ± 2.0	120.5 ± 1.7	148.3 ± 2.9

Table 5.3: Average thickness values of each film used in the single-carrier device experiments according to F8BT MW fraction.

5.5.1. Unipolar Current Measurements

To obtain a measure of how the electron and hole currents varied across all 6 fractions under the three different processing conditions, J was measured between forward bias of 0-10 V. For each pixel, the value of J at 10 V was extracted and, where possible, averaged over many pixels across 2 diode substrates to ensure the reliability of the recorded trends. This is the case for hole-only devices (figure 5.16a-b), but electron-only devices (figure 5.16c-d) were considerably more problematic and frequently short-circuited on testing; consequently it was not possible to obtain data across all variables and some of the data was calculated from a limited sample size. In each case, the same set of hole- and electron-only devices were used with only the polarity of the voltage supply reversed to obtain charge transport information through the opposite electrode.

The extracted J values for hole-only devices with the MoO_x/Au biased positively (figure 5.16a) show a very clear trend across both MW and annealing conditions. The latter sees a decrease in J as the annealing temperature increases suggesting that the induced morphological changes impair the transport of holes across the F8BT. However, these trends do appear to be dependent on the charge injecting contact: with the ITO/PEDOT:PSS biased positively, these trends change and the dependence on thermal processing becomes more complex to interpret (figure 5.16b). J increases on annealing to T_g and it does so too when annealed to T_m but this is not true across all fractions due to a shift in dependence on MW. The hole-current is significantly smaller compared to that from MoO_x/Au reflecting the ~ 0.6 eV barrier at the PEDOT:PSS/F8BT interface. Interestingly, the trends seen across figures 5.16a-b are largely observed in the device data of section 5.4, though perhaps not where one would expect. The most obvious case of this is the slow-cooled from T_m hole-current which sees a rapid asymptotic decrease with MW as also observed in the HyLED devices; in the hole-only devices, it is instead observed when current is injected from the ITO/PEDOT:PSS contact and not the MoO_x/Au contact. Furthermore, peak hole-current injected from the MoO_x/Au anode occurs around 100K - this coincides with the peak efficiencies of the PLED devices and not the HyLEDs.

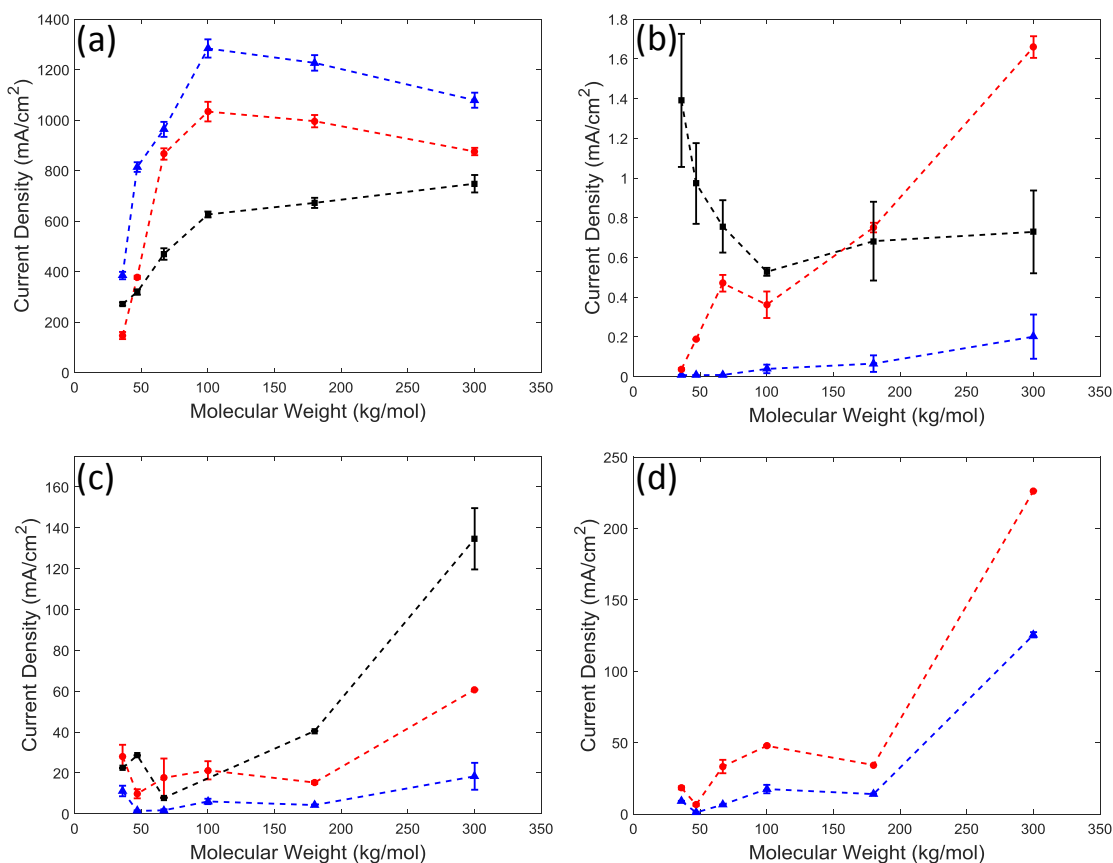


Figure 5.16: J values at 10 V from single charge carrier diodes. (a) and (b) are from hole-only devices with injection from the MoO_x/Au and ITO/PEDOT:PSS contacts, respectively. (c) and (d) are from electron-only devices with injection from ITO/ZnO and Ca/Ag contacts, respectively. Blue triangles, red circles and black squares represent as-cast, T_g -annealed and slow-cooled from T_m , respectively.

The electron-only data shows more consistency between the ITO/ZnO and Ca/Ag electrodes, though it was not possible to obtain data from T_m -annealed devices in the latter case. Even though this data comes from only a limited number of pixels in each case, there does appear to be some consistency, too, in variation between MWs across the different thermal procedures even if the trend is not particularly clear. The low device yield here may imply a poor device batch and at the very least adds a layer of uncertainty over the results of figures 5.16c-d particularly as the increase in J_e with annealing temperature goes counter to the electron transistor mobility values found reported by Donley *et al.*^[20].

It is thought that the preferred mechanism for charge transport in F8BT differs between electrons and holes. Computational studies have shown that the HOMO is delocalised over the backbone of the F8BT monomer so that intrachain hole transport should be a very efficient process with charge hopping between chains acting as a limiting step; intrachain electron transport, however, is an inefficient process due to a 1.55 eV difference in LUMO levels between

the BT and F8 units, but is just as efficient as the electron interchain transfer process^[36,37]. As a greater portion of chain backbones are likely to arrange in a parallel nature to the substrate on annealing this would certainly explain the results across the thermal treatments in figure 5.16a as more interchain hole hopping would be necessary to travel from the top to the bottom electrode. The XRD data also shows that LMW samples have a greater portion of chains oriented this way further confirming that HMW samples should exhibit a higher hole current. The different trends observed between figures 5.16a and b could be a result of interfacial effects, particularly as the bottom PEDOT:PSS/F8BT interface is known to be more disordered than that of the bulk and, by extension, the top F8BT/MoO_x interface as a consequence of the spin coating procedure^[35]. For the final analysis, an effort was made to extract the hole mobility of F8BT as a function of MW, again to complement the electron transistor mobilities reported elsewhere^[20].

5.5.2. Dependence of Charge Transport Parameters on Molecular Weight

5.5.2.1. Determination of Charge Transport Regime

The dependence of J on V is influenced by many factors including whether charge transport is bulk- or injection-limited as well as the presence and nature of trap states in the organic material^[40]. The general bulk-limited dependence (in the case of the perfect injecting ohmic contact) can be written as

$$J \propto \frac{V^{m+1}}{d^{2m+1}} \quad 5.5.6$$

where d is the thickness of the organic layer and m is some constant that defines the dependence^[40]. For example, as was seen in Chapter 1, $m = 1$ would define trap-free SCLC operation, whereas $m = 0$ signifies an ohmic response (as in, for example, a resistor) and $m = 2$ bipolar SCLC transport^[40]. Determining this dependence allows one to gain, for instance, information on the nature of the charge mobility and the presence of any charge traps for the material under investigation. This can simply be done by measuring the gradient G of a $\log J$ - $\log V$ plot, i.e.

$$G = \frac{d(\log J)}{d(\log V)}, \quad 5.5.7$$

where $G = m+1$. Typically, this is accomplished by drawing a tangent by eye over the middle linear region of the plot, but one can also accurately monitor the changes in G at every point by plotting it against $\log V$. This was done for all the currents injected from the four different interfaces shown in figure 5.16, but only that of the hole current injected from the MoO_x/Au contact is shown in figure 5.17; the data for the other three current sets displayed a large degree of uncertainty so will not be used in further analysis.

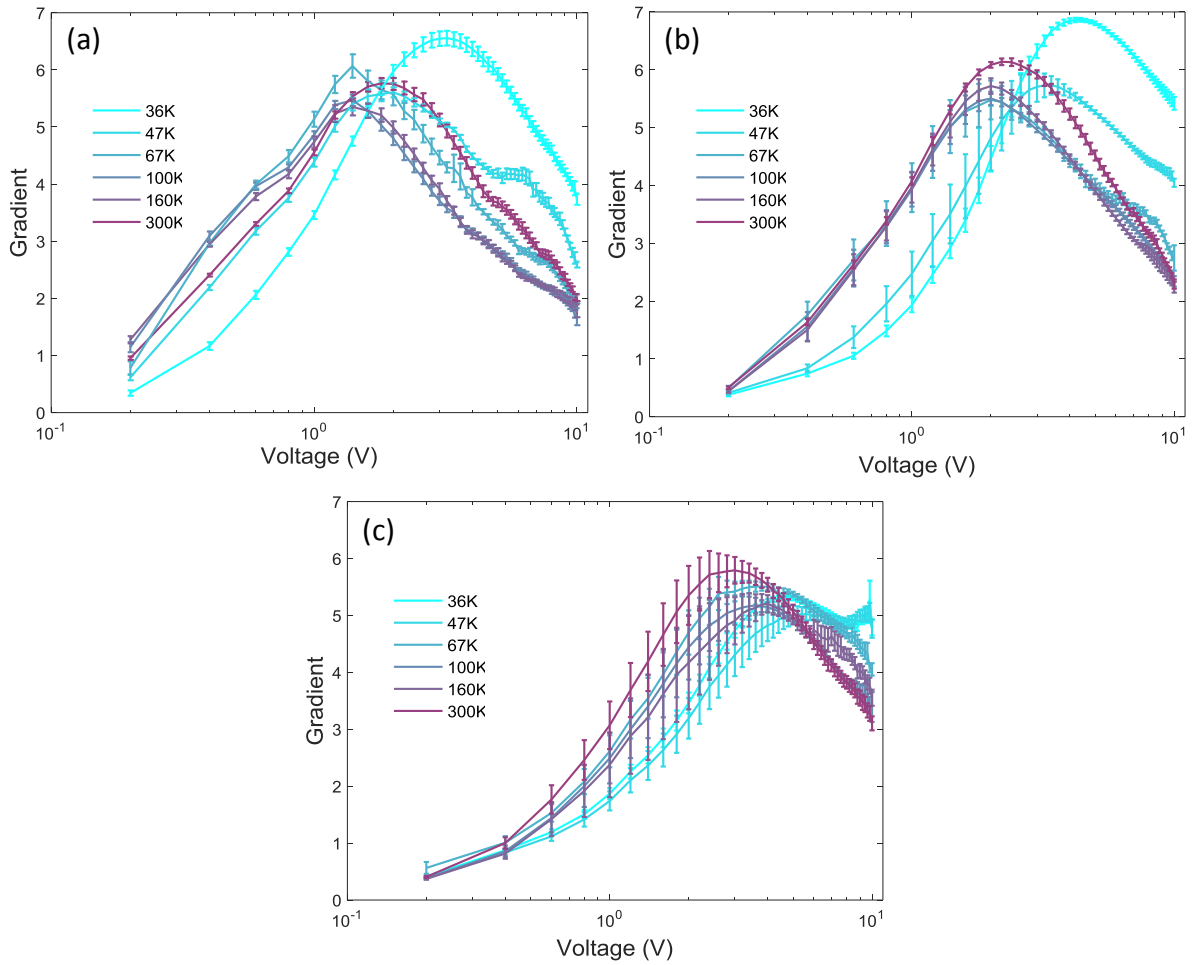


Figure 5.17: Variation of G across the fractionated samples between 0.2-10 V. (a) As-cast, (b) T_g -annealed and (c) slow-cooled from T_m .

It is clear to see from figure 5.17 that the gradients initially exceed that which is expected from a trap-free, SCLC injection contact as predicted by the Mott-Gurney equation. These gradients, however, after peaking at values between 5-7, begin to decrease as the voltage is increased towards 10 V. Should the mobility be field-dependent as predicted by the Murgatroyd equation (Chapter 1, equation 1.18), one would expect the gradient to continue to increase with increasing voltage. The gradient behaviour observed in figure 5.17 therefore implies that the mobility only shows a weak field-dependence, with the sudden current increase at low voltages being likely the result of trap filling. Such traps are due to the presence of highly localised states in the energy gap between the Fermi Level and the free carrier transport states (at the mobility edge or band edge, for disordered and crystalline materials respectively). Injected charges will spend a finite amount of time in these traps before being thermally released to the transport states. As described by Nešpůrek and Sworakowski^[41], as well as Campbell^[40], the E_F within the OSC shifts closer to the transport states at the mobility edge as more charges are injected from

the electrode, i.e. for the case of hole-only injection it will move closer to the positive polaron transport states. This means that the E_F 'scans' the trap states as it moves towards the transport states, the consequence of which is a conversion of shallow trap states to deep trap states that are unable to thermally release their occupied charges (they become permanently filled). Charges injected after this conversion can therefore contribute to the current through the diode as the influence of trap states reduces and the effective charge mobility increases. This manifests as a sudden increase in J at lower V with the shape of the $\log J$ - $\log V$ plot providing a qualitative indication of the nature of the trap states present; for example, a discrete trap level would lead to a sharp J increase over a smaller V range, while a distribution of traps will give a comparatively shallower increase (though with $m \gg 3$) over a longer V range. The decrease in gradient after a fashion represents the crossing of the E_F with the last remaining trap states and a shift towards trap-free SCLC at higher voltages; only above such voltages can it be deduced whether the mobility is then field-dependent or not.

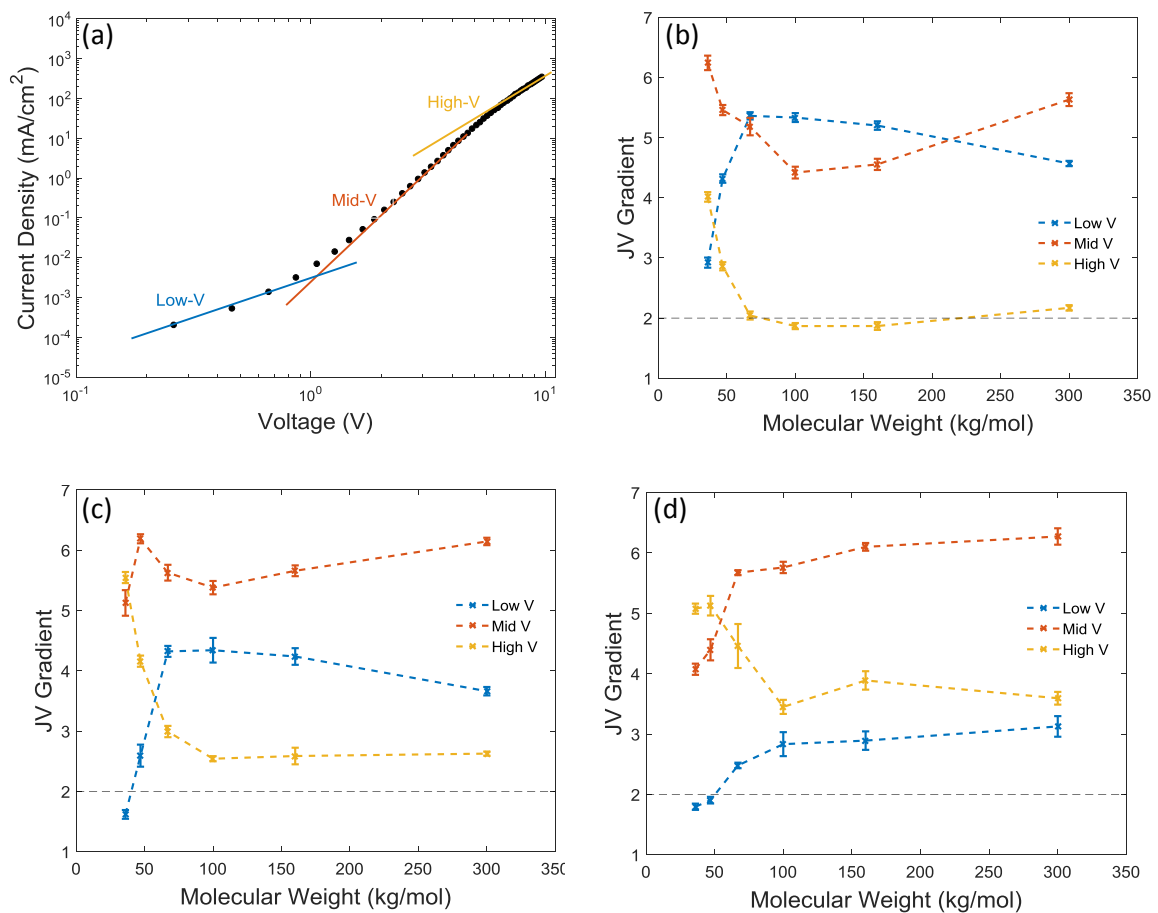


Figure 5.18: (a) The three voltage regions defined for a typical 'S-shaped' $\log J$ - $\log V$ characteristic. (b)-(d) Average low, mid and high- V gradients across all F8BT MW samples for as-cast, T_g and T_m -annealed substrates. The asymptote at the gradient value of 2 indicates the trap-free SCLC as defined by the Mott Gurney equation.

In the as-cast samples (figure 5.17a), the 47-300K samples all behave similarly reflecting a similar nature in their trap states. The 36K sample reaches a steeper gradient at a later voltage reflecting trap states that are shallower in the energy gap and have a steeper distribution in energy, possibly as a result of the more isotropic nature of the material. Annealing shifts all peaks to higher voltages, indicating that the trap distributions become shallower in the energy gap. LMW samples see a drop in peak gradient from 6-7 to ~ 5 suggesting a less-steep trap distribution in contrast to HMW material which shows little change across annealing procedures.

The alternative (though perhaps more common) method of drawing tangents through the linear regions of the $\log J$ - $\log V$ graph confirms the supralinear dependence of J on V . These graphs showed an 'S-shaped' dependence of J on V and hence three voltage regions (low, mid and high) were defined, as shown in Figure 5.18a. In SCLC theory this "S-shaped" dependence is usually related to the presence of a large trap distribution in the energy gap, the low G regions either side of the mid- V high G region being when E_F is below and above the large trap distribution, respectively. Across all measured JV characteristics, the low- V region corresponds to 0.2-1.0 V, the mid- V region to 2-5.0 V, and the high- V region to 9.0-10.0 V. Figures 5.18b-d shows average gradients across all samples at the three voltage regions for, respectively, as-cast, T_g -annealed and T_m -annealed samples. The systematic decrease in gradients in the low- V region confirms the trend in decreased deep trap formation with increasing annealing temperature. This is starkly observed in the high- V region: in the as-cast samples, MWs from 67K onwards switch to the trap-free SCLC regime by 10V as reflected by $G \approx 2$ (figure 5.18b). Upon annealing, it is clear that a higher forward bias than that utilised was required to surpass the (now shallower) trap states as indicated by the now higher G values.

The behaviour observed across figures 5.17 and 5.18 is a reflection of the microstructural changes of F8BT across MW and annealing conditions. LMW samples are more likely to exhibit a more isotropic microstructure that may result in a broader spread of trap states within the energy gap. As hole transport is facilitated along the F8BT backbone, the greater concentration of chain ends in LMW material can further contribute to the overall density of trap states. This might explain the high gradients for the LMW samples observed throughout at the mid and high- V regions - if one assumes that the shallower traps are associated with these microstructural changes. For instance, the low voltage behaviour across MWs seems to mirror the crystallinity data of figure 5.7b with the highest gradient matching the most crystalline MW fraction, 67K. As with the structural nature of P3HT analysed by others, longer chains may act as interconnects between crystalline domains, facilitating hole transport by minimising the extent

of traps associated with grain-boundaries; again, as hole transport is more efficient along the chain backbone, this may explain the smaller gradients of the HMW material at high- V .

Others have extracted charge transport information from F8BT in diode configurations using the Murgatroyd equation, i.e. using the assumption that mobility is field-dependent and changes in G are not due to the presence of traps. Under this model, one can extract the zero-field mobility μ_0 and the field-dependent Poole-Frenkel coefficient β [21,43]. The gradient data presented in figure 5.18, however, does not support such a model (m does not smoothly increase). Whether this is only true for the devices measured here or whether this statement applies also to data presented in the literature is not certain, but F8BT (like P3HT) is a semicrystalline material in which it would be physically reasonable to expect trap distributions to occur. To check this, the assumption of field-dependence is applied to the data here. As the following discussion shows, one can apply the field-dependent model and still obtain reasonable fits to the measured JV data in the high- V region under the assumption that all the traps in the energy gap have been filled, although this may not necessarily be completely valid since we cannot be certain that shallow traps are still not decreasing the free carrier density.

By rearranging the Murgatroyd equation, such that:

$$\ln\left(\frac{J}{V^2}\right) = \ln\left(\frac{9}{8} \frac{\epsilon_r \epsilon_0 \mu_0}{d^3}\right) + \frac{0.89\beta}{\sqrt{d}} \sqrt{V}, \quad 5.5.8$$

one can then extract μ_0 from the intercept C and β from the gradient G when $\ln(J/V^2)$ is plotted against \sqrt{V} , i.e.:

$$\mu_0 = \frac{8d^3}{9\epsilon_r \epsilon_0} e^C \quad 5.5.9$$

$$\beta = \frac{\sqrt{d}}{0.89} G. \quad 5.5.10$$

5.5.2.2. Estimation of Built-In Potential

Since $V = V_{app} - V_{BI}$ in equation 5.8, V_{BI} had to be determined for all samples. Theoretically, at zero bias, photogenerated charges can drift through the organic layer towards the electrodes due to V_{BI} . This current can be compensated for with the application of an externally applied bias^[42]. Therefore, an estimate to the V_{BI} can be made by measuring the $J-V$ characteristic of each device under a calibrated AM1.5 spectrum solar simulator and equating V_{oc} to V_{BI} . Although doing this at room temperature has been found to slightly overestimate V_{BI} due to a greater contribution of thermally injected charge carriers from the contacts^[42], this is still a superior method to calculating V_{BI} theoretically from literature workfunction values as this quantity is

highly sensitive to the chemistry of the material's surface. This latter approach would imply a constant V_{BI} across all samples; the photoconduction measurements show that, in reality, this is certainly not the case (figure 5.19).

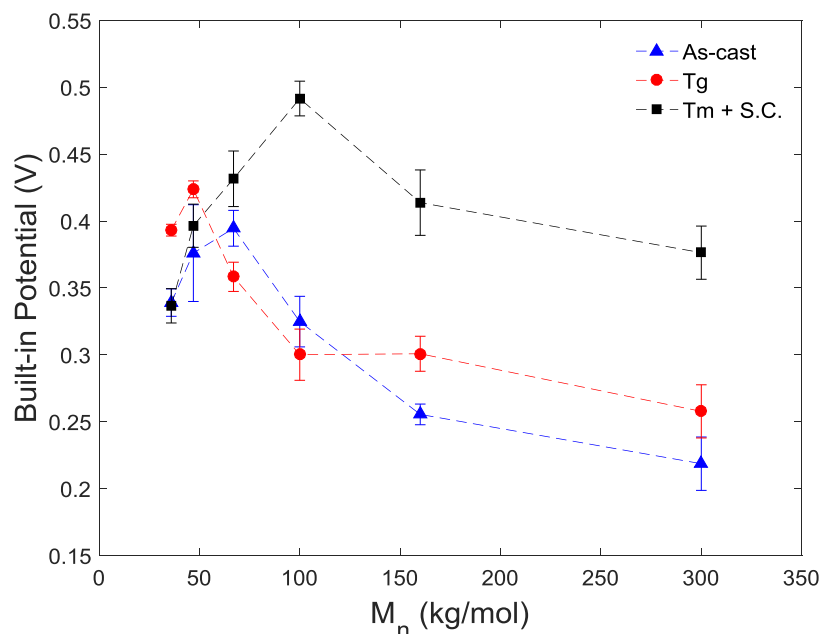


Figure 5.19: Variation of V_{BI} across all F8BT MW fractions at all deposition procedures.

A general increase in V_{BI} is observed with annealing conditions, and is especially true regarding the HMW (>100K) samples. These results may provide further indication as to which chemical groups on the F8BT chain are exposed at the interfaces. As stated earlier, others have reported that LMW films initially exhibit the smallest torsion angle compared to the HMW samples, but it decreases across all MW samples when they are annealed with the HMW films ultimately exhibiting the most planar chains^[26]. Indeed, in the slow-cooled from T_m batch the HMW films show on average greater V_{BI} values becoming comparable to the LMW samples at lower processing temperatures.

These values were included in the fits to equation 5.8 for each measured pixel across all 18 types of devices. They also show that one cannot assume V_{BI} based on literature values of contact workfunctions as the MW and processing of the organic layer has a significant impact on these values.

5.5.2.3. Extraction of hole β and μ_0

An example of applying equation 5.8 to a J - V characteristic is shown in figure 5.20. If one is to assume that the mobility may be field dependent, it is more natural to apply the linear fit to the

high- V region as the effects of field-dependence would not be so significant in the low- V region. This approach is also in good agreement with general SCLC theory, where the trap-free mobility is extracted at voltages above the large G deep trap-filling regime. Then, β and μ_0 were extracted according to equations 5.9 and 5.10 with $\epsilon_r = 3$ and d values given in table 5.3.

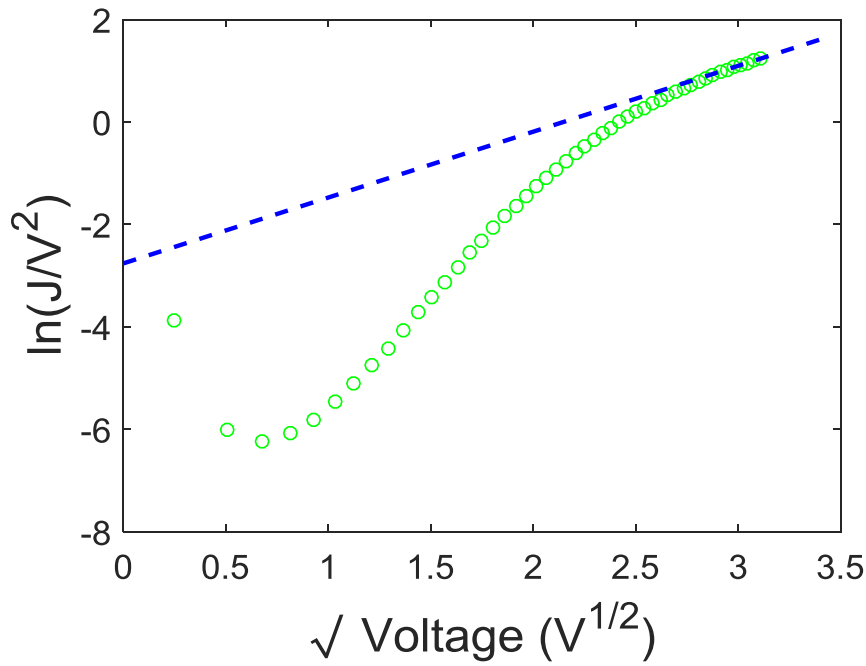


Figure 5.20: An example of applying a fit to the high-voltage linear region of a J - V characteristic processed via equation 5.8.

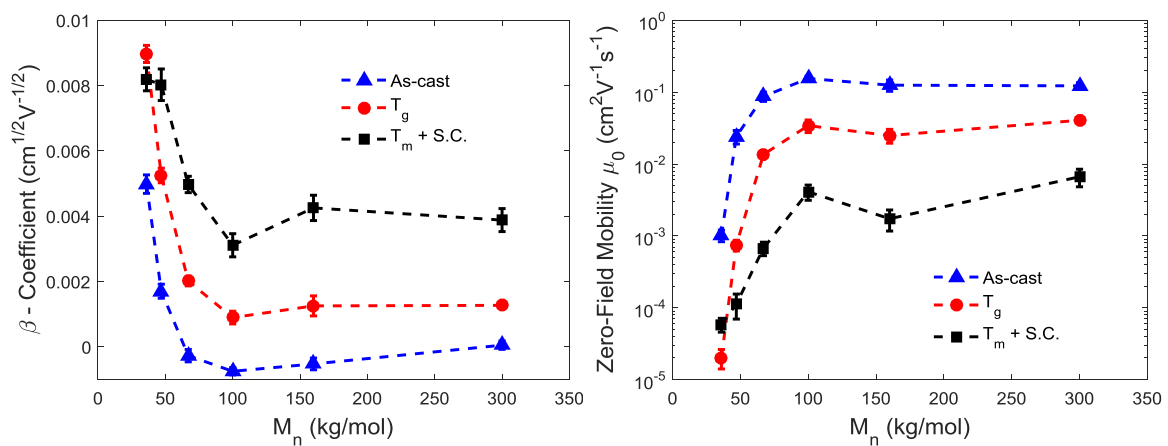


Figure 5.21: (a) Variation of the Poole-Frenkel Coefficient β and (b) the zero-field hole mobility μ_0 as a function of F8BT MW across as-cast, T_g -annealed and slow-cooled from T_m hole-only devices, assuming a field-dependent mobility.

Figure 5.21 shows the average values of β and μ_0 for all MWs across all processing conditions. Previously, Kabra *et al.* had reported values, respectively, of $0.009 \text{ cm}^{1/2} \text{ V}^{-1/2}$ and $0.5\text{-}1.8 \times 10^{-6} \text{ cm}^2 \text{ V}^{-1} \text{ s}^{-1}$ depending on the thickness of their $M_n \sim 97\text{K}$ F8BT^[43]. Martinez-Ferrero *et al.*, similarly recorded values of $0.1\text{-}4.1 \times 10^{-3} \text{ cm}^{1/2} \text{ V}^{-1/2}$ and $0.028\text{-}9.7 \times 10^{-5} \text{ cm}^2 \text{ V}^{-1} \text{ s}^{-1}$ across their MWs albeit with no clear trend with F8BT chain length^[21]. The results presented here, however, do show a clear trend with F8BT chain length with β rapidly decaying with MW, while μ_0 rises and plateaus after 100K. The relationship between MW and μ_0 is largely maintained as processing temperature increases even as μ_0 values drop in a similar fashion to that reported by Donley *et al.* for their transistor mobilities; their data, too, shows that mobilities plateau after $\sim 100\text{K}$ ^[20]. This mobility data very much follows the trends observed in P3HT, but the validity of absolute values is questionable within the context of the Murgatroyd model. Like previous work, it also assumes a perfect injection efficiency equal to 1. The T_g and T_m +S.C. β values are very much in line with those reported elsewhere and, as expected, their dependence on MW mirrors that of the gradient values of figure 5.18. However, it is the gradient information that also shows that it is not completely correct to model the charge transport through F8BT using a field-dependent model as others have done; the clearest confirmation of this is the β values for the as-cast samples which rapidly decay to zero, i.e. *no field dependence*. The resulting μ_0 values are also surprisingly high - four orders of magnitude greater than that reported by either Kabra *et al.* or Martinez-Ferrero *et al.* and higher also than the reported transistor mobilities (see Section 1.9.2.1)^[21,43].

Using the extracted μ_0 and β values, figures 5.22-5.24 compare the field-dependence model against the experimental data for as-cast, T_g and T_m +S.C. samples, respectively. For the most part, the theoretical trap-free current approximates the experimental data reasonably well from $\sim 4 \text{ V}$ onwards, significantly overestimating the current at lower voltages. This deviation considerably reduces upon annealing of the samples and in the case of LMW fractions that have been slow-cooled from the melt, it approximates the current behaviour across the voltage range almost perfectly. One could argue that this could be the result of a more field-dependent character in these thermally processed samples, but as per the discussion for figure 5.17 this is more likely due to the formation of a shallower trap state distribution increasing the dependence of the current density on the voltage at the high- V region. As shown in Appendix E, judicious selection of the voltage region over which to apply the Murgatroyd model simply results in the improvement of the fit over that region to the detriment of all others.

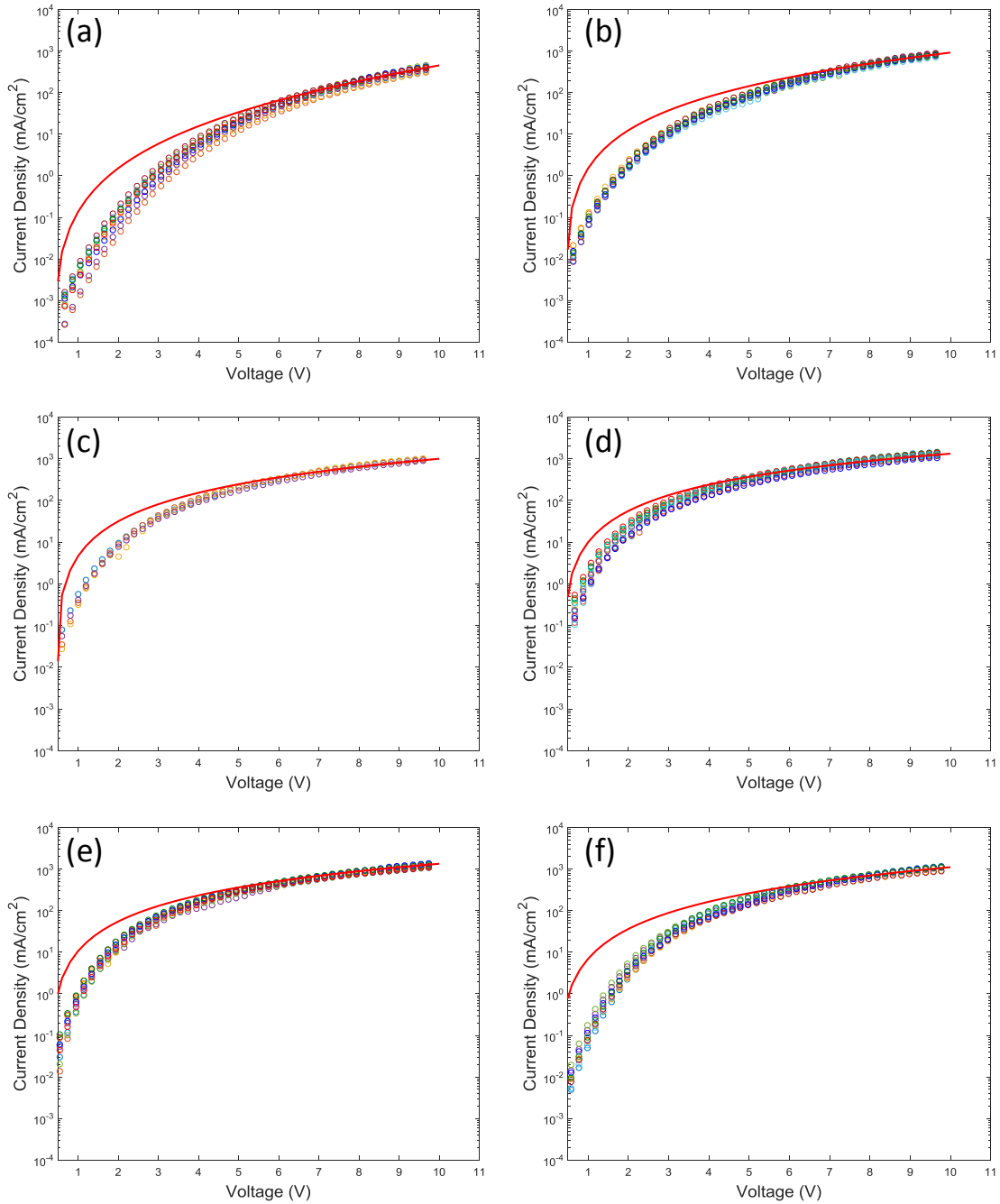


Figure 5.22: Fits of the Murgatroyd equation (solid red line) to the J - V measurements of several pixels (different coloured circles) for the as-cast hole-only diodes where (a)-(f) correspond to the fractions 36-300K respectively.

5.5.3. Summary of Single Carrier Devices

In the analysis of these single carrier devices, several literature studies point to the ohmic characteristics of the F8BT/MoO_x interface, and we have assumed this to be true. Plotting the derivative curve gave a more nuanced look at the dependence of equation 5.6 over the measured voltage range and indicated that transport of charge was occurring in the presence of

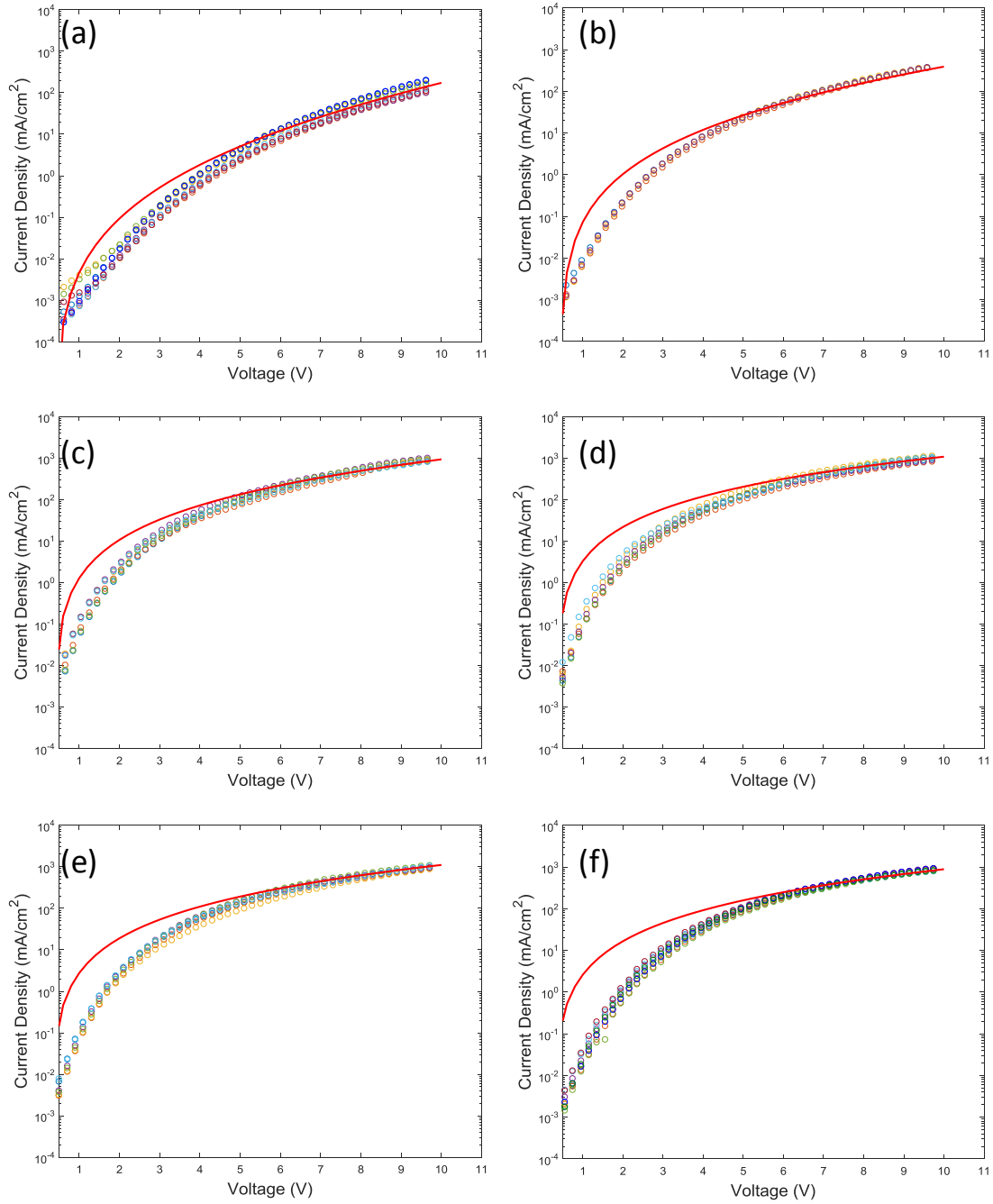


Figure 5.23: Fits of the Murgatroyd equation (solid red line) to the J - V measurements of several pixels (different coloured circles) for the T_g -annealed hole-only diodes where (a)-(f) correspond to the fractions 36-300K respectively.

trap states either present in the bulk or at the interface. This was indicated by a reduced dependence of $\log J$ on $\log V$ at higher voltages suggesting the conversion of shallower traps into deep, filled states as the Fermi level moves towards the transport states. One therefore cannot confidently apply trap-free current injection models to extract transport parameters (mobility, for instance) with any degree of accuracy. Application of either the Mott-Gurney equation or the

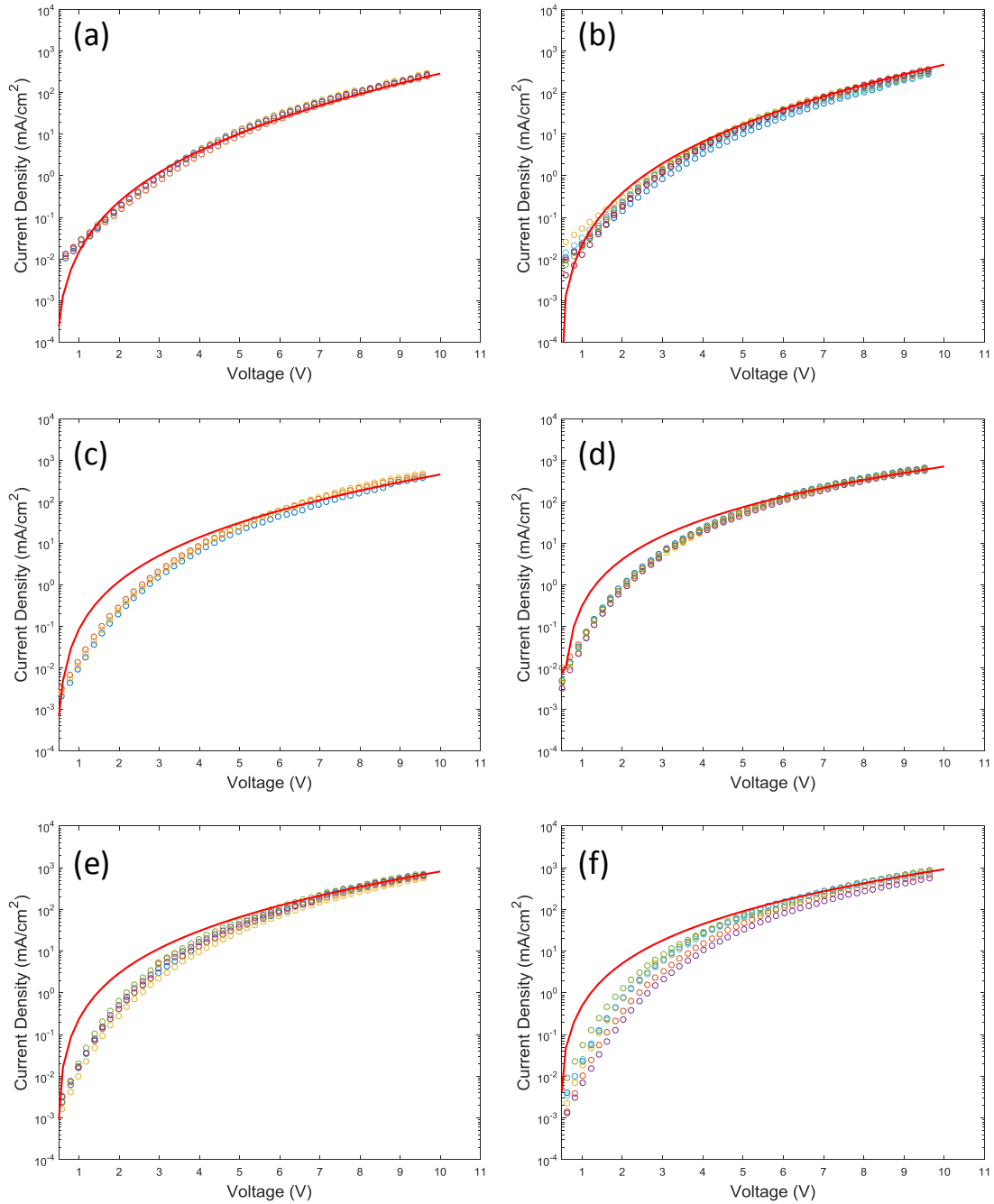


Figure 5.23: Fits of the Murgatroyd equation (solid red line) to the J - V measurements of several pixels (different coloured circles) for the slow-cooled from T_m hole-only diodes where (a)-(f) correspond to the fractions 36-300K respectively.

Murgatroyd (field-dependent) equation must be done with great care as modelling theoretical currents to experimental ones may give the impression of validity where in fact none may exist.

Future work should therefore focus on the application of models which quantify the extent of charge trapping across the MWs and annealing procedures as discussed by Nešpůrek and

Sworakowski^[41]. Qualitatively, however, one can link the trap energy 'landscape' to the microstructural changes seen across all samples. The LMW samples show a great drop in peak $\log I/\log V$ dependence from as-cast to slow-cooled from annealed procedures (~ 6.5 down to below 5, figure 5.17) reflecting a lower concentration of shallower traps that likely have arisen as a result of crystallisation. The XRD results (figure 5.8) show that the HMW samples are not able to achieve the extent of crystallinity on annealing that the LMW samples do, hence figure 5.17 shows little change in $\log I/\log V$ dependence across processing procedures; the trap states here may therefore be related to the extensive semicrystalline character which remains even after annealing.

5.6. Outlook and Conclusion

The MW of F8BT was found to significantly influence the performance of F8BT-only and bilayer HyLEDs as well as standard PLEDs. Generally, HMW fractions lead to significant improvements over LMW devices: for instance, the T_g -annealed HyLEDs showed an increase of 0.085 to 0.236 cd/A (277% increase) with brightness values increasing from 1083 to 3728 cd/m² (344% increase). Furthermore, all parameters increased on annealing the substrates just above T_g compared to the as-cast substrates. For HyLEDs, the data suggests that the ideal MW exceeds the range investigated here, though PLED efficiencies seem to peak at 100K possibly reflecting the different operating mechanisms as well as the build-up of majority charge carriers at different layer interfaces. Improvements were rationalised in terms of XRD, crystallinity, optical and PLQE measurements as well as with comparisons with the results published by others. Hole-only devices generally corroborated the trends observed in the device data through analysis of the hole-currents at particular voltages and its dependence on the applied voltage.

There are uncertainties over some aspects of this work, however. HyLED devices that were slow-cooled from the melt not only performed very poorly, but also showed a worsening trend with increasing MW (figure 5.13); F8BT/TFB-based bilayer devices generally show this (figure 5.14) proving that these results were not just due to a poor batch. This same trend was curiously observed upon analysing the hole current injected from at the PEDOT:PSS/F8BT interface, but *not* at the F8BT/MoO_x (figures 5.16b and 5.16a, respectively). Analysis of the electron-only current would have provided a significant insight, but the majority of those devices shorted and hence the data in figures 5.16c and 5.16d is seen to be unreliable. It should be noted that despite earlier assertions as to the dominance of the electron transport over hole transport in F8BT^[44], more recent results show the polymer to be more ambipolar in nature^[45,46]. For a given injection efficiency, this therefore implies that electron current would

vary similarly to the hole currents in figures 5.16a and 5.16b and that the latter figure could be used to approximate the electron injection from the ZnO/F8BT interface (since it sees a similar barrier to charge injection to the PEDOT:PSS/F8BT interface). Therefore, if the electron injection at the ZnO/F8BT interface follows the trends of the hole injection from the PEDOT:PSS/F8BT interface, this would correspond very well with the HyLED device data across all MW fractions tested under all three thermal procedures seeing as HyLEDs are limited by the electron current. As the standard PLEDs are limited by their hole transport, the peak hole current at 100K would explain the device performances also peaking at this MW. These explanations would of course be modulated by the trend in PLQE values (figure 5.11).

Verification of this hypothesis may be possible with the use of different EIL oxides. Tokmoldin, for example, showed that oxides with deeper CBs than the polymer LUMO were more prone to poor behaviour particularly on annealing with the hypothesis being that the interface becomes more intimate and more efficient at dissociating excitons; oxides with shallower CBs, e.g. Al₂O₃ (-1.7 eV), resulted in improved device efficiencies^[47].

These experiments were hindered by the small amount of polymer available for some of the MW fractions. These devices are therefore not optimised in terms of the polymer thickness. As only a very small amount of the crude polymer was left, it was difficult to fully assess the impact of purifying the F8BT, though PLQE and bilayer HyLED data seems to suggest that the influence is minimal. The impact of dispersity has also not been considered, though the values here are generally smaller than those discussed in Section 5.1.

Nevertheless, the trends reported throughout this chapter show that consideration of a LEP's chain length is as important for PLEDs as those of polymeric solar cell materials for OPVs. The author hopes that these results complement and extend the work that has been published by others regarding the effects of F8BT's MW on property and device performance and that it is beneficial when considering the purchase of commercial batches.

5.7. References

- [1] E. J. Merz, L. E. Nielsen, R. Buchdahl, *Ind. Eng. Chem.* **1951**, *43*, 1396.
- [2] T. G. Fox, P. J. Flory, *J. Appl. Phys.* **1950**, *21*, 581.
- [3] L. H. Sperling, *Introduction to Physical Polymer Science*; John Wiley & Sons, Inc.: Hoboken, NJ, USA, 2005.
- [4] A. a. Virkar, S. Mannsfeld, Z. Bao, N. Stingelin, *Adv. Mater.* **2010**, *22*, 3857.
- [5] M. Rubinstein, R. Colby, *Polymer Physics*; Oxford University Press: Oxford, 2003.
- [6] A. Katsouras, N. Gasparini, C. Koulogiannis, M. Spanos, T. Ameri, C. J. Brabec, C. L. Chochos,

- A. Avgeropoulos, *Macromol. Rapid Commun.* **2015**, *36*, 1778.
- [7] R. J. Kline, M. D. McGehee, E. N. Kadnikova, J. Liu, J. M. J. Fréchet, *Adv. Mater.* **2003**, *15*, 1519.
- [8] R. J. Kline, M. D. McGehee, E. N. Kadnikova, J. Liu, J. M. J. Fréchet, M. F. Toney, *Macromolecules* **2005**, *38*, 3312.
- [9] R. Noriega, J. Rivnay, K. Vandewal, F. P. V. Koch, N. Stingelin, P. Smith, M. F. Toney, A. Salleo, *Nat. Mater.* **2013**, *12*, 1038.
- [10] P. Schilinsky, U. Asawapirom, U. Scherf, M. Biele, C. J. Brabec, *Chem. Mater.* **2005**, *17*, 2175.
- [11] H. Kang, M. A. Uddin, C. Lee, K.-H. Kim, T. L. Nguyen, W. Lee, Y. Li, C. Wang, H. Y. Woo, B. J. Kim, *J. Am. Chem. Soc.* **2015**, 150203154946001.
- [12] L. Lu, T. Zheng, T. Xu, D. Zhao, L. Yu, *Chem. Mater.* **2015**, *27*, 537.
- [13] C. Bruner, R. Dauskardt, *Macromolecules* **2014**, *47*, 1117.
- [14] M. Knaapila, B. P. Lyons, T. P. a. Hase, C. Pearson, M. C. Petty, L. Bouchenoire, P. Thompson, R. Serimaa, M. Torkkeli, a. P. Monkman, *Adv. Funct. Mater.* **2005**, *15*, 1517.
- [15] C. T. Lai, J. L. Hong, *J. Mater. Chem.* **2012**, *22*, 9546.
- [16] K. Koynov, A. Bahtiar, T. Ahn, R. M. Cordeiro, H.-H. Hörhold, C. Bubeck, *Macromolecules* **2006**, *39*, 8692.
- [17] A. Menon, H. Dong, Z. I. Niazimbetova, L. J. Rothberg, M. E. Galvin, *Chem. Mater.* **2002**, *14*, 3668.
- [18] Q. Liu, W. Liu, B. Yao, H. Tian, Z. Xie, Y. Geng, F. Wang, *Macromolecules* **2007**, *40*, 1851.
- [19] K. Hosoi, T. Mori, T. Mizutani, T. Yamamoto, N. Kitamura, *Thin Solid Films* **2003**, *438-439*, 201.
- [20] C. L. Donley, J. Zaumseil, J. W. Andreasen, M. M. Nielsen, H. Sirringhaus, R. H. Friend, J.-S. Kim, *J. Am. Chem. Soc.* **2005**, *127*, 12890.
- [21] E. Martinez-Ferrero, S. Grigorian, J. W. Ryan, W. Cambarau, E. Palomares, *ACS Appl. Mater. Interfaces* **2015**, *7*, 1078.
- [22] M. J. Banach, R. H. Friend, H. Sirringhaus, *Macromolecules* **2003**, *36*, 2838.
- [23] J. Lee, G. Klaerner, R. D. Miller, *Chem. Mater.* **1999**, *11*, 1083.
- [24] Q. Wang, B. Zhang, L. Liu, Y. Chen, Y. Qu, X. Zhang, J. Yang, Z. Xie, Y. Geng, L. Wang, F. Wang, *J. Phys. Chem. C* **2012**, *116*, 21727.
- [25] H. K. H. Lee, Z. Li, I. Constantinou, F. So, S. W. Tsang, S. K. So, *Adv. Energy Mater.* **2014**, *4*.
- [26] J. M. Winfield, C. L. Donley, R. H. Friend, J.-S. Kim, *J. Appl. Phys.* **2010**, *107*, 024902.
- [27] H. Tanaka, H. Kajii, Y. Ohmori, *Synth. Met.* **2015**, *203*, 10.
- [28] A. P. Gray, *Thermochim. Acta* **1970**, *1*, 563.
- [29] R. Remy, E. D. Weiss, N. A. Nguyen, S. Wei, L. M. Campos, T. Kowalewski, M. E. Mackay, *J.*

- Polym. Sci. Part B Polym. Phys.* **2014**, *52*, 1469.
- [30] M. Dole, W. P. Hettinger, N. R. Larson, J. A. Wethington, *J. Chem. Phys.* **1952**, *20*, 781.
- [31] G. C. Faria, E. R. DeAzevedo, H. von Seggern, *Macromolecules* **2013**, *46*, 7865.
- [32] H. H. Ahn, S. H. Jang, B. Hwang, J. Yoon, S. Y. Kim, S. J. Noh, J. Y. Han, Y. K. Kwon, *Polymer (Guildf)*. **2013**, *54*, 4864.
- [33] P. Papadopoulos, G. Floudas, C. Chi, G. Wegner, *J. Chem. Phys.* **2004**, *120*, 2368.
- [34] J. Balko, R. H. Lohwasser, M. Sommer, M. Thelakkat, T. Thurn-Albrecht, *Macromolecules* **2013**, *46*, 9642.
- [35] K.-H. Yim, R. Friend, J.-S. Kim, *J. Chem. Phys.* **2006**, *124*, 184706.
- [36] A. Van Vooren, J.-S. Kim, J. Cornil, *ChemPhysChem* **2008**, *9*, 989.
- [37] J. Cornil, I. Gueli, a. Dkhissi, J. C. Sancho-Garcia, E. Hennebicq, J. P. Calbert, V. Lemaure, D. Beljonne, J. L. Brédas, *J. Chem. Phys.* **2003**, *118*, 6615.
- [38] J.-S. Kim, R. H. Friend, I. Grizzi, J. H. Burroughes, *Appl. Phys. Lett.* **2005**, *87*, 023506.
- [39] J. Bailey, E. N. Wright, X. Wang, A. B. Walker, D. D. C. Bradley, J.-S. Kim, *J. Appl. Phys.* **2014**, *115*, 204508.
- [40] A. J. Campbell, In *Functional Organic and Polymeric Materials*; Richardson, T. H., Ed.; John Wiley & Sons, Inc.: Chichester, 2000; pp. 201–232.
- [41] S. Nešpůrek, J. Sworakowski, *Phys. Status Solidi* **1978**, *49*, K149.
- [42] G. G. Malliaras, J. R. Salem, P. J. Brock, J. C. Scott, *J. Appl. Phys.* **1998**, *84*, 1583.
- [43] D. Kabra, L. P. Lu, M. H. Song, H. J. Snaith, R. H. Friend, *Adv. Mater.* **2010**, *22*, 3194.
- [44] A. J. Campbell, D. D. C. Bradley, H. Antoniadis, *Appl. Phys. Lett.* **2001**, *79*, 2133.
- [45] Y. Kim, S. Cook, S. a. Choulis, J. Nelson, J. R. Durrant, D. D. C. Bradley, *Chem. Mater.* **2004**, *16*, 4812.
- [46] J. Zaumseil, C. L. Donley, J. S. Kim, R. H. Friend, H. Sirringhaus, *Adv. Mater.* **2006**, *18*, 2708.
- [47] N. Tokmoldin, Fabrication and characterization of hybrid metal-oxide/polymer light-emitting diodes, Imperial College Imperial, 2010.

Chapter 6 – General Conclusions and Future Work

It is now a decade since Morii *et al.* first demonstrated the potential of inserting conducting metal oxide layers in otherwise all organic OLEDs with the aim of increasing the stability and lifetime of these devices^[1]. Throughout the development of HyLEDs, efforts were made to demonstrate their viability to compete with more established OLED devices through increases to efficiencies, luminance values and, recently, lifetimes. This was accomplished through the use of different oxides, interlayers and OSCs^[2]. The aim of this thesis was to further explore how the properties of the individual polymer and oxide layers influenced overall diode performance.

The presence of ZnO as a standard EIL was exploited to make use of one of the oxide's most distinguishing properties: the ability of it to form vertical NRAs using simple solution-based methods^[3]. Chapter 3 discussed the methods used to deposit HyLEDs with a ZnO NRA EIL demonstrating, for the first time, luminance and efficiency values for vertical NRA devices. With luminance values of 8600 cd/m² and a max efficiency of 1.66 cd/A, these values further showed the potential of such devices for display applications^[4]. Electron-only devices show that the array acts to improve the injection of electrons into the F8BT layer.

As shown by the literature on ZnO NRA OPVs, these devices are complex and influenced by variables relating from the physical dimensions of the nanorods themselves, to the processing conditions of the organic material. Efforts were made to test the impact of nanorod length on device performance, but the large spread in data makes it clear that the next immediate step should be to improve the stability of these devices. Thick, homogenous polymer layers are difficult to achieve from the spin-coating of more viscous solutions and the exposure of nanorods through the polymer layer was identified as a likely - and major - cause of device instability. Improving the stability may then initially involve reducing the nanorod length so as to cast thinner - and more homogeneous - polymer layers. Though it is desirable for devices in this field to be deposited via solution-processing, at this stage of development it would be worth infilling the array with evaporated small molecules - Alq₃, for instance - due to the greater control of deposition variables and insensitivity to, for example, surface wetting effects. Following the realisation of stable devices, further work would diverge along three paths. One would showcase the compatibility of ZnO NRAs with current interlayers, LEPs, and so on. This would allow for the demonstration of NR HyLEDs emitting across the entire visible spectrum, including white light emission with phosphorescent molecules, and further modification of the charge balance by coating the array with, for example, Cs₂CO₃ or Ba(OH)₂ as demonstrated in

planar HyLED literature^[5,6]. The second route would involve fundamental research into the exact role of the NRA in these devices, for instance, how and why changes to the array morphology influence the electron current density J_e and by how much these changes are due to changes in the surface area and/or due to changes in the built-in electric field (see Section 3.5.1.). As nanostructured layers are more frequently used to improve outcoupling in OLEDs rather than enhance the charge balance^[7], investigations of how the NRA facilitates the extraction of photons would constitute the third research path; a layer which can improve charge injection, whilst also aiding the outcoupling of photons would be highly attractive.

The preparation of a F8BT/TFB bilayer for inverted HyLEDs was discussed in Chapter 4 as was the effect on the EL due to changing the TFB thickness. While the impetus for this work originated from the NR HyLED investigation, the EL shifts were the first of their kind to be reported for HyLEDs and has since informed the work of others^[8,9]. The inclusion of a TFB layer lead to dramatic increases in efficiency values and across all the investigations reported in this thesis, HyLED devices with the F8BT/TFB bilayer were consistently the most efficient and stable.

Using contact angle and AFM measurements, it was clear that the procedure induced changes to the F8BT surface that would make the adherence of the TFB layer more favourable. However, it was not possible to identify using just these techniques the specific nature of these changes. Chapter 4 discussed the possibility of different surface groups being exposed during the procedure; these could be potentially identified using photoelectron spectroscopy techniques. Here, a sample surface is illuminated by high energy photons causing the emission of core electrons from atoms present at the surface; the energies of these electrons are specific to the chemical environment and hence would provide an indication of the groups present. The identification of these groups (if they are indeed responsible for the improved wetting of the TFB layer) would help to inform future multilayer device depositions.

Finally, in Chapter 5, The MW of F8BT was seen to strongly effect the performance of both HyLED and standard PLED devices with HMW batches being favourable to high efficiency, high luminance performance. Though it is generally assumed that higher MW polymers will lead to better device performance, the literature in support of this is generally sparse beyond a few studies on light-emitting oligomers. This particular investigation attempted to address this whilst extending the previous work by others on the properties of F8BT as a function of MW^[10-12]. The reasons for the improvements were explained in terms of the chain packing, leading to better PL efficiency and improved hole transport. However, F8BT layers which were slow-cooled from the melt lead to devices with worsening performance as MW increased. This was

likely to be due to a worsening of the hole transport due to a greater proportion of chains aligning parallel to the substrate. It is thought that such changes to the hole charge transport would be mirrored by the electron transport, but it was not possible to obtain reliable data from electron-only devices.

Though the study was somewhat hampered by the small amounts of material available, the results pertaining to device performance should be clear enough to inform future device work in pursuit of maximising light output and efficiencies. It would be important, too, to quantify the distribution of the trap states present and further relate this to the microstructural changes across the MWs and annealing conditions. Measuring the current density at higher voltage ranges would also enable the Murgatroyd equation (or, indeed, the Mott-Gurney equation) to be applied with more confidence as the gradient dependence was seen to tend to trap-free behaviour above 10 V.

Many of the explanations given in Chapter 5 are quite specific to F8BT; for instance, while hypsochromic shifts are typically observed in optical measurements when a polymer is annealed, F8BT shows the opposite case. As has been done for polymers in OPV literature, it is therefore important to conduct a similar study to other common LEPs, such as PPV, PFO and MEH-PPV beyond oligomer chain lengths to test the generality of the results reported in Chapter 5 and elsewhere.

In general, the studies carried out throughout this thesis show that HyLEDs are an ideal system for which to conduct fundamental research on the two material classes - metal oxides and OSCs - that constitute a typical device stack and their combined effects on device performance. Conductive metal oxides can be doped, can demonstrate a range of controllable stoichiometries and can form stable nanostructures - these properties are only beginning to be investigated within HyLEDs^[13-16]. With recent demonstrations of HyLEDs now matching the efficiencies of standard OLED devices whilst also demonstrating superior resistance to black-spot formation (Chapter 1, Section 1.8), the field should capitalise on this momentum and move on to the next step: the demonstration of larger-area, minimally-encapsulated HyLED lighting panels.

6.1. References

- [1] K. Morii, M. Ishida, T. Takashima, T. Shimoda, Q. Wang, M. K. Nazeeruddin, M. Grätzel, *Appl. Phys. Lett.* **2006**, *89*, 183510.
- [2] M. Sessolo, H. J. Bolink, *Adv. Mater.* **2011**, *23*, 1829.
- [3] L. Vayssieres, *Adv. Mater.* **2003**, *15*, 464.
- [4] J. C. D. Faria, A. J. Campbell, M. A. McLachlan, *Adv. Funct. Mater.* **2015**, *25*, 4657.

- [5] L. P. Lu, D. Kabra, R. H. Friend, *Adv. Funct. Mater.* **2012**, *22*, 4165.
- [6] H. J. Bolink, E. Coronado, J. Orozco, M. Sessolo, *Adv. Mater.* **2009**, *21*, 79.
- [7] M. Gerken, In *Organic light-emitting diodes (OLEDs): Materials, devices and applications*; Buckley, A., Ed.; Woodhead Publishing: Cambridge, 2013; pp. 235–261.
- [8] J. C. D. Faria, A. J. Campbell, M. A. McLachlan, *J. Mater. Chem. C* **2015**, *3*, 4945.
- [9] J. Xu, L. Yu, L. Hu, R. He, W. Yang, J. Peng, Y. Cao, *J. Mater. Chem. C* **2015**, *3*, 9819.
- [10] E. Martínez-Ferrero, S. Grigorian, J. W. Ryan, W. Cambarau, E. Palomares, *ACS Appl. Mater. Interfaces* **2015**, *7*, 1078.
- [11] C. L. Donley, J. Zaumseil, J. W. Andreasen, M. M. Nielsen, H. Sirringhaus, R. H. Friend, J.-S. Kim, *J. Am. Chem. Soc.* **2005**, *127*, 12890.
- [12] M. J. Banach, R. H. Friend, H. Sirringhaus, *Macromolecules* **2003**, *36*, 2838.
- [13] R. L. Z. Hoye, K. P. Musselman, M. R. Chua, A. Sadhanala, R. D. Raniaga, J. L. MacManus-Driscoll, R. H. Friend, D. Credgington, *J. Mater. Chem. C* **2015**, *3*, 9327.
- [14] M. Vasilopoulou, L. C. Palilis, D. G. Georgiadou, P. Argitis, S. Kennou, L. Sygellou, I. Kostis, G. Papadimitropoulos, N. Konofaos, A. a. Iliadis, D. Davazoglou, *Appl. Phys. Lett.* **2011**, *98*, 123301.
- [15] M. Vasilopoulou, G. Papadimitropoulos, L. C. Palilis, D. G. Georgiadou, P. Argitis, S. Kennou, I. Kostis, N. Vourdas, N. a. Stathopoulos, D. Davazoglou, *Org. Electron.* **2012**, *13*, 796.
- [16] E. Martínez-Ferrero, A. Forneli, C. Boissière, D. Grosso, C. Sanchez, E. Palomares, *Appl. Mater. Interfaces* **2011**, *3*, 3248.

Appendix A

For the convenience of the reader, the relevant ZnO seed layer and nanorod characterisation carried out as part of the Masters project prior to the commencement of the current PhD work is included in this appendix. This information is particularly relevant to Chapter 3.

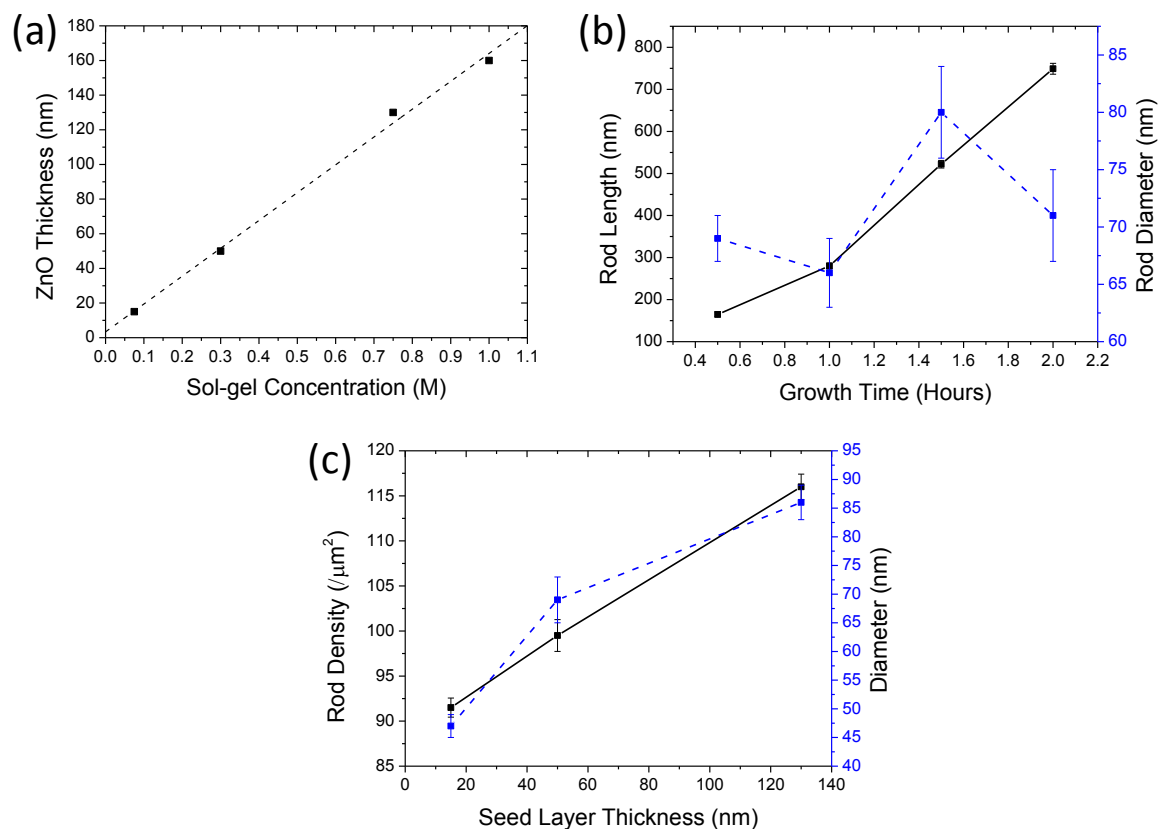


Figure A.1: (a) Variation of ZnO seed layer thickness as a function of sol-gel concentration. (b) Variation of nanorod length and diameter as a function of hydrothermal growth time. (c) Variation of nanorod density and diameter as a function of seed layer thickness at 2 hours of growth time. Black solid line corresponds to the left graph axis, whilst the blue-dashed line corresponds to the right graph axes. The data from graphs (b) and (c) were extracted from SEM images.

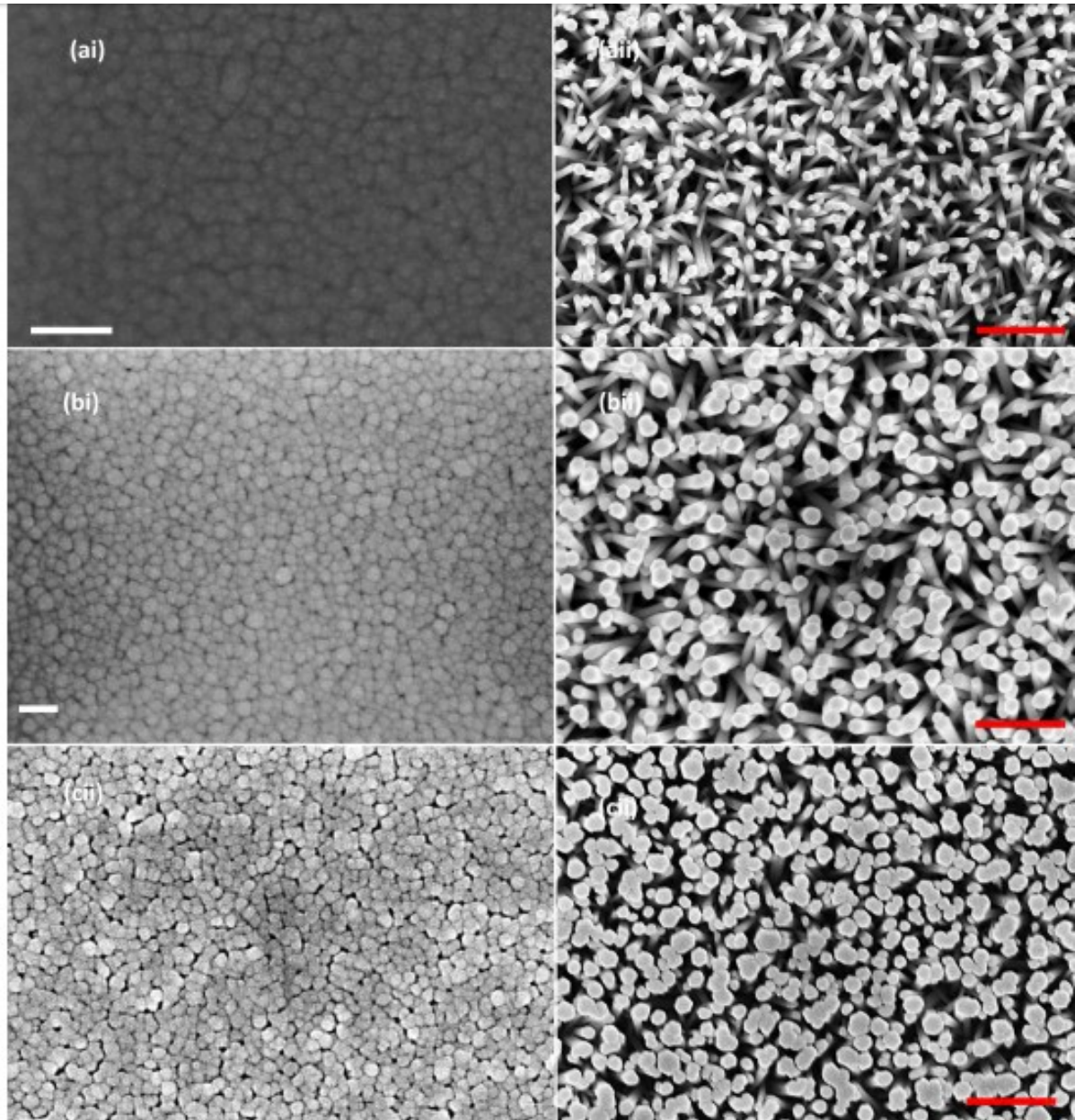


Figure A.2: SEMs showing the influence of the seed layer morphology as a function of thickness (left hand side) on the nanorod array morphology (right hand side). The seed layer thicknesses are (a) 15, (b) 50 and (c) 130 nm. White scale bars = 100 nm. Red scale bars = 500 nm.

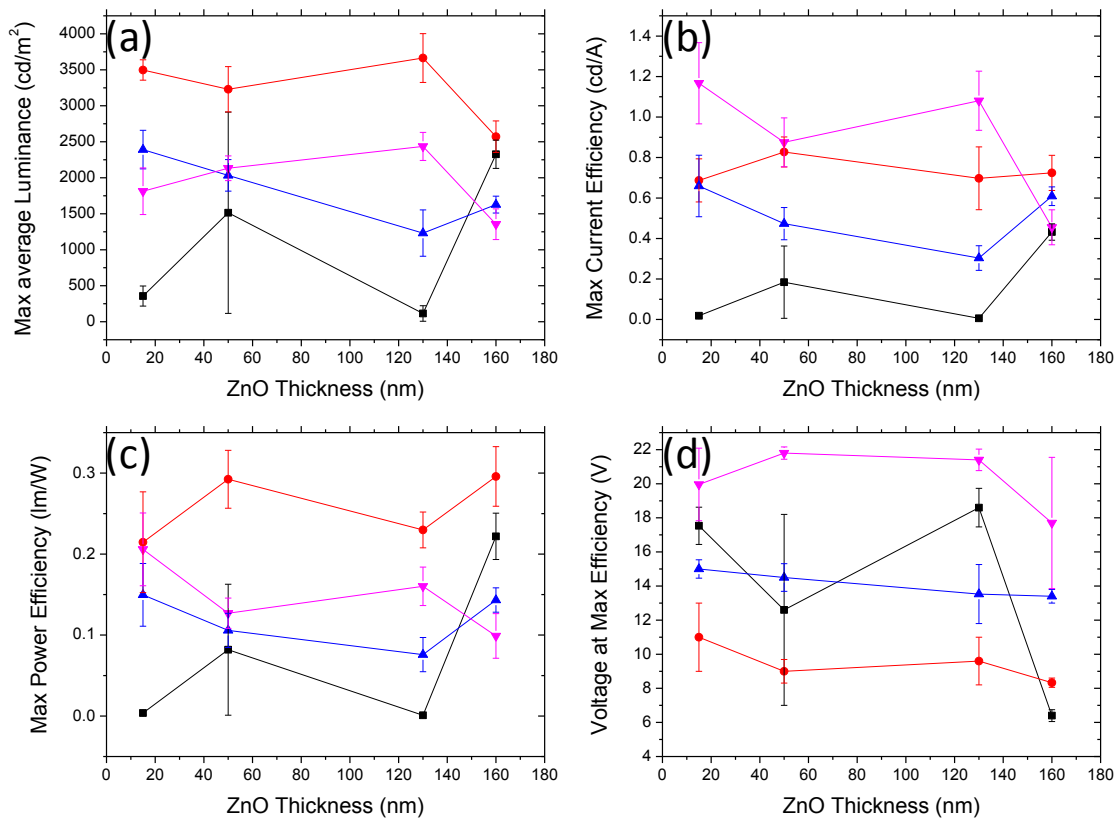
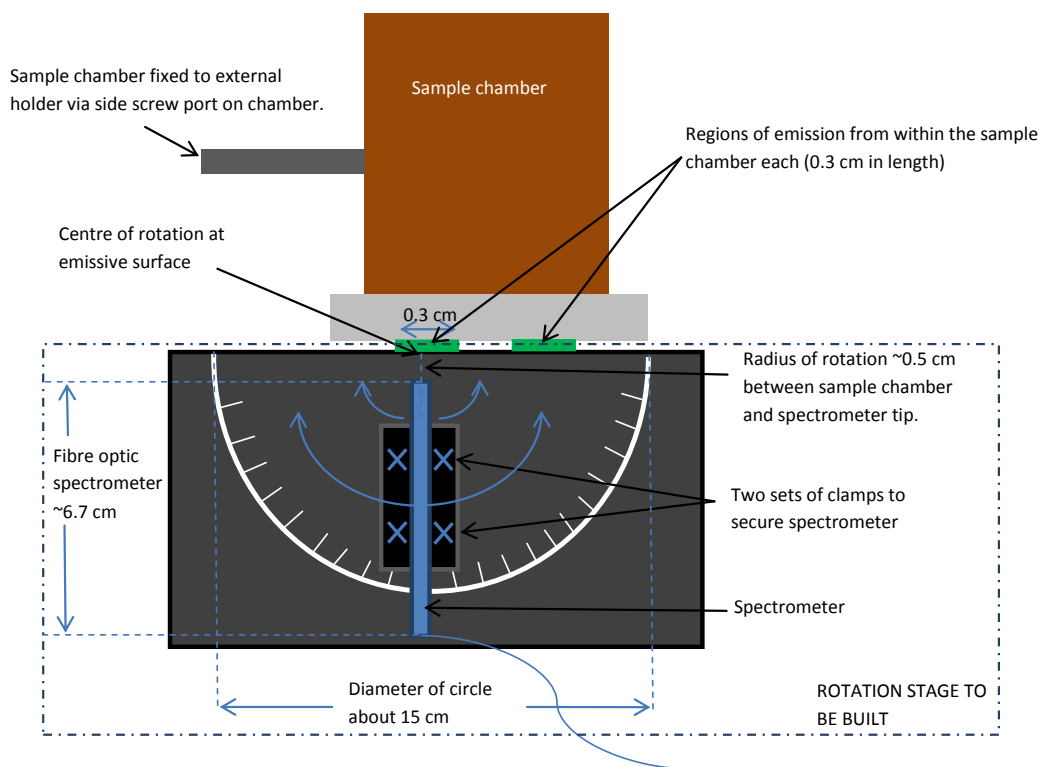


Figure A.3: The behaviour of planar ITO/ZnO/F8BT/MoO_x/Au HyLEDs as a function of ZnO and F8BT thickness. Shown are the max average (a) luminance, (b) current efficiency and (c) power efficiency with the voltage at maximum current efficiency shown in (d). Black squares, red circles, blue triangles and pink inverted triangles correspond to F8BT thicknesses of 50, 80 150 and 230 nm, respectively.

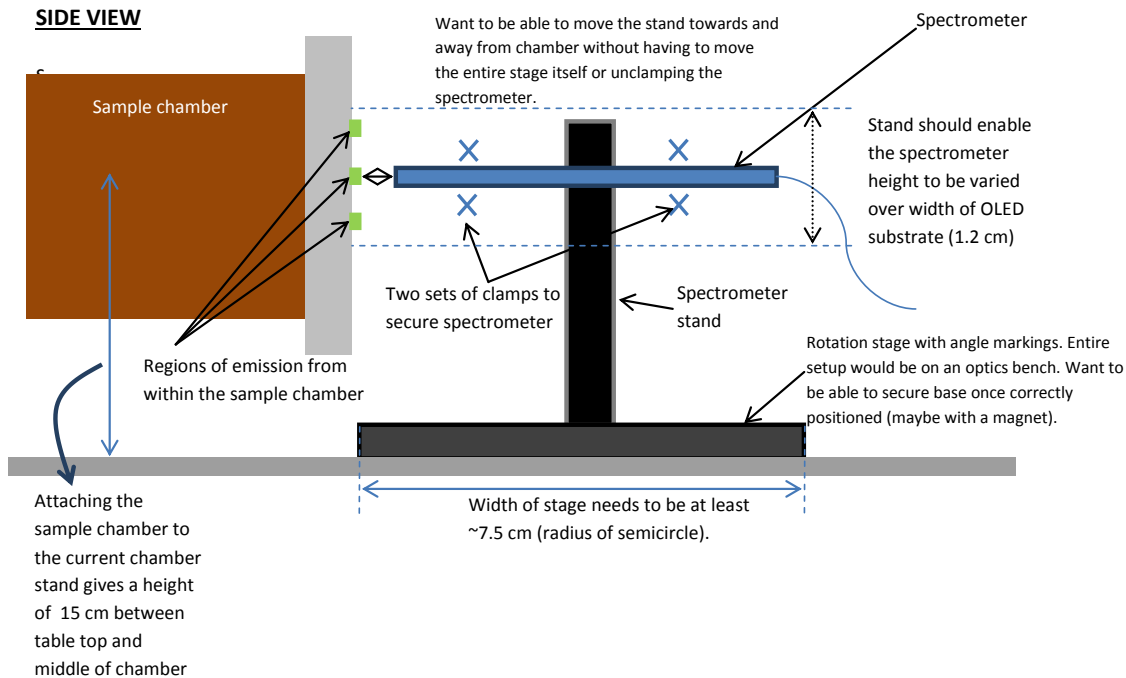
Appendix B

Below are the schematics for the rotating stage constructed for the measurements of angle-dependent electroluminescence discussed in Chapter 4. The stage was subsequently constructed by Martin Pettifer of the Imperial College London Black Laboratory mechanical workshop.

PLAN VIEW



SIDE VIEW



Appendix C

Commercially purchased F8BT was purified and fractionated for the molecular weight study detailed in chapter 5 by Dr Bob C. Schroeder. Here, the experimental details and analysis are included here as received by Dr Schroeder with the addition of figure captions:

"Soxhlet extraction with acetone, hexane & finally dichloromethane – catalytic impurities (mainly ligands) and insoluble material (colourless plastic bits) were removed. The polymer dissolved in chloroform was washed with aqueous sodium diethyldithiocarbamate solution to remove residual impurities. Polymer was precipitated from chlorobenzene into acetone, filtered-off and dried for 24 hours under reduced pressure. Polymer was dissolved in chlorobenzene and injected on our recycle GPC system at a flow rate of 4mL/min.

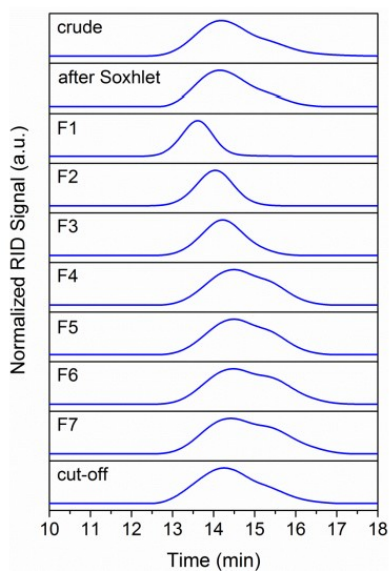


Figure C.1: GPC Chromatogram of purified F8BT.

[Figure C.1 shows] a typical chromatogram of the F8BT polymer (after Soxhlet extractions), when I injected in on our recGPC system. The areas in red were cut-off and the green area was fractionated into 7 different fractions (F1 to F7) [as shown in figure C.2].

Conclusions

Crude polymer contained various impurities, but could be purified by Soxhlet and GPC to a higher degree. Broad [dispersity] of the starting material was mainly caused by low molecular weight oligomers. Those were removed during the purification, but it was not possible to recover this material by precipitation, therefore a significant weight loss is observed and only 500 mg of material were recovered after all the purification steps. Overall the purification was very difficult and laborious. Next time you should consider talking to a chemist before buying expensive polymer. In this case it would have been much cheaper and faster to buy the two monomers and to convince a chemist to synthesize the polymer for you."



Polymer	M_n / M_w (kg/mol)	PDI	Amount (mg)
crude	46 / 172	3.7	~ 1 g
after Soxhlet	67 / 177	2.6	~ 800 mg
F1	300 / 400	1.3	28 mg
F2	160 / 230	1.4	66 mg
F3	100 / 180	1.8	82 mg
F4	67 / 140	2.1	66 mg
F5	47 / 124	2.6	53 mg
F6	36 / 117	3.3	90 mg
F7	35 / 123	3.5	14 mg
cut-off	55 / 176	3.2	102 mg

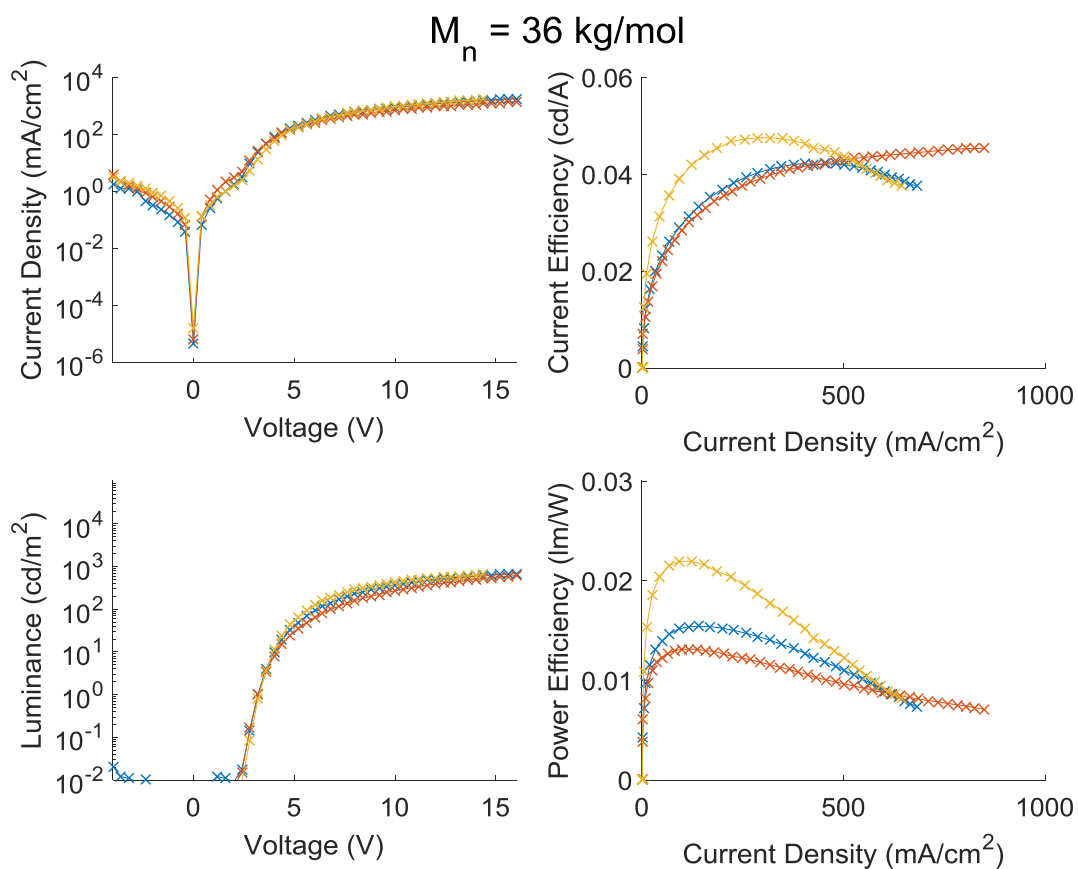
Figure C.2: Full results of the completely fractionated F8BT.

Appendix D

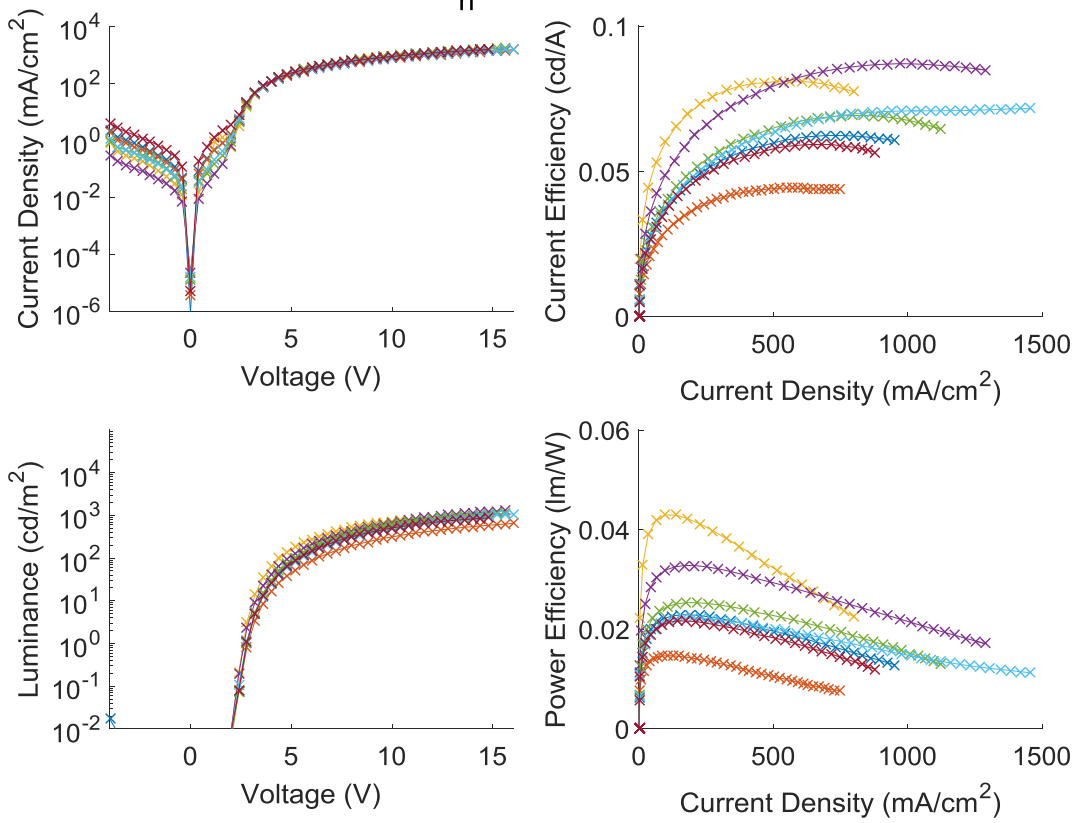
This Appendix contains all the raw device data for Chapter 5 organised by device type and annealing conditions. For each MW there are 4 graphs representing the measured performance metrics. Different coloured curves simply indicate the measurements for a particular pixel.

D.1. F8BT-Only HyLED Devices

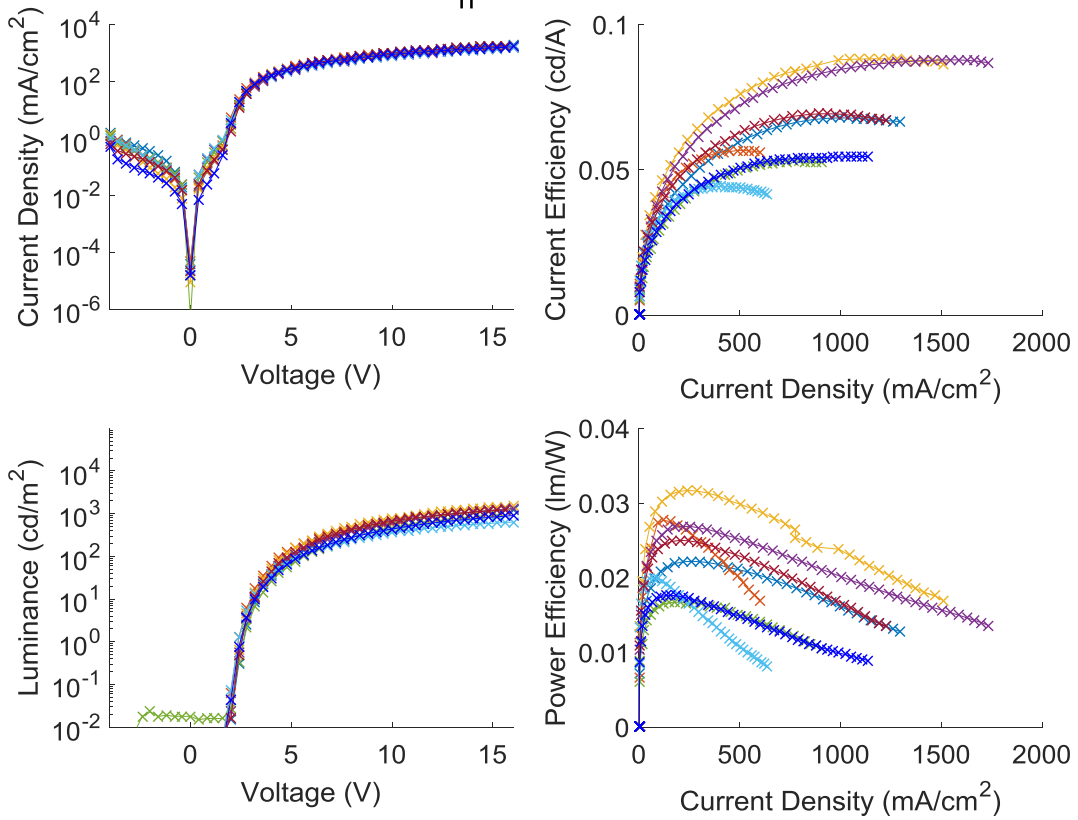
D.1.1. As-cast devices



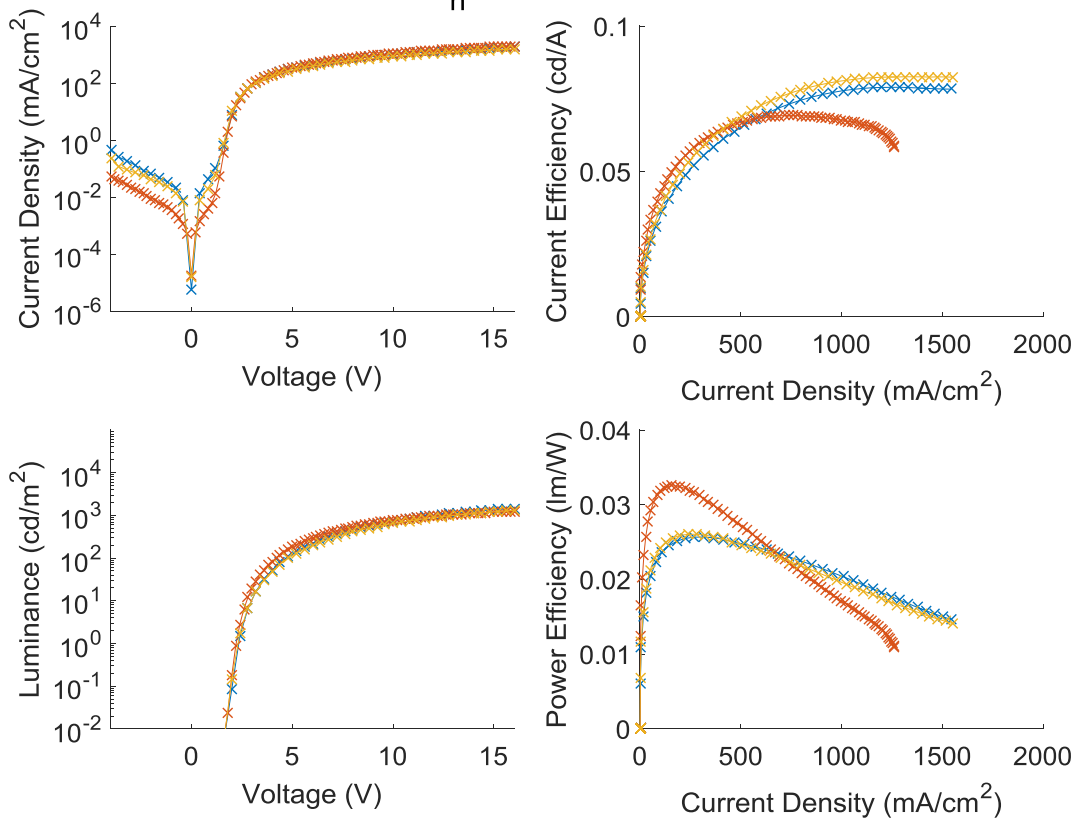
$M_n = 46 \text{ kg/mol}$



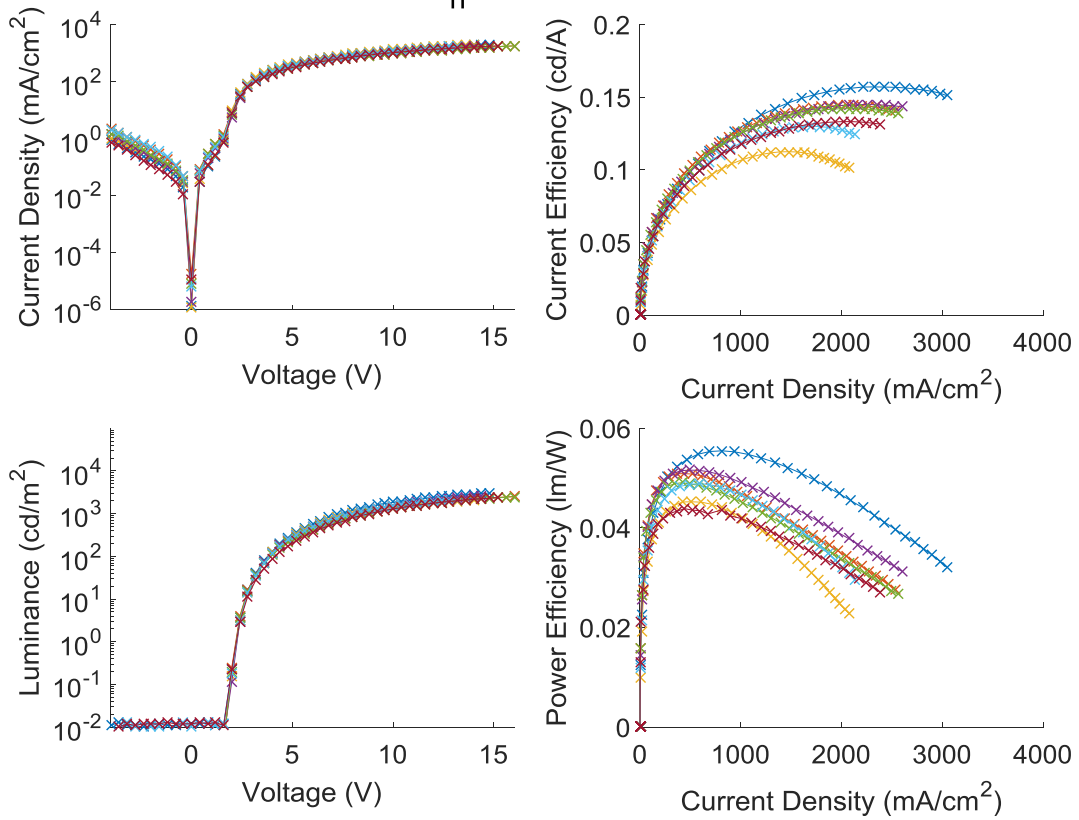
$M_n = 67 \text{ kg/mol}$



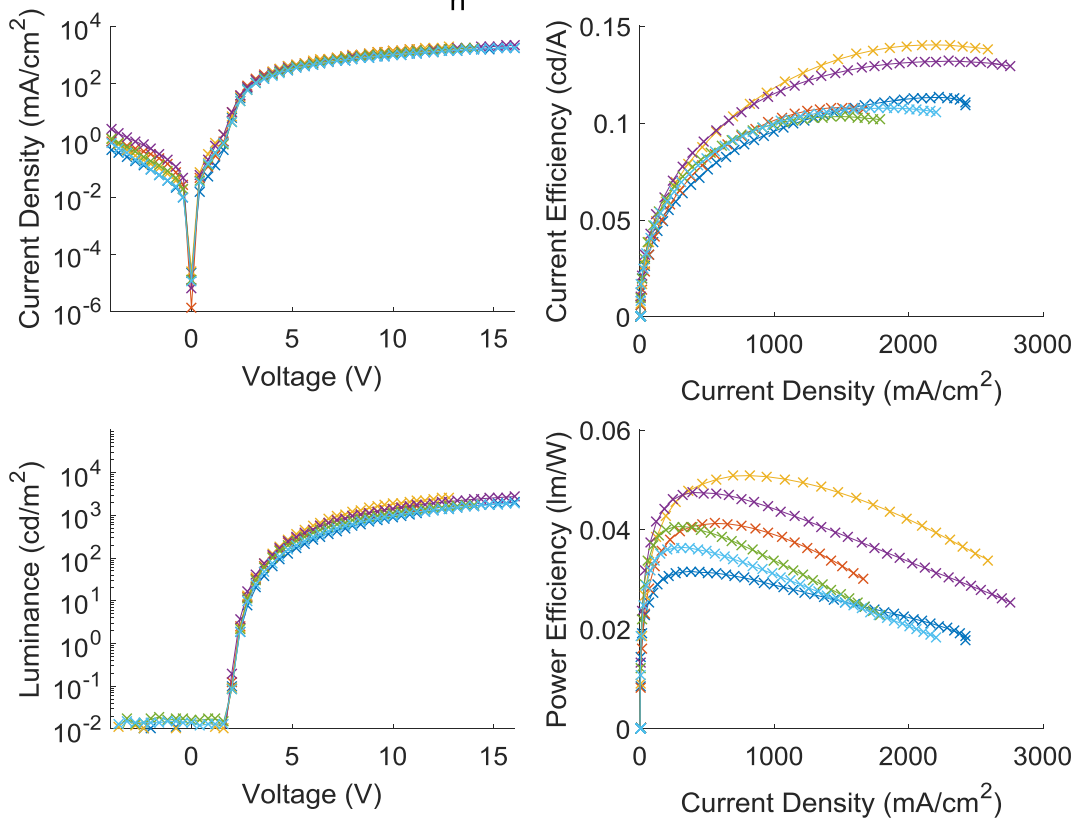
$M_n = 100 \text{ kg/mol}$



$M_n = 160 \text{ kg/mol}$

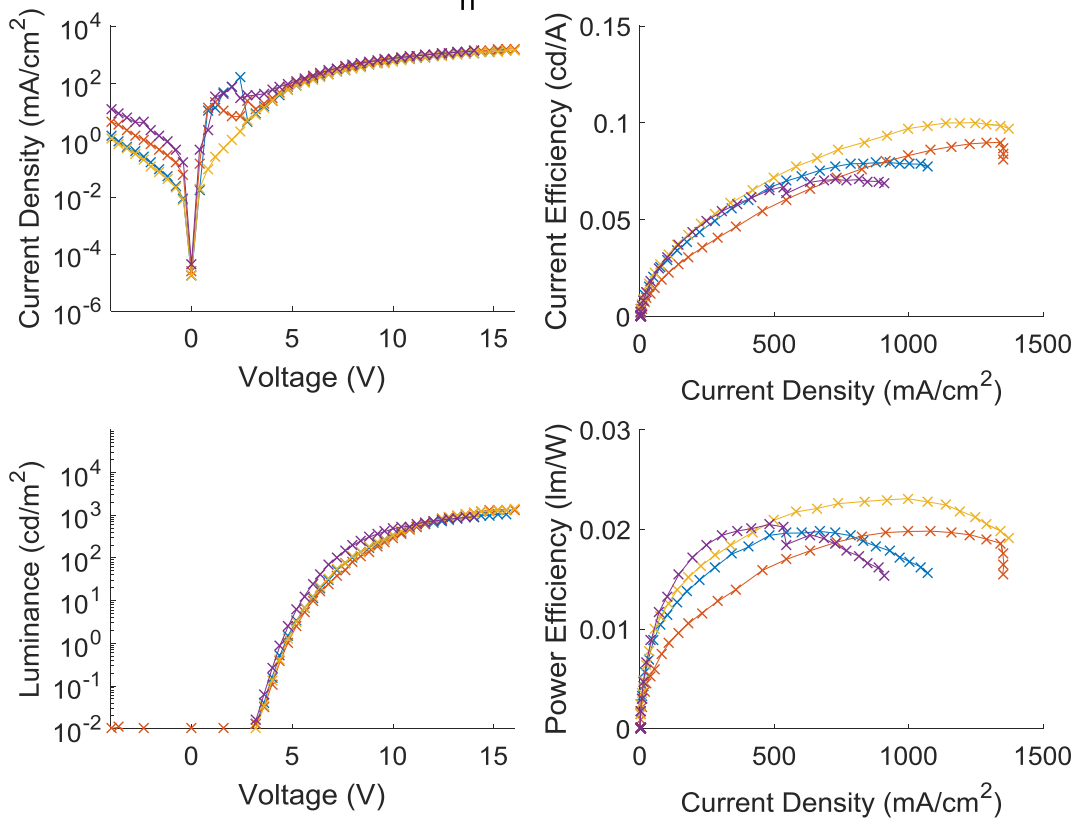


$M_n = 300 \text{ kg/mol}$

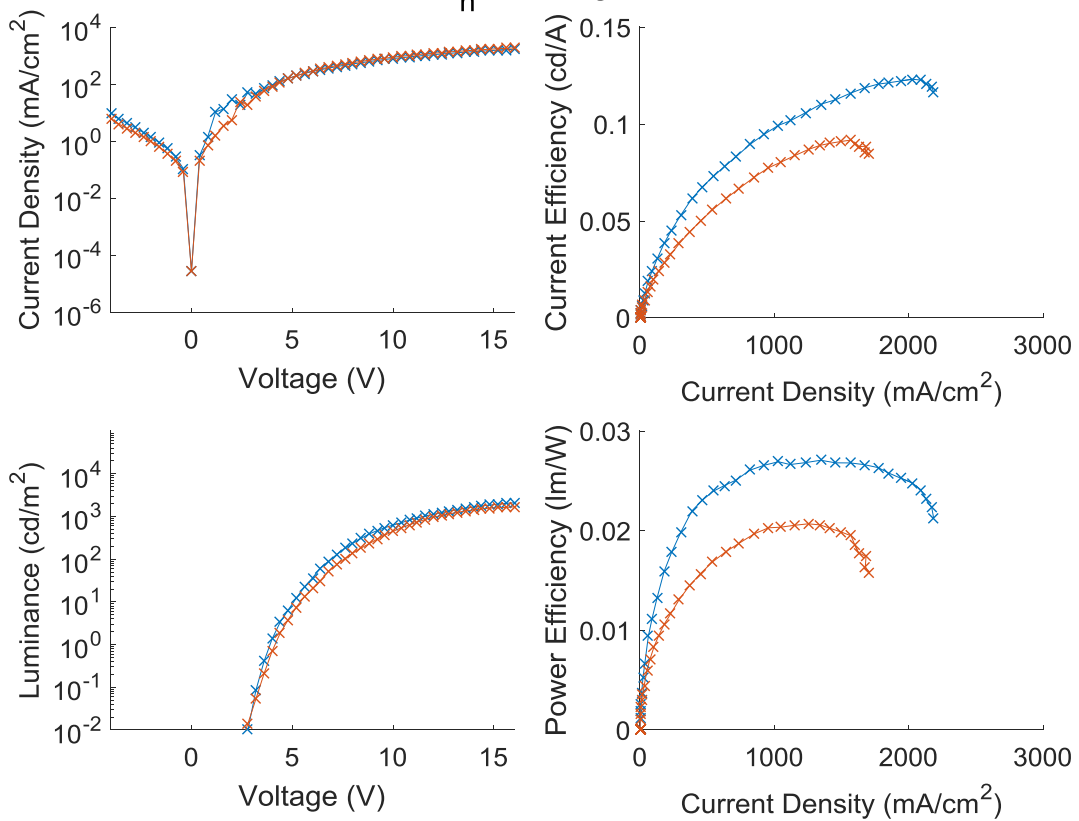


D.1.2. T_g devices

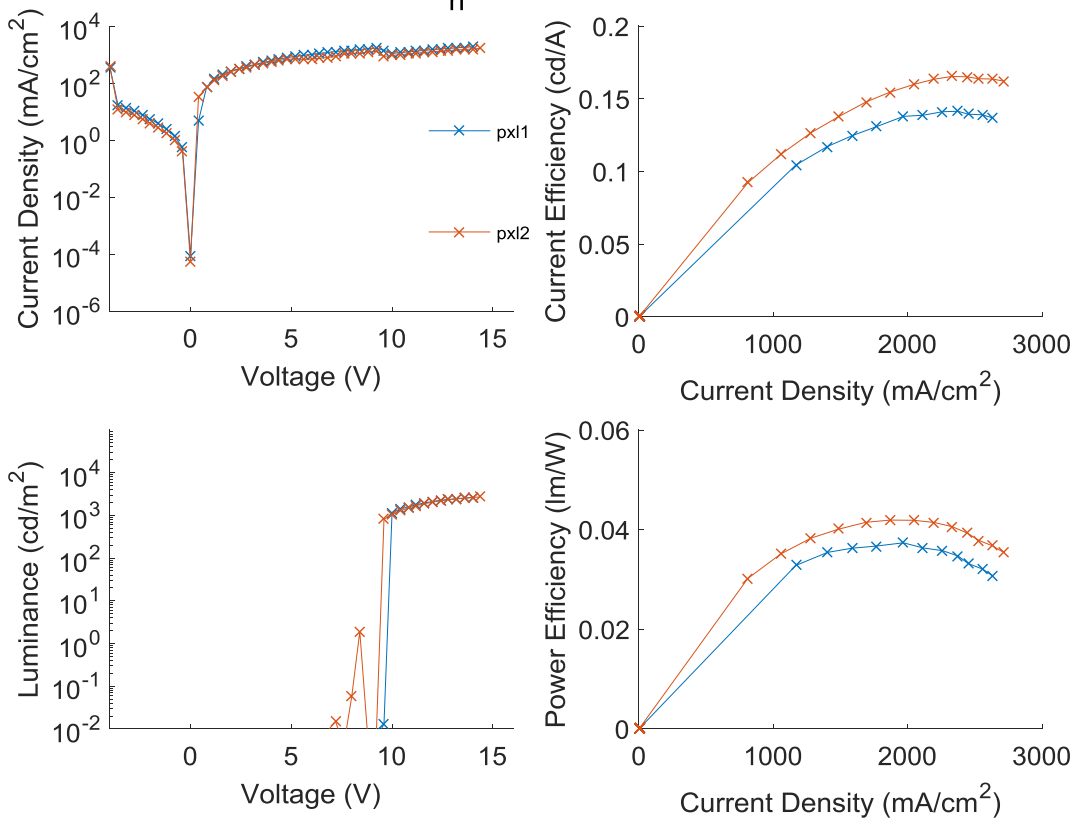
$M_n = 36$ kg/mol



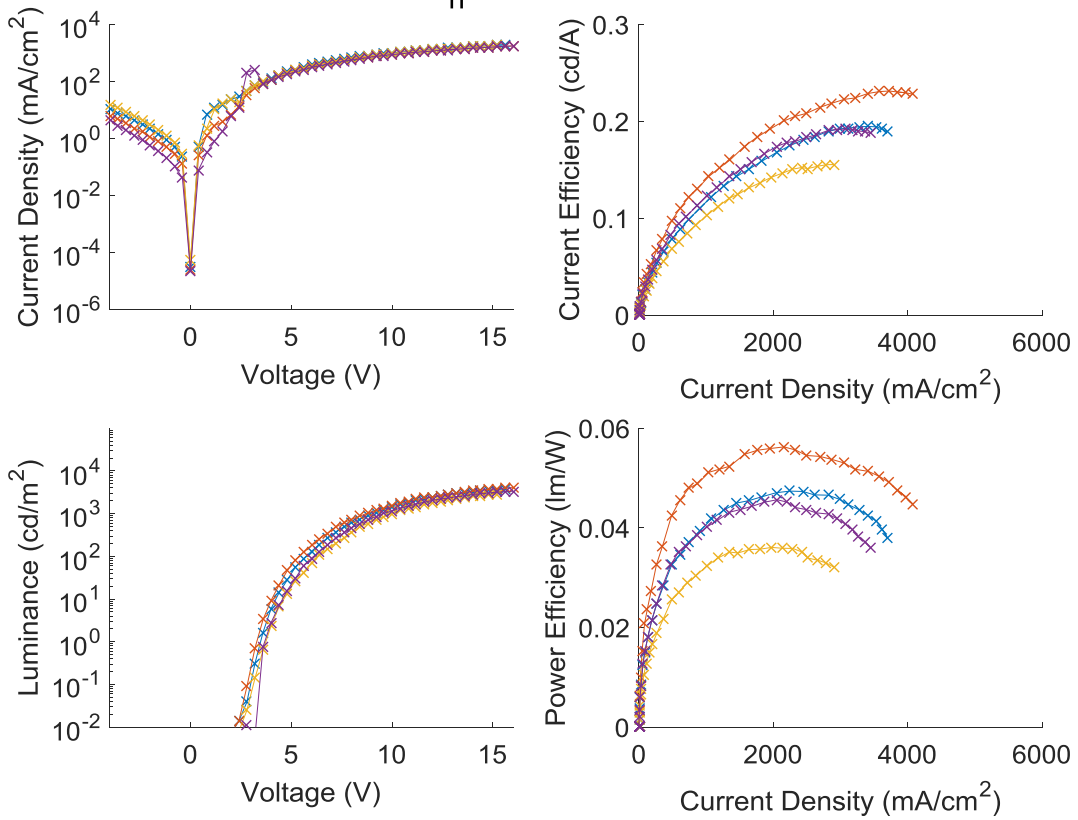
$M_n = 67$ kg/mol



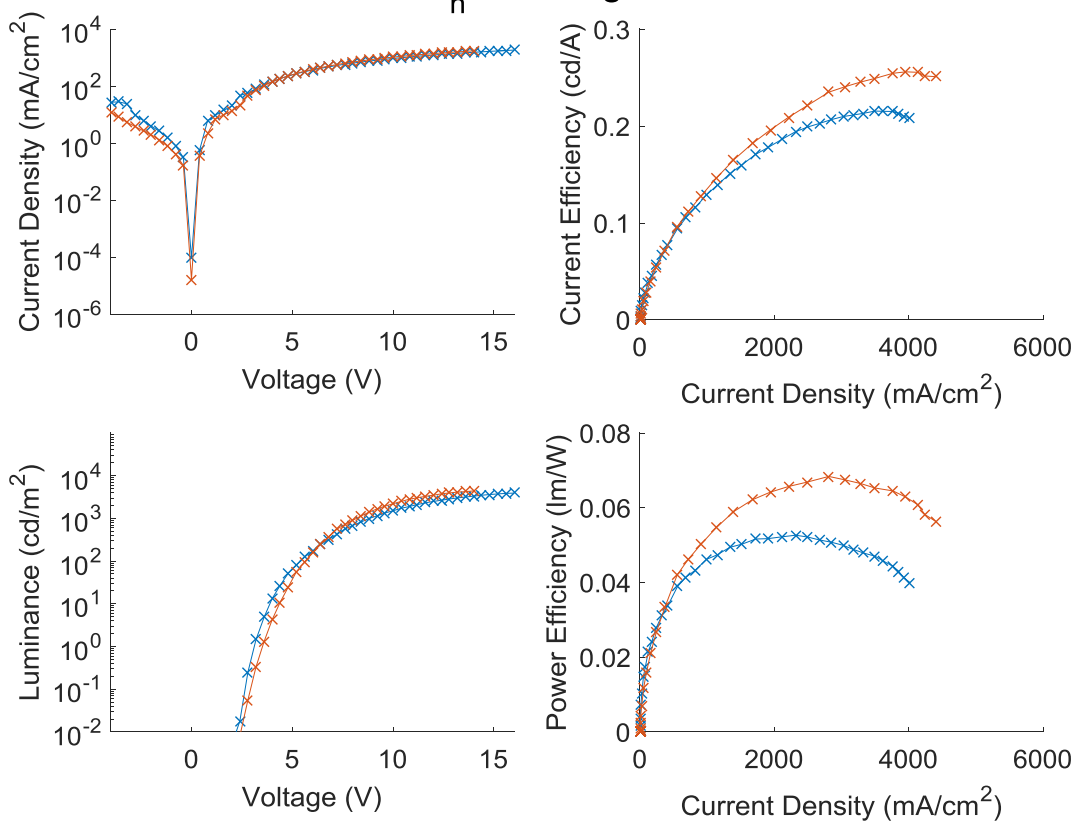
$M_n = 100 \text{ kg/mol}$



$M_n = 160 \text{ kg/mol}$

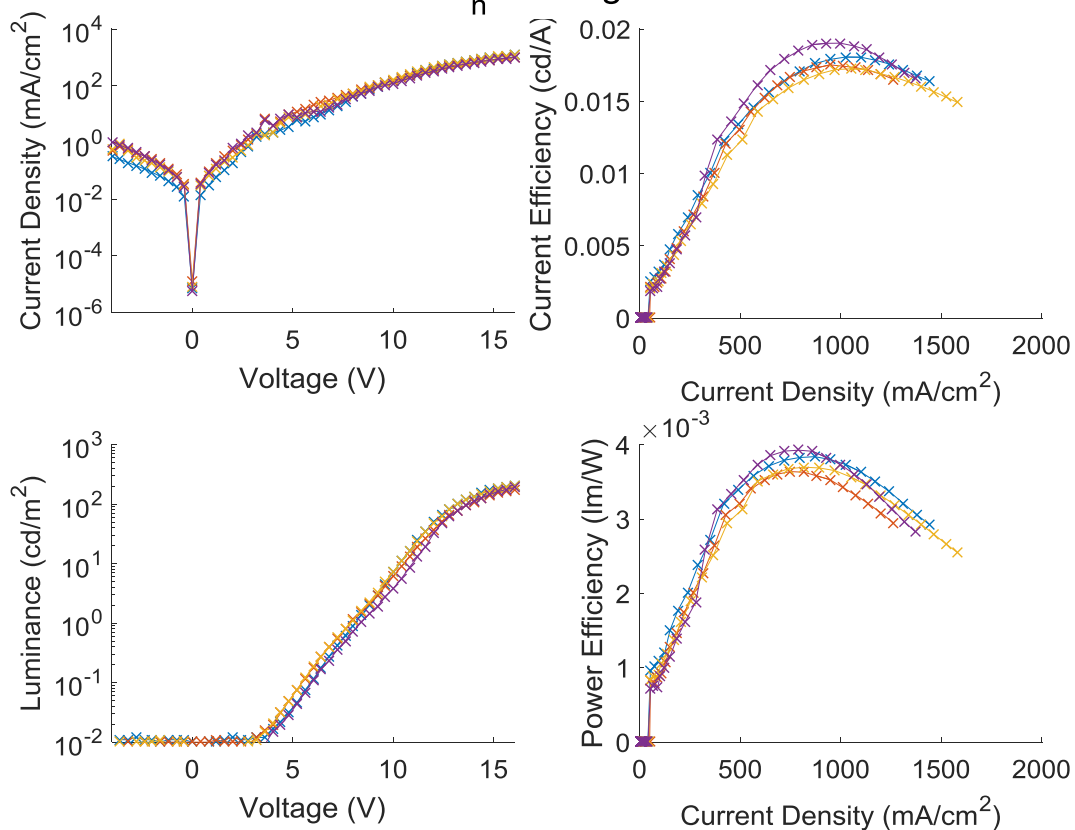


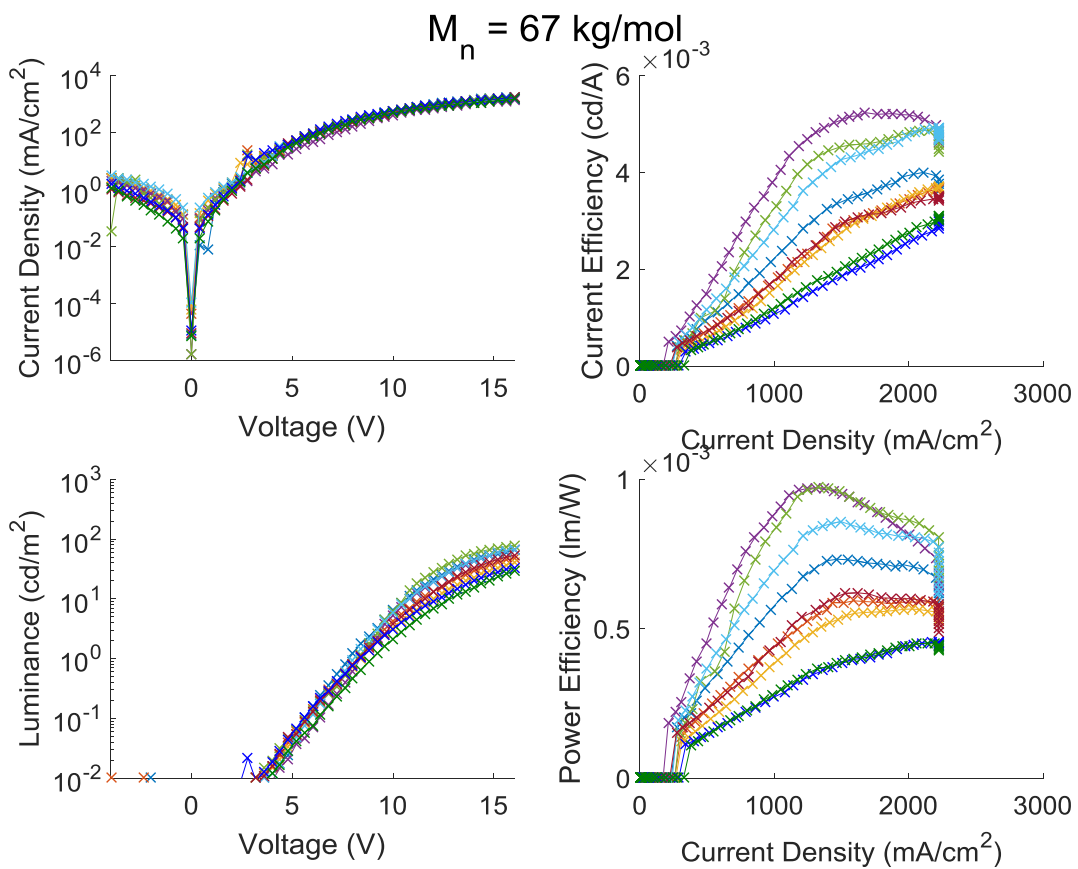
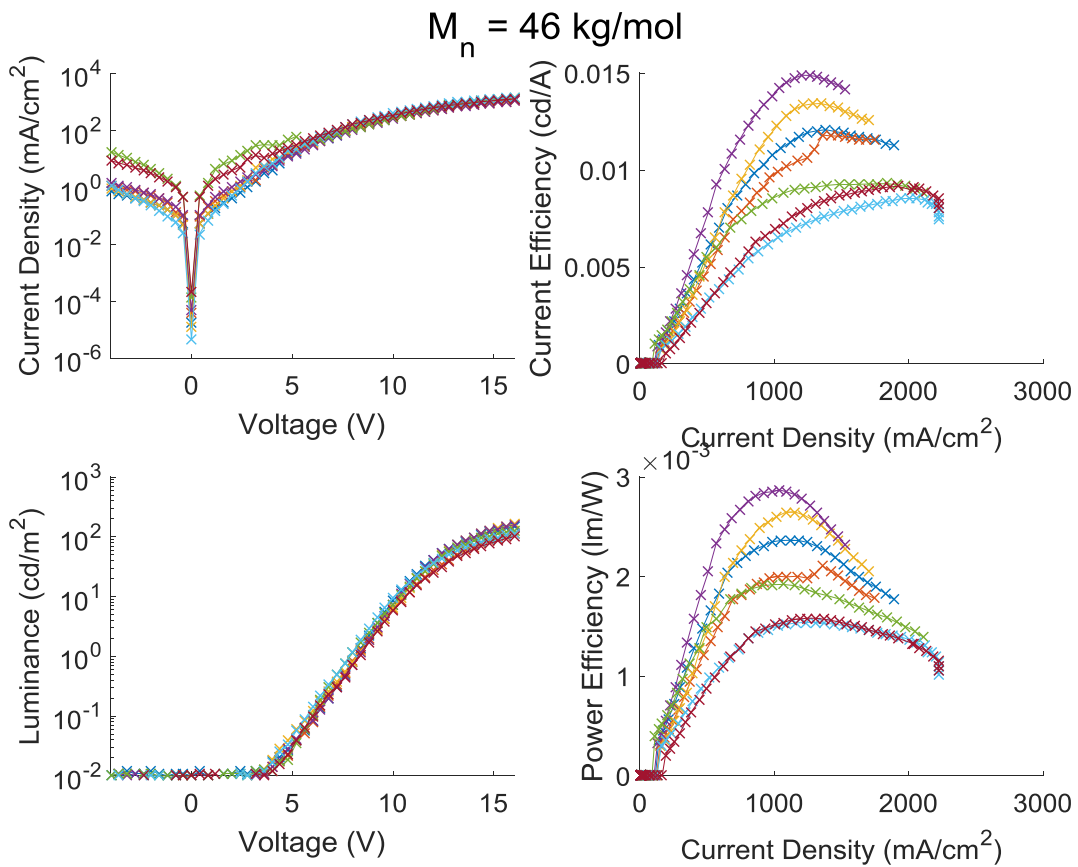
$M_n = 300 \text{ kg/mol}$

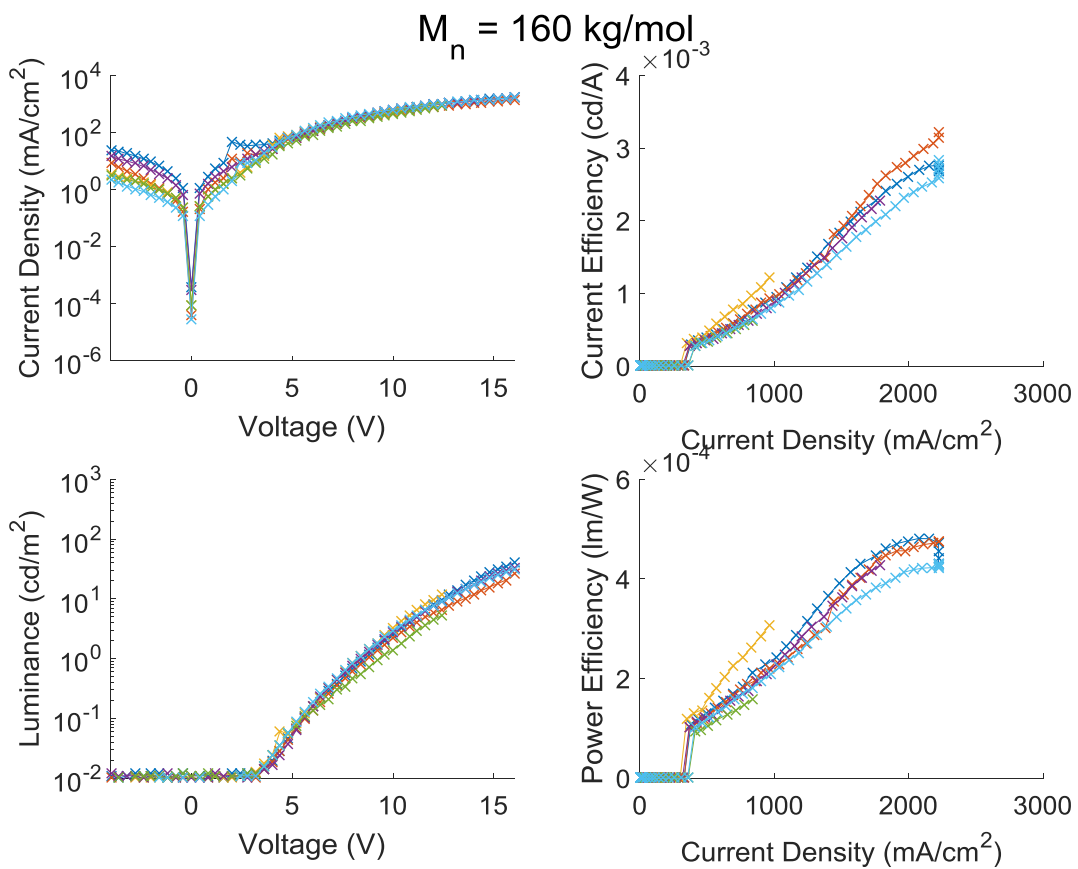
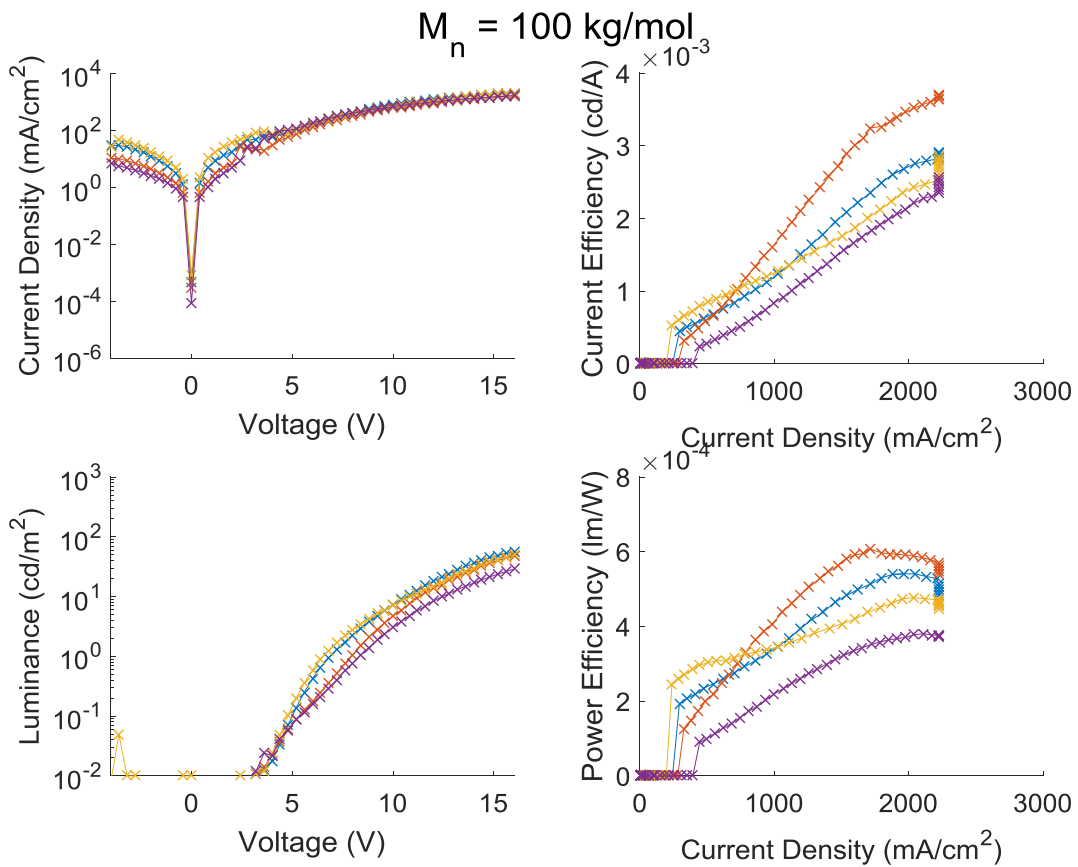


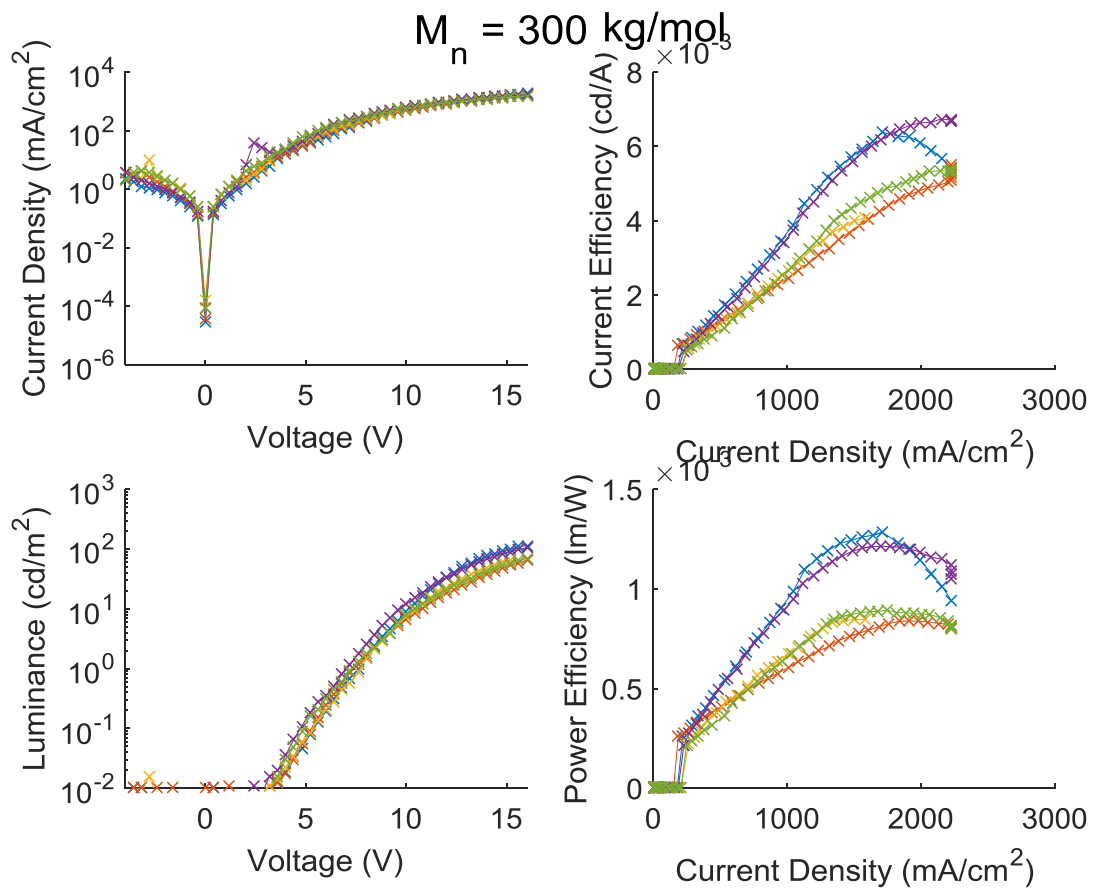
D.1.3. T_m devices

$M_n = 36 \text{ kg/mol}$



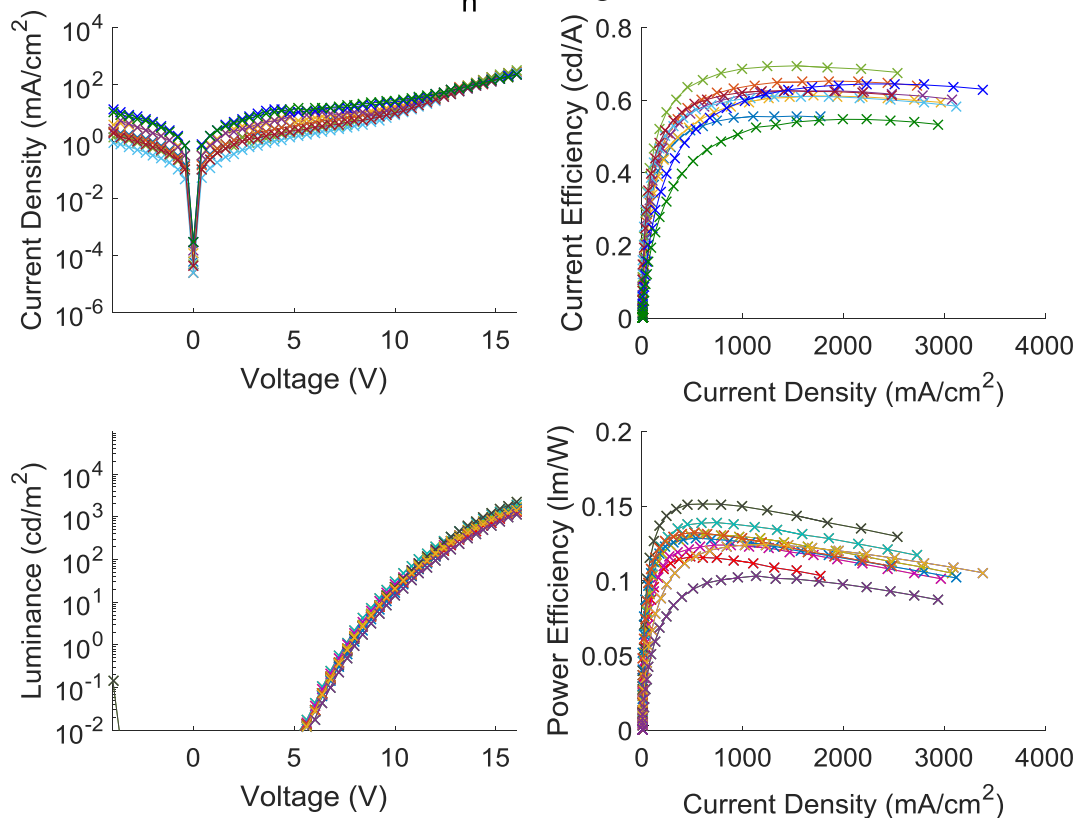




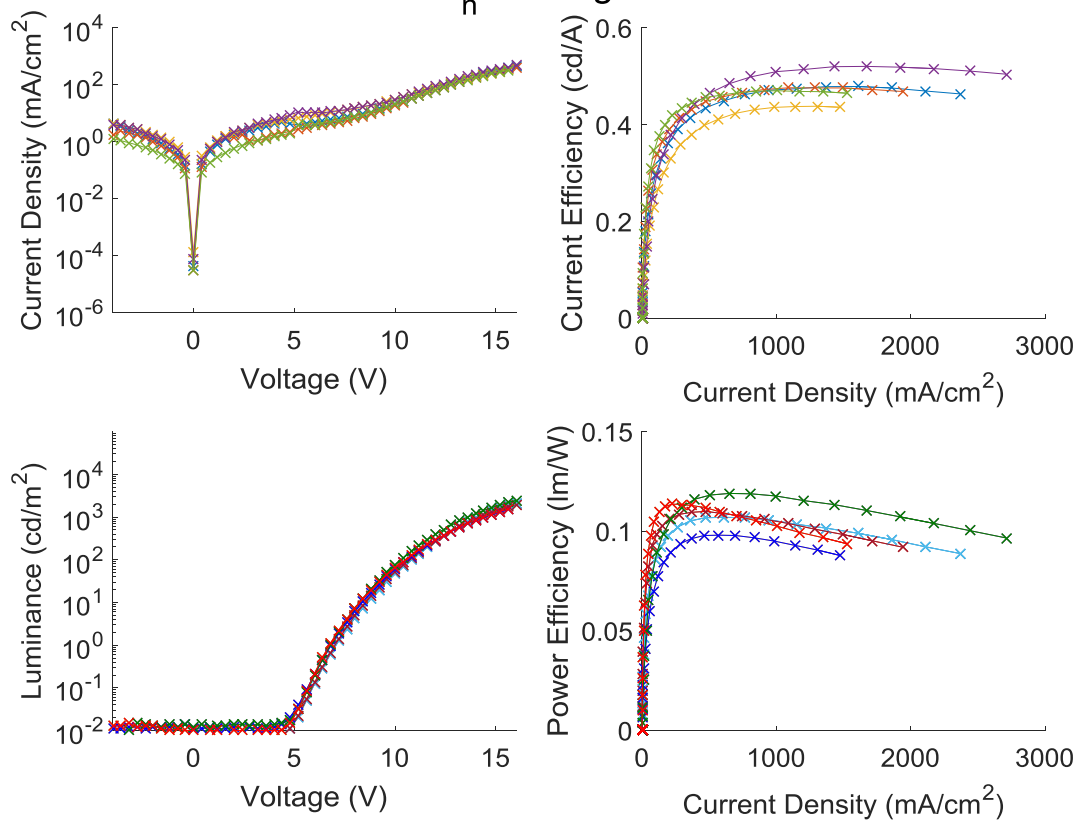


D.2. Bilayer HyLED Devices

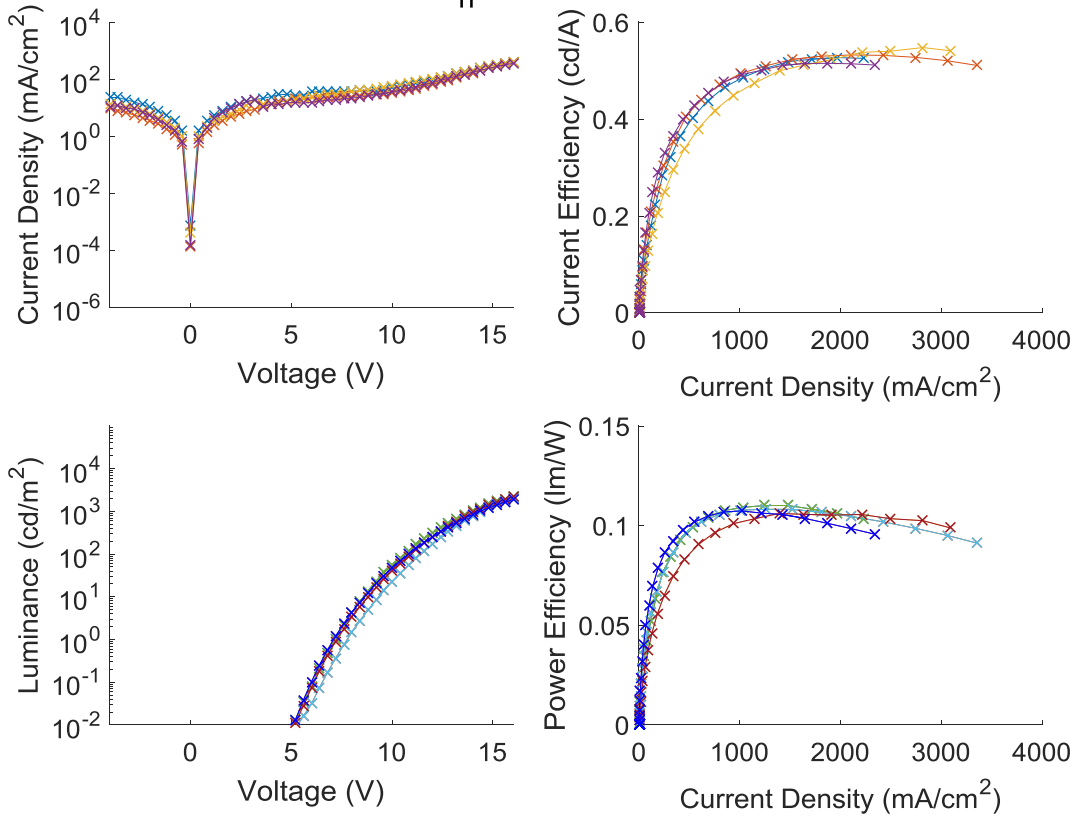
$M_n = 36 \text{ kg/mol}$



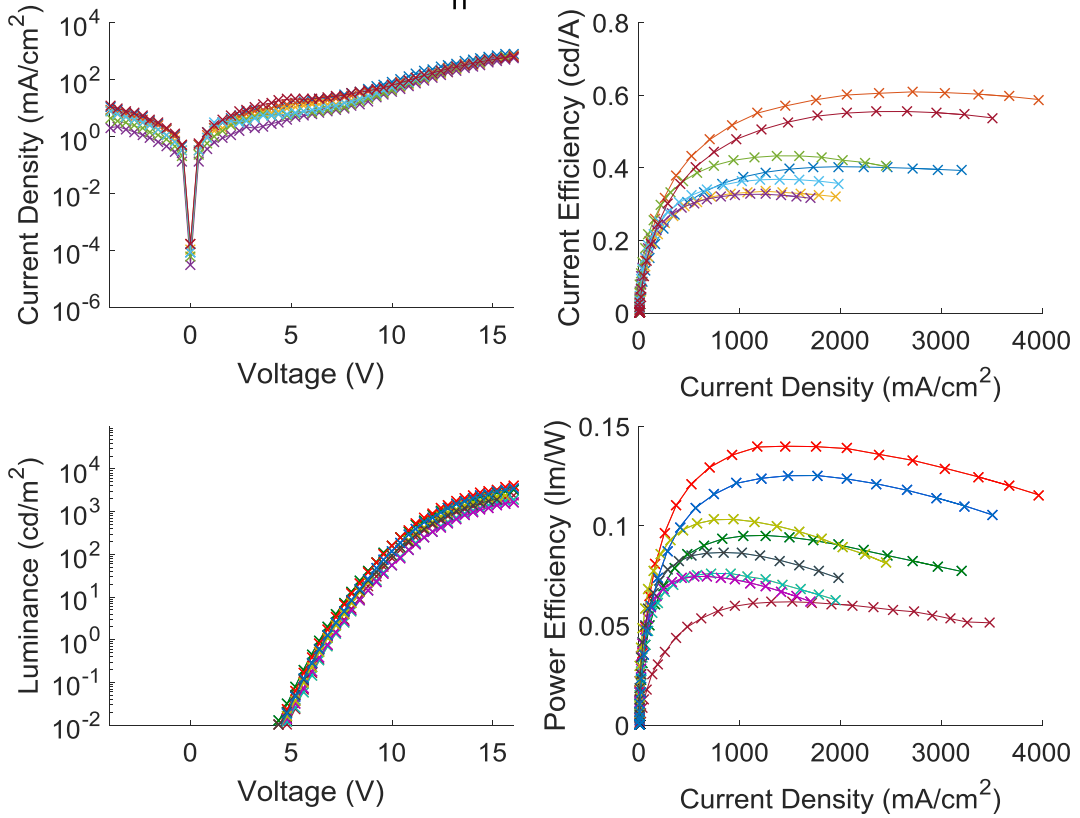
$M_n = 46 \text{ kg/mol}$



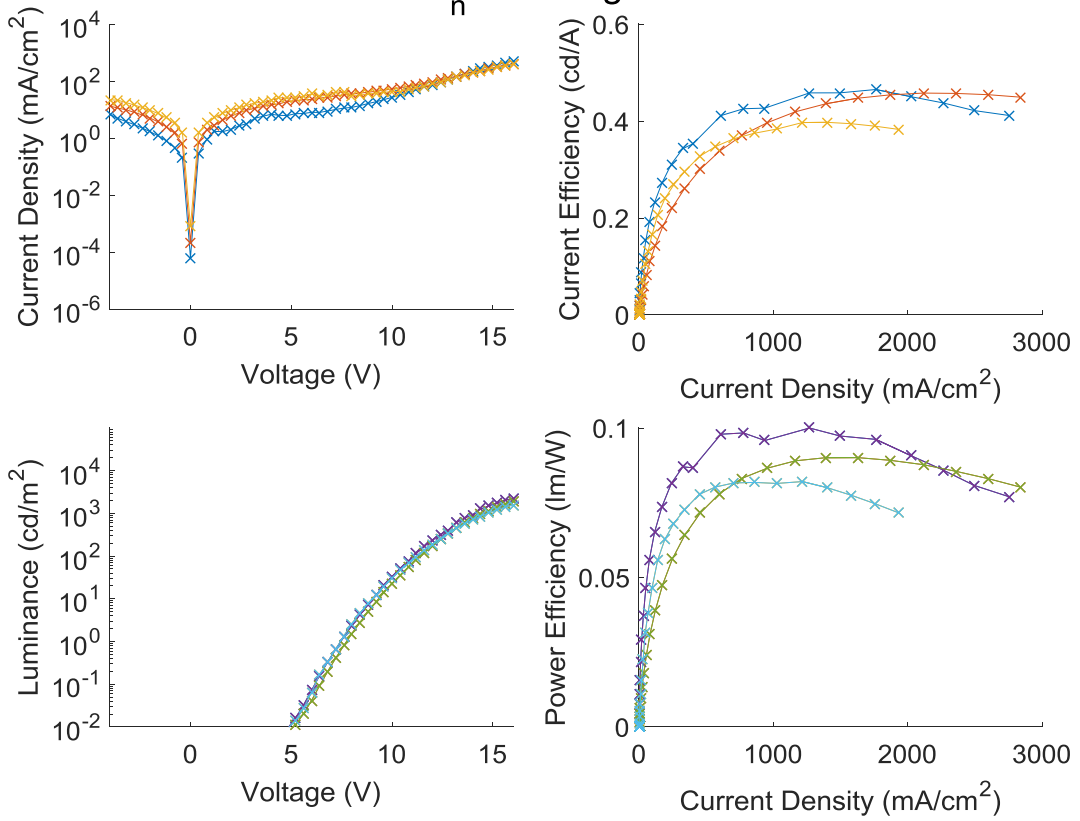
$M_n = 67 \text{ kg/mol}$



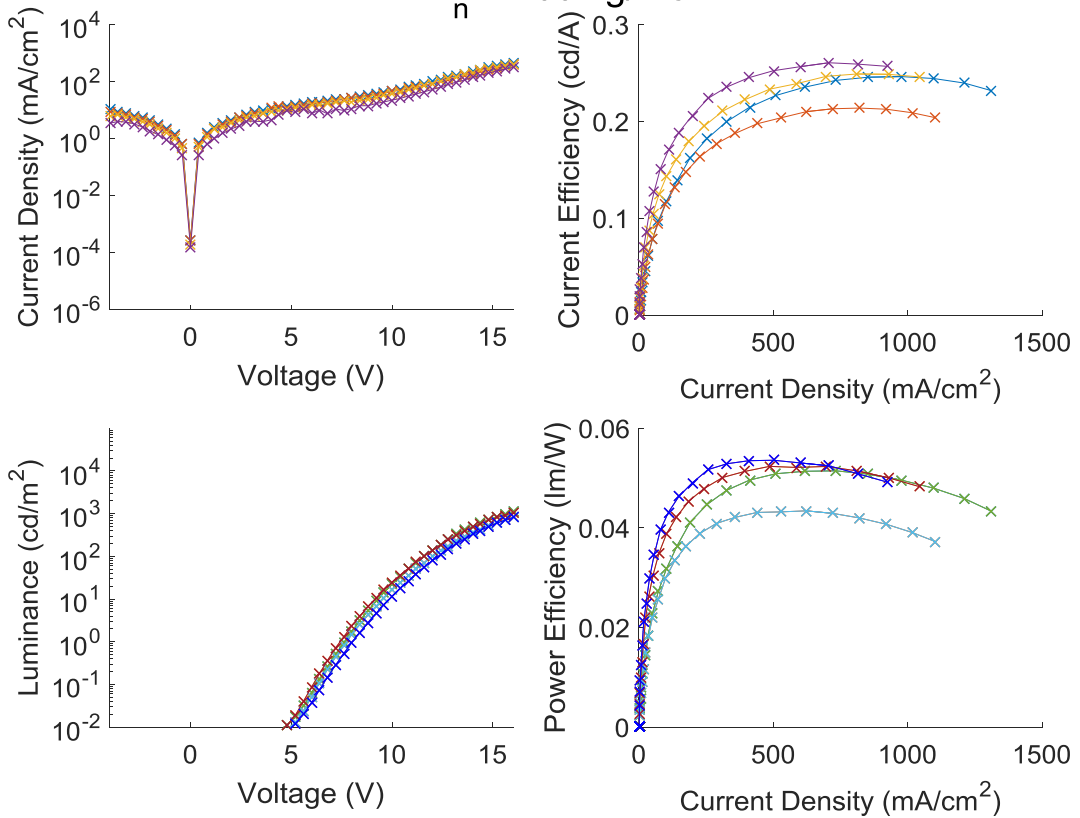
$M_n = 47^* \text{ kg/mol}$



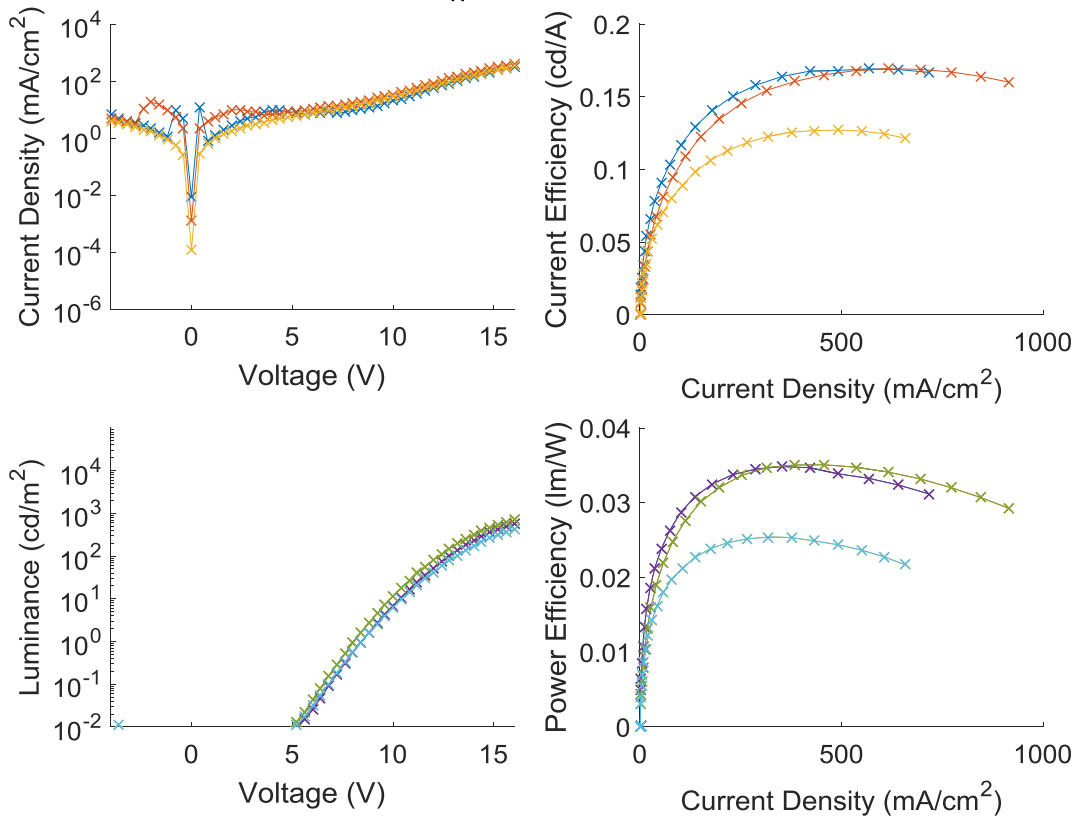
$M_n = 100 \text{ kg/mol}$



$M_n = 160 \text{ kg/mol}$

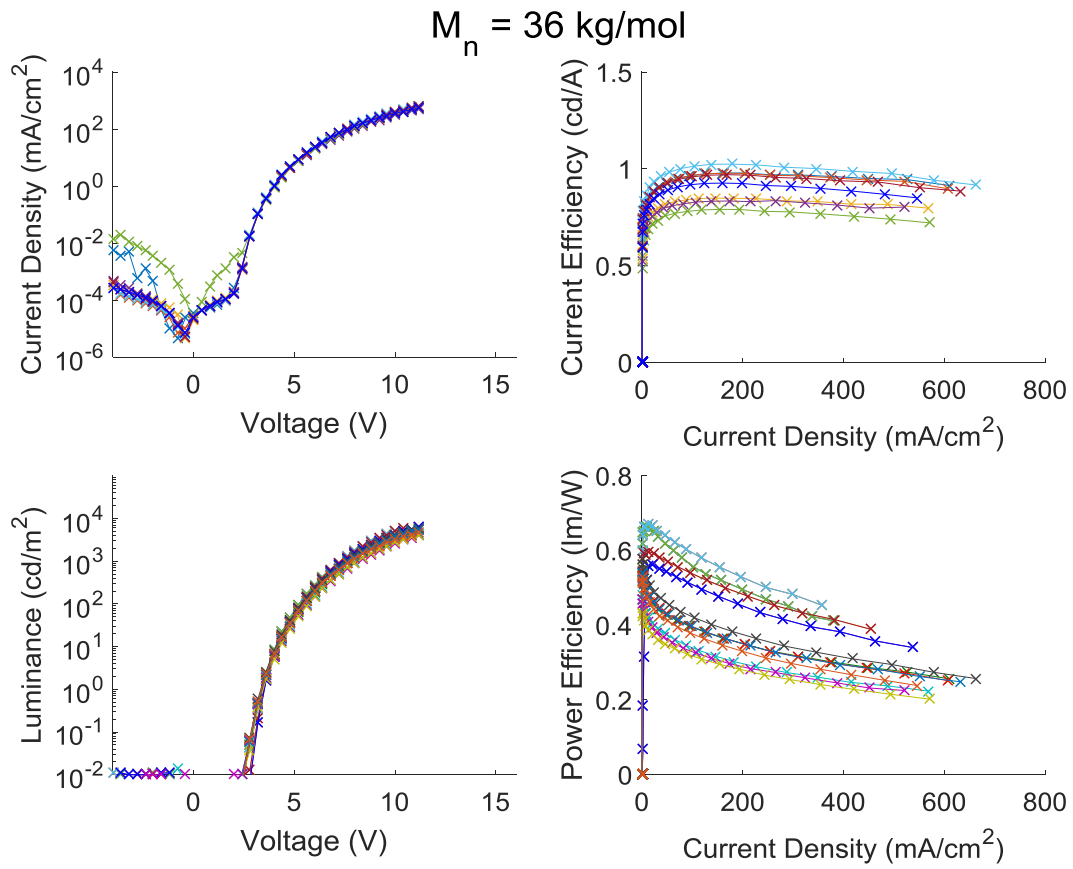


$M_n = 300 \text{ kg/mol}$

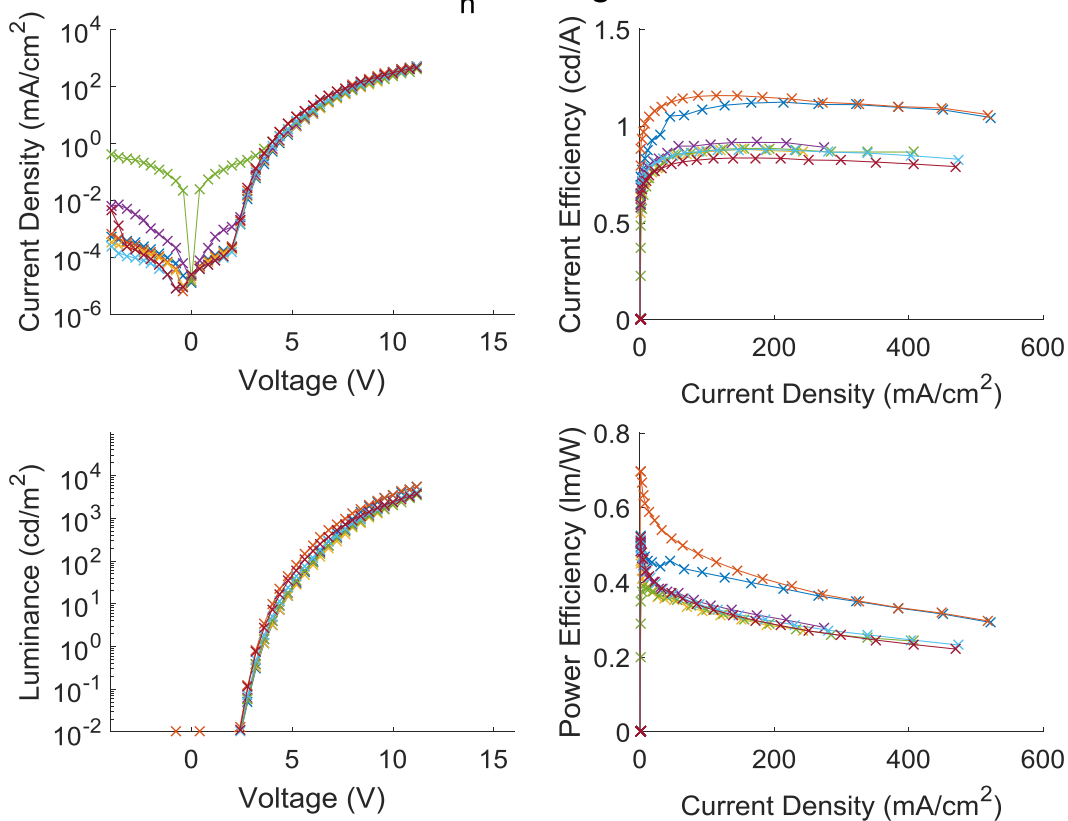


D.3. Standard PLED Devices

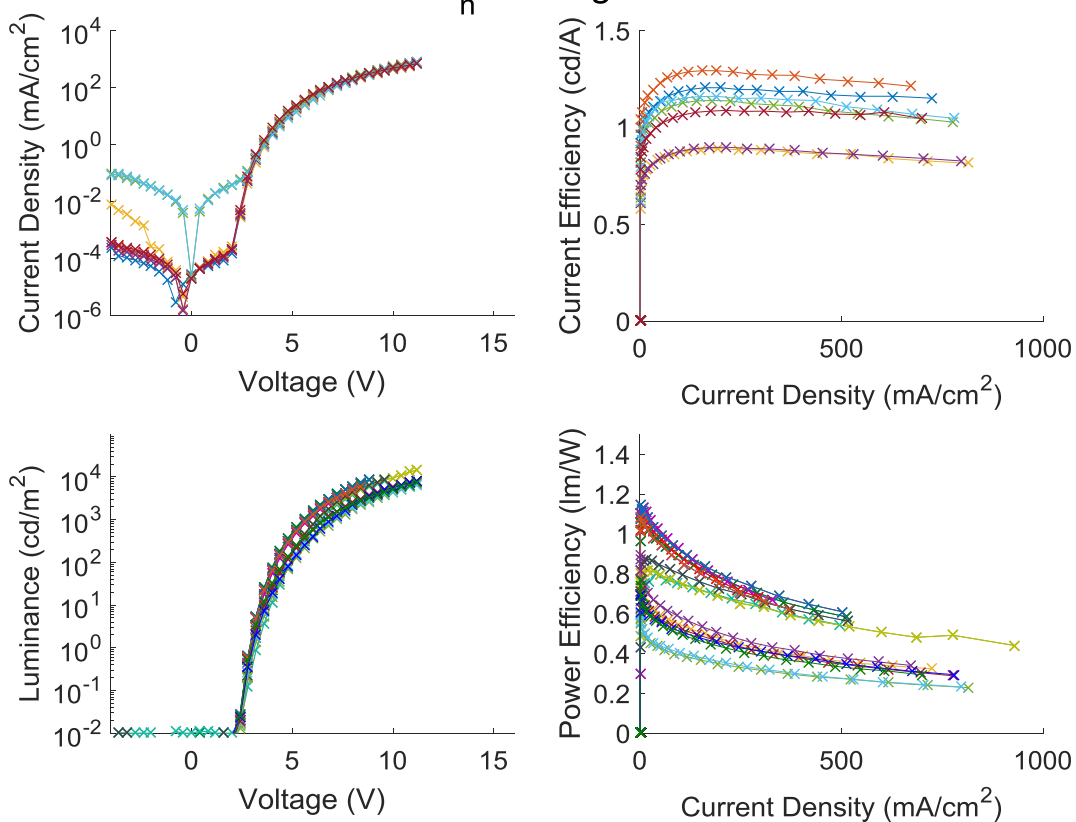
D.3.1. As-cast devices



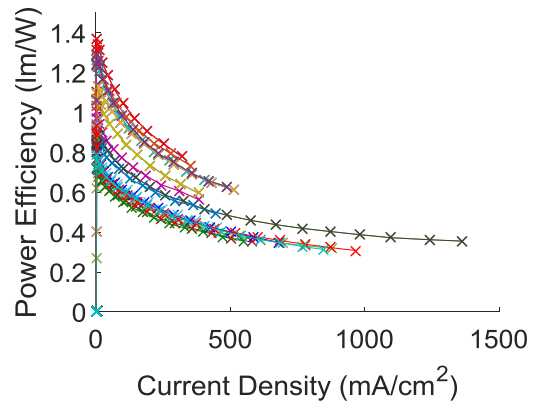
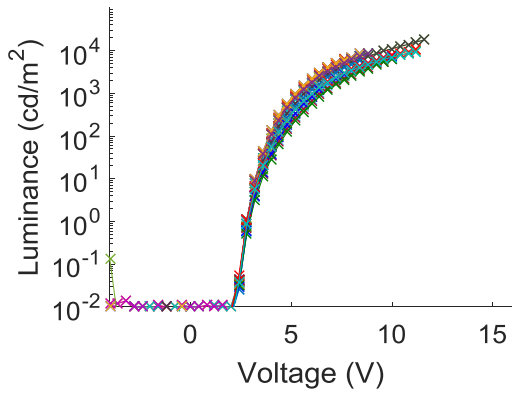
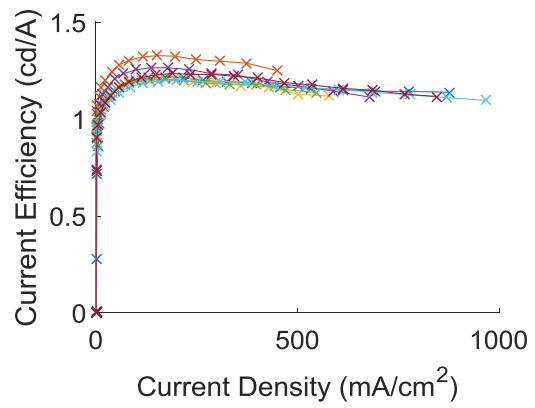
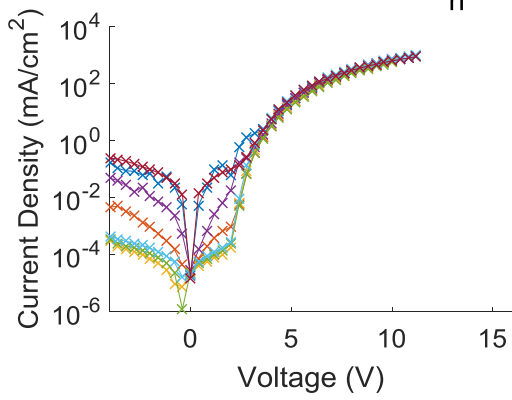
$M_n = 46 \text{ kg/mol}$



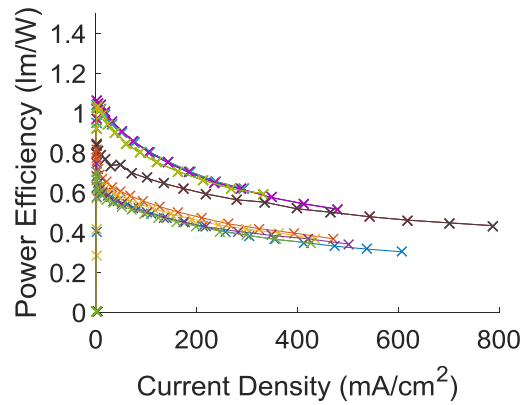
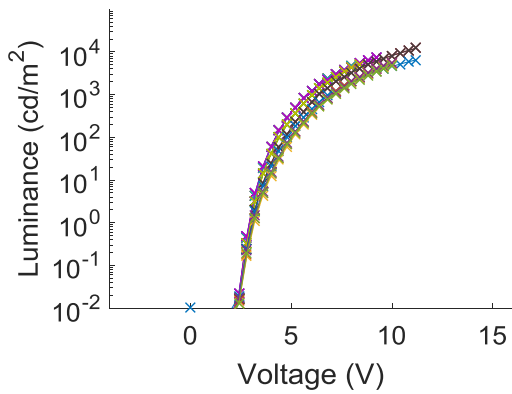
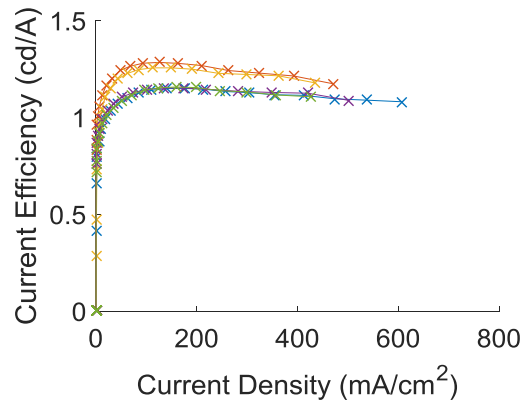
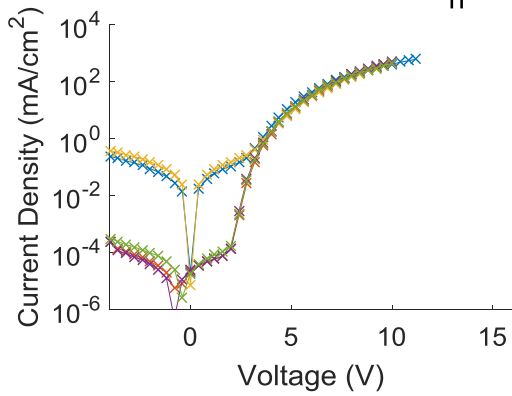
$M_n = 67 \text{ kg/mol}$



$M_n = 100 \text{ kg/mol}$

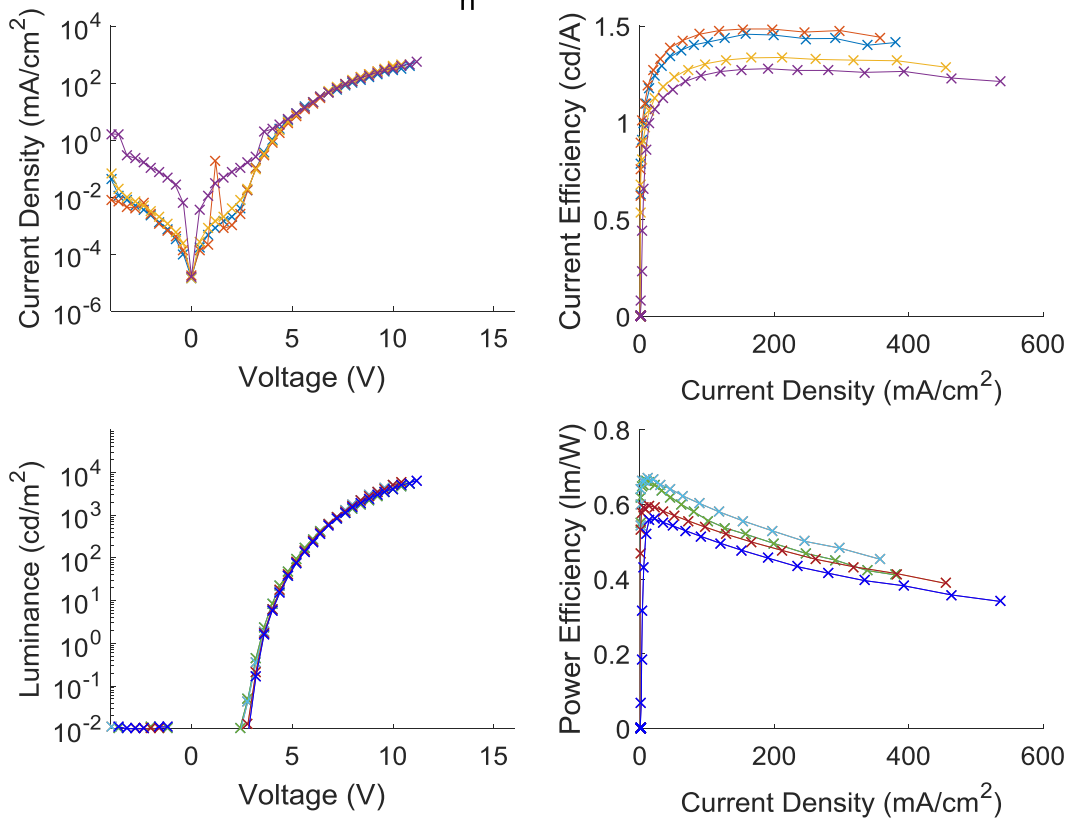


$M_n = 160 \text{ kg/mol}$

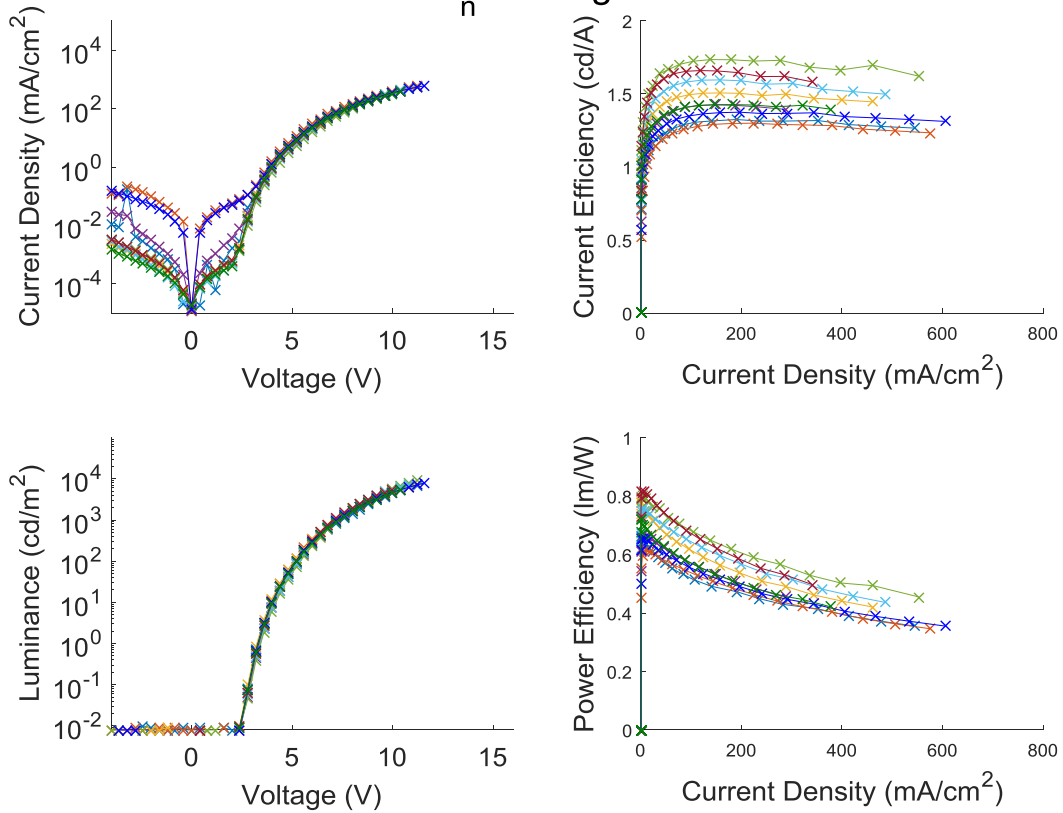


D.3.2. T_g devices

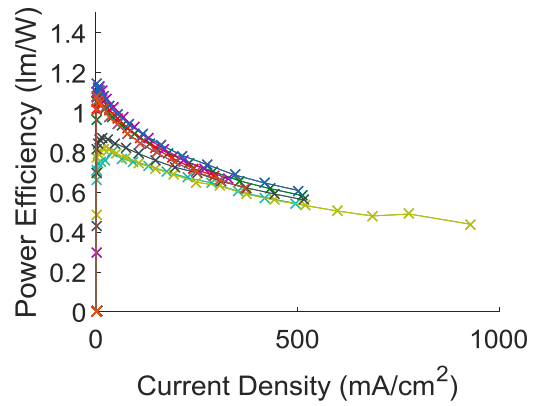
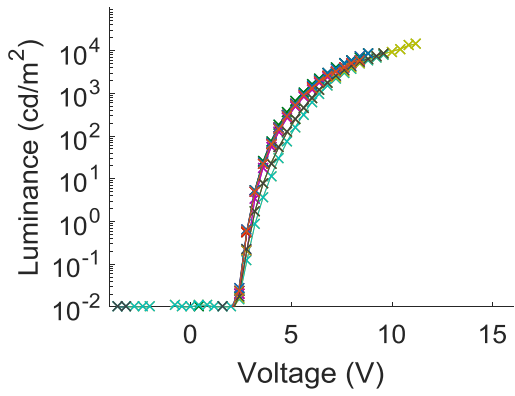
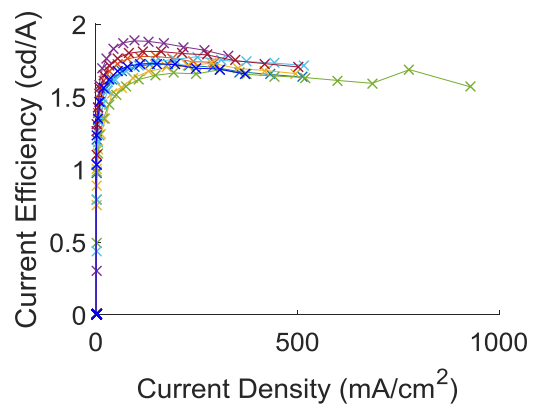
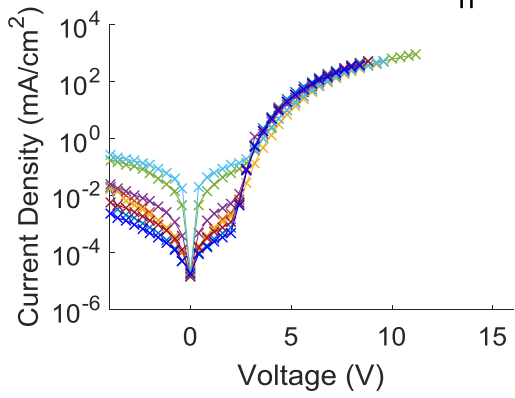
$M_n = 36$ kg/mol



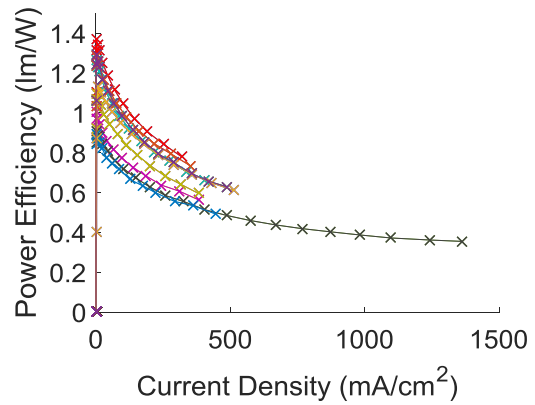
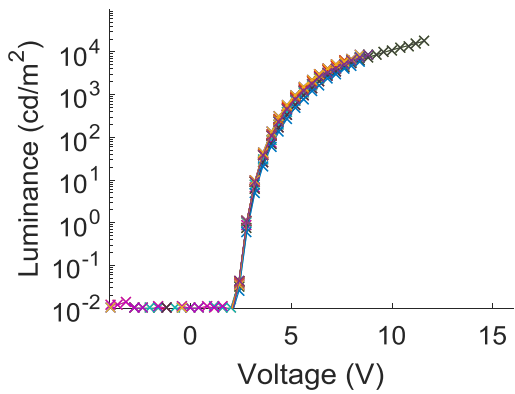
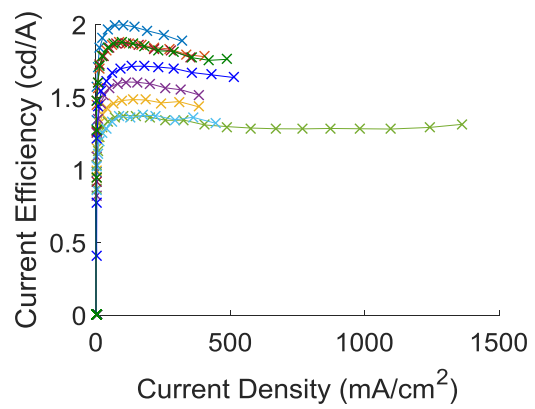
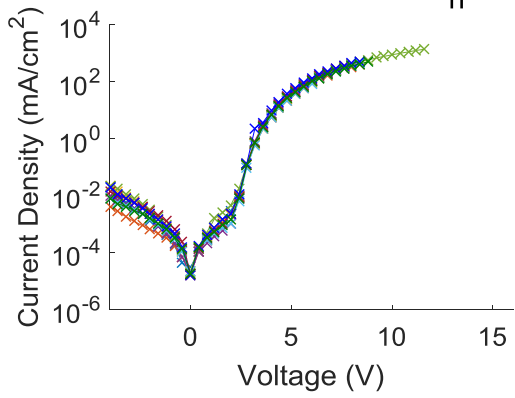
$M_n = 46$ kg/mol



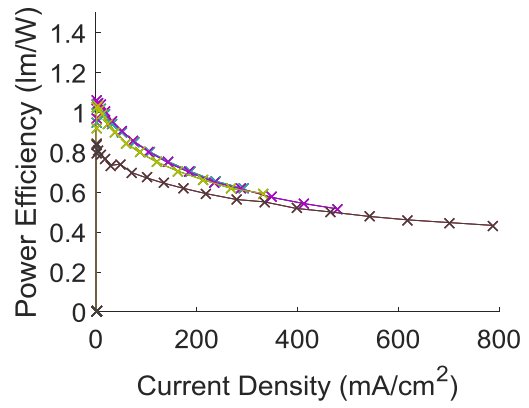
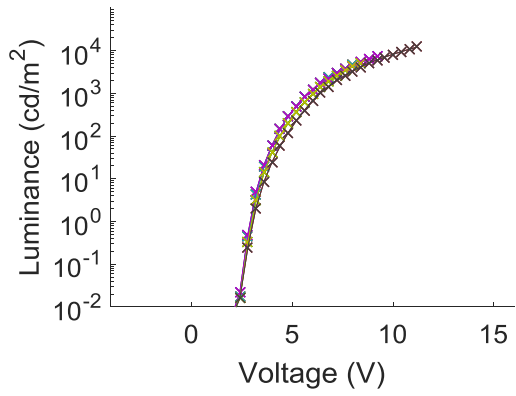
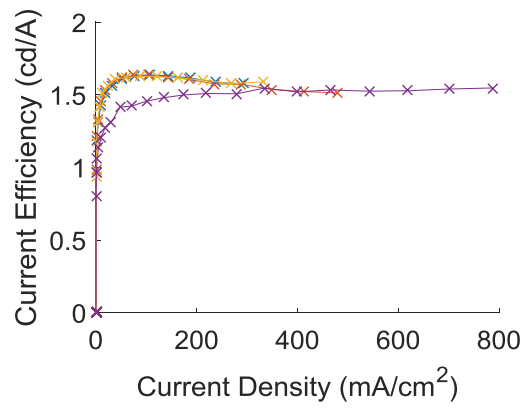
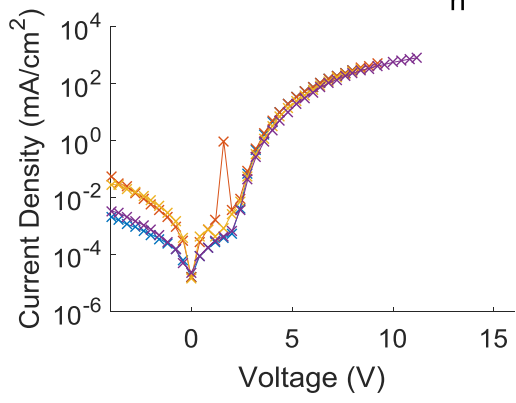
$M_n = 67 \text{ kg/mol}$



$M_n = 100 \text{ kg/mol}$



$M_n = 160 \text{ kg/mol}$



Appendix E

In Chapter 5, the Murgatroyd model of field-dependent charge transport was applied to the high voltage region (9-10 V) of JV measurements of hole-only devices. Modelling each device current density with the extracted β and μ_0 values resulted in perfect fits over the mid-to-high voltage regimes, though it overestimated the expected current at lower voltages. This demonstrated that the application of a field-dependent model is not appropriate when there is evidence that the current density is being modulated by the existence of localised trap states as shown in figure 5.17. This Appendix complements Section 5.5.2. by demonstrating that one can extract β and μ_0 values over a particular voltage range, resulting in a perfect fit over those particular voltages to the detriment of other voltages. Here, the JVs are plotted according to equation 5.8, but with the linear fit applied over the low forward bias regime (figure E.1). Extracted β and μ_0 are shown in figure E.2 (differing considerably to that shown in figure 5.21). Figures E.3-E.5 plot the theoretical fits over the experimental data.

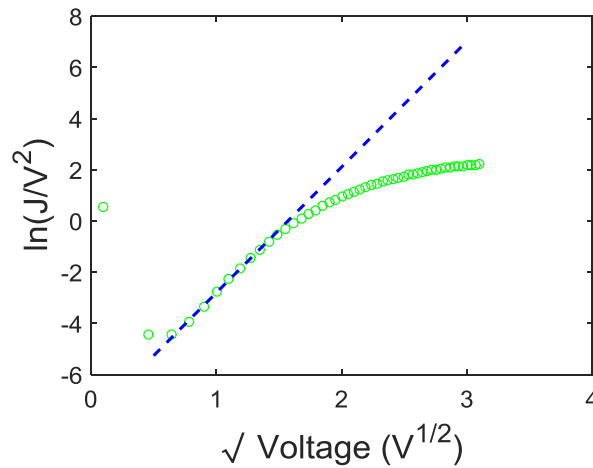


Figure E.1: An example of applying a fit to the low voltage linear region of a J - V characteristic processed via equation 5.8.

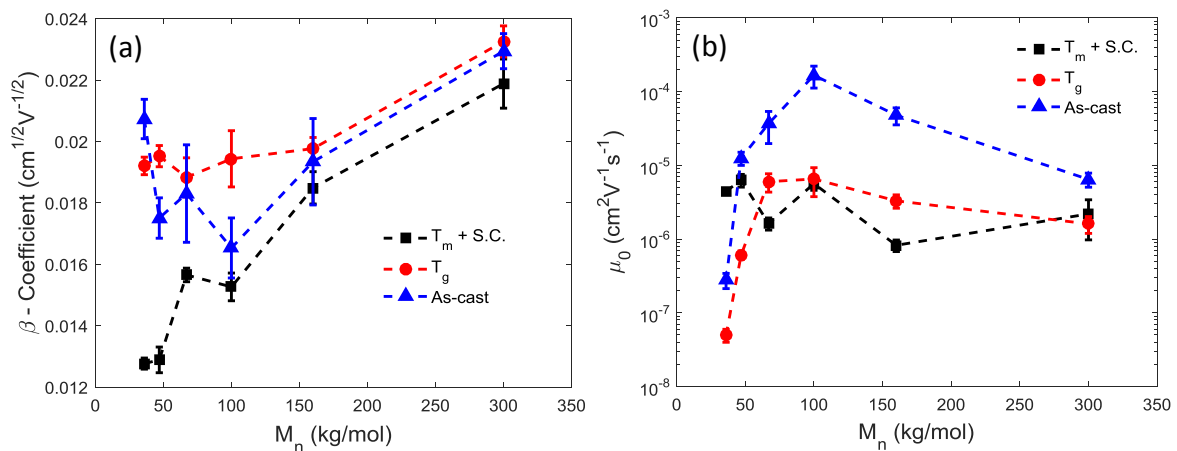


Figure 5.20: (a) Variation of the Poole-Frenkel Coefficient β and (b) the zero-field hole mobility μ_0 as a function of F8BT MW across as-cast, T_g -annealed and slow-cooled from T_m hole-only devices. Extracted from the low voltage region.

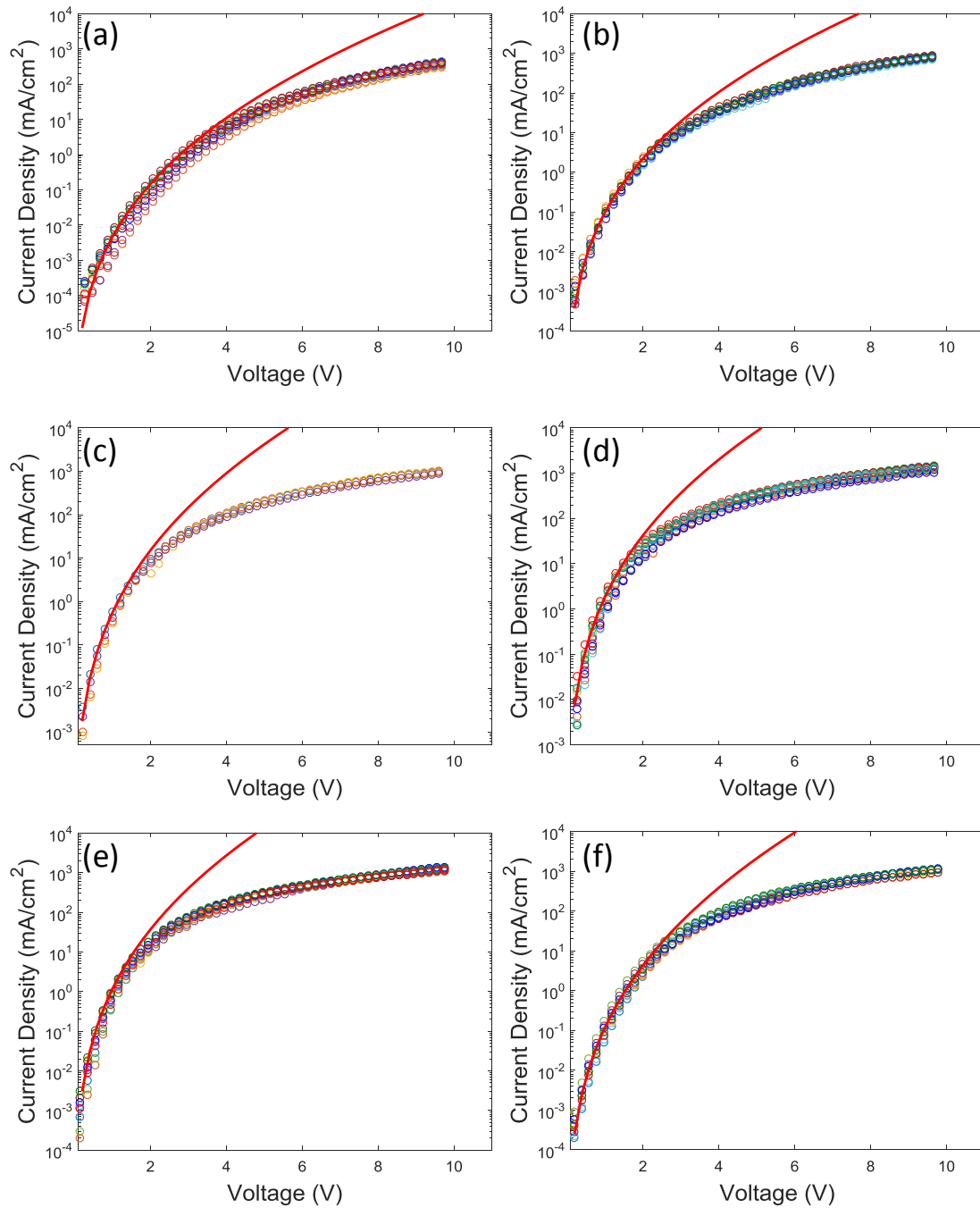


Figure 5.21: Fits of the Murgatroyd equation (solid red line) to the J - V measurements of several pixels (different coloured circles) for the as-cast hole-only diodes where (a)-(f) correspond to the fractions 36-300K respectively.

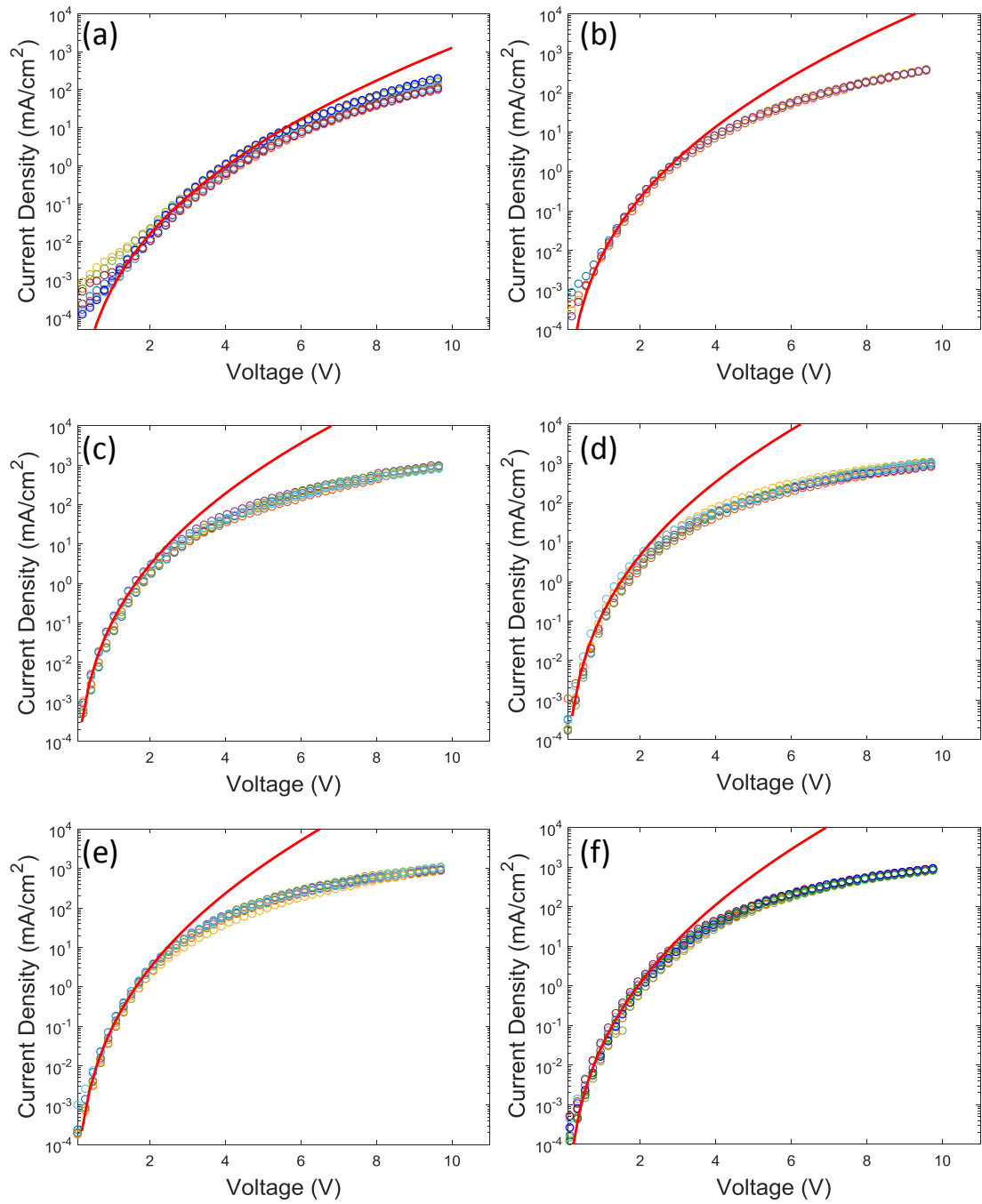


Figure 5.22: Fits of the Murgatroyd equation (solid red line) to the J - V measurements of several pixels (different coloured circles) for the T_g -annealed hole-only diodes where (a)-(f) correspond to the fractions 36-300K respectively.

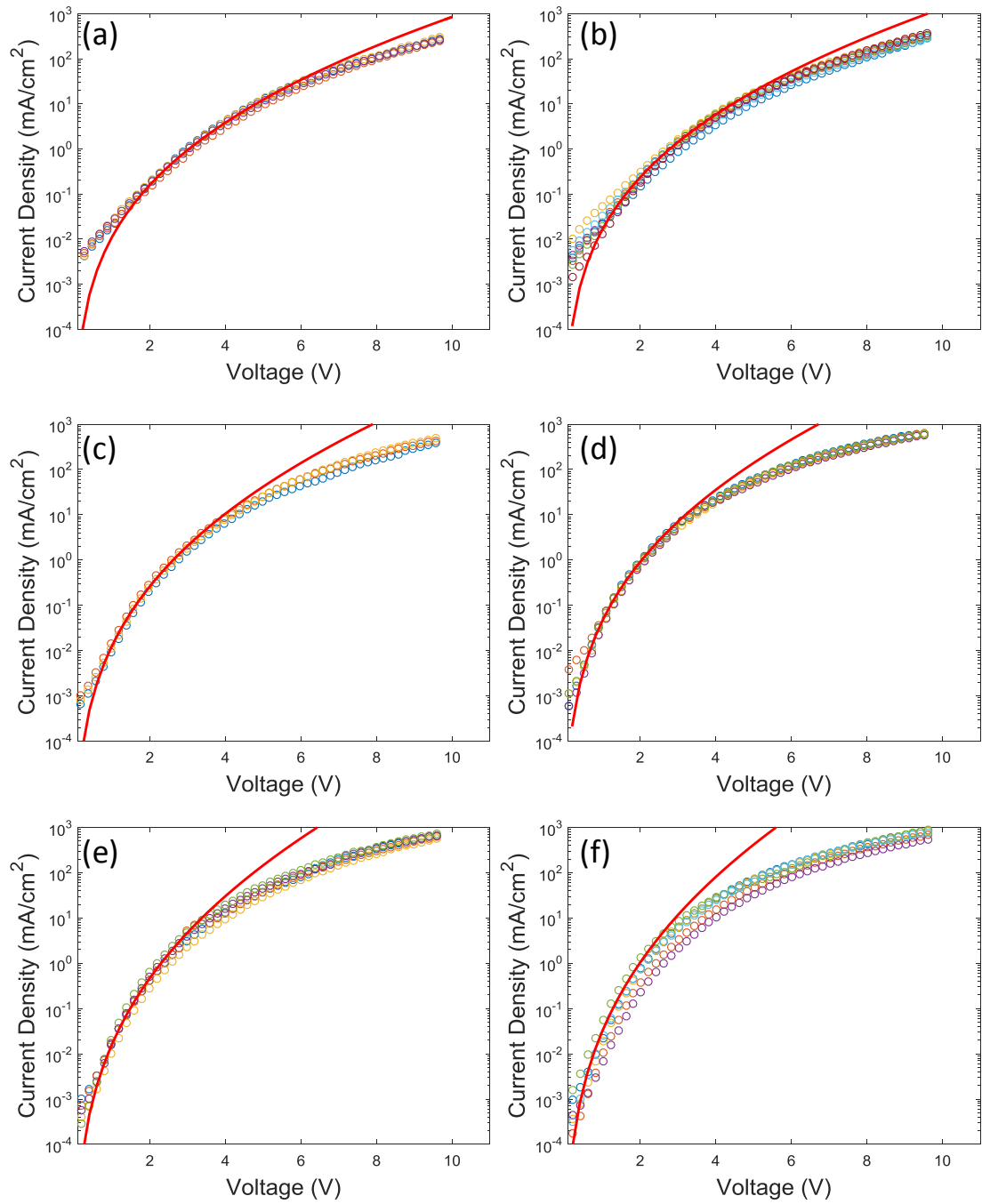


Figure 5.23: Fits of the Murgatroyd equation (solid red line) to the J - V measurements of several pixels (different coloured circles) for the slow-cooled from T_m hole-only diodes where (a)-(f) correspond to the fractions 36-300K respectively.